

Department Of Chemistry  
University of Cambridge

---

# Higher Order Structure in the Energy Landscapes of Model Glass Formers

---

This dissertation is submitted to the University of Cambridge for the  
degree of Doctor of Philosophy

**Samuel Peter Niblett**  
St Catharine's College

April 2018

---

# Higher Order Structure in the Energy Landscapes of Model Glass Formers

Samuel Peter Niblett

## Abstract

The study of supercooled liquids and glasses remains one of the most divisive and divided fields in modern physics. Despite a vast amount of effort and research time invested in this topic, the answers to many central questions remain disputed and incomplete. However, the link between the behaviour of supercooled liquids and their energy landscapes is well established and widely accepted. Understanding this link would be a key step towards resolving many of the mysteries and controversies surrounding the glass transition. Therefore the study of glassy energy landscapes is an important area of research.

In this thesis, I report some of the most detailed computational studies of glassy potential energy landscapes ever performed. Using geometry optimisation techniques, I have sampled the local minima and saddle points of the landscapes for several supercooled liquids to analyse their dynamics and thermodynamics.

Some of my analysis follows previous work on the binary Lennard-Jones fluid (BLJ), a model atomic liquid. BLJ is a fragile glass former, meaning that its transport coefficients have super-Arrhenius temperature dependence, rather than the more usual Arrhenius behaviour exhibited by strong liquids. The difference in behaviour between these two classes of liquid has previously been attributed to differing degrees of structure in the relevant energy landscapes.

I have studied models for both fragile and strong glass formers: the molecular liquid ortho-terphenyl (OTP) and viscous silica ( $\text{SiO}_2$ ) respectively. My results for OTP agree closely with trends observed for BLJ, suggesting that the same diffusion mechanism is applicable to fragile molecular liquids as well as to atomic. However, the dynamics and energy landscape of OTP are made complicated by the molecular orientational degrees of freedom, making the analysis more challenging for this system.

Dynamics of BLJ, OTP and silica are all dominated by cage-breaking events: structural rearrangements in which atoms change their nearest neighbours. I propose a robust and general method to identify cage breaks for small rigid molecules, and compare some properties of cage breaks between strong and fragile systems.

The energy landscapes of BLJ and OTP both display hierarchical ordering of

---

potential energy minima into metabasins. These metabasins can be detected by the cage-breaking method. It has previously been suggested that metabasins are responsible for super-Arrhenius behaviour, and are absent from the landscapes of strong liquids such as  $\text{SiO}_2$ . My results indicate that metabasins are present on the silica landscape, but that they each contain fewer minima than metabasins in BLJ or OTP.

Metabasins are associated with anticorrelated particle motion, mediated by reversed transitions between minima of the potential energy landscape. I show that accounting for time-correlation of particle displacement vectors is essential to describe super-Arrhenius behaviour in BLJ and OTP, but also required to reproduce strong behaviour in silica. I hypothesise that the difference between strong and fragile liquids arises from a longer correlation timescale in the latter case, and I suggest a number of ways in which this proposition could be tested.

I have investigated the effect on the landscape of freezing the positions of some particles in a BLJ fluid. This “pinning” procedure induces a dynamical crossover that has been described as an equilibrium “pinning transition”, related to the hypothetical ideal glass transition. I show that the pinning transition is related to (and probably caused by) a dramatic change in the potential energy landscape.

Pinning a large fraction of the particles in a supercooled liquid causes its energy landscape to acquire global structure and hence structure-seeking behaviour, very different from the landscape of a typical supercooled liquid. I provide a detailed description of this change in structure, and investigate the mechanism underlying it.

I introduce a new algorithm for identifying hierarchical organisation of a landscape, which uses concepts related to the pinning transition but is applicable to unpinned liquids as well. This definition is complementary to metabasins, but the two methods often identify the same higher-order structures. The new “packings” algorithm offers a route to test thermodynamic theories of the glass transition in the context of the potential energy landscape.

Over the course of this thesis, I discuss several different terms and methods to identify higher-order structures in the landscapes of model glass formers, and investigate how this organisation varies between different systems. Although little variation is immediately apparent between most glassy landscapes, deeper analysis reveals a surprising diversity, which has important implications for dynamical behaviour in the vicinity of the glass transition.

# Declaration

This dissertation is the result of my own work and includes nothing which is the outcome of work done in collaboration except where specifically indicated in the text.

I further state that no substantial part of my dissertation has already been submitted, or, is being concurrently submitted for any such degree, diploma or other qualification at the University of Cambridge or any other University or similar institution except as declared in the Preface and specified in the text

It does not exceed the prescribed word limit for the relevant Degree Committee.

Signature: \_\_\_\_\_

Date: \_\_\_\_\_

# Acknowledgements

Neither this thesis nor the work that it describes would have been possible without the support and assistance of a large number of people. I would like to thank a few of those people here.

Firstly, and most importantly, I would like to thank Professor David Wales for his guidance and encouragement throughout the project, and for creating a positive research environment in which I have felt able to make my own decisions.

I would like to thank the various people with whom I have collaborated during my PhD, particularly Dr Vanessa de Souza, whose mentorship and supervision of my various projects was invaluable, and Dr Jacob Stevenson for his patience in teaching me good programming style and practice. Thanks also to Dr Robert Jack, who provided the motivation for chapter 5 and valuable expertise in the literature of the RFOT theory, and to Myra Biedermann who carried out some of the initial work for chapter 4.

I am also very grateful to any and all members of the Wales group who have fielded my various pleas for help and advice, particularly in navigating the more obscure parts of the group software.

I gratefully acknowledge the financial support of the Cambridge Home Scholarship Scheme and the Chemistry department for the duration of my PhD.

Particular thanks are due to several people for helping to proof-read parts of this thesis: Dr Aatreyee Banerjee, Peter Niblett and Ruth Price.

Many thanks to everyone who has provided moral support and distraction during my PhD, especially the last few months. To my housemates, to the Woodlarks, to my family, thank you all. I promise I won't put you through this again.

Lastly, and always, I owe a huge debt of thanks to my wonderful fiancée Mary, for her comfort, support and wisdom in all aspects of my life. She has shared in all the trials and successes of my PhD, and I could not have done it without her.

# Glossary of Abbreviations

AA	Angle-Axis system
AG	Adam-Gibbs theory
BLJ	Binary Lennard-Jones fluid
BKS	van Beest, Kramer, and van Santen model
CB	Cage Break
CELS	Cambridge Energy Landscapes Software
CoM	Centre of Mass
CRR	Cooperatively Rearranging Region
DF	Dynamical Facilitation theory
DNEB	Doubly Nudged Elastic Band
EMB	Energy Metabasin
MD	Molecular Dynamics
HEF	Hybrid Eigenvector-following
INM	Instantaneous Normal Mode
IS	Inherent Structure
iSLERP	Incremental Spherical Linear Interpolation scheme
KCM	Kinetically Constrained Model
L-BFGS	Limited Memory Broyden-Fletcher-Goldfarb-Shanno algorithm
LFS	Locally Favoured Structures
LJ	Lennard-Jones potential
MB	Metabasin
MCB	Molecular Cage Break

---

MCT	Mode Coupling Theory
MEP	Minimum Energy Pathway
m.s.d.	Mean Square Displacement
NEB	Nudged Elastic Band
NMR	Nuclear Magnetic Resonance Spectroscopy
OTP	Ortho-terphenyl
PEL	Potential Energy Landscape
PELE	Python Energy Landscape Explorer
PTBH	Parallel Tempering Basin-hopping
RDF	Radial Distribution Function
REM	Random Energy Model
RFOT	Random First Order Transition theory
RPGT	Random Pinning Glass Transition
SANN	Solid Angle Nearest Neighbours algorithm
SCB	Site Cage Break
SDP	Steepest-Descent Pathway
SHD	Spatially Heterogeneous Dynamics
TS	Transition State
VTF	Vogel-Tammann-Fulcher fitting form

# Frequently-used Symbols

$\alpha_2(t)$	The non-Gaussian parameter for measuring ergodicity
$\Delta \mathbf{r}_i(j)$	Displacement of particle $i$ in the $j^{\text{th}}$ time interval
$\Delta S(T)$	Entropy difference between liquid and crystal
$\Delta t$	MD time step
$\Delta x$	Basin-hopping step size
$\epsilon_{\mu\nu}$	Lennard-Jones energy unit for interaction between atom types $\mu$ and $\nu$
$\epsilon_0$	Natural energy unit for the Stoddard-Ford Lennard-Jones potential
$\eta$	Viscosity
$\Sigma$	Complexity
$\theta_{jk}$	Angle between displacement vectors in time intervals $j$ and $k$
$\rho_{\text{IS}}(V)$	Density of local minima identified by basin-hopping
$\sigma_{\mu\nu}$	Lennard-Jones distance unit for interaction between atom types $\mu$ and $\nu$
$\tau_s$	Structural relaxation time
$\tau_\alpha$	$\alpha$ -relaxation time constant
$\tau_{\text{MB}}$	Average metabasin lifetime
$\tau$	Non-ergodic time interval
$\Omega(t)$	Mountain-Thirumulai energy fluctuation metric
$C_p(T), C_v(T)$	Constant-pressure and constant-volume heat capacities
$c$	Fraction of pinned particles
$c^*(T)$	Critical pinned fraction
$c_s$	Correction factor for correlated cage breaks
$D(T)$	Self-diffusion constant

---

$D(\tau, T)$	Reduced-time diffusion constant
$D^*(\tau, T)$	Correlation-corrected reduced-time diffusion constant
$D_{\text{CB}}(T)$	Effective cage-breaking diffusion constant
$D_{\text{CB}}^*(T)$	Correlation-corrected cage-breaking diffusion constant
$D_{\text{prod}}(T)$	Productive cage-breaking diffusion constant
$D(k, l)$	Euclidean distance between two system configurations, $k$ and $l$
$d_c$	Displacement cutoff to define nearest-neighbour changes
$d_{\text{rev}}$	Threshold parameter for detecting reversed cage breaks
$e$	Electronic charge
$F(\mathbf{k}, t)$	Intermediate scattering function
$f(T), \tilde{f}(T)$	Frustration metric, renormalised frustration metric
$\tilde{f}_p(T)$	Packings frustration metric
$G(\mathbf{r}, t)$	van Hove correlation function
$g(r)$	Radial distribution function
$g_{\text{IS}}(V)$	Potential-energy density of inherent structures
$g_{\text{MB}}(V)$	Potential-energy density of metabasins
$\mathbf{g}(\mathbf{X})$	Potential energy gradient
$\mathbf{g}_{\text{band}}$	Elastic band energy gradient
$\mathbf{g}^{\text{NEB}}, \mathbf{g}^{\text{DNEB}}$	Nudged and doubly-nudged elastic band energy gradients
$\mathbf{H}(\mathbf{X})$	Potential energy Hessian matrix
$k_{\text{B}}$	Boltzmann's constant
$k_{\text{spr}}$	(D)NEB spring constant
$L$	Simulation cell side length
$l$	Cage break reversal chain length
$m$	Lennard-Jones mass unit
$N$	Number of atoms in a system
$N_r$	Number of rigid bodies in a molecular system
$\mathcal{N}$	Number of accessible quasistates
$p_{\alpha}^{\text{eq}}(T)$	Equilibrium occupation probability of minimum $\alpha$

---

---

$\tilde{p}_\alpha^{\text{eq}}$	Renormalised occupation probability of minimum $\alpha$
$Q(\mathbf{X}_i, \mathbf{X}_j)$	Overlap between two configurations
$Q_0(\mathbf{X})$	Overlap with the reference minimum
$Q_p(i, j)$	Overlap between two packings
$Q^*$	Critical overlap to define structural similarity
$q_\mu$	Atomic charge on atom type $\mu$
$R_i^{(m)}$	SANN nearest-neighbour cutoff for atom $i$ with $m$ nearest neighbours
$\mathbf{r}_i(t)$	Position vector of particle $i$ at time $t$
$\langle \mathbf{r}^2(t) \rangle$	Mean squared displacement at time $t$
$r_{ij}$	Distance between particles $i$ and $j$
$r_c$	Cutoff distance for pairwise potentials
$r_{\text{NN}}$	Cutoff distance to define the nearest-neighbour shell
$S_{\text{IS}}$	Landscape entropy
$S_{\text{vib}}$	Vibrational entropy
$T_{\text{VTF}}$	VTF divergence temperature
$T_c$	MCT critical temperature
$T_g$	Kinetic glass transition temperature
$T_K$	Kauzmann temperature
$T_m$	Melting temperature
$T_0$	Pinning reference temperature
$T^*(c)$	RPGT transition temperature
$T_{\text{bh}}$	Basin-hopping temperature
$T_{\text{bh},i}$	Replica temperature in PTBH
$t_p$	Caging plateau time
$t_v$	Vibrational time
$t_c$	Correlation time for cage breaks
$U(u, v)$	UNTRAP weight for a pair of minima $u$ and $v$
$V(\mathbf{X})$	Potential energy landscape
$\tilde{V}(\mathbf{X})$	basin-hopping transformed energy landscape

---

---

$V_i$	Potential energy of minimum $i$
$\langle V_{\text{IS}} \rangle$	Average inherent structure energy
$V_{ij}(r_{ij})$	Isotropic pair potential
$V_{\text{band}}$	Elastic band energy
$V_{uv}^\dagger$	Energy of the highest TS on the lowest-energy path between minima $u$ and $v$
$\mathbf{v}_i(t)$	Velocity of particle $i$ at time $t$
$W(u, v)$	Dijkstra weight for a connection between minima $u$ and $v$
$\mathbf{X}$	Vector containing coordinates of a single system configuration
$\mathbf{X}^*$	Pinning reference structure
$\mathbf{X}_0$	Pinning reference minimum
$Z(T)$	Total partition function
$Z_\alpha(T)$	Partition function associated with minimum $\alpha$

# Contents

<b>1</b>	<b>Introduction</b>	<b>1</b>
1.1	The Glass Transition . . . . .	1
1.2	Phenomenology of Supercooled Liquids . . . . .	3
1.2.1	Dynamical Properties . . . . .	3
1.2.1.1	Super-Arrhenius Behaviour . . . . .	3
1.2.1.2	Diffusion of Supercooled Liquids . . . . .	5
1.2.1.3	Relaxation in Supercooled Liquids . . . . .	7
1.2.1.4	Dynamic Heterogeneity . . . . .	9
1.2.2	Thermodynamic Properties . . . . .	10
1.2.2.1	Heat Capacity Feature . . . . .	10
1.2.2.2	The Kauzmann Paradox . . . . .	11
1.3	Dynamical Theories of the Glass Transition . . . . .	12
1.3.1	Mode Coupling Theory . . . . .	13
1.3.2	Caging and Jumping . . . . .	15
1.3.2.1	Single-particle Jumps . . . . .	15
1.3.3	Slow and Fast Particles . . . . .	17
1.3.4	Dynamical Facilitation Theory . . . . .	19
1.4	Thermodynamic Theories of the Glass Transition . . . . .	21
1.4.1	Entropy and the Ideal Glass Transition . . . . .	22
1.4.2	Adam-Gibbs Theory . . . . .	23
1.4.3	RFOT Theory . . . . .	24
1.5	The Pinning Transition . . . . .	26
1.6	Potential Energy Landscapes . . . . .	27
1.6.1	Introduction to Potential Energy Landscape Theory . . . . .	28
1.6.1.1	Minima of the PEL . . . . .	29
1.6.1.2	Thermodynamics from the PEL . . . . .	30
1.6.1.3	Transition States . . . . .	31
1.6.1.4	Funnel Structures . . . . .	32
1.6.1.5	System Sizes for PEL exploration . . . . .	33

1.6.2	Potential Energy Landscapes of Glass Formers . . . . .	34
1.6.2.1	Statistical Theory of Landscapes . . . . .	34
1.6.2.2	Inherent Structure Trajectories . . . . .	36
1.6.2.3	Energy Metabasins . . . . .	37
1.6.2.4	CTRW for Metabasins . . . . .	40
1.6.2.5	Structure of the PEL . . . . .	40
1.6.2.6	Alternative Characterisations of the PEL . . . . .	41
1.6.3	Outlook . . . . .	43
1.7	Diffusion and Energy Landscape of a Fragile Atomic Glass Former . .	43
1.7.1	Correlation Effects in BLJ Diffusion . . . . .	44
1.7.2	A Geometric Definition of Cage Breaks . . . . .	44
1.7.3	Cage Breaks on the PEL . . . . .	46
1.7.4	The Role of Connectivity . . . . .	48
<b>2</b>	<b>Methods</b>	<b>49</b>
2.1	Molecular Dynamics . . . . .	49
2.1.1	Fundamentals of Molecular Dynamics . . . . .	49
2.1.2	Practical Considerations . . . . .	51
2.1.3	Molecular Dynamics of Rigid Bodies . . . . .	53
2.1.4	Determining Local Ergodicity . . . . .	53
2.1.4.1	Mountain-Thirumalai Fluctuation Metric . . . . .	54
2.1.4.2	Non-Gaussian Parameter . . . . .	54
2.2	Potential Energy Landscape Exploration . . . . .	56
2.2.1	Identifying Local Minima . . . . .	56
2.2.1.1	Basin-hopping Global Optimisation . . . . .	57
2.2.1.2	Parallel Tempering Basin-hopping . . . . .	59
2.2.2	Transition State Searches . . . . .	60
2.2.2.1	Double-Ended Transition State Searches . . . . .	61
2.2.2.2	Transition State Refinement . . . . .	64
2.2.2.3	Discrete Paths and Connection Attempts . . . . .	65
2.2.3	Database Connection Strategies . . . . .	67
2.2.3.1	The UNTRAP Method . . . . .	67
2.2.4	Representing and Characterising the PEL . . . . .	68
2.2.4.1	The Frustration Index . . . . .	70
2.3	Rigid Body Methods . . . . .	72
2.3.1	Coordinate Systems . . . . .	72
2.3.2	The Angle-Axis System . . . . .	73
2.3.2.1	Euclidean Distance in Angle-Axis Coordinates . . . . .	74

<b>3</b>	<b>Energy Landscapes of Atomic and Molecular Fragile Glass Formers</b>	<b>76</b>
3.1	Introduction . . . . .	76
3.2	Model and Simulation Details . . . . .	77
3.2.1	Molecular Dynamics Simulation . . . . .	78
3.2.2	Sampling the PEL . . . . .	79
3.3	Cage-breaking Analysis . . . . .	80
3.3.1	Defining a Cage Break . . . . .	80
3.3.1.1	SANN Method . . . . .	82
3.3.2	Diffusion Constants . . . . .	82
3.4	Landscape Analysis . . . . .	86
3.4.1	Cage-Breaking Analysis of the Landscape . . . . .	87
3.5	Conclusions and Future Directions . . . . .	94
<b>4</b>	<b>Comparing Fragile and Strong Glass Formers</b>	<b>97</b>
4.1	Introduction . . . . .	97
4.2	Model . . . . .	99
4.2.1	Simulation Details . . . . .	102
4.3	Cage Breaking . . . . .	103
4.3.1	Defining a “Cage Break” in Silica . . . . .	103
4.3.2	Cage-Breaking Results . . . . .	105
4.3.2.1	Reversed Cage Breaks . . . . .	107
4.4	Potential Energy Landscape Analysis . . . . .	109
4.4.1	Disconnectivity Graph for Silica . . . . .	110
4.4.2	Cage-Breaking Analysis of the Landscape . . . . .	110
4.4.3	Geometric Metabasin Analysis . . . . .	112
4.5	Energy Landscapes for Different Classes of Glass Former . . . . .	115
4.5.1	Simple Landscape Metrics . . . . .	115
4.5.2	Frustration Metric . . . . .	117
4.6	Conclusions . . . . .	118
<b>5</b>	<b>Random Particle Pinning on the Potential Energy Landscape</b>	<b>120</b>
5.1	Methods . . . . .	121
5.1.1	Model . . . . .	121
5.1.2	Pinning Particles . . . . .	121
5.1.3	Comparing Structures . . . . .	122
5.1.4	Metastable States . . . . .	123
5.2	Potential Energy Minima . . . . .	124
5.2.1	Return Times . . . . .	125

5.2.2	Distribution of Local Minima . . . . .	126
5.2.2.1	Effect of Reference Temperature . . . . .	130
5.2.3	Disorder Averages . . . . .	130
5.2.4	Effect of System Size . . . . .	132
5.3	Organisation of the Landscape . . . . .	133
5.3.1	Disconnectivity Graphs . . . . .	133
5.3.2	Packings on the PEL . . . . .	137
5.3.2.1	Packings in Unpinned Landscapes . . . . .	139
5.3.3	Comparing Pinned Landscapes . . . . .	139
5.4	Evolution of the PEL with Pinning Fraction . . . . .	142
5.4.1	Evolution of Minima . . . . .	143
5.4.2	Evolution of the Packings . . . . .	144
5.5	Conclusions . . . . .	147
<b>6</b>	<b>Correlated Motion in Model Glass Formers</b>	<b>149</b>
6.1	Introduction . . . . .	149
6.2	Short-time Diffusion Constants . . . . .	149
6.2.1	Correlation-corrected Diffusion Constants . . . . .	150
6.3	Fragile Glass Formers . . . . .	151
6.3.1	A More Sophisticated Intermolecular Potential for OTP . . . . .	154
6.4	Strong Glass Formers . . . . .	155
6.4.0.1	Correlation Times Scales in Cage Breaks . . . . .	159
6.5	Pinned Glass Formers . . . . .	160
6.6	Conclusions . . . . .	163
<b>7</b>	<b>Conclusions</b>	<b>165</b>
	<b>References</b>	<b>169</b>

# Chapter 1

## Introduction

### 1.1 The Glass Transition

A structural glass is a mechanically solid material that lacks the long-range periodic order of a crystal. There are several naturally-occurring glasses, notably obsidian<sup>1</sup> and other volcanic materials. A much larger number of synthetic glasses are known, with a huge variety of uses, from the ubiquitous silica glass through to more exotic metallic glasses<sup>2</sup> and amorphous organic solids used as pharmaceuticals.<sup>3</sup>

The commercial and industrial significance of glasses would be sufficient to motivate their study, but amorphous solids are also a subject of intense theoretical interest, because they are among the simplest physical systems that exist out of thermodynamic equilibrium on experimentally accessible time scales.

Crystals are more stable than liquids at low temperatures because the periodically-repeating pattern of strong chemical bonds (or other intermolecular forces) gives the crystal structure a low potential energy. In liquids, the lack of translational symmetry often reduces the number of favourable nearest-neighbour contacts and raises the energy. Of course, this disorder ensures that liquids have higher entropy than crystals. At high temperatures the entropy term dominates the free energy of the system, so the liquid becomes the thermodynamically preferred state.

A glass has a disordered molecular structure, similar to a liquid, but exists at low temperatures where entropy is less important than potential energy. Consequently, glass has higher free energy than the corresponding crystal and is a metastable, out-of-equilibrium phase.

The concept of equilibrium depends on the time scale of observation.<sup>4</sup> Given sufficient time, a glass will relax to the more stable crystal. For a material to qualify as a glass, its structural relaxation time must be large enough that this crystallisation is negligible on any reasonable experimental time scale. The structural relaxation

time,  $\tau_s$ , is a measure of how quickly the system recovers from an applied perturbation. Different measurement techniques yield different values of  $\tau_s$ , but for the present discussion all values are similar enough that we may consider this quantity to be well defined.  $\tau_s \propto \eta$ , the viscosity. It is generally agreed that  $\eta > 10^{12}$  Pa s is sufficient to define glassy behaviour.<sup>5,6</sup> The equivalent criterion in the relaxation time is approximately  $\tau_s > 100$  s.<sup>7</sup>

How does one obtain a metastable glass? At low temperatures, a crystal will form if the system is allowed time to explore its entire configuration space, so glasses must be prepared rapidly to break ergodicity. The most common approach is rapid cooling of a liquid, so that crossing diffusive energy barriers becomes a rare event and atomic transport slows down, dramatically retarding crystallisation. A liquid may thus be supercooled below its melting temperature without forming the stable crystal.

On continued cooling, transport coefficients decrease further and the material becomes mechanically solid (*vitrifies*) near to  $\eta = 10^{12}$  Pa s. The corresponding temperature  $T_g$ , identifies the *kinetic glass transition*. However, this event is not an equilibrium phase transition, because  $T_g$  varies with cooling rate. Difficulties in measuring large viscosities mean that  $T_g$  is often determined calorimetrically (see §1.2.2). In many cases  $T_g \approx 2T_m/3$ , where  $T_m$  is the melting point.<sup>8</sup>

The kinetic glass transition corresponds to a frustration of the intermolecular bond network, which remains disordered as in the liquid, but rearrangements are so slow that conversion to the crystal is essentially impossible. The requirement to frustrate the bond network means that only certain types of liquid form glasses easily. Single-component atomic materials (e.g. silicon and most metals) very rarely form glasses because the interatomic interactions in these materials are isotropic and uniform between particles. Molecular liquids and binary mixtures, on the other hand, are much easier to frustrate and hence vitrify at cooling rates slow enough to be experimentally achievable.<sup>9,10</sup>

Alternative methods of preparing glasses are known, particularly vapour deposition.<sup>11,12</sup> The mechanism of formation of these materials is clearly rather different from vitrification of supercooled liquids, and so lies beyond the scope of this thesis, despite being a fascinating and important problem.

Supercooled liquids and the kinetic glass transition have been studied for many years. In that time, a qualitative picture has emerged of the origins and nature of the transition, supported by the simple thermodynamic arguments outlined above. But a single quantitative theory to predict the behaviour of supercooled liquids and glasses is still lacking. Instead, a plethora of competing and possibly contradictory

approaches have developed that attempt to explain some or all aspects of glass transition phenomenology. Each theory has failures as well as successes, and there is no clear explanation for many of the fundamental discrepancies between them.

Resolving the conflicts between the different theories of the glass transition is, in my opinion, one of the key challenges of the coming decades for the condensed matter community. It seems likely that many of these theories are compatible, and probably describe the same phenomena, but in different ways and with different regimes of applicability. One of the objectives of this thesis (particularly chapters 3-4) is to draw links between different methods of identifying the structural transitions that contribute to diffusion in model glass formers.

Both experimental and computational studies of glass-forming liquids have revealed multiple types of anomalous behaviour, and explaining them is a key task of simulation and theory. Some of these anomalies will be relevant to the results presented in later chapters, and so a few of the most important and most relevant issues will be introduced in the following section. In §1.3-§1.6, some of the main theories of the glass transition are discussed. Particular emphasis will be given to methods based on the potential energy landscape (§1.6.1), which I have used in this work.

## 1.2 Phenomenology of Supercooled Liquids

### 1.2.1 Dynamical Properties

Since the laboratory glass transition is an out-of-equilibrium kinetic event, it is no surprise that many of the phenomena associated with it are dynamical and kinetic in nature. The volume of literature concerning these phenomena is so large that a comprehensive survey is impractical, but here I introduce several unusual properties of supercooled liquids that will be particularly relevant to the subsequent discussion.

#### 1.2.1.1 Super-Arrhenius Behaviour

The essential characteristic of a kinetic glass former is the rapid variation of its structural relaxation time with temperature. Relaxation is readily measured in computer simulations, through diffusion coefficients<sup>13-16</sup> and calculated scattering functions.<sup>17-19</sup> Transport coefficients such as viscosity<sup>20</sup> are accessible to experiment, as are relaxation times measured by NMR<sup>21</sup> and dielectric loss spectroscopy.<sup>22-24</sup>

Transport processes related to crossing a fixed energy barrier obey the Arrhenius law: their rates vary with temperature according to  $e^{(\pm B/T)}$  for constant  $B$ . However

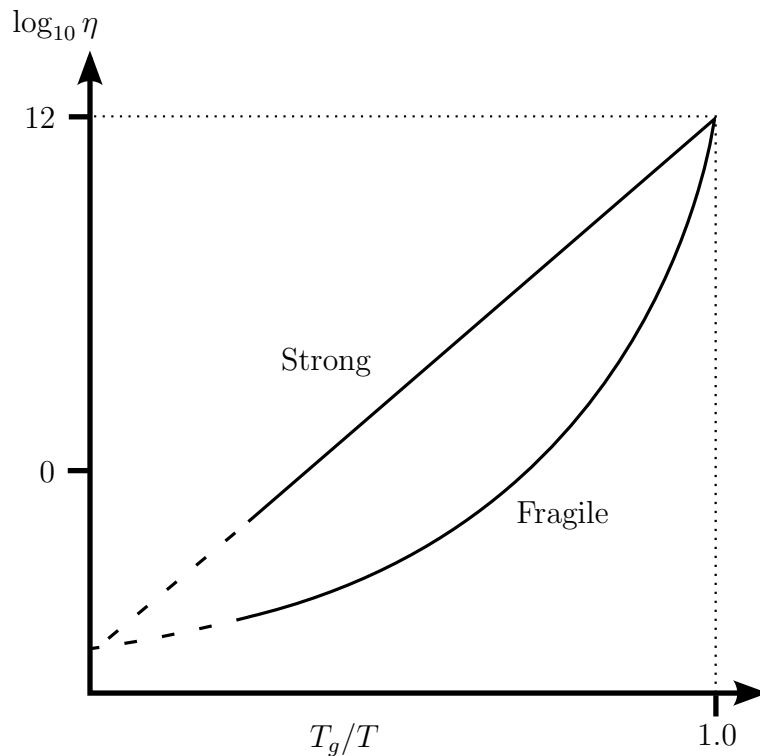


Figure 1.1: Schematic figure showing the difference between transport properties in strong liquids (Arrhenius temperature-dependence) and fragile (super-Arrhenius).

a stronger “super-Arrhenius” temperature dependence is observed in the supercooled regime. This behaviour is often modelled using the Vogel-Tammann-Fulcher (VTF) equation:<sup>25,26</sup>

$$\tau_s = \tau_0 e^{D_T T_{\text{VTF}} / (T - T_{\text{VTF}})}. \quad (1.1)$$

Here  $\tau_s$  represents a structural relaxation time, for example  $\tau_\alpha$  measured from the intermediate scattering function.  $\tau_0$  is a constant that depends on the method of measuring  $\tau_s$ , and  $T_{\text{VTF}}$  is a constant that depends on the liquid.  $D_T$  is the “strength parameter”<sup>25</sup> which is used to classify liquids as *strong* or *fragile*. High  $D_T$  and/or low  $T_{\text{VTF}}$  correspond to a strong liquid, showing approximately Arrhenius behaviour over a wide temperature range, while a fragile liquid with low  $D_T$  and high  $T_{\text{VTF}}$  shows a highly non-linear increase in  $\log \tau_s$  as  $T \rightarrow T_g$ . This distinction is demonstrated in fig. 1.1, which represents the viscosity  $\eta \propto \tau_s$  as a function of inverse temperature.

Strong molecular liquids seem to be quite rare,<sup>8</sup> and it has been hypothesized that strong liquids are those with highly directional intermolecular/interatomic forces, while fragile liquids have isotropic interactions.<sup>27,28</sup>

Note that the VTF form (eq. (1.1)) implies a divergence of the relaxation time

at  $T = T_{\text{VTF}}$ , where the system enters permanent dynamic arrest. This divergence is incompatible with the metastable nature of laboratory glasses, which probably indicates that the VTF form does not describe relaxation processes correctly at temperatures close to  $T_g$ .<sup>29</sup> However, some authors have equated the divergence temperature  $T_{\text{VTF}}$  with the Kauzmann temperature  $T_K$  that corresponds to the hypothetical “ideal glass transition”.<sup>30–32</sup> This theory will be discussed in detail in §1.2.2.2 and §1.4.

A quantitative explanation of super-Arrhenius behaviour is desirable because understanding the temperature dependence of relaxation processes is fundamental to understanding the kinetic glass transition. Moreover, fragility seems to be a good predictor for other properties of supercooled liquids.<sup>8</sup>

Super-Arrhenius behaviour is observed in the viscosity, relaxation time and the diffusion constants,  $D(T)$ . In simple liquids, these three properties have the same temperature dependence, but near to  $T_g$  they appear to decouple, violating both the well-known Stokes-Einstein relation  $D \propto T/\eta$  and the common approximation  $\tau_s \sim \eta/T$ .<sup>14,33</sup> This thesis is primarily concerned with the diffusivity of model supercooled liquids, and therefore the question of decoupling from other transport coefficients is set aside.

Super-Arrhenius behaviour must arise from one of two possible routes: either individual particles experience temperature-dependent energy barriers to relaxation, or each particle relaxes with Arrhenius temperature dependence but different particles have different average barrier heights for relaxation.<sup>34</sup> The latter idea is one manifestation of “dynamic heterogeneity”, discussed further in §1.2.1.4.

### 1.2.1.2 Diffusion of Supercooled Liquids

Translational self-diffusion of particles is the most fundamental transport process in a supercooled liquid, and the subject of extensive investigation. There are several experimental approaches to compute the diffusion constant,  $D(T)$ , also called the diffusivity. For example,  $D(T)$  may be inferred from the signal strength of stimulated echo NMR experiments,<sup>21,35,36</sup> or by fitting the measured relaxation time of a concentration gradient to Fick’s law.<sup>37,38</sup>

$D(T)$  is sometimes obtained from simulations using a Green-Kubo relation:<sup>39</sup>

$$D(T) = \int_0^\infty \langle v_{i,u}(t) \cdot v_{i,u}(0) \rangle_{i,u} dt \quad (1.2)$$

where  $v_{i,u}(t)$  is the velocity of particle  $i$  in Cartesian direction  $u$  at time  $t$ .  $\langle \dots \rangle_{i,u}$  indicates an average over particles, Cartesian directions and time origins, so  $\langle v_{i,u}(t) \cdot v_{i,u}(0) \rangle_{i,u}$

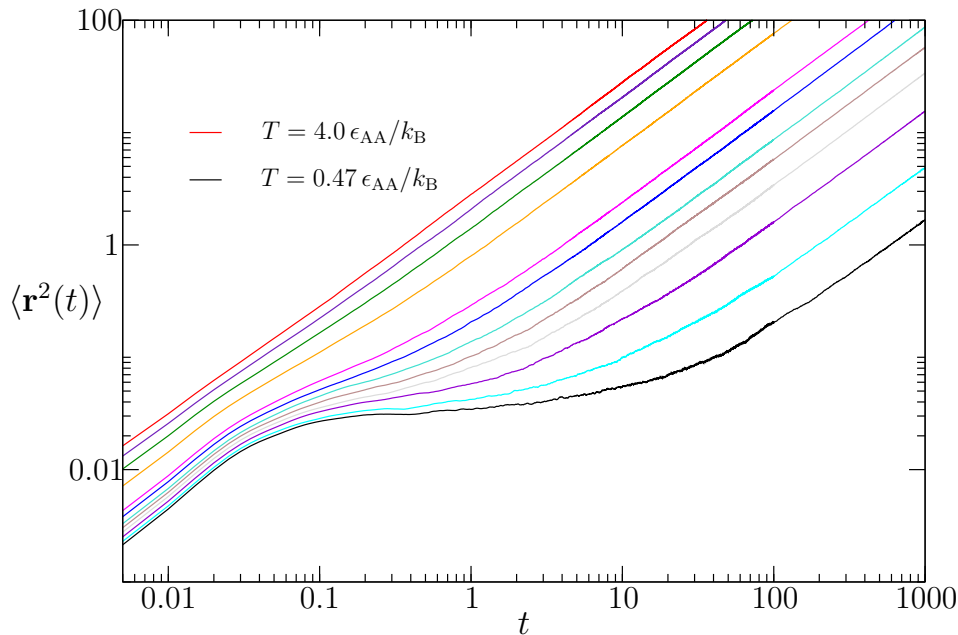


Figure 1.2: Plot of mean squared displacement  $\langle \mathbf{r}^2(t) \rangle$  against time for simulations of the BLJ fluid at a range of temperatures.

is the velocity autocorrelation function, which is accessible to molecular dynamics simulation.<sup>40–42</sup>

The most direct method of determining  $D(T)$  is using the Einstein equation:

$$D(T) = \lim_{t \rightarrow \infty} \frac{1}{6t} \langle |\mathbf{r}_i(t) - \mathbf{r}_i(0)|^2 \rangle, \quad (1.3)$$

where  $\mathbf{r}_i(t)$  is the position of atom  $i$  at time  $t$ .  $\langle \dots \rangle$  represents an average over particles and time origins. I will use the shorthand notation  $\langle \mathbf{r}^2(t) \rangle$  to denote the mean square displacement,  $\langle |\mathbf{r}_i(t) - \mathbf{r}_i(0)|^2 \rangle$ .

$\langle \mathbf{r}^2(t) \rangle$  is very simple to extract from a simulation,<sup>10,14,17,43</sup> but very challenging to determine experimentally for atomic or molecular glasses, since it requires direct observation of individual molecular trajectories. However, colloidal suspensions can be used to model hard-sphere glass formers, and confocal microscopy has been used to measure  $\langle \mathbf{r}^2(t) \rangle$  in these systems.<sup>44–46</sup>

The temperature variation of  $\langle \mathbf{r}^2(t) \rangle$  for the binary Lennard-Jones (BLJ) fluid is shown in fig. 1.2 (see also [10,44]). At all temperatures, the mean squared displacement is quadratic in  $t$  at short times, indicating a ballistic regime where each atom behaves like a free particle with its motion largely unaffected by the forces acting on it. At long times,  $\langle \mathbf{r}^2(t) \rangle \propto t$ , corresponding to diffusive motion. In this regime the effect of intermolecular collisions and interactions is averaged out, so that each particle follows an effective random walk.

At high temperatures, the ballistic and diffusive regimes are connected directly, but at low temperatures they are separated by a plateau in  $\langle \mathbf{r}^2(t) \rangle$  where the system is in temporary dynamical arrest. This time regime corresponds to particle caging. Each particle is confined in a cavity by repulsive interactions from nearby particles, and when ballistic motion brings the central particle to the walls of this “cage” it will usually be reflected. The plateau in  $\langle \mathbf{r}^2(t) \rangle$  represents a time scale on which most particles are confined in their cages, so particle displacements on this timescale are strongly negatively correlated<sup>47</sup> and the net motion is close to zero.

For a particle to escape from its cage (known as a cage breaking process) requires crossing a relatively high energy barrier. These events are consequently quite rare, particularly at low temperatures. The diffusive regime begins once every particle has had time to execute multiple cage breaks, so that the dynamics appear smooth and continuous rather than consisting of discrete jumps. The width of the caging plateau increases with decreasing temperature.

Particle caging is a fundamental component of the mode-coupling theory of the glass transition (§1.3.1) and must be reproduced by any other successful theory of supercooled liquid dynamics. Cage-breaking motions have been studied by a number of different approaches (§1.3.2) and will be very important to the subsequent arguments of this thesis.

As noted above, many fragile glass formers are molecular, meaning that they undergo both translational and rotational diffusion. The temperature dependence of these two components is identical at high temperatures, but decouples in the supercooled regime. However, the observed decoupling effect seems to vary with the method of measuring the rotational diffusion constant.<sup>13,36,44,48,49</sup>

The origin and nature of translational-rotational decoupling is still a matter of debate. Chapter 3 concerns a molecular glass former, but the analysis will be confined to translational diffusion to facilitate comparison with atomic glass formers, so translational-rotational decoupling will not be discussed in much detail.

### 1.2.1.3 Relaxation in Supercooled Liquids

In addition to the super-Arrhenius behaviour of characteristic structural relaxation times, the shapes of the corresponding relaxation functions are often anomalous. For undercooled liquids, a generic relaxation process  $\theta(t)$  is approximately exponential and characterised by a single time  $\tau_s$ . For glass-forming liquids near or below  $T_m$  this is often not the case.<sup>7,50</sup>

Structural relaxation can be measured in several ways. Here, I will focus upon the intermediate scattering function  $F(\mathbf{k}, t)$ , which measures correlations in the local

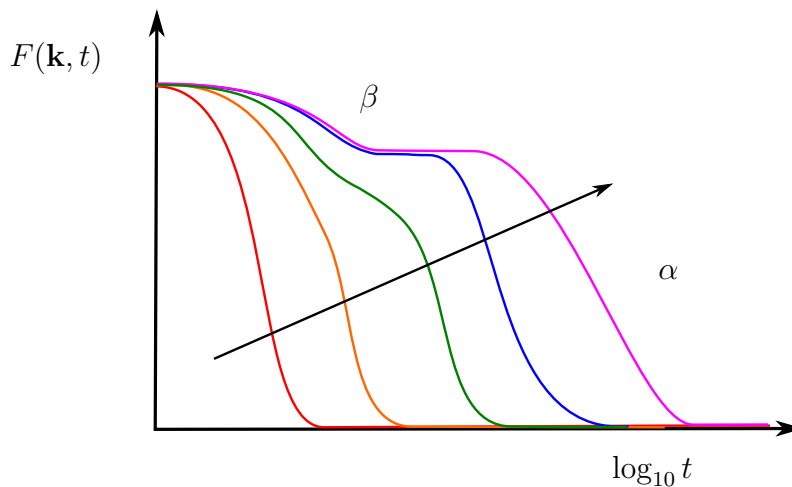


Figure 1.3: Idealised plot of the intermediate scattering function  $F(\mathbf{k}, t)$  against time for an arbitrary value of  $\mathbf{k}$  and a range of temperatures. The arrow indicates decreasing temperature. The time regions corresponding to  $\alpha$  and fast- $\beta$  relaxations are indicated. Experimental and simulation data are reported in the references.<sup>17,19,52</sup>

density as a function of time and correlation length scale:

$$F(\mathbf{k}, t) = \frac{1}{N} \langle \rho_{\mathbf{k}}(t) \rho_{-\mathbf{k}}(0) \rangle \quad (1.4)$$

where  $\rho_{\mathbf{k}}(t)$  is the Fourier transform of the fluid density:

$$\begin{aligned} \rho_{\mathbf{k}}(t) &= \int e^{i\mathbf{k}\cdot\mathbf{r}} \sum_i \delta(\mathbf{r} - \mathbf{r}_i(t)) d\mathbf{r} \\ &= \sum_i e^{i\mathbf{k}\cdot\mathbf{r}_i(t)}. \end{aligned} \quad (1.5)$$

$\mathbf{k}$  is the wavenumber (with dimensions of inverse length) that characterises the length scale of the density correlations.

$F(\mathbf{k}, t)$  is accessible from scattering experiments.<sup>51</sup> The time variation of  $F(\mathbf{k}, t)$  for typical  $\mathbf{k}$  is shown in fig. 1.3.

Since  $F(\mathbf{k}, t)$  is a correlation function, it has its maximum value at  $t = 0$  and decays as the system relaxes. At high temperature  $F(\mathbf{k}, t)$  displays simple liquid behaviour: exponential decay with a single time scale  $\tau_s$ .

At lower temperatures, three distinct time regimes are apparent, analogous to those in fig. 1.2. Initial exponential decay of  $F(\mathbf{k}, t)$ , called the fast- $\beta$  relaxation,<sup>4</sup> corresponds to the ballistic regime in fig. 1.2 and leads swiftly to a plateau caused by particle caging. The width of this plateau increases with decreasing temperature,

as before. Decay of  $F(\mathbf{k}, t)$  away from the plateau, described as the  $\alpha$  relaxation,<sup>53</sup> corresponds to cage escape motion. The relaxation function in this regime is not exponential, and instead is often fitted by a stretched exponential form:<sup>54,55</sup>

$$F(\mathbf{k}, t) \approx F(\mathbf{k}, t_p) \exp\left(-\frac{t}{\tau_\alpha}\right)^{\beta_s} \quad \text{for } t > t_p. \quad (1.6)$$

$t_p$  is the time at which the plateau terminates,  $\tau_\alpha$  is the characteristic time of the decay and  $\beta_s$  is the stretching parameter.  $\beta_s$  increases with temperature, recovering the simple-liquid limit  $\beta_s = 1$  at  $T > T_m$ .<sup>22,56</sup>

Dielectric loss experiments<sup>57–60</sup> yield similar information on structural relaxation. They suggest, however, that the slow cage-escape regime in fig. 1.3 is actually comprised of two relaxation processes: the  $\alpha$  relaxation described above, and a “slow- $\beta$ ” or “Johari-Goldstein  $\beta$ ” process at times intermediate between the two.<sup>57,60</sup>

It is generally assumed that the three different relaxation processes (fast- $\beta$ , Johari-Goldstein  $\beta$  and  $\alpha$ ) each correspond to different structural mechanisms. The fast process is assigned to exploration of a nearest-neighbour cage. The Johari-Goldstein process has been the subject of some debate,<sup>58–61</sup> but it seems clear that the slowest process, the  $\alpha$  relaxation, is the one that controls glass formation.

#### 1.2.1.4 Dynamic Heterogeneity

Non-exponential relaxation in eq. (1.6) shows that more than one time scale is required to describe the relaxation process.<sup>50</sup> This observation is explained by the presence of spatially heterogeneous dynamics (SHD) over anomalously long time scales,<sup>50</sup> meaning that different local regions of the system relax at different rates.

Indirect evidence for SHD is available through experiments.<sup>62–65</sup> For example, multidimensional NMR analyses slow- or fast-moving particles selectively,<sup>66,67</sup> and dynamic hole-burning<sup>68,69</sup> can selectively excite a subensemble of particles and follow their time evolution. Both methods show that fast particles remain spatially correlated for long time periods.

SHD are observed directly in simulations.<sup>70–74</sup> Single-particle relaxation times and diffusivity measured on short time scales can vary by several orders of magnitude between different regions of a sample, even separated by several nm.<sup>53</sup> Over longer periods of time, particles can sample both more- and less-mobile dynamic “environments”, with the result that the dynamics appear homogeneous on these time scales.<sup>75</sup>

The size of dynamically correlated domains defines a length scale that grows with decreasing temperature.<sup>73,76</sup> This growth may be related to breakdown of the

Stokes-Einstein relation, because different transport coefficients correspond to different averages over the distribution of local relaxation times.<sup>73</sup>

Reproducing SHD is an important test for any first-principles theory of supercooled liquids, particularly thermodynamic theories that require growing characteristic length scales as temperature decreases. Several computational methods for detecting fast and slow dynamical regions will be introduced in §1.3.3.

## 1.2.2 Thermodynamic Properties

The fact that  $T_g$  depends on the cooling rate tells us that the laboratory glass transition occurs out of equilibrium, and therefore there is no immediate reason to expect a role for equilibrium thermodynamics. However, thermodynamic quantities calculated for structural glass formers display two surprising features near the glass transition, which have led many authors to consider the possibility of an associated equilibrium phase transition that is not experimentally accessible.<sup>30,31,77,78</sup> A brief review of these ideas is given in §1.4, but first the key findings of experiment and simulation will be discussed.

### 1.2.2.1 Heat Capacity Feature

Several thermodynamic response functions, including the specific volume and refractive index, change abruptly close to the laboratory glass transition of some liquids.<sup>79</sup> We consider the constant-pressure heat capacity,  $C_p(T)$ , typically measured using differential scanning calorimetry.<sup>80,81</sup>

Fig. 1.4 shows the behaviour of  $C_p(T)$  when a fragile liquid is first cooled through its kinetic glass transition, and subsequently heated back above  $T_g$ . The drop in  $C_p$  on cooling is sudden but monotonic, suggesting a discontinuous jump related to a thermodynamic transition. However, fig. 1.4 also exhibits hysteresis: the heating curve displays a peak before regaining the liquid-like value of  $C_p$ , but the cooling curve does not. This asymmetry indicates that the heat capacity crossover is out of equilibrium, although it could still be connected to a different thermodynamic transition nearby in parameter space.<sup>79</sup>

The  $C_p$  peak detected during heating is a distinctive feature of the kinetic glass transition in fragile liquids. The onset temperature of this peak is easily reproducible and varies only slowly with heating rate so that it is often used as an alternative definition of the transition temperature  $T_g$ . The values of  $T_g$  obtained by this approach and by measuring the viscosity (§1.1) usually agree quite well.<sup>79</sup>

Strong liquids, particularly network glass formers such as silica,<sup>28</sup> have a very

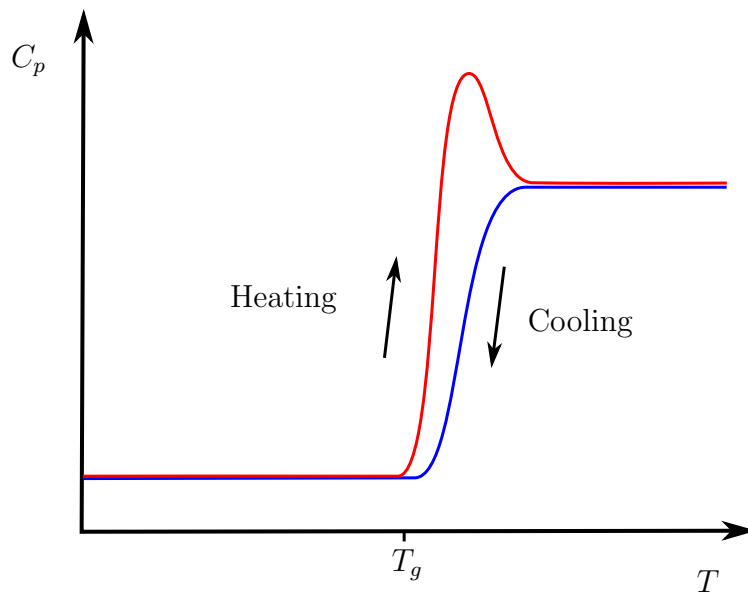


Figure 1.4: Pictorial representation of  $C_p(T)$ , the constant-pressure heat capacity, for a fragile glass former. Data such as these are obtained by differential scanning calorimetry, first cooling from liquid to glass and then heating from glass to liquid. Experimental data may be found in [82–84].

different  $C_p(T)$  profile: there is no sharp transition, no significant peak, and the limiting values of  $C_p$  for solid and liquid are closer than for fragile glasses. This difference has been taken to indicate a smaller liquid density of states in the strong case, brought about by the network structure.<sup>28</sup>

### 1.2.2.2 The Kauzmann Paradox

The idea that the kinetic glass transition masks a true equilibrium phase transition dates back at least to Kauzmann,<sup>77</sup> who integrated the experimental heat capacities of several liquids and crystals to compute the corresponding entropies. He demonstrated that when these data are extrapolated to a temperature  $T_K$  far below  $T_g$ , the entropy of the disordered supercooled liquid falls below that of the ordered crystal - an apparent paradox.

$T_K$  is too low to be accessed by equilibrium experiments: the kinetic glass transition always intervenes at higher temperature. However, Kauzmann’s scenario has stimulated extensive research because  $T_K$  coincides remarkably closely with  $T_{VTF}$ , the fitted divergence temperature of the VTF equation, for many liquids.<sup>31,53,85</sup> If one accepts the extrapolation of both the entropy and diffusivity below their experimentally accessible temperature range, one could conclude that structural arrest arises from the “entropy crisis” occurring at  $T_K$ , which would then correspond to an

equilibrium phase transition.

The entropy of a crystal arises mostly from vibration of the particles around a single equilibrium structure. In contrast, the entropy of liquids includes a significant contribution from the large number of amorphous structures explored. To achieve the condition  $\Delta S(T_K) = S_{\text{liquid}}(T_K) - S_{\text{crystal}}(T_K) = 0$ , some workers believe that the liquid must be confined to a single amorphous structure, known as an “ideal glass”. Therefore the event at  $T_K$  is sometimes referred to as an “entropy-vanishing transition”. This argument is described more fully in §1.4. The qualitative phase behaviour predicted by the Kauzmann scenario is shown pictorially in fig. 1.5.

Subsequent studies of hard sphere crystallisation have demonstrated that there is nothing paradoxical about the entropy of a crystal exceeding that of a liquid, because the greater free volume available to each particle in a crystal can lead to a greater vibrational density of states.<sup>86–89</sup> Moreover, there are plausible mechanisms by which the entropy crisis may be avoided, for example the kinetic spinodal argument<sup>32</sup> suggests that the kinetic glass transition must always and inevitably intervene before  $T_K$  is reached. It is also possible that the entropy extrapolation is simply wrong, although recent experiments<sup>90</sup> and simulations<sup>91</sup> that obtain equilibrium measurements very close to  $T_K$  are broadly consistent with Kauzmann’s scenario.

The hypothetical ideal glass transition is probably the most controversial topic in the glasses literature today.<sup>74,79,92</sup> Although it has limited practical use, the existence or otherwise of this transition has been promoted as a clear test for the various theories discussed in subsequent sections.

## 1.3 Dynamical Theories of the Glass Transition

In this section, I will introduce several key theories of supercooled liquids that make no explicit use of equilibrium thermodynamics. These theories are diverse both in their objectives and their mathematical approaches, so it is unsurprising that they have different regimes of validity.

Mode coupling theory (§1.3.1) and dynamical facilitation theory (§1.3.4) are the most comprehensive methods in this section, predicting observable quantities such as  $T_g$  by fitting experimental data to predicted functional forms. Mode coupling theory has been remarkably successful at predicting relaxation behaviour at mildly supercooled temperatures, but fails at lower temperatures where dynamical facilitation theory becomes more accurate.

Other methods described in §1.3.2 and §1.3.3 are more limited in scope. They

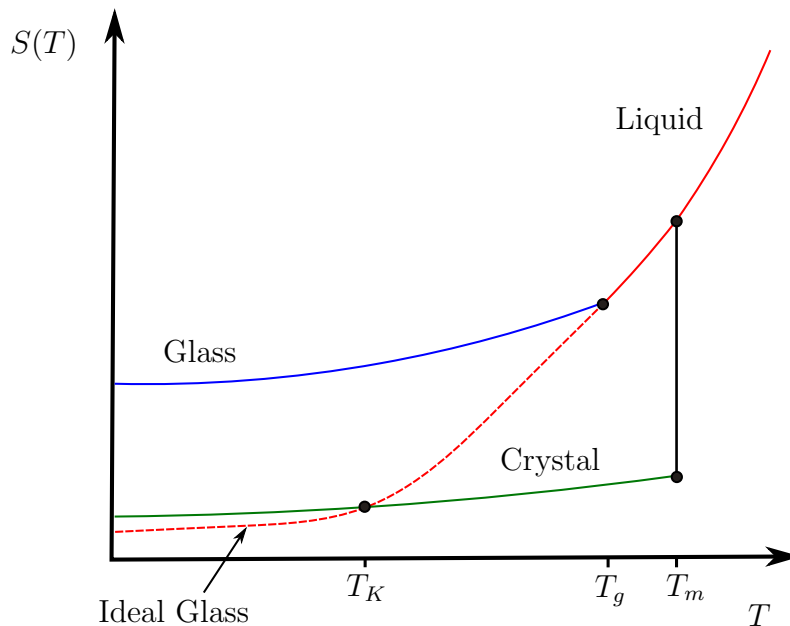


Figure 1.5: Pictorial phase diagram showing  $S(T)$  for a model glass former. The melting temperature,  $T_m$ , kinetic transition temperature,  $T_g$ , and extrapolated ideal glass temperature,  $T_K$ , are all shown. The red curve indicates liquid-like states, the green curve indicates an equilibrium crystal and the blue curve shows a representative kinetic glass (recall that  $T_g$  and the  $S(T)$  of the kinetic glass both depend on the cooling rate). The dashed red line is an extrapolation of the supercooled liquid entropy below the measurement limit of  $T_g$ .

seek to obtain mathematical descriptions of phenomena such as dynamical heterogeneity and the caging plateau, and to predict rates of diffusion and relaxation in the corresponding time and temperature regimes.

### 1.3.1 Mode Coupling Theory

One of the most common kinetic models for the behaviour of supercooled liquids is mode coupling theory (MCT), which attempts to explain transport properties by deriving analytical expressions for density autocorrelation functions and fluctuations.

Most importantly, MCT predicts the intermediate scattering function  $F(\mathbf{k}, t)$ , eq. (1.4), which is the main property measured by scattering experiments.<sup>51</sup> Therefore the predictions of MCT are easily tested.

Application of the projection operator formalism to Hamilton's equations yields an exact integro-differential equation for  $F(\mathbf{k}, t)$ . With several approximations this equation may be reduced to a soluble form,<sup>93</sup> the *mode coupling equations*, which comprise a damped harmonic oscillator and a nonlinear term in the *memory kernel*,  $m(\mathbf{k}, t)$ . This kernel contains most of the approximations associated with MCT, and

accounts for two time scales of relaxation: fast local relaxations and the “viscosity feedback” effect.<sup>4</sup>

Viscosity feedback arises from the caging effect described in §1.2.1.2: each atom is caged by its nearest neighbours but also forms part of their cages, so the vibrational modes of different cages are dynamically coupled. This feedback means that escape from cages must be partly cooperative, and hence that relaxation time depends on viscosity as well as viscosity depending on relaxation time.<sup>94</sup>

When the mode coupling equations are solved numerically, the temperature- and time-dependence of  $F(\mathbf{k}, t)$  is obtained.<sup>95</sup> The three regimes corresponding to ballistic, caged and diffusive motion are all reproduced correctly at moderately low temperatures, including correct prediction of stretched-exponential relaxation in the  $\alpha$  regime.

The caging plateau grows with decreasing  $T$ , and the original formulation of MCT predicts that the size of this plateau diverges when  $T = T_c$ , the MCT critical temperature. At this temperature, all particles are trapped within a particular set of cages with infinite lifetime, and the system enters dynamic arrest. According to the theory,  $T_c = T_g$  and the MCT critical point corresponds to the kinetic glass transition. However, fitting experimental and simulation data to MCT functional forms reveals that  $T_c$  and  $T_g$  do not coincide, and the absolute structural arrest predicted by MCT does not occur even below  $T_g$ .<sup>28,96–98</sup>

This failure of MCT occurs because the idealised expression for  $m(\mathbf{k}, t)$  neglects activated rearrangements, i.e. transitions across energy barriers. In the MCT literature these rearrangements are termed *hopping* events.<sup>95</sup> Activated processes dominate the dynamics at lower temperatures, allowing mass transport to continue after the collective modes described by MCT have arrested.

Some attempts have been made to extend MCT to account for hopping processes and other omissions.<sup>95,99</sup> These generalisations predict that  $F(\mathbf{k}, t)$  decays to zero at long times for all temperatures, and so also fail to predict the glass transition correctly.

Nevertheless, the original form of MCT has proved remarkably successful at predicting properties of liquids for weakly supercooled temperatures and/or short times. Several other theories (e.g. §1.4.3) only describe dynamics below  $T_c$ , because they consider MCT to be exact for  $T > T_c$  where continuous liquid-like rearrangements of a glass former are possible.<sup>31,74</sup>

Molecular dynamics simulations are often restricted to the time regime in which MCT is successful, hence they agree very well with MCT. In general MCT is better at predicting the properties of fragile liquids than strong.<sup>7</sup>

### 1.3.2 Caging and Jumping

The concept of particle caging was introduced in §1.2.1.2 and §1.3.1 to explain the plateaux in  $\langle \mathbf{r}^2(t) \rangle$  and  $F(\mathbf{k}, t)$ , respectively. As the temperature of a liquid decreases, particles spend increasingly long times trapped within cages of their nearest neighbours and long-time diffusion must occur via motions that disrupt these cages. Such motions become rarer as  $T$  decreases, eventually dominating diffusion.<sup>47,100</sup>

Consequently, low-temperature dynamical behaviour of glasses should be predictable using properties of the cage jumping processes, and methods to identify these events are of interest. Caging refers to the trapping of each particle by its nearest neighbours, hence methods based on changes to the nearest neighbours of an atom are particularly promising.

Rabani *et al.* developed a cage correlation function using this concept, which estimates the typical residence time within a given configuration of cages.<sup>101,102</sup> This function was used to reproduce non-exponential relaxation behaviour for fragile glass formers.<sup>103,104</sup>

Widmer-Cooper *et al.* used neighbour changes to diagnose *irreversible reorganisations* in simulations of hard-disc glass formers.<sup>105</sup> They determined that the probability of a particle recovering its original environment after losing four nearest neighbours was small ( $< 5\%$ ), and used this as a criterion for structural change (i.e. cage breaking).

De Souza and Wales proposed a more sophisticated definition of a cage-breaking processes using changes to the nearest neighbours of an atom. Extending and analysing their method is an important part of this thesis, so the original definition is presented in full in §1.7.2.

Doliwa and Heuer used single-particle three-time correlation functions to detect the negative correlations in particle displacements that arise from caging motion.<sup>47,106</sup> This method, and the Rabani approach, have both been tested on experimental hard-sphere colloid systems.<sup>45,46</sup>

#### 1.3.2.1 Single-particle Jumps

Near to  $T_c$ , small jumps may be seen in plots of  $|\mathbf{r}_i(t) - \mathbf{r}_i(0)|^2$  for an individual particle,  $i$ . Each particle spends long periods oscillating around a fixed position, before suddenly jumping to a new position.<sup>53</sup>

These jumps are significantly smaller than the typical interparticle distance, so they are probably not the same processes that are probed by measures of dynamical heterogeneity.<sup>107</sup> This observation also questions whether these small jumps actually describe cage-breaking motion, as is often claimed.<sup>108</sup> Nevertheless, attempts have

been made to approximate diffusion behaviour as a continuous time random walk (CTRW) of uncorrelated jumps.<sup>100,109,110</sup>

Jumps may be identified in a simulation or microscopy experiment by averaging an atomic position over a time interval comparable with the vibrational period. A measure of the maximum movement over this time period is compared with a cutoff to determine whether a jump has taken place. There are several cutoffs, and several measures of jump size, in use.<sup>100,110–112</sup>

Alternatively, some authors have identified jumps by dividing the trajectory of each particle into segments such that the centres of mass of the segments have maximal separation.<sup>113,114</sup> Jumps occur at the junctions between segments.

Given model distributions of jump lengths and waiting times between jumps, the CTRW model predicts a jump rate and average jump length, from which the diffusion constant and relaxation time may be calculated.<sup>107</sup> Helfferich *et al.* have shown that the Gamma distribution  $\psi(t) = At^{\alpha-1}e^{-\lambda t}$  is a good choice for the waiting time distribution.<sup>110</sup>

The CTRW model allows global long-time quantities (e.g. the diffusivity) to be predicted from local, short-time information (the properties of rapid cage-jumping events).<sup>100</sup> This property extends the range of temperatures that can be studied to include “aging” dynamics below  $T_g$ .<sup>115</sup>

The major weakness of CTRW is its assumption of markovian behaviour and its neglect of correlations between jumps, whereas simulation evidence suggests that single-particle jumps are clustered in time and space.<sup>107,113,114</sup> Moreover, a cluster of nearby jumps can facilitate another cluster a short time later, creating an “avalanche” that propagates through the system. These avalanches correspond to mobile regions in the SHD picture.<sup>107</sup>

Significant correlations have also been observed in sequences of jumps for individual particles. In particular, jump directions are negatively correlated so that jumps are often reversed.<sup>111</sup> Reversals can be detected when a particle returns to a previously occupied time-averaged position.<sup>112</sup> The CTRW method may be improved by excluding reversed jumps.<sup>109,110</sup>

The proportion of reversed jumps becomes much larger in low-temperature simulations of glasses.<sup>111,112</sup> This observation is attributed to slower relaxation of cold liquids, so that each jump leaves an empty space behind which may be quite long-lived.<sup>112</sup> The mobile particle is then very likely to jump back into this cavity. The same mechanism is believed to govern reversals of the larger cage-breaking motions, and this idea is elaborated significantly in §1.7 and the remainder of this thesis.

Given the omission of correlation effects, the CTRW gives surprisingly good

agreement with simulations of very simple model glass formers<sup>116</sup> and experiments on colloidal suspensions<sup>117</sup> at moderately supercooled temperatures.

### 1.3.3 Slow and Fast Particles

There are several approaches to detect and classify dynamical heterogeneities by dividing a supercooled liquid into slow and fast spatial domains. The main theoretical objective of this classification is to identify growing correlation length scales (i.e. domain sizes) as the temperature is decreased. If these lengths diverge at low  $T$ , then the kinetic glass transition may be related to a fixed sharp transition temperature.

The simplest way to divide particles into fast and slow is to compute a local relaxation time,<sup>118</sup> the average time taken for a particle to move by more than  $r_c$ . However, the success of these definitions depends heavily on the choice of  $r_c$ . Less subjective measures often make use of the van Hove correlation function,<sup>10,119</sup>

$$G(\mathbf{r}, t) = \left\langle \frac{1}{N} \sum_{i=1}^N \sum_{j=1}^N \delta(\mathbf{r} - [\mathbf{r}_j(t) - \mathbf{r}_i(0)]) \right\rangle \quad (1.7)$$

$$= G_s(\mathbf{r}, t) + G_d(\mathbf{r}, t), \quad (1.8)$$

where  $\delta$  is the Dirac delta function and  $\langle \dots \rangle$  indicates an ensemble average.  $G_s(\mathbf{r}, t)$  is the self part of the function, i.e. the sum of the terms in eq. (1.7) for which  $i = j$ , and  $G_d(\mathbf{r}, t)$  is the distinct part (the sum of terms for which  $i \neq j$ ). All parts of this function are straightforward to extract from a simulation.  $G(\mathbf{r}, t)$  and its components are often spherically averaged to produce two-dimensional functions e.g.  $G(r, t)$ , where  $r(t) = |\mathbf{r}(t)|$ .

For undercooled liquids,  $G_s(r, t)$  is Gaussian to a good approximation, but “fat tails” appear in the function at lower temperatures and intermediate times, particularly at large  $r$ .<sup>53,70</sup> These tails indicate a population of particles that are significantly more mobile than expected in the Gaussian approximation.

Glotzer *et al.* showed that these mobile particles are correlated in space, forming mobile clusters.<sup>70</sup> They plotted the contribution of the mobile particles to  $G_d(r, t)$ , and found that a strong peak appears at  $r = 0$  for  $t = t^*$ ,<sup>120</sup> indicating that mobile particles replace each other on times comparable to  $t^*$ . Mobile particles are grouped into elongated strings, rather than compact regions. Motion within a string is highly collective, with each particle moving to take the place of its nearest neighbour along the string.<sup>120</sup>

The average number of particles in a string increases with decreasing temperature,<sup>120</sup> which indicates a growing length scale. This growth may explain super-

Arrhenius behaviour: the typical energy barrier to a collective motion probably increases with the number of participating particles, and so increasing the average string length increases the observed activation barrier.<sup>120</sup>

The existence of strings suggests that particles in a supercooled liquid are correlated not by their positions but by their positions and velocities. Therefore, correlation functions describing the glass transition should employ information on both of these variables.<sup>72</sup> One example<sup>121,122</sup> is the four-point susceptibility  $\chi_4(t)$ ,<sup>72</sup> which measures the extent of replacement dynamics and space-time correlation.

For a BLJ system,  $\chi_4(t)$  reveals that velocity correlations of nearby particles reach a maximum around the characteristic caging time.<sup>72</sup> These correlations are dominated by clusters of slow-moving particles. The height of the peak in  $\chi_4(T)$  scales approximately as  $(T - T_c)^{-0.8}$ . This scaling suggests that correlations between slow-moving particles may diverge when  $T = T_c$ ,<sup>123</sup> although this prediction requires an ambitious extrapolation.

$\chi_4$  and the string picture provide convenient descriptions of space-time correlations in fragile atomic glass formers. For strong liquids such as silica, the behaviour of  $\chi_4(t)$  is much the same as for BLJ,<sup>124</sup> indicating that dynamics are still heterogeneous on the time scales of cage events. However, strings of mobile particles are much shorter and less relevant in silica.<sup>125</sup> This observation agrees with the earlier suggestion that string motion can be used as an explanation for super-Arrhenius behaviour.

There are several other methods for identifying fast-moving particles or regions in a supercooled liquid. Widmer-Cooper *et al.* plotted maps showing the probability of a particle undergoing an irreversible reorganisation (see §1.3.2). This probability was determined by averaging over an *isoconfigurational ensemble* of 100 simulations which start from the same initial configuration but with different momenta.<sup>105</sup> Regions of high mobility were attributed to the presence of soft modes (i.e. low-energy vibrations) in the initial configuration that were mostly localised on particular atoms.

Other authors have used similar approaches, to study both supercooled liquids<sup>126,127</sup> and the closely-related problem of jammed soft discs under shear stress.<sup>128</sup> Low-frequency modes were used to identify regions of the sample where the particles are particularly mobile, which correlate well with structural relaxations and which are long-lived compared to the intervals between rearrangements. This approach links SHD to the instantaneous structure of the liquid, and also to properties of the potential energy landscape. Mosayebi *et al.* related soft modes to the metabasin concept (see §1.6.2.3) noting that the spatial localisation of soft modes for different

inherent structures within a metabasin are similar, but modes in different metabasins are very different.<sup>127</sup>

In a similar spirit, Cubuk *et al.* have used an unsupervised machine learning method to identify particles with a high propensity for rearrangement.<sup>129,130</sup> Their program is trained on a particular system using liquid configurations extracted from a simulation, and constructs a *softness* parameter,  $s_i$ , using a combination of local structural indicators, e.g. nearest neighbour properties and bond angles.  $s_i$  is found to correlate well with rearrangement probability in simulations that were not part of the training set.<sup>130</sup> Particles with similar  $s_i$  are spatially correlated, indicating SHD.<sup>131</sup> The most important indicator for BLJ turns out to be the density of nearest neighbours: fewer neighbours implies a weaker cage and more probable rearrangement.

A final class of structure-based methods for identifying slow particles makes explicit the connection between nearest-neighbour contacts and single-particle dynamics. The locally favoured structures (LFS) approach of Royall and co-workers seeks to identify low-energy structural motifs within a liquid, typically resembling the preferred structures of atomic clusters.<sup>132</sup>

The number of LFS in a configuration is negatively correlated with the potential energy.<sup>132</sup> LFS are long-lived and aggregate into kinetically slow domains, which grow in size and lifetime with decreasing  $T$ . The emergence of these domains has been associated with the onset of super-Arrhenius behaviour<sup>133</sup> and with the trajectory-space first order transition of dynamical facilitation theory (see §1.3.4).<sup>134</sup>

For a 50:50 BLJ fluid the dominant LFS are icosahedra. They are so persistent that Pinney *et al.* constructed a coarse-grained model of this system as a population of rigid icosahedra that aggregate into domains.<sup>135</sup> Although the validity of this model is difficult to assess, it makes some interesting predictions. Neither the relaxation time nor the lifetime of the aggregate domains show signatures of low-temperature divergence, and neither scales with the system size. These results are inconsistent with a thermodynamic ideal glass transition.

### 1.3.4 Dynamical Facilitation Theory

The dynamical facilitation (DF) theory of Chandler and co-workers was originally inspired by one-dimensional kinetically constrained models (KCMs): lattice spin systems where a cell can only change state if certain conditions of its environment are fulfilled.<sup>136</sup> Kinetic constraints usually come with an energy penalty, so that fewer spins can flip in a low-energy state than a high-energy state, and the system dynamics slow down as the average energy decreases.

Several of the methods described in the previous section suggest that structural rearrangement in a real liquid mostly occurs in regions of reduced density where the confining effect is weaker. This density requirement can be viewed as a kinetic constraint, allowing KCMs to be used as analytically-soluble models for atomic glass formers.<sup>137</sup>

DF theory for KCMs is formulated in trajectory space. A trajectory is a path through configuration space that lasts for a fixed length of time. The set of possible trajectories given an initial condition constitutes an ensemble (similar to the isoconfigurational ensemble of Harrowell and coworkers).<sup>138</sup> The probability of following a particular trajectory is determined by its action,  $S_0$ , relative to the partition sum (a sum of probabilities for all possible trajectories).

At low temperatures this partition sum is dominated by trajectories that contain dynamically slow domains, where few particles satisfy the kinetic constraint. The domain sizes and lifetimes grow as the temperature decreases. Therefore, DF theory predicts dynamic heterogeneity.

The probability distribution of  $S_0$  for different trajectories is Gaussian with a long exponential tail at low action.<sup>139</sup> When the structural relaxation time is shorter than the trajectory length (i.e. the observation time), the Gaussian part dominates and the number of available trajectories is exponential in the system size. Below  $T_g$ , where the relaxation time exceeds the trajectory length, only the exponential tail of the action distribution is accessible to the system so the number of possible rearrangement trajectories becomes sub-exponential. The kinetic glass transition in the DF approach is an entropy-vanishing transition in trajectory space, rather than static configuration space. For KCMs this event is a first-order dynamical transition in Ruelle’s thermodynamic formalism of trajectory space.<sup>140,141</sup>

Unlike many other theories of the glass transition, DF theory is able to predict  $T_g$  quantitatively because it explicitly includes the observation time as a parameter (i.e. the length of the trajectories being considered). Predictions for the height of the  $C_p$  peak at  $T_g$  agree qualitatively with experimental values.<sup>137</sup>

In atomistic model glass formers (as opposed to KCMs), the dynamical transition is associated with a set of space-time “order parameters”, e.g.:

$$K = \Delta t \sum_{t=0}^{t_{obs}} \sum_{i=1}^N |\mathbf{r}_i(t + \Delta t) - \mathbf{r}_i(t)|^2, \quad (1.9)$$

where  $t_{obs}$  is the observation time and  $\Delta t$  is a coarse-graining time step.  $K$  measures the total mobility of the system in short time periods through the trajectory.

The DF dynamic transition may be shifted into computationally-accessible tem-

perature regimes using a bias parameter,  $s$ , to reweight an equilibrium distribution obtained by transition path sampling<sup>142,143</sup> in favour of low- $K$  trajectories.<sup>74</sup> This process reveals signatures of a transition between a high- $K$  “phase” containing both high- and low-activity trajectories, and a non-ergodic glassy phase where only low-mobility trajectories are possible. In off-lattice models, where the kinetic constraint may be violated by paying an energy penalty, coexistence between these phases is only possible at a small positive  $s$ , however the influence of the transition extends into equilibrium measurements.<sup>74</sup>

Breaking  $K$  up into components that are local in time and space reveals heterogeneous dynamics which are facilitated (i.e. the presence of a highly-mobile domain allows nearby regions to become mobile soon afterwards) and hierarchical (i.e. small-amplitude motions are faster and more frequent than large).<sup>74</sup> The fast regions identified by this mobility field clearly resemble elongated strings.

Facilitated dynamics may be sufficient to explain breakdown of the Stokes-Einstein relation. The relaxation time  $\tau_s = 1/\eta$  is determined by the waiting time until a fast rearrangement, but the diffusivity  $D(T)$  is related to the average waiting time between consecutive rearrangements, and facilitated dynamics causes the ratio between these two waiting times to increase as temperature decreases.<sup>74</sup>

Another key prediction is that the relaxation time  $\tau_s$  is length-scale dependent: relaxation processes measured over large distances correspond to Fickian diffusion controlled by facilitated rearrangements, but on short length scales the relaxation is dominated by non-facilitated waiting times and  $\tau_s$  increases anomalously. This crossover between Fickian and non-Fickian behaviour has been observed several times by different methods.<sup>73,144–146</sup>

DF theory provides a description of the glass transition that does not invoke any changes in structure or equilibrium thermodynamics, and which accounts for many of the phenomena discussed in §1.2. However, debate continues regarding the experimental evidence for and theoretical basis of DF theory.<sup>147–150</sup>

## 1.4 Thermodynamic Theories of the Glass Transition

Although the kinetic glass transition occurs out of equilibrium, several features suggest that it may be accompanied by a thermodynamic event. These observations include the sharpness of the kinetic glass transition, which resembles behaviour near a critical point, and the features discussed in §1.2.2.

Thermodynamic theories of the glass transition make an explicit connection be-

tween static equilibrium properties and the emergence of glassy behaviour. Here, I briefly review two of the most popular models.

### 1.4.1 Entropy and the Ideal Glass Transition

Both of the models in this section invoke the idea of an “entropy-vanishing” ideal glass transition at the Kauzmann temperature  $T_K$  (§1.2.2.2), where a supercooled liquid is hypothetically confined to a single amorphous structure. To quantify the discussion, it is essential to define the relevant entropy. Unfortunately, the literature is imprecise and occasionally contradictory on this subject.

Thermodynamic theories of the glass transition typically divide the entropy of a glass former into a component from the multiplicity of different stable configurations, and a component that arises from the vibrations around those configurations.<sup>6,30,32,96,151</sup> This division arises naturally from the energy landscape concept (see §1.6), where the stable configurations correspond to local potential energy minima. Then  $S = S_{\text{vib}} + S_{\text{IS}}$ , where  $S_{\text{vib}}$  is the vibrational part and  $S_{\text{IS}}$  is the landscape entropy, which enumerates the local minima accessible to the system. However, this number of minima is always large, even below  $T_g$ , so  $S_{\text{IS}}$  does not vanish at the Kauzmann temperature.<sup>4,92</sup>

Instead, thermodynamic theories use the concept of a long-lived amorphous structure, or *metastable state*.<sup>30,32,152</sup> These states are well defined for mean-field model glass formers, but not for realistic finite-dimensional liquids. Therefore an approximate definition of metastable states, called *quasistates*, is required.<sup>153</sup> Unlike mean-field metastable states, quasistates have a finite characteristic lifetime, which should not be negligible compared to the structural relaxation time.<sup>32</sup> Possible definitions of quasistates will be discussed in chapter 5.

The number of quasistates accessible to the system is denoted  $\mathcal{N}(T)$ , and the associated entropy is called the *complexity*.<sup>32,154</sup>

$$\Sigma(E) = \frac{1}{N} \ln \mathcal{N}(E), \quad \text{or} \quad (1.10)$$

$$\Sigma(T) = - \sum_i^{\mathcal{N}} p_i(T) \ln p_i(T). \quad (1.11)$$

In eq. (1.11),  $p_i(T)$  is the occupation probability of quasistate  $i$ .

We shall see that thermodynamic theories generally predict  $\Sigma(T_K) = 0$ , which requires that  $\mathcal{N}(T_K)$  be sub-exponential in  $N$ . The ideal glass transition is then associated with thermodynamic trapping of the system in a small number of amorphous

structures.

The glasses literature frequently refers to the “configurational entropy”,  $S_c$ , usually defined by  $S_c = S - S_{\text{vib}}$ .<sup>6,30,32,96</sup> Depending on the method of calculating  $S_{\text{vib}}$ ,  $S_c$  may be equal to either  $S_{\text{IS}}$  or to  $\Sigma(T)$  for some definition of a quasistate. To avoid this ambiguity, and to avoid confusion with the configurational entropy related to the total volume in configuration space (which includes vibrational coordinates), I will refrain from using the symbol  $S_c$  in this thesis.

### 1.4.2 Adam-Gibbs Theory

As noted above, the VTF divergence temperature  $T_{\text{VTF}}$  and the extrapolated Kauzmann temperature  $T_K$  are found to be similar for many glass formers,<sup>31,53,85</sup> possibly suggesting a link between the kinetic anomaly of super-Arrhenius behaviour and the thermodynamic Kauzmann paradox. These two concepts are linked theoretically<sup>155</sup> by the Adam-Gibbs (AG) relation.<sup>30</sup>

The key assumption in the AG theory is that supercooled liquids can be separated into co-operatively rearranging regions (CRRs) - defined as the largest region that can rearrange its configuration independently of the rest of the system.<sup>30,32</sup> Making the reasonable but uncontrolled assumption that the energy barrier to rearrangement scales with the number of particles in the CRR (denoted  $n$ ), the relaxation time is given by:

$$\tau_s = \tau_0 \exp(-A\langle n\rangle/k_{\text{B}}T) \quad (1.12)$$

where  $\tau_0$  and  $A$  are constants. To compute  $\tau_s$ , an expression for  $\langle n\rangle$  is required.

Let  $\Omega_i$  be the number of metastable quasistates accessible to a CRR with index  $i$ . Adam and Gibbs assumed this number to be roughly constant in  $T$  and  $n$ , but greater than one.<sup>30,32</sup> Then the number of states available to the whole system is

$$\mathcal{N} = \prod_{i \in \text{CRRs}}^{N/\langle n\rangle} \Omega_i = \langle \Omega \rangle^{N/\langle n\rangle}. \quad (1.13)$$

Note that  $N/\langle n\rangle$  is the total number of CRRs. Then the complexity  $\Sigma = \frac{1}{N} \ln \mathcal{N} = \ln \langle \Omega \rangle / \langle n\rangle$ , which rearranges to  $\langle n\rangle \propto 1/\Sigma$ .

Substituting this result into eq. (1.12), we obtain the Adam Gibbs equation:

$$\tau_s = \tau_0 \exp\left(\frac{-B}{T\Sigma}\right). \quad (1.14)$$

Here,  $B$  is a new positive constant. The AG relation was one of the first serious attempts to connect the dynamics ( $\tau_s$ ) and thermodynamics ( $\Sigma$ ) of a glass.

If the VTF equation is correct,  $\tau_s$  diverges at temperature  $T_{\text{VTF}} \approx T_K$ . In eq. (1.14), this divergence implies that  $\Sigma(T_K) = 0$ , which corresponds to the entropy-vanishing interpretation of the Kauzmann event, discussed in the previous section. The AG relation unifies the Kauzmann and AG pictures. Indeed, making some further assumptions regarding the entropies of the liquid and crystal, eq. (1.14) may be recast in exactly the VTF form.<sup>32</sup>

The AG relation provides an attractive link between glassy behaviour and equilibrium thermodynamics. However, its derivation relies on several uncontrolled and occasionally dubious assumptions, which lead some authors to reject it.<sup>29,32</sup> It has had some success at correlating relaxation data with thermodynamic measurements,<sup>8,151,156</sup> but has largely been superseded by the related RFOT theory.<sup>154</sup>

### 1.4.3 RFOT Theory

The random first order transition (RFOT) theory of Wolynes and coworkers<sup>31,32,154</sup> was originally developed by translating analytical results for the  $p$ -spin mean-field model into real-space concepts,<sup>32,152,157–159</sup> and subsequently refined by Mézard and Parisi using a replica coupling method.<sup>78</sup> RFOT theory is exact for mean field models, but testing its applicability to realistic finite-dimensional systems is an open problem.<sup>32</sup> A substantial body of evidence from simulation and experiment now supports this approach.<sup>65,160,161</sup>

The key prediction of RFOT theory is that the kinetic glass transition is related to two equilibrium transitions. Similar to the CRRs of AG theory, this approach divides a supercooled liquid into a “mosaic” of weakly-interacting subsystems or *domains* that each adopt different amorphous structures (quasistates).

The characteristic domain size,  $\xi^*$ , is determined by the balance between interfacial energy and complexity. Decreasing  $\xi^*$  increases the number of domains and hence the total number of states  $\mathcal{N}$  accessible to the system.  $\Sigma$  turns out to be extensive in the number of domains, favouring small  $\xi^*$ . However, different amorphous structures are energetically incompatible and interfaces between them carry an energy penalty (e.g. in silica, the bonding network is disrupted at an interface where the amorphous structure changes). As  $\xi^*$  decreases, the interfacial area grows and the energy increases, opposing the entropic effect from  $\Sigma$ . At low temperature, the energy term dominates and the domains grow in size.

Physical arguments predict that the interfacial energy vanishes above the mode-coupling critical point  $T_c$ .<sup>32</sup> At these high temperatures, activated motion no longer dominates diffusion and the lifetimes of metastable states become very short, so the mosaic state is not a valid description of the system. The first phase transition

predicted by RFOT occurs at  $T_c$ , where the mosaic domains first become stable, and is first-order in a localisation parameter  $\alpha$ .<sup>31,162</sup> However, the new state is not a single ordered phase but rather a collection of distinct microphases each randomly selected from the ensemble of amorphous structures, so the transition is described as “random first order”.

Structural relaxation in the mosaic state consists of domains slowly changing their quasistate, either via nucleation of a new amorphous phase within a domain,<sup>163</sup> or by rare rearrangement modes with a length scale  $\xi > \xi^*$  that can mix and destroy domains.<sup>154</sup> These processes become less favourable with increasing domain size, and hence become rarer with decreasing temperature.

RFOT predicts a second thermodynamic transition at the Kauzmann temperature  $T_K$ , where  $\xi^*$  diverges and there exists only one domain, which spans the system. The number of amorphous structures in this domain is certainly sub-exponential, so  $\Sigma(T_K) = 0$  in agreement with AG theory. This prediction combines a diverging length scale ( $\xi^*$ ), diverging time scale ( $\tau_s$ ) and a free energy singularity, so it has all the characteristics of a thermodynamic phase transition to an ideal glass state.<sup>31</sup>

Bouchaud and Biroli<sup>154</sup> present a convenient quantitative formulation of the RFOT theory using the random energy model (REM) as inspiration. They consider a domain as being the set of particles within a sphere of radius  $\xi$ , and all particles outside this sphere are frozen in place (an early application of the pinning procedure described in §1.5). The frozen particles impose a boundary condition on the mobile particles, which must pay an energy penalty whenever the amorphous structures within and outside the domain differ.

The partition function of the mobile domain then decomposes into a term where the mobile domain matches its boundary condition, and a term where the amorphous structure differs either side of the interface. When  $\xi$  is large, the latter term dominates and the domain will be stable in a randomly-selected amorphous structure distinct from its surroundings.  $\xi^*$  is the smallest radius for which such a distinct structure is possible. From this comparatively simple model, most of the results of the RFOT theory may be derived.

RFOT theory explains several phenomena of glass-forming liquids, including super-Arrhenius behaviour and non-exponential relaxation.<sup>31</sup> Its quantitative predictions for properties such as fragility indices<sup>164</sup> and stretched-exponential  $\beta_s$  parameters<sup>165</sup> agree fairly well with simulation and experiment for a wide range of materials. Moreover, numerous studies have reported evidence of growing static length scales in supercooled liquids,<sup>166,167</sup> some of which appear to scale in the manner predicted for  $\xi^*$ .<sup>168,169</sup>

Many aspects of the RFOT theory, particularly the presence of the entropy-vanishing transition at  $T_K$ , remain controversial. However, it is certainly the most popular thermodynamic approach to explain the glass transition.

## 1.5 The Pinning Transition

In recent years, the method of random pinning has stimulated renewed theoretical interest in the concept of an ideal glass transition. The method is conceptually simple: a fraction  $c$  of the configurational degrees of freedom in a glass former are artificially fixed, establishing a constant external field in which the remainder of the system evolves. For an atomistic liquid, this procedure is equivalent to freezing the positions of some atoms.

There are various approaches to selecting which atoms to pin, and where to pin them,<sup>170</sup> but most involve obtaining a “reference configuration” from an equilibrium ensemble and pinning a subset of atoms at their positions in this reference. Several geometries for pinned subsets are possible,<sup>170</sup> but the discussion here will assume that atoms to be pinned are selected uniformly at random.

The pinning procedure was originally used in atomistic simulations to model the presence of interfaces or porous solid matrices,<sup>171,172</sup> but was quickly adapted to test various aspects of the RFOT theory<sup>154</sup> and to probe “point-to-set” length scales (roughly equivalent to  $\xi^*$  in the RFOT theory).<sup>169,170,173</sup> Even for small pinning fraction  $c$ , relaxation times increase dramatically,<sup>174</sup> and it was suggested that these times might diverge at a critical temperature and pinning fraction, corresponding to structural dynamical arrest and a thermodynamic phase transition.<sup>170,175</sup>

Pinning some particles inhibits the dynamics of the remainder because the pinned particles act as immovable barriers. Moreover, freezing particles reduces the entropy, because many possible positions of the mobile atoms are blocked by pinned atoms. Therefore a sufficiently high value of  $c$  might cause an entropy-vanishing phase transition.

Cammarota and Biroli<sup>175</sup> explained that in the RFOT picture, a true divergence of the relaxation time is expected at a critical pinning fraction  $c^*(T) > 0$  (or equivalently  $T^*(c) > T_K$ ). This random pinning glass transition (RPGT) is analogous to the entropy-vanishing transition predicted at  $T^*(0) = T_K$ , and corresponds to the entire system adopting a single amorphous structure.

Renormalisation group analysis for the mean-field REM proves that the RPGT occurs in equilibrium, and that it connects with the RFOT Kauzmann-like transition when  $c = 0$ .<sup>175</sup> Various aspects of the behaviour of pinned systems have since been

studied, particularly their dynamical properties<sup>16,175–179</sup> and structural features such as amorphous order and growing length scales.<sup>173,180,181</sup>

The mean field approach assumes infinite dimensionality and introduces unphysical energy barriers. Therefore, an important next step is to establish whether the pinning transition remains thermodynamic for more realistic model glass formers. Attempts have already been made to compute such a phase diagram<sup>180,182</sup> but debate continues over the nature and validity of the transition lines that have been obtained.<sup>183–185</sup>

An attractive aspect of the pinning method is that increasing  $c$  raises  $T^*$  to sufficiently high temperatures that equilibrium simulations of dynamics are computationally accessible - unlike simulations in the region of  $T_K$  for an unpinned glass former. If the RPGT is an extension into the  $(T, c)$  plane of the ideal glass transition, then construction of a phase diagram in this plane and extrapolating the transition line towards  $(T_K, 0)$  will be much easier than extrapolating in  $T$ .<sup>175</sup>

The pinning method continues to be of great interest to the theoretical and computational community. Chapter 5 describes the effect of pinning on the potential energy landscape of a structural glass former, providing a qualitative explanation for the changes in dynamics under the pinning operation and suggesting some complementary approaches for identifying the pinning transition.

## 1.6 Potential Energy Landscapes

The concept of a potential energy landscape (PEL) that controls the behaviour of a physical or chemical system has found many uses in a wide variety of fields of the past several decades.<sup>4,186–192</sup> This approach converts the problem of describing the behaviour of a many-body system into a real analysis problem, with the complication that the function to be analysed has very high dimensionality, so that sophisticated numerical techniques are required to extract useful information.

The PEL idea has been used to explain the behaviour of supercooled liquids and glasses for longer than it has been used in some other fields,<sup>193–195</sup> and many of the theories outlined in the previous sections may be reformulated in terms of PEL concepts.

Some fundamental aspects of PEL theory will be laid out in §1.6.1, and their applications to glass formers discussed in §1.6.2.

### 1.6.1 Introduction to Potential Energy Landscape Theory

The PEL of a system is simply its potential energy expressed as a function of all its degrees of freedom,  $V(\mathbf{X})$ , where  $\mathbf{X}$  is a vector containing all the configurational coordinates. The PEL gradient vector is defined by  $\mathbf{g}(\mathbf{X}) = \nabla V(\mathbf{X})$ , and the Hessian matrix,  $\mathbf{H}$ , is defined by  $H_{ij} = \partial^2 V / \partial \mathbf{X}_i \partial \mathbf{X}_j$ . Note that  $\mathbf{H}$  is real and symmetric.

$\mathbf{X}$  contains all the configurational degrees of freedom, which for an unconstrained system of  $N$  atoms is  $3N$  (Cartesian) coordinates. Therefore  $V(\mathbf{X})$  may be thought of as a surface in  $3N + 1$  dimensions (the last being the energy). Any given configuration corresponds to a single value of  $\mathbf{X}$ , i.e. a single point on the landscape.  $\mathbf{g}(\mathbf{X})$  gives the slope of the landscape, and the eigenvalues of  $\mathbf{H}$  give the curvature in the directions of the corresponding eigenvectors. As the system evolves under the influence of the force  $\mathbf{F} = -\mathbf{g}(\mathbf{X})$ , the configuration changes. The system can be represented as a “state point” moving across the landscape as a function of time.

The Schrödinger equation tells us that all properties of a system are determined by its wavefunction, which is uniquely specified by the corresponding Hamiltonian,  $\hat{H} = \hat{T} + \hat{V}$ . The kinetic energy operator  $\hat{T}$  has the same form for all systems, and thus all details of a quantum system are encoded in the potential energy operator  $\hat{V}$ , which is equivalent to the PEL.<sup>4</sup> Hence there is a one-to-one correspondence between a closed physical system and the corresponding PEL, and  $V(\mathbf{X})$  uniquely determines the equilibrium and dynamical properties.

Extracting these properties typically requires evaluating  $V(\mathbf{X})$  at a great many configurations, so using the correct quantum PEL is often impractical. Instead, simple model potentials are commonly used, often parameterised using experimental data, to describe the motion of atoms classically.

In this thesis I will not attempt to verify whether these models provide realistic descriptions of the systems they represent. This omission is because glassy behaviour is reproduced satisfactorily for very simple potentials. Glassy phenomenology in these models will be explained qualitatively, and quantitative predictions regarding real materials will not be made.

The PEL is a function of the configuration space alone, which depends on the number and density of the particles, but not their masses or the temperature. However, the motion of the state point on the PEL is affected by temperature, causing different regions of the PEL to be explored as  $T$  decreases.

The high dimensionality of PELs for non-trivial systems means that analysing their behaviour at all points in space is impractical. However, observable properties can be approximated very accurately using only knowledge of the stationary points of  $V(\mathbf{X})$ , where  $\mathbf{g}(\mathbf{X}) = 0$ . The important types of stationary points will now be

discussed.

### 1.6.1.1 Minima of the PEL

Minima of  $V(\mathbf{X})$  are stationary points for which  $\mathbf{H}$  has no negative eigenvalues: any infinitesimal coordinate displacement raises the energy. Consequently, each minimum corresponds to a mechanically stable structure lying at the bottom of a basin of attraction.<sup>4</sup> These basins completely partition the configuration space, so nearly any point can be uniquely mapped to a minimum by a steepest-descent path (SDP).

An SDP is a curve in configuration space that always lies antiparallel to the gradient vector, defined as the solution to a first-order differential equation:

$$\frac{d\mathbf{X}}{ds} \propto -\mathbf{g}(\mathbf{X}), \quad (1.15)$$

where  $s$  is a variable parameterising the path length. The SDP terminates when  $\mathbf{g}(\mathbf{X})$  vanishes (usually at a local minimum). In practice, SDPs are determined from the configurations visited by a numerical minimisation algorithm (see §2.2.1).

Under constant-temperature conditions, the equilibrium occupation probability of states is given by the Boltzmann distribution. As temperature decreases, this distribution is increasingly weighted towards low- $V$  regions of configuration space and hence the system mostly explores the bottoms of the basins of attraction. At low  $T$ , the structural ensemble explored by the system is approximated reasonably well by the set of local minima. The continuous PEL is then replaced by a set of discrete energy levels (minima), with relative populations given by the Boltzmann distribution. The minimum of  $V(\mathbf{X})$  with the lowest energy is the global minimum, and the rest are local minima.

The number of local minima is generally exponential in the number of degrees of freedom.<sup>196,197</sup> For all viable models of condensed matter this number is far too large to enumerate systematically, and the structural ensemble is approximated using a representative sample. Methods for obtaining such a sample are discussed in §2.2.1.

Energetically, the global minimum would always be the preferred structure, and the behaviour of many systems can be predicted simply by identifying it and characterising its properties.<sup>4</sup> However, at finite temperature the equilibrium population of the global minimum may be significantly less than the total weight of the other local minima. Also, the energy barriers to reach the global minimum may be too large to surmount quickly, which leads to kinetic trapping in one or more local minima. In these situations, having a representative sample of local minima becomes

important.

The number of minima at a particular energy will turn out to be a useful quantity.  $g_{\text{IS}}(V)$  is defined such that  $g_{\text{IS}}(V)dV$  gives the number of minima with energies in the range  $[V, V + dV]$ .  $g_{\text{IS}}(V)$  is continuous because the total number of minima is essentially infinite for a macroscopically large system.<sup>4</sup>

### 1.6.1.2 Thermodynamics from the PEL

A finite system is uniquely specified by its PEL, therefore  $V(\mathbf{X})$  must contain information on the entropy of the system as well as on the potential energy. This entropy is divided into two parts: the vibrational entropy associated with each minimum, determined by the phase volume contained within the basins of attraction, and the *landscape entropy*,  $S_{\text{IS}}$ . This latter quantity is defined by  $S_{\text{IS}}(V) = k_{\text{B}} \ln g_{\text{IS}}(V)$ .<sup>198</sup> Both  $S_{\text{IS}}$  and the separation  $S(T) = S_{\text{vib}} + S_{\text{IS}}$  were previously encountered in the discussion of the Kauzmann paradox, §1.2.2.2. This separation is only exact when the average vibrational frequencies of minima do not depend on their energy,<sup>199</sup> but seems to be a reasonable approximation for some popular model glass formers.<sup>198</sup>

The superposition approach calculates both  $S_{\text{vib}}$  and  $S_{\text{IS}}$ , allowing global thermodynamics to be approximated using an appropriately weighted sample of local minima.<sup>4</sup> In this approach, the total partition function is obtained by summing over the partition functions associated with each minimum, which are approximated using a model form for  $V(\mathbf{X})$  in the basins of attraction. The most popular model is the harmonic superposition approximation (HSA)<sup>4,200,201</sup> which assumes that all basins are harmonic and non-overlapping. The vibrational partition function of this model is analytic, and requires only knowledge of the energies and Hessian eigenvalues of the local minima.

The HSA allows partition functions (and hence most other thermodynamic quantities) to be estimated quickly once a database of minima has been obtained. Its accuracy depends on the validity of the harmonic basin model. This approximation can be improved at significant computational expense by fitting anharmonic corrections to the potential energy,<sup>202</sup> or by using perturbation theory to apply a temperature-dependent correction to the normal mode frequencies.<sup>203</sup>

Equilibrium properties of the system may be obtained by computing averages of the form:

$$\langle A \rangle = \sum_{\alpha} p_{\alpha}^{\text{eq}}(T) A_{\alpha} = \sum_{\alpha} \frac{Z_{\alpha}(T)}{Z(T)} A_{\alpha} \quad (1.16)$$

where  $A_{\alpha}$  is the value of quantity  $A$  for minimum  $\alpha$ , and  $p_{\alpha}^{\text{eq}}(T) = Z_{\alpha}/Z$  is the occupation probability of  $\alpha$ .  $Z_{\alpha}(T)$  is the partition function for minimum  $\alpha$ , and

$$Z(T) = \sum_{\alpha} Z_{\alpha}(T).$$

### 1.6.1.3 Transition States

Knowledge of the potential energy minima allows equilibrium structural and thermodynamic properties to be calculated fairly accurately. To compute out-of-equilibrium and dynamical properties, knowledge of the energy barriers and pathways between these minima is also required.

Simple kinetic theory tells us that the transition rate across a single constant barrier depends exponentially on the height of that barrier, and so the ensemble of possible transition paths between a pair of minima is dominated by the pathway that has the lowest energy barrier.

The Murrell-Laidler theorem<sup>204</sup> shows that this minimum-energy pathway between two minima always passes through a saddle point of  $V(\mathbf{X})$  with Hessian index one, i.e. a stationary point where the landscape has one unique direction of negative curvature and positive curvature in all other directions. Such a point is hereafter referred to as a transition state (TS). A representative sample of transition states provides important information about the dynamics of a system.

Unlike local minima, TSs cannot be located by solving a differential equation, and more complex search methods are required (see §2.2.2). Moreover, it is not always clear what is the correct sample needed for an accurate description of dynamics.<sup>4</sup> Therefore, studies of transition states are still comparatively rare.

The methods described in §2.2.2.3 provide two coherent approaches for sampling transition states to explain dynamic behaviour qualitatively. The discrete path sampling approach<sup>205</sup> is a quantitative method for obtaining global dynamics of systems that have well-defined “reactant” and “product” structures.

There are always exactly two SDPs leading downhill away from a TS,<sup>4</sup> which are located by stepping an infinitesimal distance away from the TS either parallel or antiparallel to the direction of negative curvature. Each of these SDPs leads to a local minimum (or another saddle point, with vanishing probability). The energy barriers between two minima are the energy differences between the minima and the TS that connects them.

Once the lowest energy barrier between a pair of minima is known, unimolecular rate theory may be used to predict the rate constant for the transition between them. Given a network of minima and the transition rates between them, with an initial distribution of occupation probabilities, the exact dynamics are given by a set of coupled first-order differential equations. This *master equation* can be solved either by diagonalising a symmetrised transition matrix,<sup>4</sup> or using graph transformation

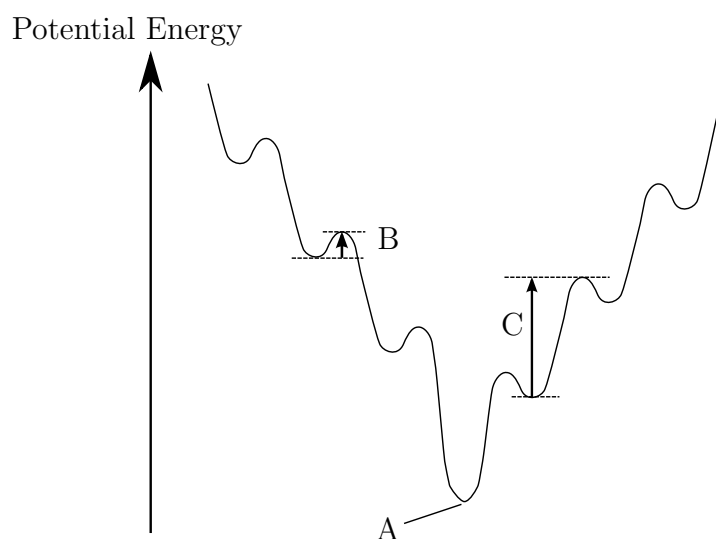


Figure 1.6: 1-dimensional cartoon of a funnelled landscape. The horizontal coordinate represents an arbitrary direction in configuration space.

A: Global minimum. B: Downhill barrier. C: Uphill barrier.

methods.<sup>206,207</sup>

Calculating transition rates from the PEL is often more efficient than the alternative molecular dynamics or transition path sampling<sup>142,143</sup> approaches, because determining energy barriers using geometry optimisation methods is independent of the structural relaxation time. Therefore the rates of very slow processes may be calculated quite accurately,<sup>4,208</sup> in problems where conventional methods would require unfeasibly long simulation times.

#### 1.6.1.4 Funnel Structures

A “funnel” is a group of minima for which the downhill energy barriers (barriers to go from one minimum to a lower minimum) are smaller on average than the uphill barriers. Relaxation to the lowest-energy minimum in the group is rapid, because it is accessible from other minima via relatively small energy barriers. Escape from the lowest minimum is slow due to the higher uphill barriers.

Local funnels are mainly used as a qualitative concept for visualisation on connectivity graphs (see §2.2.4) and hence have not been rigorously defined. A cartoon depiction of a local funnel is shown in fig. 1.6. Minima within a local funnel are typically close in configuration space and can often be grouped together using an “order parameter”, which may be defined using structural measures or chemical characteristics, such as NMR shifts.<sup>209</sup>

For many systems, including small atomic clusters and many biomolecules, the

PEL contains a single large funnel.<sup>208,210</sup> These systems are “structure seekers”, which exhibit relaxation to the global minimum. This efficient relaxation explains the rapid folding of many proteins to the native structure, and thus provides a resolution to Levinthal’s paradox.<sup>4,211,212</sup> The protein folding problem was probably where the idea of a funnelled landscape was first proposed.

Glassy systems have PELs that are not globally funnelled. Although there may be low-energy minima corresponding to crystal structures, which are probably surrounded by local funnels,<sup>213</sup> these structures occupy a small region of configuration space and relaxation to this region exceeds the observation time scale.

### 1.6.1.5 System Sizes for PEL exploration

Atomistic computer models of liquids usually simulate  $N$  atoms under periodic boundary conditions, as explained in §2.1.2. This technique introduces errors known as finite size effects, with different magnitudes for different computed properties. To reduce these errors, we wish to make  $N$  as large as possible, but for calculations that explore the PEL directly this may not be desirable.

The number of minima of  $V(\mathbf{X})$  increases dramatically with  $N$  and so extracting useful information becomes more difficult for larger systems. Moreover, Heuer has argued<sup>197,214–217</sup> that many properties of the PEL which relate to local dynamics are lost when the system studied becomes too large.

This loss of information arises because a large enough system with finite-range intermolecular forces can always be decomposed into subsystems<sup>217,218</sup> whose energies and dynamics are largely independent. Each subsystem explores different regions of its PEL, so measuring a PEL property across the entire supersystem corresponds to an average of several independent stochastic quantities, removing fluctuations and disguising features of interest.<sup>197</sup>

Determining an appropriate system size that minimises finite size effects while retaining important PEL properties is not straightforward. Thermodynamic properties of simple model glass formers are often unchanged for system sizes greater than  $N \approx 100$ ,<sup>216</sup> but errors in dynamical properties can persist to significantly larger systems.<sup>219,220</sup> In this thesis, we focus on systems of size  $N \sim O(100)$  to limit finite size effects, while allowing reasonably straightforward analysis of the PEL.

## 1.6.2 Potential Energy Landscapes of Glass Formers

The use of the PEL framework to study structural glass formers has a long history. The current section is presented broadly in chronological order.

### 1.6.2.1 Statistical Theory of Landscapes

The first reference to the PEL in the context of glasses was probably made by Goldstein,<sup>193</sup> who argued convincingly (but without direct numerical evidence) that dynamics in the supercooled regime are influenced by high potential energy barriers.

Stillinger and Weber made the first quantitative studies of glassy PELs by using local energy minimisation to map the configurations of a simulated trajectory onto the corresponding minima of the PEL.<sup>194</sup> They described this procedure as “quenching”, because the mapping is equivalent to relaxation of the system after instantaneous cooling to absolute zero. Local minima were referred to as *inherent structures* (ISs) because they reveal stable positions of particles that are normally obscured by vibrational motion.<sup>194</sup> This name is still common in the glasses literature.

By examining the properties of consecutive local minima visited in a simulated trajectory, Stillinger and Weber concluded that elementary rearrangements between minima usually involve small numbers of atoms.<sup>195</sup> They also realised that the number of minima increases exponentially with system size, and that the waiting time between minimum-minimum transitions decreases with  $N$ .

Finally, they proposed that glass-forming behaviour can be explained by the fact that the PEL of a supercooled liquid contains a huge number of minima corresponding to amorphous structures, and comparatively few corresponding to crystalline configurations. Even though the latter are much lower in potential energy, rapid cooling traps the system in an amorphous region of the landscape, and transition rates between minima are too small for the system to locate the crystalline region on the experimental time scale.<sup>195</sup>

These observations were combined to produce a statistical theory of glassy landscapes<sup>27,92,221</sup> using the “basin evaluation function”,  $\sigma_b(V)$ , which is related to  $S_{\text{IS}}$ . The theory may also be expressed in terms of the density of minima,  $g_{\text{IS}}(V)$ , if one assumes that all basins of attraction have equal curvature. Then the partition function in the superposition approximation can be written as

$$Z(T) = \int \langle Z_\alpha(T, V) \rangle g_{\text{IS}}(V) dV. \quad (1.17)$$

$\langle Z_\alpha(T, V) \rangle$  is the average value of the partition function for a single minimum at energy  $V$ , which may be obtained using the harmonic approximation with or without anharmonic corrections (see §1.6.1.1) or by numerical methods such as nested sampling.<sup>222,223</sup> Other thermodynamic quantities are straightforward to obtain from  $Z(T)$ .<sup>198</sup> Eq. (1.17) must often be solved using a maximum-term approximation for

the integral in eq. (1.17), but this is often reasonable for macroscopic systems.<sup>92,199</sup>

Stillinger used the statistical theory to argue that a second-order transition in which the landscape entropy  $S_{\text{IS}}$  vanishes, as originally proposed by Adam and Gibbs, is impossible.<sup>92</sup> This scenario corresponds to freezing in the lowest-energy amorphous minimum, but this concept is actually not well-defined because there exists a continuous range of minima connecting the amorphous configuration space with the crystal.<sup>213</sup> Stillinger argued that the number of excitations out of this hypothetical lowest minimum must be at least exponential in the system size, and that the corresponding excitation energies are linear in  $N$ . The density of accessible minima,  $g_{\text{IS}}(V)$ , would then have an infinite slope at the energy of the “ideal glass”, and hence  $S_{\text{IS}}(T_K) > 0$ . Even if a well-defined lowest amorphous minimum did exist, Stillinger’s argument would not affect more recent thermodynamic theories, since they are framed in terms of a quasistate complexity  $\Sigma$ , rather than the landscape entropy.<sup>32</sup>

Heuer *et al.* have reported accurate measurements of  $g_{\text{IS}}(V)$  for both strong and fragile glass formers (the BKS model of silica and BLJ fluid, respectively).<sup>201,215</sup> They first obtain the distribution of IS energies visited by a simulation, and then reweight this distribution to remove the Boltzmann factor at each value of  $V$ , obtaining  $g_{\text{IS}}(V)$  up to a constant of proportionality. This constant is eliminated by performing the analysis at several temperatures, and scaling the distributions for each so that they overlap. If the anharmonic contribution to the average partition function  $\langle Z(T, V) \rangle$  is significantly temperature-dependent, the collapse of the distributions upon scaling will be poor, so this method provides a simple way to assess the importance of the anharmonic terms.<sup>197</sup>

It turns out that  $g_{\text{IS}}(V)$  is approximately Gaussian for many supercooled liquids.<sup>27,201</sup> This Gaussian behaviour persists to very low energies for BLJ, but for silica the distribution has a low-energy cutoff where  $g_{\text{IS}}(V)$  suddenly drops to a negligible value.<sup>197,215</sup> This cutoff corresponds to the disappearance of coordination number defects, and it was suggested that increasing the concentration of these defects is the primary mechanism for exciting the silica system into higher-energy minima.<sup>215</sup> The limit of zero defects therefore represents a lower limit to the energy of an amorphous configuration. At higher densities of silica the network structure disappears, and so the concept of a coordination defect is not well defined. At these densities, there is no low-energy cutoff to  $g_{\text{IS}}(V)$ .<sup>224</sup>

The presence or absence of a low-energy cutoff in  $g_{\text{IS}}(V)$  turns out to be a key factor in determining strong or fragile dynamical behaviour for a liquid - see §1.6.2.4. However, the cutoff is only apparent for small system sizes: when  $N$  is large enough

for non-interacting subsystems to exist, the cutoff in each may have slightly different values which are averaged out when  $g_{\text{IS}}(V)$  is calculated for the whole system.

### 1.6.2.2 Inherent Structure Trajectories

PEL minima of supercooled liquids are typically sampled using *inherent structure trajectories* produced by quenching a molecular dynamics simulation. Sastry *et al.*<sup>225</sup> used this method to prove Goldstein’s assertion that potential energy barriers influence the dynamics of supercooled liquids. They calculated the average energy,  $\langle V_{\text{IS}} \rangle$ , of inherent structures visited by a system with decreasing temperature. Idealised results are shown in fig. 1.7.

At mildly supercooled temperatures, most energy barriers are too small to affect the dynamics, and  $\langle V_{\text{IS}} \rangle$  is roughly constant with  $T$ . On further cooling the system enters a *landscape-influenced regime*<sup>225</sup> where barriers to reach some regions of configuration space are not crossed on the observation time scale, and  $\langle V_{\text{IS}} \rangle$  decreases significantly with decreasing  $T$ . This regime has been linked to the onset of super-Arrhenius behaviour in fragile liquids.<sup>197</sup>

At a sufficiently low temperature (which has been claimed to correspond to the mode coupling  $T_c$ )<sup>123</sup> many potential energy barriers are larger than the thermal energy, and  $\langle V_{\text{IS}} \rangle$  reaches a plateau. Transitions between minima still occur in this *landscape dominated regime*, so the plateau does not correspond to the kinetic glass transition, but the transitions are much slower and the system is unable to “anneal”, i.e. cross higher barriers into lower-energy regions, on the simulation time scale. The plateau value of  $\langle V_{\text{IS}} \rangle$  varies with the cooling rate, because lower rates allow more time for annealing to occur before reaching the landscape-dominated regime.

Jund and Jullien<sup>226</sup> obtained inherent structure trajectories for viscous silica in which they measured the properties of the SDPs during quenching. At low temperatures, the energy difference and Cartesian distance between an instantaneous configuration and the corresponding minimum both depended linearly on temperature. At higher  $T$ , however, the temperature dependence was much stronger and the differences between the minimised and unminimised configurations grew rapidly. This crossover was attributed to the onset of anharmonicity in the PEL basins. In the case of silica, this temperature coincides quite closely with the “fragile-to-strong crossover” (see chapter 4), hinting that both these effects may arise from anharmonic features of the landscape.

Büchner and Heuer<sup>227</sup> obtained inherent structure trajectories for a BLJ glass former at a high time-resolution and low temperature, and found that the inherent structure energy remains relatively constant for long periods of time, repeatedly

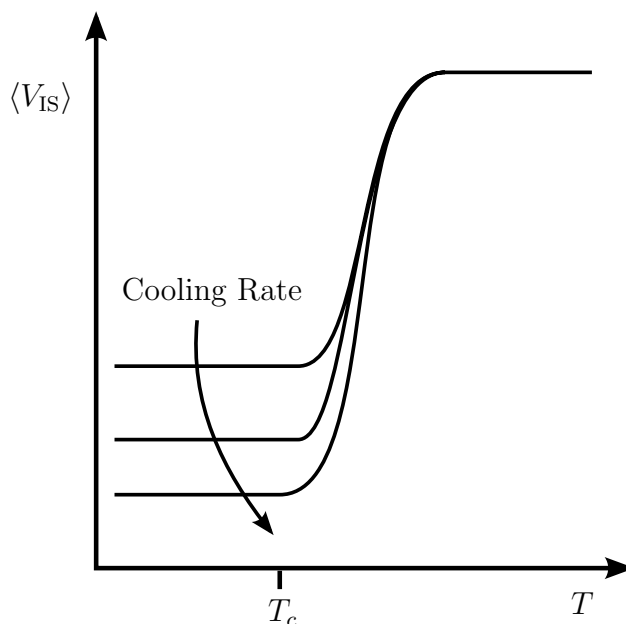


Figure 1.7: Idealised plot showing how the average energy in an inherent structure trajectory varies with temperature. Three different cooling rates are shown, the rate decreases in the direction of the arrow.

hopping between a small number of inherent structures. These “immobile” periods are separated by brief excursions to minima at much higher energies, where no such revisiting of minima was detected. They concluded that the immobile periods correspond to exploration of “valleys” on the PEL, and the excursions correspond to the system crossing high barriers between valleys. This idea was subsequently developed into a robust definition of *metabasins*.

### 1.6.2.3 Energy Metabasins

The idea that some supercooled liquids have PELs with minima organised into groups, called metabasins, was first proposed by Stillinger<sup>221</sup> as an explanation for the difference between strong and fragile liquids. He took the VTF expression for the diffusion constant, eq. (1.1), and argued that strong glass formers have  $T_{VTF} \approx 0$  while fragile liquids have  $T_{VTF} \approx T_g$ . He hypothesised that strong liquids have “uniformly rough” landscapes, with many amorphous minima but only a single characteristic barrier height. In contrast, the minima of a fragile liquid were supposed to be grouped into *metabasins*, corresponding to landscape funnels. The high barriers between metabasins would be harder to surmount at low temperatures, producing a finite  $T_{VTF}$  for fragile liquids. Stillinger’s picture is represented in fig. 1.8.

This picture has several problems. Firstly, it assumes that the VTF equation

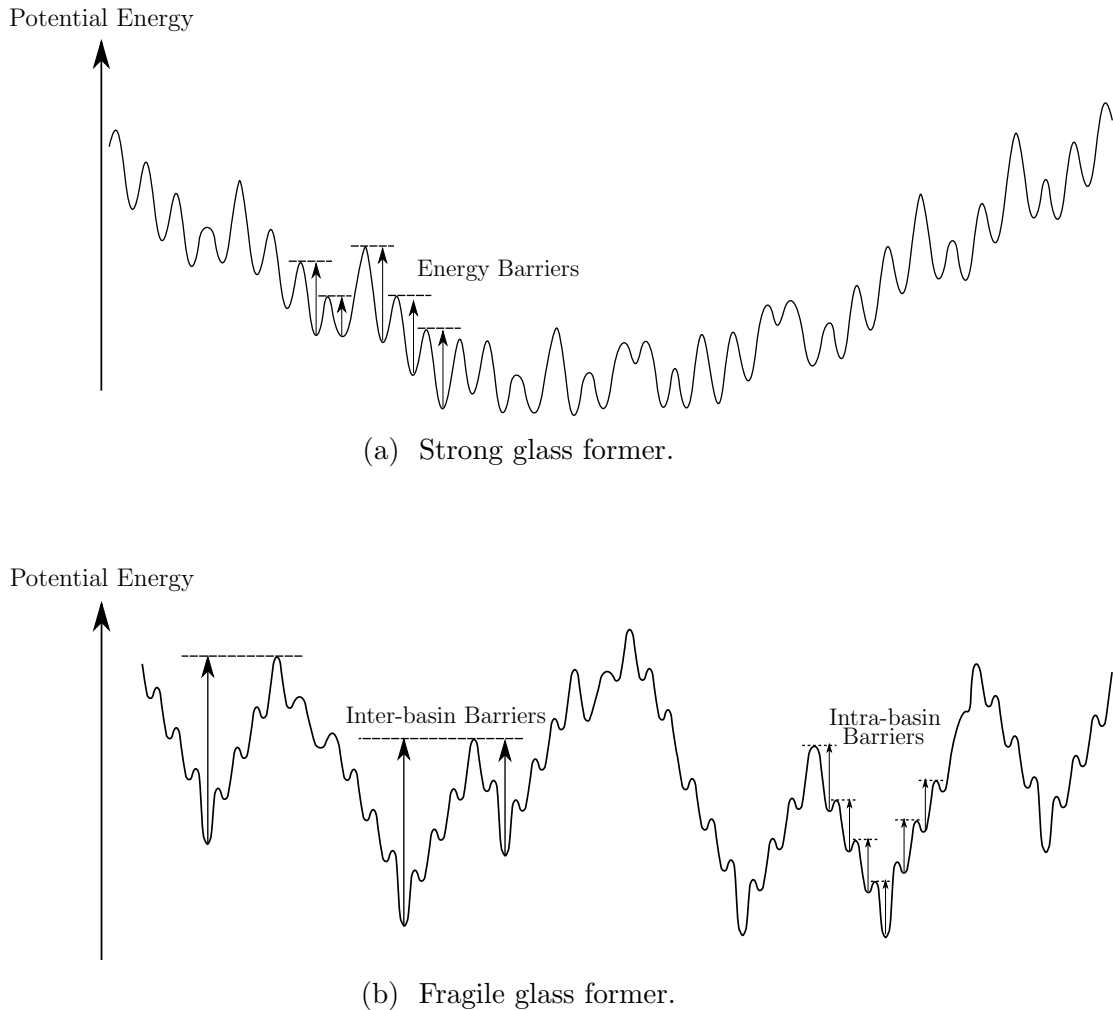


Figure 1.8: One-dimensional cartoons showing Stillinger's speculation for how the PELs of strong and fragile liquids would differ.

describes the diffusion constant down to very low temperatures, even for strong glass formers, which is only predicted within the Adam-Gibbs and RFOT theories. Secondly, the presence of two characteristic barrier heights on the PEL does not explain why the effective barrier height increases at reduced temperature. However, the idea of a clear structural difference between the landscapes of strong and fragile glass formers was appealing, and began a substantial effort to explain and properly characterise the structure of glassy landscapes.<sup>197,228–233</sup>

Heuer explained the importance of reversed minimum-minimum transitions using model single-funnel landscapes with a similar form to fig. 1.6.<sup>197</sup> The process of escaping from a low-lying minimum that is surrounded by higher-energy minima will involve many reversed transitions, because the downhill barriers are smaller than the uphill barriers. Therefore, the system may still return to the lower energy

starting minimum even after many elementary transitions, and hence the waiting time in an inherent structure is not well correlated to the structural relaxation time.

By considering instead the waiting time within a metabasin that contains both a low-energy minimum and all nearby higher-energy minima, this problem can be avoided. All the back-and-forth motion is then contained within the metabasin and every jump between metabasins contributes to a structural relaxation.<sup>197,229,231</sup>

Metabasins may be identified by grouping together all sets of minima that are revisited by the trajectory:<sup>197,229</sup>

1. For each minimum  $i$ , determine the time interval  $[t_i^*, t_i^\dagger]$  between its first and last occurrence in the IS trajectory
2. Calculate the overlap  $q_{\text{MB},ij} = [t_i^*, t_i^\dagger] \cap [t_j^*, t_j^\dagger]$  for each pair of minima  $j > i$ .
3. If  $q_{\text{MB},ij} < \tau_{\text{mol}}$ , truncate the two intervals such that  $q_{\text{MB},ij} = 0$ .  $\tau_{\text{mol}}$  is an estimate for the time scale of molecular motion.
4. Otherwise, assign minimum  $j$  to the metabasin of minimum  $i$ .

Minima that are visited sequentially, without being revisited, each represent a metabasin with one member. Whenever the trajectory revisits a minimum one or more times, all the intervening minima are included in the same metabasin.

Using this algorithm, the inherent structures explored by the system are divided into sets that mutually interconvert easily, here referred to as energy metabasins (EMBs). By analogy to model funnelled landscapes, we expect that each EMB has a single low-energy minimum surrounded by a group of higher-energy minima. By definition, transitions between EMBs are unreversed on the time scale of the inherent trajectory, so the system wanders between EMBs via a random walk.

EMBs are present for both BLJ and silica models,<sup>234</sup> implying that the landscapes of both models contain two scales of energy barrier, and contradicting Stillinger's view that the PEL of the fragile liquid would be more structured than the strong. The results of chapter 4 will demonstrate that in fact Stillinger's picture was partly correct, but the difference between the two types of landscape is quantitative rather than qualitative and more subtle than he envisaged. This conclusion is in agreement with recent numerical work not based on the PEL description.<sup>235,236</sup>

Other methods exist for defining metabasins, one of which will be described in detail in §1.7 and used throughout this thesis. A third approach uses the distance matrix,<sup>237</sup>  $\Delta(t', t'') = \langle |\mathbf{r}_i(t'') - \mathbf{r}_i(t')|^2 \rangle$ . Metabasins are indicated by intervals  $[t', t'']$  for which  $\Delta(t', t'')$  is small, indicating proximity in configuration space. The metabasins defined by this approach are compact, contradicting the string approach

described in §1.3.3.<sup>238</sup> Their boundaries are sharp, indicating that metabasin transitions are abrupt in real space as well as in configuration space.

#### 1.6.2.4 CTRW for Metabasins

The EMB definition is trajectory-dependent: different inherent trajectories across the same landscape might produce different sets of EMBs. However, the average properties of the EMB energy distribution  $g_{\text{MB}}(V)$ , the jump length distribution, and the waiting time distribution all seem to be unchanged when multiple simulations are compared.<sup>197</sup> Measuring these properties allows the calculation of observable quantities.

The CTRW model used previously for single-particle jumps has also been applied to EMB transitions. This method requires that jumps between EMBs are uncorrelated, both in waiting time and configuration space, which seems to be true for the simple glass formers studied so far.<sup>230,231,239,240</sup> Elementary minimum-to-minimum transitions, on the other hand, are negatively correlated in space, and the size of the correlations is temperature-dependent.<sup>197,241</sup>

The CRTW model predicts that  $D(T) \propto 1/\tau_{\text{MB}}$ , the average metabasin waiting time. Fitting an idealised form for  $g_{\text{MB}}(V)$  to the simulation data allows these quantities to be calculated. It turns out that a purely Gaussian  $g_{\text{MB}}(V)$  (as observed for BLJ) gives super-Arrhenius behaviour of  $D(T)$ , but a Gaussian with a low-energy cutoff (e.g. silica) produces Arrhenius temperature dependence.<sup>197,215</sup> Hence, the difference between strong and fragile liquids arises directly from the PEL.

Stokes-Einstein violation, stretched-exponential relaxation, and the form of the van Hove correlation function are all predicted by the EMB CTRW approach.<sup>197,242,243</sup> This model gives a remarkably complete description of supercooled dynamics.

#### 1.6.2.5 Structure of the PEL

The main subject of this thesis will be the elucidation of higher-order structure in the PELs of supercooled liquids. To aid in the subsequent discussion I will briefly summarise the key results from earlier work.<sup>199,228,232,244</sup>

The number of minima on a glassy landscape is exponential in the system size  $N$ ,<sup>4,196,197</sup> and the vast majority of these minima correspond to amorphous structures. Usually there will also be one or more low-energy regions of the landscape which correspond to crystal structures. One example of a pathway between such a crystalline region and the amorphous region has been characterised.<sup>213</sup> The crystalline regions have low entropy and the energy barriers to reach them are large, so

crystallisation in glass-forming liquids is slow and easily avoided by simulation and experiment.

Outside the crystalline region, the PEL of a supercooled liquid is highly “frustrated”: it contains many competing low-energy minima separated by barriers that are comparable with  $k_B T$  in the supercooled region.<sup>193,197,233</sup> The distribution of local minimum energies and barrier heights is broad, and the landscape is not globally funnelled.<sup>233,245</sup>

Single-funnel landscapes permit efficient relaxation to the global minimum, whereas frustrated landscapes do not. A metric for landscape frustration was recently proposed,<sup>246</sup> based on databases of stationary points, which quantified the greater frustration of glassy landscapes compared with most proteins and atomic clusters.

A significant development over the past two decades has been the recognition of local structure in glassy landscapes. Following Heuer’s work on metabasins, an alternative definition using both geometrical and dynamical information was proposed by de Souza and Wales.<sup>233</sup> This method is discussed in §1.7.3. Both definitions require that transitions between minima within a metabasin are reversible, while transitions between metabasins are irreversible. It is now clear that metabasins are present in the PELs of both strong and fragile glass formers.<sup>234,245</sup>

Both metabasin definitions correspond roughly to local funnel structures on the PEL, as introduced in §1.6.1.4. Disconnectivity graphs for the BLJ fluid<sup>233</sup> indicate that glassy landscapes contain a large number of funnels corresponding to different low-lying amorphous structures. Presumably the lowest minimum in each funnel corresponds to a locally-optimal disordered arrangement of atoms, and the higher-energy minima consist of relatively small perturbations of that arrangement.

The presence of local funnels indicates hierarchical ordering of the PEL minima. A major aim of this thesis will be to investigate characteristics of this ordering, in particular its generalisation to other types of glass former.

### 1.6.2.6 Alternative Characterisations of the PEL

The discussion of PELs has focussed upon properties of minima and transition states, since these encode the equilibrium thermodynamics and dynamics of the system. For completeness, two contrasting approaches to the PEL will now be mentioned. These methods are not used in this thesis, for reasons that will be made clear.

The first approach is to consider the properties of all stationary points, not just minima and transition states. These points are obtained from a simulated trajectory by minimising the auxiliary function  $W(\mathbf{X}) = \frac{1}{2}|\mathbf{g}(\mathbf{X})|^2$ .<sup>247</sup> The Hessian index of each configuration is calculated to classify it.

The mean Hessian index is large at high  $T$ , indicating that the system samples high-energy configurations near to saddle points. At low  $T$ , the average Hessian index is near to 0, i.e. configurations near minima now dominate the structural ensemble. Linear extrapolation suggests that the average index reaches 0 at  $T_c$ , the MCT critical temperature,<sup>248</sup> but in fact the index continues to follow an Arrhenius law at lower temperatures so this extrapolation is misleading.<sup>197,229</sup>

Various “universal” relationships have been reported<sup>249</sup> connecting dynamical properties (such as the activation energy of diffusion) to properties of the stationary points. However, the sample of stationary points obtained by minimising  $W$  will inevitably include many high-order saddles. The Murrell-Laidler theorem tells us that such saddles must always lie higher in energy than the minimum energy barrier, therefore their contribution to the dynamics must be small, and the theoretical basis underlying the use of these configurations is questionable.

Another, qualitatively different, approach to studying the PEL is the instantaneous normal mode (INM) theory. Normal modes for a liquid are given by the mass-weighted eigenvectors of  $\mathbf{H}(\mathbf{X})$  evaluated at a minimum. INMs are obtained by performing the same operation at a configuration that is not a stationary point,<sup>250,251</sup> and therefore include some negative eigenvalues corresponding to unstable directions on the PEL with imaginary vibration frequency.

INM theory attempts to relate dynamical quantities such as  $D(T)$  and relaxation times to the density of states of these unstable modes (or “free directions”).<sup>251</sup> Equilibrium static properties are obtained from the density of states for the stable modes.<sup>250</sup>

Assumption of a locally harmonic PEL is inherent in the INM approach, which is unlikely to be true away from energy-minimised configurations. It was suggested that this problem might be mitigated by identifying and discarding so-called “shoulder modes”, i.e. INMs that arise from anharmonicities rather than pointing towards a saddle point.<sup>251,252</sup> The other significant problem with the use of INM theory is that not all minimum-minimum transitions contribute significantly to diffusion, and therefore not all free directions are relevant to long-time dynamics.

Neither the INM approach nor the use of higher-index saddles can provide the same insight into supercooled dynamics that can be obtained from analysis of local minima and transition states.

### 1.6.3 Outlook

The PEL concept as a quantitative tool has declined slightly in popularity in recent years,<sup>79</sup> because it is framed in terms of configuration space and not real space, which leads to difficulties in accounting quantitatively for dynamic heterogeneity,<sup>98</sup> and because static length scales associated with the PEL do not seem to grow with decreasing temperature.<sup>73</sup>

However, heterogeneities in the PEL/EMB framework arise naturally from decomposition of the liquid into non-interacting subsystems, each of which explores a different region of the PEL with a different average mobility. Even a simple model with two subsystems, that can each occupy either a fast state or a slow state, is sufficient to produce the expected Stokes-Einstein violations.<sup>197</sup>

Heuer has suggested that decreasing the temperature causes the mobilities of adjacent subsystems to become increasingly correlated,<sup>197,218</sup> due to exchange interactions between them. In this case, the subsystems are no longer really independent and it may be more appropriate to describe this effect as a growth of the subsystems with decreasing temperature. The subsystem size is therefore a growing static length scale.

The energy landscape framework holds a unique position among theories of the glass transition in that many of the other methods described in this chapter may be described using PEL concepts. This universality of the energy landscape idea offers the possibility of a bridge between several of the different approaches, using Goldstein's original principle supercooled liquids are strongly influenced by potential energy barriers. A major ongoing task is to use PEL methods to find connections between different theories, and to validate or falsify some of the numerous alternative models.

## 1.7 Diffusion and Energy Landscape of a Fragile Atomic Glass Former

Much of the work presented in this thesis follows on from the efforts of de Souza and Wales, who conducted an extensive study of the dynamics and PEL of the Kob-Andersen binary Lennard-Jones (BLJ) fluid<sup>10</sup> - probably the most popular atomic model fragile glass former.

Kob-Andersen BLJ is an 80:20 mixture of large A atoms and small B atoms, which interact via the 12-6 Lennard-Jones potential<sup>253</sup> that provides a crude model for dispersion interactions and short-ranged repulsion. The A-B interaction is stronger

than the A-A or B-B interactions, to prevent phase-separation and therefore promote glass formation. On the simulation time scale crystallisation may safely be neglected for the densities and temperatures considered here. Full details of the potential and simulation conditions can be found in the original papers.<sup>26,254,255</sup>

Part of the motivation for this project was to establish whether the conclusions reached for BLJ also apply to other types of glass former. For ease of reference in subsequent chapters, the important conclusions of the BLJ study will now be reviewed.

### 1.7.1 Correlation Effects in BLJ Diffusion

The first part of the BLJ study investigated the timescale dependence of the self-diffusion constant  $D(T)$ .<sup>26,254,255</sup>

The diffusivity was evaluated over short time intervals of length  $\tau$  (see chapter 6 for details). This quantity neglects correlations in particle motion between different time intervals, with the surprising result that super-Arrhenius temperature dependence of the diffusion constant disappeared.<sup>254,255</sup> On short time scales, the liquid experiences a constant free energy barrier to diffusion, producing Arrhenius behaviour. As the observation time  $\tau$  increases, increasing negative correlations of the particles' displacement causes the diffusion constant to decrease, and hence the apparent activation barrier increases.

It turns out that only correlations between adjacent short time intervals are significant, which allows the correlation effect to be quantified.<sup>254,255</sup> A first-order correction term was obtained, that reintroduces this average correlation to the short-time diffusivity. The correction term is simple to compute from short MD trajectories and is quite effective, allowing the long-time diffusive behaviour of BLJ to be approximated from short, non-ergodic simulations.

The success of the correlation correction method is convincing evidence that negative correlation of particle displacement vectors over short time intervals is responsible for super-Arrhenius curvature of the diffusion constant. The next stage of the investigation was to examine the source of this correlation behaviour.

### 1.7.2 A Geometric Definition of Cage Breaks

Reviewing the standard plot of mean squared displacement against time, fig. 1.2, the time regime in which reversals of particle direction are most expected is the caging plateau. Diffusive motion only occurs on a time scale long enough for particles to break out of their nearest-neighbour cages. At low temperatures, this process can

be very slow.

De Souza and Wales proposed a microscopic definition of a cage-breaking rearrangement for BLJ, using only the initial and final configurations of the system.<sup>233</sup> These configurations are first mapped onto local minima of the PEL to remove the effects of vibrational “rattling” motion.

Since each molecule resides in a cage made by its nearest neighbours, the definition of a cage-breaking process must involve changes to these neighbours. For BLJ, atom  $j$  is a nearest neighbour of atom  $i$  when  $|\mathbf{r}_j - \mathbf{r}_i| < r_{\text{NN}}(\alpha, \beta)$ . Here  $\alpha$  and  $\beta$  are the atom types of  $i$  and  $j$ .  $r_{\text{NN}}(\alpha, \beta)$  is the position of the first minimum in the radial distribution function (RDF) for atom types  $\alpha$  and  $\beta$ .<sup>233</sup> Since the RDF has a small value either side of  $r_{\text{NN}}(\alpha, \beta)$ , the nearest-neighbour shell is well defined.

A cage break (CB) is defined as a rearrangement where an atom loses or gains two nearest-neighbours. This requirement ensures that when a single atom moves, it can only produce a single cage break.

To prevent small movements of neighbours near the edge of the nearest-neighbour shell from being registered as neighbour changes, a displacement cutoff  $d_c(\alpha, \beta)$  is used.  $d_c(\alpha, \beta)$  is set equal to the equilibrium pair separation of two atoms of types  $\alpha$  and  $\beta$ .

Consider a rearrangement (elementary or otherwise) in which a nearest neighbour  $j$  of atom  $i$  moves to a new position  $\mathbf{r}'_j$ . The neighbour is only considered lost if  $|\mathbf{r}'_j - \mathbf{r}'_i| > r_{\text{NN}}(\alpha, \beta)$  and also  $|\mathbf{r}'_j - \mathbf{r}_j| > d_c(\alpha, \beta)$ . For a nearest neighbour  $k$  to be gained, we require  $|\mathbf{r}'_k - \mathbf{r}'_i| < r_{\text{NN}}(\alpha, \beta)$  and  $|\mathbf{r}'_k - \mathbf{r}_k| > d_c(\alpha, \beta)$ .

To analyse diffusion, cage breaks are identified in an inherent structure trajectory. Each molecule is classified as either cage-breaking or non-cage-breaking for each pair of consecutive minima. An effective cage-breaking diffusion constant can be calculated:

$$D_{\text{CB}}(T) = \frac{1}{6t} \sum_i^N \frac{1}{N_{\text{CBs},i}} \sum_{j \in \text{CBs}}^{N_{\text{CBs},i}} \Delta \mathbf{r}_{i,j}^2, \quad (1.18)$$

where the index  $j$  runs over the list of cage-breaking jumps made by atom  $i$ .  $N_{\text{CBs},i}$  is the number of cage breaks made by  $i$  and  $\Delta \mathbf{r}_{i,j}$  is the displacement vector of  $i$  in its  $j^{\text{th}}$  cage break.

$D_{\text{CB}}(T)$  was found to overestimate  $D(T)$  quite significantly, and also fails to reproduce super-Arrhenius behaviour. This is because  $D_{\text{CB}}(T)$  neglects negative correlation in  $\Delta \mathbf{r}_{i,j}$ . This correlation is accounted for by identifying and discarding all CBs that are immediately reversed. Reversals can be “direct”, meaning that the molecule returns to its original cage via a second CB, or “indirect” where the return step is by one or more non-cage-breaking transitions. Direct reversals were

identified when the total squared displacement for a particular particle after two consecutive CBs was less than  $d_{\text{rev}} = 10^{-5} \sigma_{\text{AA}}^2$ .<sup>233</sup> Indirect reversals were identified when the total squared displacement after two consecutive CBs was identical within  $d_{\text{rev}}$  to the squared displacement in either of the individual CB events. This scenario indicated that the atom returned to its original position during the interval between the two CBs, and hence that a non-cage-breaking reversal took place.

A CB that is not subsequently reversed is called *productive*.  $D_{\text{prod}}(T)$  is defined by eq. (1.18) with the sum in  $j$  restricted to run over productive CBs only.  $D_{\text{prod}}(T)$  was found to approximate  $D(T)$  quite well, especially at low temperatures, indicating that productive CBs provide a good description of the transport processes involved in long-time diffusion. The geometrical cage-breaking approach is an efficient and comparatively simple method for identifying important local rearrangements.

At lower temperatures, cage-breaking transitions become less common because they are associated with high energy barriers (see §1.7.3). Additionally, reversal events become more likely at lower temperatures because the caging particles rearrange more slowly following an escape of the central particle, so that immediately returning to the original position is energetically and entropically favourable. Since productive cage breaks dominate the diffusion constant, reduced frequency of cage breaks and increased reversal probability at lower temperature increases the effective energy barrier to diffusion and leads to super-Arrhenius behaviour.<sup>112</sup>

Cage-breaking analysis yields a simplified microscopic description of diffusion in BLJ that complements the coarse-grained picture provided by short-time diffusion constants. These two methods give similar explanations for the origin of super-Arrhenius behaviour in this system.

### 1.7.3 Cage Breaks on the PEL

Beyond their dynamical significance, de Souza and Wales showed that cage breaks are fundamentally linked to the structure of the BLJ potential energy landscape. Transition states in a PEL database may be classified as either cage-breaking, if one or more atoms undergo a CB during the transition, or non-cage-breaking if no atoms break their cages.

Energy barriers that pass through a cage-breaking transition state are systematically larger than non-CB barriers,<sup>233</sup> which explains why CB motion dominates diffusion at low  $T$ : crossing the high CB barriers becomes the limiting factor in transport across the energy landscape.

It turns out that removing cage-breaking transition states splits the stationary point database into many small disconnected fragments, most of which are confined

to a single funnel on the PEL. This fragmentation indicates that cage-breaking motion is necessary to traverse the entire landscape, and in particular it is necessary to cross between funnels. In contrast, removing non-cage-breaking transition states has almost no effect on the connectivity of the landscape and all local funnels remain connected. Cage-breaking motion is therefore sufficient to traverse all important regions of the PEL.

The landscape databases used in this study were produced by finding discrete paths of transition states and intermediates between each pair of consecutive minima in an inherent trajectory (see §2.2.1 and §2.2.2 for details). This procedure preserves the time-ordering of minima and transition states visited by the system, so that reversed cage breaks can be identified. CB rearrangements are then classified either as *productive transition states*, in which no cage-breaking atoms undergo any reversals, or as *unproductive transition states* in which at least one CB is subsequently reversed.

It turns out that most of the cage breaks within local funnels are easily reversible. Therefore removing the productive CB transition states causes the landscape to fragment into regions that closely match the landscape funnels visible on a disconnectivity graph (see §2.2.4). This result is significant for several reasons. Firstly, productive cage-breaking transition states represent the first simple numerical tool capable of defining a funnel structure on a disconnectivity graph, and hence provide direct evidence of hierarchical structure on the PEL.

Secondly, the regions of the landscape whose boundaries are defined by productive cage breaks seem to be analogous to the metabasins detected by Heuer and others, which are also hierarchical structures of minima.<sup>229,230,238</sup> A key characteristic of metabasins is that transitions between them are not reversed on the observation time scale, which is also true of productive cage breaks. Productive cage breaks therefore allow diffusion to be described as a random-walk process between landscape funnels: a potentially powerful theoretical description of glassy dynamics. The diffusion constant of BLJ has been estimated from a random walk model using only the average CB waiting time and proportion of reversed cage breaks - both local quantities that can be determined from short simulations.

A useful attribute of the cage-breaking definition of metabasins is that the important jumping process is identified for a single particle. This opens the possibility to detect metabasin transitions in large simulated systems, whereas the EMB definition becomes increasingly difficult to apply when multiple subsystems are present.<sup>218</sup>

### 1.7.4 The Role of Connectivity

To obtain a more rigorous quantitative explanation of the entropic barrier that promotes reversals of particle motion at low temperatures, de Souza and Wales studied the effective connectivity of local minima as a function of temperature.<sup>256</sup>

They performed extensive local sampling of the PEL using short microcanonical MD trajectories originating at a local minimum, and recorded the first minimum visited by each trajectory which was separated from the starting point by a cage break. From these simulations, they estimated the number of cage-breaking routes out of each minimum, which depends strongly on the temperature because many fewer diffusive routes are available at low temperature than high.

An “effective connectivity” for each minimum was obtained by combining the number of CB connections with the probabilities of taking each escape route. The decrease of this quantity with  $T$  causes super-Arrhenius behaviour, although it is unclear whether this effect completely accounts for the anomaly observed for  $D(T)$  in BLJ.

The temperature dependence of effective connectivity is affected by the density of the fluid, which correlates with the fragility in BLJ. Number densities of 1.1 and  $1.3\sigma_{AA}^{-3}$  were compared, and it was found that the connectivity decreases much faster with  $T$  in the more fragile system, consistent with this decrease being a cause of super-Arrhenius behaviour.

The result of this study is a coherent, simplified picture of diffusion in BLJ, which describes the origin of super-Arrhenius transport behaviour using the three concepts of cage breaking rearrangements, negative correlation of displacement vectors, and connectivity on the potential energy landscape. A major objective of this project, which is the subject of chapters 3, 4 and 6, was to take the conclusions of the BLJ study and determine whether they apply to other model glass formers.

# Chapter 2

## Methods

Exploring the configuration space of model glass formers is a common theme throughout this thesis. Two principle methods are used for this exploration: molecular dynamics simulation, which attempts to replicate true dynamic behaviour and which can generate an unbiased ergodic sample of the available configuration space if run for sufficiently long times, and energy landscape exploration, which is explicitly guided by the details and structure of the PEL to obtain a simplified mathematical description of dynamics and thermodynamics.

In this chapter, several important tools within these two approaches are introduced and explained. The focus is on methods that sample configurations, rather than methods of analysing those configurations. Details of the analysis methods are presented in the appropriate results chapters.

### 2.1 Molecular Dynamics

Molecular dynamics (MD) simulation is one of the most common approaches to model properties of a physical system, and by far the most common method to simulate atomistic dynamics.<sup>257</sup> There are many different MD protocols, which have been extensively discussed and compared.<sup>39,258–260</sup>

#### 2.1.1 Fundamentals of Molecular Dynamics

Classical dynamics are governed by Newton's equations of motion, particularly the second law:

$$m_i \ddot{\mathbf{r}}_i = -\mathbf{g}_i(\mathbf{X}) = -\frac{\partial V(\mathbf{X})}{\partial \mathbf{r}_i}, \quad (2.1)$$

where  $m_i$  and  $\mathbf{r}_i$  are the mass and position of particle  $i$ ,  $V(\mathbf{X})$  is the potential energy for the system configuration  $\mathbf{X} = \{\mathbf{r}_i\}$  and  $\mathbf{g}(\mathbf{X})$  is the gradient of  $V$ . All of the

potential energy functions used in this thesis are pairwise additive and isotropic, i.e.

$$V(\mathbf{X}) = \sum_i^N \sum_{j>i}^N V_{ij}(|\mathbf{r}_i - \mathbf{r}_j|), \quad (2.2)$$

where  $V_{ij}(r)$  is a pair potential acting between atoms  $i$  and  $j$ .

Eq. (2.1) determines the instantaneous acceleration of each particle. In principle, continuous integration of this equation with respect to time, starting from initial conditions  $\mathbf{X}(t=0)$  and  $\dot{\mathbf{X}}(t=0)$ , would generate the correct classical motion of the system.

In practice, MD programs perform numerical integration in discrete time steps, solving eq. (2.1) for  $\ddot{\mathbf{r}}_i$  at time  $t$  and hence calculating the positions and velocities of each particle at time  $t + \Delta t$ . This process is repeated many times, and the resulting time series of position and velocity vectors constitute an *MD trajectory*. The timestep  $\Delta t$  is the most important parameter of an MD simulation, and must be significantly smaller than the period of the fastest process being studied, if the dynamics are to be described correctly.

There are many different numerical integration schemes employed by MD packages.<sup>261–264</sup> In this thesis the velocity Verlet integrator<sup>258,261,262</sup> is used to simulate atomic systems (BLJ and silica). The equations used to update the system are:

$$\begin{aligned} \mathbf{r}_i(t + \Delta t) &= \mathbf{r}_i(t) + \Delta t \mathbf{v}_i(t) + \frac{\Delta t^2}{2m_i} \mathbf{F}_i(t) \\ \mathbf{v}_i(t + \Delta t) &= \mathbf{v}_i(t) + \frac{\Delta t}{2m_i} [\mathbf{F}_i(t) + \mathbf{F}_i(t + \Delta t)], \end{aligned} \quad (2.3)$$

where  $\mathbf{F}_i(t) = -\mathbf{g}_i(t)$  is the force on atom  $i$  at time  $t$ , and  $\mathbf{v}_i(t) = \dot{\mathbf{r}}_i(t)$  is the velocity of  $i$ .

Numerical errors arising from discrete time integration can cause slow drift in quantities that should be conserved, such as the total energy.<sup>39,259</sup> Different integration schemes have different magnitudes of drift. Good integrators respect time-reversal symmetry and are symplectic - i.e. they conserve the areas of shapes in phase space during time integration and thus obey Liouville's theorem.<sup>258</sup> Velocity Verlet satisfies both conditions.<sup>258</sup>

MD simulation is simple to implement, can be made very efficient, and generates very complete information about the system. However, two major approximations limit its usefulness. The first is that Newton's equations neglect quantum dynamical effects such as delocalisation and tunnelling. Fortunately, these effects are unimportant for most structural glasses, since the particles involved are too heavy, and the

temperatures too high, for quantum effects to be significant.

The second major approximation of MD is the use of discrete time to solve the equations of motion. MD algorithms with finite  $\Delta t$  suffer from “Lyapunov instability”, i.e. two trajectories with nearly-identical initial conditions will diverge exponentially over time.<sup>39,259</sup> Consequently, MD simulations should not be considered to reproduce uniquely the correct dynamics, but instead they generate representative possible trajectories in configuration space that the system might follow.

Despite these problems, MD trajectories are widely used to investigate dynamic behaviour. They can also be used to compute static equilibrium properties by virtue of the ergodic hypothesis, which states that in the long time limit a system visits all of its accessible microstates with equal probability.<sup>258</sup> If ergodicity is satisfied, the time average of any dynamic variable over the trajectory will be equal to the equilibrium ensemble average. A long MD trajectory with constant total energy  $E$  will sample all configurations that are accessible without crossing barriers greater than  $E$ . A density of states can then be calculated for this configuration space.<sup>258</sup> Methods for confirming whether the trajectory being used is long enough to calculate average properties are discussed in §2.1.4.

## 2.1.2 Practical Considerations

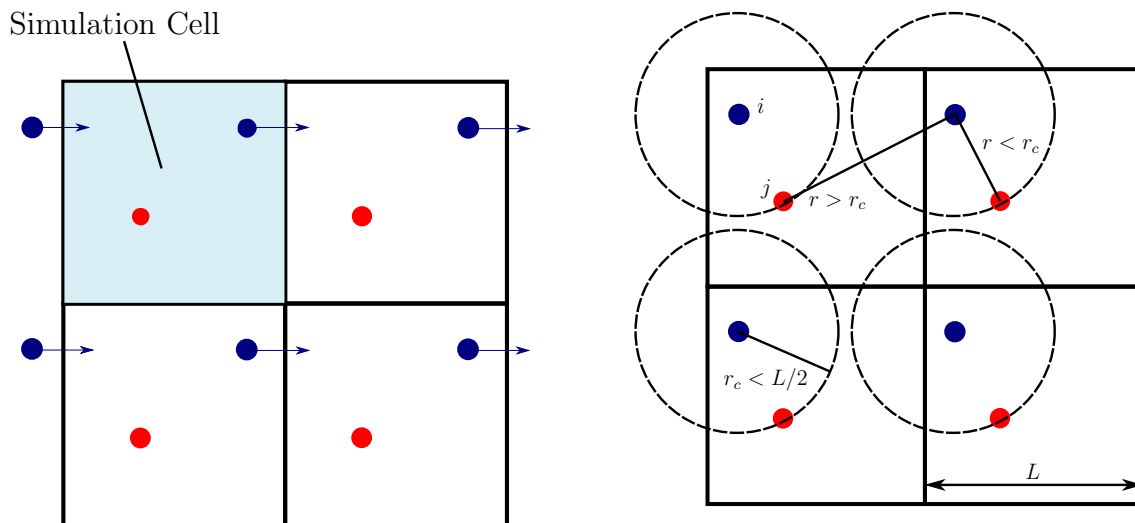
The simplest MD algorithms generate configuration space samples that correspond to the microcanonical ensemble - conditions of constant system size, volume and energy. Using the equipartition principle,<sup>259,265</sup> the instantaneous kinetic temperature may be calculated according to

$$T(t) = \frac{1}{3k_{\text{B}}N} \sum_{i=1}^N m_i \mathbf{v}_i^2(t). \quad (2.4)$$

In general, one is interested in properties of systems at constant temperature rather than constant energy. In moderately supercooled liquids,  $T(t)$  is often quite constant, so microcanonical simulation is sufficient for a reasonable description of dynamics and thermodynamics.

For more complex energy landscapes,  $T(t)$  may vary considerably in which case the MD algorithm must be extended to generate the canonical ensemble, which replaces constant energy conditions by constant temperature. This ensemble is enforced using a stochastic algorithm to adjust the total energy, such as the Andersen<sup>266</sup> or Nosé thermostats.<sup>267,268</sup>

The computational cost of an MD simulation depends strongly on the system



(a) Illustration of PBCs. Every image of the blue atom moves between images of the simulation cell. The number of atoms in each cell is conserved.

(b) The truncation radius  $r_c$  must be small enough that the interaction spheres for the different images of atom  $i$  do not overlap.

size  $N$  (since evaluating a naive pairwise potential scales as  $N^2$ ). Condensed-phase systems containing  $O(10^{23})$  particles are represented using periodic boundary conditions (PBCs): explicit simulation is confined to  $N$  atoms in a primary simulation cell (which in our case is cubic with side length  $L$ ), and the complete liquid is represented by infinitely many identical copies of this cell, tiling three-dimensional space.

When a particle passes out of the primary simulation cell through one of its walls, another copy (or “image”) of the same particle simultaneously enters the simulation cell with identical velocity through the opposite wall - see fig. 2.1a. PBCs are efficient and simple to implement, but they impose limits on the potential: to avoid double counting, the pair potential  $V_{ij}(r_{ij})$  must therefore be truncated at a distance  $r_c < L/2$  (see fig. 2.1b). If  $V_{ij}(r_c) \gg 0$ , this truncation can cause discontinuities and serious inaccuracies in  $V(\mathbf{X})$ .

Initial conditions for MD simulation of glasses are often obtained by starting from a periodic lattice structure with random particle velocities, and performing an initial MD run at high temperature, to break up the lattice and reach a liquid-like structure. The main MD run begins from this liquid configuration, and further configurations are saved every  $n$  time steps.

### 2.1.3 Molecular Dynamics of Rigid Bodies

The model of ortho-terphenyl (OTP) studied in chapter 3 is a rigid molecule composed of triangles of atoms with fixed internal geometry. There are two possible ways to treat this system in an MD simulation. Each atom may be simulated explicitly, with molecular geometries enforced by additional constraints added to the equations of motion - for example the SHAKE<sup>269</sup> and RATTLE<sup>270</sup> algorithms. Alternatively, each molecule may be treated in the equations of motion as a single particle with its position and orientation described by a set of generalised coordinates. The potential energy evaluation is the only part of the simulation that takes account of the positions of individual atoms.

The second approach is used in this thesis, because it is computationally cheaper and more compatible with geometry optimisation methods (see §2.3). Constant temperature MD simulations of OTP were performed using a program written by Dr Dwaipayan Chakrabarti. The discrete-time numerical integrator used in this program was developed by Okumura *et al.*<sup>271</sup> for canonical ensembles of rigid body particles. The position of the rigid bodies is specified by centre-of-mass Cartesian coordinates. The orientation is specified by quaternions, because of their numerical stability.<sup>272</sup>

The algorithm combines a symplectic integrator with the Nosé-Poincaré thermostat, leading to a complicated Hamiltonian that depends on positional, orientational and thermostat degrees of freedom. Okumura *et al.* provide equations of motion to update the values of each of these components in discrete time steps.

### 2.1.4 Determining Local Ergodicity

As explained in §2.1.1, computing static equilibrium properties of a system requires an ergodic trajectory. However, supercooled liquids are never truly ergodic, since this would require exploring the entire configuration space - including the crystal region. Simulations of a model glass former should therefore achieve local ergodicity: complete exploration of the liquid-like regions of the potential energy landscape so that a time average over the trajectory corresponds to an ensemble average over this restricted phase space.<sup>4,26</sup>

Often, local ergodicity is assumed when the simulation time exceeds  $10\tau_\alpha$  -  $100\tau_\alpha$ , the slowest structural relaxation time. Where possible, we have used more rigorous methods to test local ergodicity: the Mountain-Thirumalai energy fluctuation metric<sup>26,273</sup> and the non-Gaussian parameter for translational displacement.<sup>254,274</sup>

### 2.1.4.1 Mountain-Thirumalai Fluctuation Metric

The energy fluctuation metric is defined as:<sup>273</sup>

$$\Omega(t) = \frac{1}{N} \sum_{\alpha} \sum_{j=1}^{N_{\alpha}} [\epsilon_j(t; \alpha) - \bar{\epsilon}(t; \alpha)]^2, \quad (2.5)$$

where  $\bar{\epsilon}(t; \alpha) = \frac{1}{N_{\alpha}} \sum_{j=1}^{N_{\alpha}} \epsilon_j(t; \alpha)$

and  $\epsilon_j(t; \alpha) = t^{-1} \int_0^t E_j(t'; \alpha) dt'$ .

$\alpha$  denotes the particle type in multicomponent systems (e.g.  $\alpha = \text{Si}$  or  $\text{O}$  in silica).  $E_j(t; \alpha)$  is the energy of the  $j^{\text{th}}$  particle at time  $t$ : kinetic energy plus half of each pairwise potential term involving  $j$ .  $\epsilon_j(t; \alpha)$  is the time average of  $E_j(t; \alpha)$ , and  $\bar{\epsilon}(t; \alpha)$  is the  $\alpha$ -particle average of  $\epsilon_j(t; \alpha)$ .

$\Omega(t)$  measures how far the time-averaged energies of individual particles deviate from the ensemble average, which need not cover the entire configuration space.  $\Omega(t)$  vanishes at long times for any trajectory which is ergodic within a particular region.

We diagnose a locally ergodic trajectory when  $\Omega(t)/\Omega(0) < 0.01$ .<sup>275</sup> However, we also follow de Souza and Wales' argument that any trajectory for which  $\Omega(t)$  tends to a non-zero value, no matter how small, is not locally ergodic.<sup>26</sup> Therefore, if any trajectory reaches a plateau in  $\Omega(t)$  we continue the simulation until  $\Omega(t)$  is once again decreasing.

Fig. 2.2 shows the decay of  $\Omega(t)/\Omega(0)$  for OTP trajectories at several temperatures. The curve for the 260 K trajectory remains significantly higher than the others and decays at a slower rate. This trajectory may not be locally ergodic, so results arising from it will be treated with caution.

### 2.1.4.2 Non-Gaussian Parameter

An alternative test of local ergodicity, that measures very different properties to the energy fluctuation metric, uses the non-Gaussian parameter:<sup>274</sup>

$$\alpha_2(t) = \frac{3\langle |\mathbf{r}_i(t) - \mathbf{r}_i(0)|^4 \rangle}{5\langle |\mathbf{r}_i(t) - \mathbf{r}_i(0)|^2 \rangle^2} - 1. \quad (2.6)$$

As usual,  $\mathbf{r}_i(t)$  is the position vector of particle  $i$  at time  $t$ , and  $\langle \dots \rangle$  denotes an average over particles and time origins.

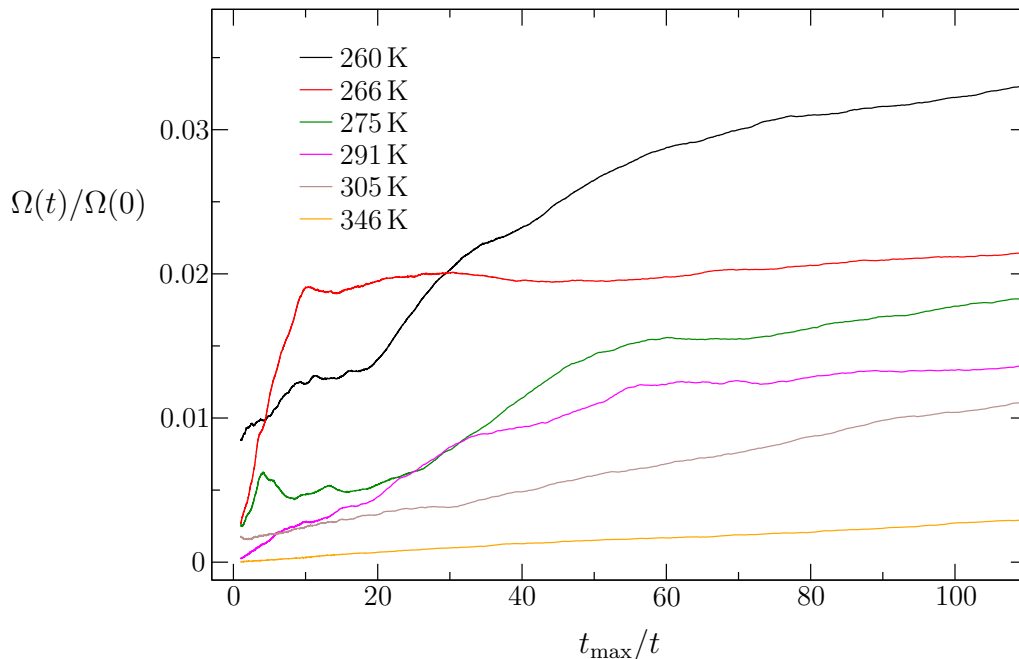


Figure 2.2: Mountain-Thirumalai fluctuation metric plotted against inverse time for MD trajectories of OTP at several temperatures.  $t_{\max}$  is the total simulation time.

$\alpha_2$  quantifies the deviation of particle displacements from the Gaussian distribution expected for isotropic diffusion. At long times,  $\alpha_2$  decays to 0 for ergodic trajectories. At very short times, particles move ballistically, so motion is homogeneous and  $\alpha_2 = 0$  again. Between these limits there is heterogeneous behaviour due to the cage effect, and  $\alpha_2$  reaches a maximum.<sup>70,254,255</sup>

Fig 2.3 shows the time variation of  $\alpha_2$  for several OTP simulations. All trajectories decay towards zero at long times, suggesting local ergodicity, but the three lowest temperatures reach a non-zero plateau for which there is no clear interpretation. At short times all trajectories adhere to a master curve,  $\alpha_2 \propto t^{\frac{1}{2}}$ , which indicates the extent of the caging region. Departure from the master curve occurs later at lower temperatures, reflecting increased difficulty in escaping cages. Assigning local ergodicity on the basis of  $\alpha_2(t)$  is not straightforward, but the small value of the parameter at long times suggests that all of these trajectories are locally equilibrated.

The  $\alpha_2$  parameter probes the dynamics of the system, rather than the extent to which its configuration space is explored. For that reason, the Mountain-Thirumalai metric was preferred for diagnosing local ergodicity, although this was often confirmed using  $\alpha_2(t)$ .

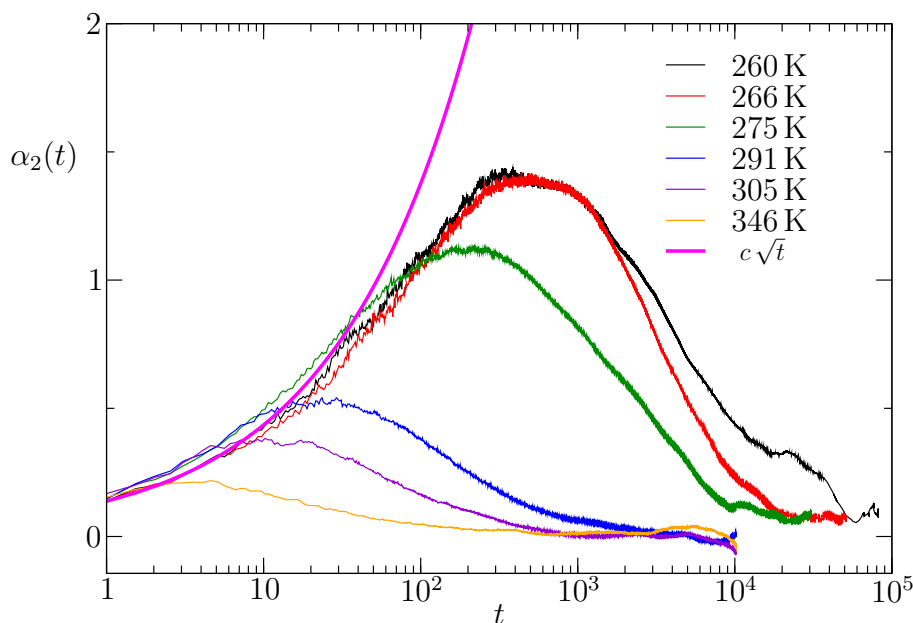


Figure 2.3: Non-Gaussian parameter plotted against time (in dimensionless units) for MD trajectories at several temperatures. A master curve  $\alpha_2 = c\sqrt{t}$  is also shown, where  $c \approx 0.1$ , which fits the short-time data for all temperatures.

## 2.2 Potential Energy Landscape Exploration

Knowledge of every stationary point of a PEL would tell us most properties of the corresponding system. However, the number of these stationary points is exponential in  $N$ ,<sup>4,196,197</sup> and generally much too large for exhaustive exploration. Instead, geometry optimisation methods aim to generate a representative sample of local minima and transition states.

Identifying local minima of  $V(\mathbf{X})$  is fairly straightforward (see §2.2.1) but obtaining an unbiased and meaningful sample of different regions of the landscape can be challenging. Transition states are much harder to locate numerically. Since the methods used to locate these two types of configuration are rather different, they will be discussed separately.

The landscape studies in this thesis were all carried out using the Cambridge Energy Landscapes Software package (CELS), which comprises the three Fortran programs `GMIN`,<sup>276</sup> `OPTIM`<sup>277</sup> and `PATHSAMPLE`,<sup>278</sup> or using the Python Energy Landscape Explorer (PELE).<sup>279</sup>

### 2.2.1 Identifying Local Minima

Local minima of  $V(\mathbf{X})$  are easily identified by applying the L-BFGS algorithm to a starting configuration. L-BFGS (the limited memory Broyden-Fletcher-Goldfarb-

Shanno algorithm)<sup>280,281</sup> is a very efficient quasi-Newton optimisation method that requires only the first derivatives of the objective function, but which uses a numerical estimate of the curvature to accelerate convergence.<sup>282</sup>

The method of choosing configurations to minimise is very important. There are several approaches to generate a meaningful sample of minima,<sup>195,283–285</sup> which are each suitable for addressing different problems.

To describe the diffusion dynamics of a model glass-former (chapters 3 and 4) we wish to sample the same minima that the diffusing system explores. This sampling is achieved by first generating a locally ergodic MD trajectory, then applying the L-BFGS algorithm to configurations extracted from the trajectory at regular intervals of simulated time. This process is known as *quenching*. The resulting series of minimized configurations is known as an *inherent structure trajectory* (or simply *inherent trajectory*) after Stillinger and Weber.<sup>195</sup> The process is shown schematically in fig. 2.4. Because the original MD trajectory was (locally) ergodic, the minima contained in the inherent trajectory constitute an equilibrium sample of the configuration space accessible to the supercooled liquid.

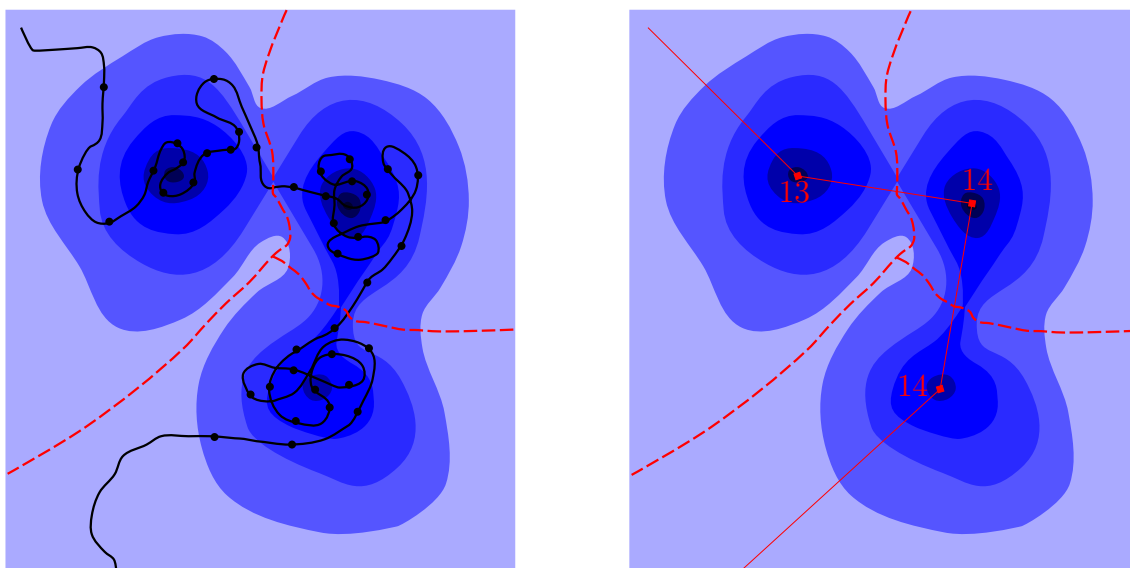
The PEL is temperature-independent object, but the inherent trajectory approach can depend quite strongly on the temperature of the original MD trajectory, since systems at different temperatures may explore different regions of the PEL.<sup>225</sup> At low temperatures, the system may reside in each basin of attraction for long periods of time, hence many successive quenches lead to the same local minimum.

The limitation of the inherent trajectory approach is that sampling of the landscape can only be as complete as the original MD trajectory, and that obtaining locally ergodic trajectories at low temperatures may be very expensive. Methods that rely entirely on geometry optimisation can be significantly more efficient than MD-based sampling.

### 2.2.1.1 Basin-hopping Global Optimisation

The principal geometry optimisation method for obtaining local minima is basin-hopping global optimisation,<sup>284</sup> which is a stochastic method that explores a transformed landscape. It does not aim to sample the equilibrium distribution of minima  $g_{\text{IS}}(V)$ , nor does it attempt to represent true dynamics of the system. Instead, basin-hopping is an efficient method for locating low-energy PEL minima, particularly the global minimum.

The basin-hopping transformation is equivalent to applying L-BFGS minimisation to every point in configuration space,  $\tilde{V}(\mathbf{X}) = \min\{V(\mathbf{X})\}$ . This transformation removes all downhill energy barriers between minima, so basin-hopping is



(a) Choropleth of model 2D landscape (darker colour indicates lower energy) with three local minima. The black line indicates an MD trajectory. Black circles indicate configurations to be quenched. Dashed red lines indicate the boundaries of the basins of attraction.

(b) Model 2D landscape with inherent structure trajectory shown in red. Dashed red lines indicate the boundaries of the basins of attraction. The numbers indicate how many quenches map to each local minimum.

Figure 2.4

more efficient than MD for seeking out low-energy regions of the landscape. The transformation is shown schematically in fig. 2.5.

In practice, we do not transform the entire landscape, but only the sequence of configurations visited by the algorithm. Each basin-hopping step consists of a structural perturbation followed by energy minimisation to identify a local minimum. This new minimum is accepted with probability given by the Metropolis criterion,  $\min\{1, \exp(-\Delta E/T_{\text{bh}})\}$ .  $\min$  indicates the minimum of the two arguments,  $\Delta E$  is the energy change from the last-accepted minimum to the new minimum, and  $T_{\text{bh}}$  is a fictitious “temperature” used to control the acceptance rate.

If the new minimum is accepted, it is stored in a database and the next basin-hopping step begins at this configuration. If the minimum is rejected, it is not stored and the next step starts from the last-accepted minimum.

The basin-hopping algorithm does not obey detailed balance between minima unless all basins of attraction have equal volume in configuration space. Instead, exploration is deliberately biased towards the most important low-energy minima, and those with the largest basin volumes.

We denote the distribution of minima obtained from basin-hopping by  $\rho_{\text{IS}}(V)$ .

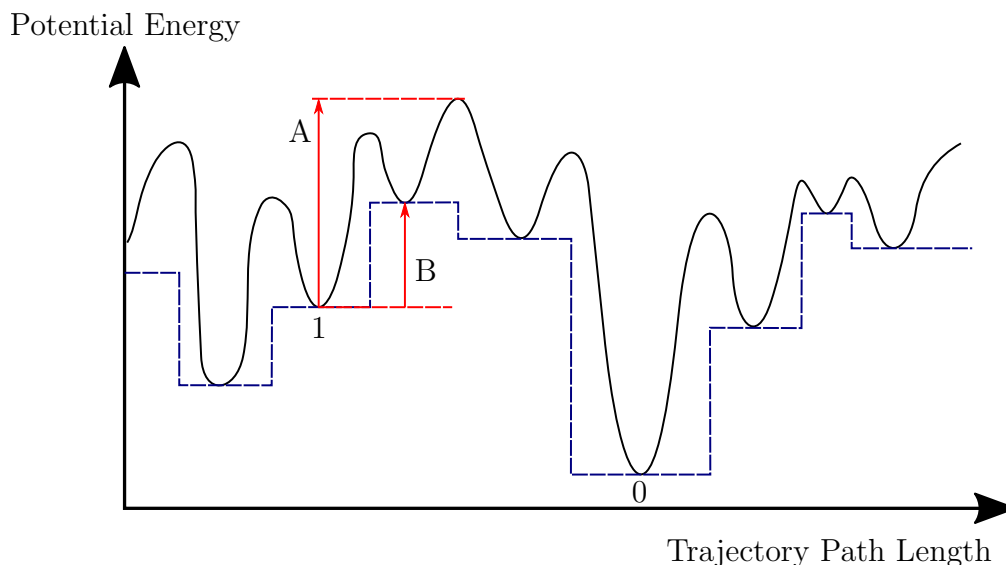


Figure 2.5: Schematic of the basin-hopping landscape transformation. The true landscape is shown in black, as a function of distance along an (arbitrary) trajectory in configuration space. The dashed blue line represents the transformed landscape  $\tilde{V}(\mathbf{X})$ . The red arrows A and B represent energy barriers from minimum 1 to the global minimum 0. Arrow A corresponds to the barrier in  $V(\mathbf{X})$ , B corresponds to the barrier in  $\tilde{V}(\mathbf{X})$ . Arrow B is smaller, hence the transformed landscape is easier to explore.

Without normalisation,  $\rho_{\text{IS}}(V) \leq g_{\text{IS}}(V)$ , and  $g_{\text{IS}}(V) = 0 \implies \rho_{\text{IS}}(V) = 0$ . For a sufficiently long basin-hopping calculation, we expect that  $\rho_{\text{IS}}(V) \approx g_{\text{IS}}(V)$ , particularly at low  $V$ .

The structural perturbation used to generate new minima is normally a random perturbation for each component of  $\mathbf{X}$ , selected from a uniform distribution on  $[-\Delta x, \Delta x]$ , where  $\Delta x$  is the maximum step size parameter.

Both  $\Delta x$  and  $T_{\text{bh}}$  may be varied during the calculation so that the rate at which new minima are accepted remains roughly constant. Typically,  $\Delta x$  is linked to the fraction of basin-hopping steps that generate a trial minimum different from the last-accepted minimum.  $\Delta x$  is increased when this fraction is smaller than a predefined limit, or decreased when the fraction is larger than that same limit.  $T_{\text{bh}}$  is varied in the same way to maintain a constant acceptance rate of the Metropolis criterion, typically around 50%.

### 2.2.1.2 Parallel Tempering Basin-hopping

Basin-hopping may not be sufficient to explore a complex PEL with many funnels. The algorithm will usually search downhill within a funnel rather than jumping to a different funnel, and may therefore miss the global minimum. This problem can be

avoided by increasing  $T_{\text{bh}}$  so that high-energy minima are accessible, but then the algorithm may not explore the lowest-energy minima in each funnel, and a major advantage of basin-hopping is lost.

To achieve effective exploration of many funnels without compromising the search for low-energy minima, parallel tempering basin-hopping (PTBH) may be employed.<sup>286</sup> Similar to conventional parallel-tempering simulations,<sup>39</sup>  $N_r$  replicas of the basin-hopping calculation are propagated independently with different basin-hopping temperatures  $\{T_{\text{bh},1}, T_{\text{bh},2}, \dots, T_{\text{bh},N_r}\}$ . Every  $N_e$  steps, an exchange of last-accepted configurations is attempted between two replicas with neighbouring temperatures. An exchange between replicas  $i$  and  $j = i + 1$  is accepted with probability

$$\min\{1, \exp(-(T_{\text{bh},i}^{-1} - T_{\text{bh},j}^{-1})(V_i - V_j))\}, \quad (2.7)$$

where  $V_i$  is the potential energy of the last local minimum accepted by replica  $i$ . Careful selection of  $T_{\text{bh},i}$  and  $T_{\text{bh},j}$  is required to obtain significant overlap between the energy distributions of minima visited by replicas  $i$  and  $j$ . When this overlap is small, the acceptance probability is negligible.

PTBH allows effective sampling of multi-funnel landscapes and generates a distribution of minima  $\rho_{\text{IS}}(V)$  that is quite accurate at low  $V$ . However, with many high-temperature replicas there may be significant over-sampling of high-energy minima relative to  $g_{\text{IS}}(V)$ .

## 2.2.2 Transition State Searches

As discussed in §1.6.1, the local minima of a PEL control its thermodynamic properties but the dynamical properties are determined by the transition states (TSs) - saddle points with exactly one negative Hessian eigenvalue. These configurations are harder to locate than minima, because they cannot be obtained by either local minimisation or local maximisation algorithms. However, several methods have been developed to identify the TSs that lie on minimum-energy pathways between a pair of known minima.<sup>4,287-290</sup> The ability to compute accurate energy barriers by precise identification of transition states is one of the major strengths of geometry optimisation methods.

The minima-searching methods described in §2.2.1 are used to define the region of configuration space being searched. Transition states within this region are identified by finding low-energy pathways between the set of known minima. Transition state searches are performed by the OPTIM package.

In this thesis, all transition state searches are double-ended: given a pair of

“endpoint” minima  $A$  and  $B$ , we attempt to find a discrete path between them. A discrete path is a sequence of transition states and intermediate minima, with each adjacent pair of points connected by a steepest-descent path. There are many discrete paths between any pair of minima, and the search strategy implemented in `OPTIM` does not guarantee to find the minimum-energy pathway (MEP), though it will usually find a fairly short and direct path. The connection algorithm is as follows:

1. The doubly-nudged elastic band (DNEB) method is used to obtain an approximate MEP between  $A$  and  $B$ , identifying candidate TS structures.
2. The TS candidates are refined by Hybrid Eigenvector Following.
3. Pushoff paths are used to identify the pair of minima connected by each TS.
4. If a complete discrete path between  $A$  and  $B$  is now known, exit successfully.
5. Use a modified Dijkstra algorithm to choose a new pair of minima to connect.
6. Go back to step 1 with the new pair of minima.

This approach is fairly robust, but in the case of paths with many transition states or very high energies, it may take many iterations of steps 1-5 to complete. One iteration is called an `OPTIM cycle`. Each step of the algorithm will now be discussed in detail.

### 2.2.2.1 Double-Ended Transition State Searches

There are numerous double-ended methods for generating transition states and approximate MEPs between known endpoints. The nudged elastic band (NEB)<sup>287,288</sup> and doubly-nudged elastic band (DNEB)<sup>289,290</sup> approaches are two of the most robust and popular. Both algorithms use a chain of  $N_i$  “images” (replicas of the system): two fixed endpoint minima and  $(N_i - 2)$  free images which can move in coordinate space. The initial coordinates of the free images are determined by linear interpolation between the endpoints.

Neighbouring images are connected by a harmonic spring potential with force constant  $k_{\text{spr}}$ , so the total energy of the chain (the “elastic band”) is given by:

$$V_{\text{band}}(\{\mathbf{X}_i\}) = \underbrace{\sum_{i=1}^{N_i} V(\mathbf{X}_i)}_{\text{landscape energy}} + \underbrace{\frac{1}{2}k_{\text{spr}} \sum_{i=2}^{N_i} |\mathbf{X}_i - \mathbf{X}_{i-1}|^2}_{\text{spring energy}}, \quad (2.8)$$

where  $\mathbf{X}_i$  is the coordinate vector of image  $i$ .

The (D)NEB procedure is to relax the band by using the L-BFGS algorithm to minimise the gradient  $\mathbf{g}_{\text{band}} = \nabla V_{\text{band}}$  with respect to the image coordinates. The resulting path is an approximate MEP, and the images that sit at maxima on this path are candidate transition states.<sup>290</sup>

The spring potential in eq. (2.8) maintains approximately equal separation between all pairs of adjacent images, and prevents images from sliding down the landscape gradient towards local minima. If  $k_{\text{spr}}$  is too small, the resulting path will be poorly constrained in the high-energy regions of the landscape, but if it is too large then the band will take the shortest path between the endpoints rather than the lowest-energy path.  $k_{\text{spr}}$  is often varied dynamically during an NEB calculation to avoid both extremes.

$V_{\text{band}}$  defined by eq. (2.8) suffers from coupling between the landscape and spring energies, which results in undesired corner-cutting of the MEP and images sliding down towards the minima.<sup>289,290</sup> These problems are reduced by minimising a “nudged” gradient  $\mathbf{g}^{\text{NEB}}$  in place of  $\mathbf{g}_{\text{band}}$ . In  $\mathbf{g}^{\text{NEB}}$ , the components of the landscape gradient that are parallel to the path are projected out, as are the components of the spring gradient that are perpendicular to the path:

$$\mathbf{g}_i^{\text{NEB}} = \mathbf{g}_i^\perp + \mathbf{g}_i^\parallel, \quad (2.9)$$

$$\text{where } \mathbf{g}_i^\perp = \mathbf{g}_i^{\text{PEL}} - (\mathbf{g}_i^{\text{PEL}} \cdot \hat{\tau}_i)\hat{\tau}_i \quad (2.10)$$

$$\text{and } \mathbf{g}_i^\parallel = (\mathbf{g}_i^{\text{spr}} \cdot \hat{\tau}_i)\hat{\tau}_i.$$

Here,  $\mathbf{g}_i^{\text{NEB}}$  is the component of  $\mathbf{g}^{\text{NEB}}$  due to the coordinates of image  $i$ .  $\mathbf{g}_i^\parallel$  is the component of the spring gradient that is parallel to the path, which maintains roughly equal image separation, and  $\mathbf{g}_i^\perp$  is the perpendicular component of the landscape gradient, which causes the band to relax to lower energies.  $\mathbf{g}_i^{\text{PEL}} = \nabla_i V(\mathbf{X}_i)$  is the gradient of the landscape energy with respect to the coordinates of image  $i$ .  $\hat{\tau}_i$  is a tangent vector to the chain of images at image  $i$ .  $\mathbf{g}_i^{\text{spr}}$  is the gradient of the spring energy:

$$\begin{aligned} \mathbf{g}_i^{\text{spr}} &= \frac{\partial V_i^{\text{spr}}}{\partial \mathbf{X}_i} \\ &= \frac{k_{\text{spr}}}{2} \frac{\partial}{\partial \mathbf{X}_i} (|\mathbf{X}_i - \mathbf{X}_{i-1}|^2 + |\mathbf{X}_i - \mathbf{X}_{i+1}|^2). \end{aligned} \quad (2.11)$$

The difference between the NEB and DNEB methods is that in DNEB a second “nudging”, or gradient modification, is applied. Retaining a component of the spring gradient perpendicular to the path improves the stability of the algorithm by holding

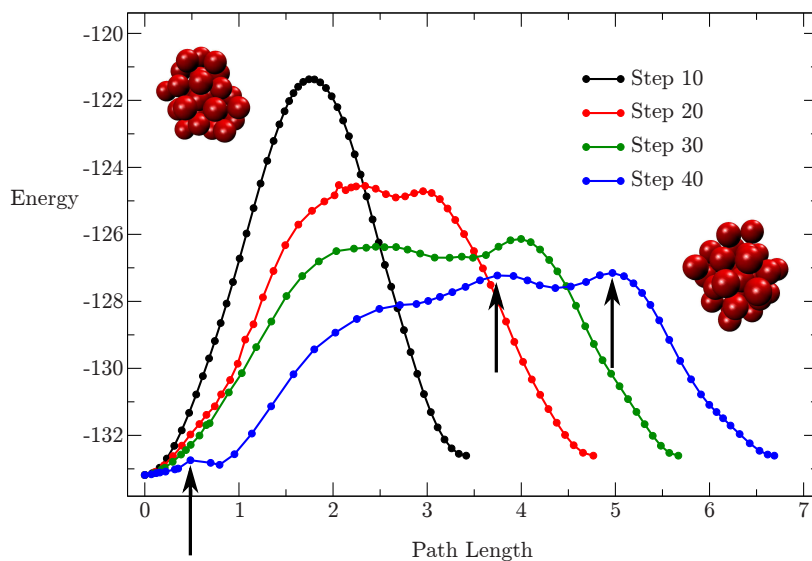


Figure 2.6: Representation of the DNEB algorithm applied to two minima of the LJ<sub>31</sub> cluster. Each line represents the energy profile of the elastic band after a certain number of L-BFGS steps. Points on each line represent images. Images indicated by arrows are candidate TSs. The 3D structures represent the endpoint minima.

the path straighter.<sup>289</sup> So  $\mathbf{g}^{\text{DNEB}}$  is minimised in place of  $\mathbf{g}^{\text{NEB}}$ :

$$\begin{aligned} \mathbf{g}_i^{\text{DNEB}} &= \mathbf{g}_i^{\text{NEB}} + \mathbf{g}_i^*, & (2.12) \\ \text{where } \mathbf{g}_i^* &= \mathbf{g}_i^{\text{spr},\perp} - (\mathbf{g}_i^{\text{spr},\perp} \cdot \hat{\mathbf{g}}_i^\perp) \hat{\mathbf{g}}_i^\perp \\ \text{and } \mathbf{g}_i^{\text{spr},\perp} &= \mathbf{g}_i^{\text{spr}} - \mathbf{g}_i^\parallel \end{aligned}$$

Here,  $\mathbf{g}_i^*$  is the DNEB correction to the gradient.  $\mathbf{g}_i^{\text{spr},\perp}$  is the perpendicular component of the spring gradient (not to be confused with  $\mathbf{g}_i^\perp$ ).  $\hat{\mathbf{g}}_i^\perp$  is a unit vector in the direction of the previous quantity.

Minimising  $\mathbf{g}^{\text{DNEB}}$  instead of  $\mathbf{g}^{\text{NEB}}$  is significantly more stable and efficient for finding approximate MEPS.<sup>282,289</sup> Fig. 2.6 shows several stages in the relaxation process.

Successful convergence of the (D)NEB method is highly dependent on careful selection of various parameters, particularly  $k_{\text{spr}}$  and  $N_i$ . Ideally, each candidate TS should be a stationary point diagnosed by vanishing of  $\mathbf{g}(\mathbf{X})$ , the landscape gradient. However, this condition is impossible to guarantee using NEB. Moreover, candidate TSs obtained from DNEB are usually less well converged than those from NEB.<sup>290</sup> To obtain tightly-converged transition states, a refinement step is applied to the candidate TS structures.

### 2.2.2.2 Transition State Refinement

The Hybrid Eigenvector-Following (HEF) algorithm used to refine transition state candidates is as follows:<sup>4,291,292</sup>

1. The lowest Hessian eigenvalue and corresponding eigenvector are determined for the current geometry
2. A step is made parallel to this lowest eigenvector in the uphill direction
3. A (small) number of iterations of the L-BFGS minimiser are performed in the coordinate subspace perpendicular to the lowest eigenvector
4. Steps 1 - 3 are repeated until the energy gradient at the current coordinates falls below a given tolerance

Hessian eigenvalues correspond to curvatures of the PEL along the corresponding eigenvectors. Any point that is not a local minimum has at least one negative eigenvalue. Therefore steps 1 and 2 correspond to an uphill step along the direction of greatest negative curvature, towards a saddle point or maximum. Step 3 moves downhill, away from maxima or saddle points with index greater than one. Eventually this procedure converges tightly to a transition state.

The lowest eigenvalue in step 1 can be calculated by diagonalising  $\mathbf{H}(\mathbf{X})$ , but this process is often expensive. Instead, the eigenvalue may be determined variationally using the Rayleigh-Ritz ratio:

$$\lambda(\mathbf{x}) = \frac{\mathbf{x}^T \mathbf{H} \mathbf{x}}{\mathbf{x}^2}. \quad (2.13)$$

Expansion of the small coordinate displacement  $\mathbf{x}$  in the eigenvectors of  $\mathbf{H}$  reveals that  $\lambda$  is an upper bound for the lowest Hessian eigenvalue,<sup>4</sup> and so the vector  $\mathbf{x}$  which minimises  $\lambda$  is a good estimate for the corresponding eigenvector. The minimisation is performed using L-BFGS, as usual.

Each continuous symmetry operation of a system corresponds to a zero eigenvalue of  $\mathbf{H}(\mathbf{X})$ .  $V(\mathbf{X})$  is flat along the corresponding eigenvector. These zero values may cause unstable behaviour of the HEF algorithm. For supercooled liquids, global translation is the only continuous symmetry that is always present, and the corresponding eigenvectors  $\mathbf{e}_x, \mathbf{e}_y, \mathbf{e}_z$  are known analytically. These vectors may be projected out of  $\mathbf{x}$  to avoid interfering with the uphill step taking.

Often, calculating second derivatives to evaluate  $\mathbf{H}(\mathbf{X})$  is too expensive. Instead, an approximate gradient-only formulation of the ratio may be employed:<sup>293</sup>

$$\lambda(\mathbf{x}) \approx \frac{[\mathbf{g}(\mathbf{X} + \delta\mathbf{x}) - \mathbf{g}(\mathbf{X} - \delta\mathbf{x})] \cdot \mathbf{x}}{2\delta\mathbf{x}^2}. \quad (2.14)$$

The gradient is usually much cheaper to calculate than the Hessian, hence this expression is much more efficient than eq. (2.13) - a significant advantage for large systems.

HEF can converge to a TS structure with precision specified by the user. The pair of minima that are connected to it are then identified using steepest-descent paths. The unique negative eigenvalue of the TS is identified, and a small step is taken away from the TS parallel to the corresponding eigenvector. L-BFGS minimisation then leads to one of the connected minima. The other minimum is found by stepping away from the TS antiparallel to the same eigenvector. The two minima obtained from these “pushoff paths” may be the original endpoints,  $A$  and  $B$ , but often one or other of them will be a new minimum that is not currently known.

### 2.2.2.3 Discrete Paths and Connection Attempts

The DNEB-HEF scheme will usually identify at least one converged transition state and pair of connected minima. Sometimes, this set of connections is sufficient to define a full discrete path between the endpoint minima  $A$  and  $B$ , but this is often not the case: initial connection attempts can fail because the candidate structures obtained by DNEB were a long way from real transition states, or because the HEF procedure converges to a transition state that is not part of the desired MEP.

If the initial connection attempt fails, the known minima form two or more disconnected sets, and further DNEB-HEF cycles are required to find the missing connections.

The next pair of minima that OPTIM attempts to connect are selected using the Dijkstra algorithm.<sup>294</sup> The database of known stationary points is represented as a complete graph. Each minimum is a node, and edge weights are given by:<sup>295</sup>

$$w(u, v) = \begin{cases} 0 & \text{if } u \text{ and } v \text{ are connected by a single known TS,} \\ \infty & \text{if } n(u, v) = n_{\max}, \\ n(u, v)f(D(u, v)) & \text{otherwise.} \end{cases} \quad (2.15)$$

Here  $n(u, v)$  is the number of previous attempts that have been made to connect minima  $u$  and  $v$ .  $n_{\max}$  is a parameter to limit the number of times that the pro-

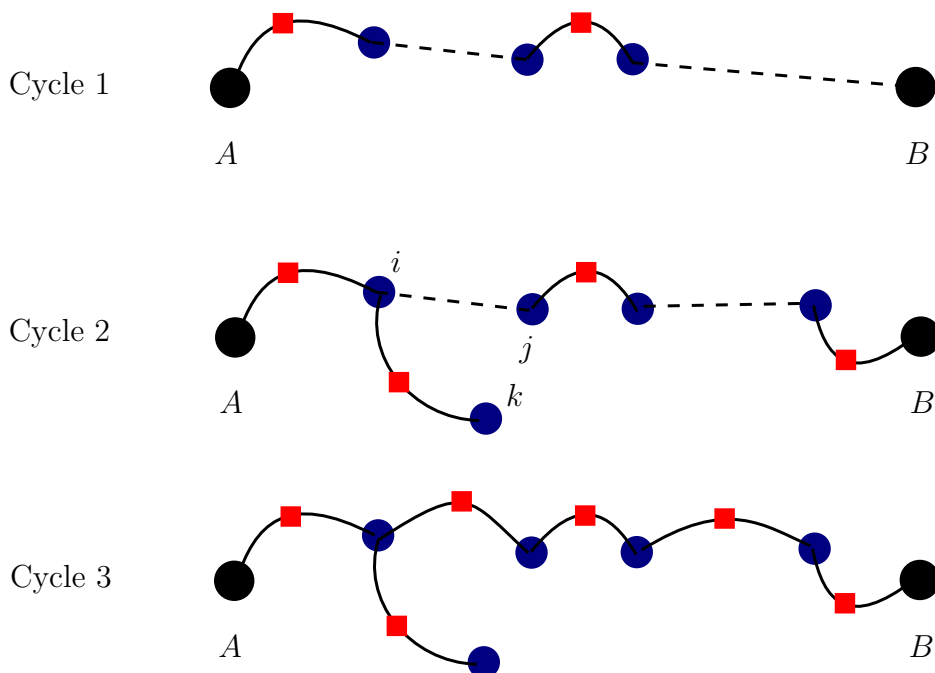


Figure 2.7: Schematic of the Dijkstra algorithm for identifying short missing connections. The figure shows three OPTIM cycles. Black and blue circles represent endpoint and intermediate minima, respectively. Red squares are transition states and solid black lines represent known steepest-descent paths. Dashed black lines indicate the pairs of minima selected for connection by the Dijkstra algorithm.

gram will attempt to connect each pair.  $f$  is a monotonically-increasing functional, typically  $f = D(u, v)^n$  or  $f = \exp(D(u, v))$ . The exact choice matters little for supercooled liquids.  $D(u, v)$  is a measure of the expected computer time required to connect  $u$  and  $v$ , normally the Euclidean distance:

$$D(u, v) = \left( \sum_{i=1}^N (\mathbf{X}_{i,u} - \mathbf{X}_{i,v})^2 \right)^{\frac{1}{2}}, \quad (2.16)$$

where  $\mathbf{X}_{i,u}$  is a coordinate of the  $i^{\text{th}}$  particle in the  $u^{\text{th}}$  minimum.

The Dijkstra algorithm finds the minimum-weight route between two specified nodes,<sup>294</sup> in this case the endpoint minima  $A$  and  $B$ . The minimum-weight path typically contains the fewest pairs of minima without a connecting transition state. The edge on the path with the smallest non-zero weight is selected for the next connection attempt. This procedure is illustrated in fig. 2.7.

The Dijkstra algorithm using the weights  $w(u, v)$  is generally very successful at generating discrete paths that contain few transition states in a small number of cycles. By combining this algorithm with DNEB and HEF, OPTIM is a robust and

efficient tool for locating discrete paths between pairs of minima.

### 2.2.3 Database Connection Strategies

Connecting individual pairs of minima is not sufficient to obtain a useful sample of PEL stationary points. There are several different strategies to select pairs of end-point minima to connect and hence grow the database, two of which are introduced here. Note that a “connection attempt” in this section refers to an entire OPTIM execution, which may comprise many cycles of the DNEB-HEF procedure.

The first method, *exhaustive connection*, is used in chapter 5. This strategy makes one connection attempt for each pair of minima in an initial database. This approach can be time consuming, but it generates a dense sample of the stationary points within the configuration space spanned by the initial set of minima.

The second method starts from an inherent trajectory, and attempts to connect every consecutive pair of minima. If the inherent trajectory corresponds to a locally ergodic MD simulation, the resulting database of stationary points will faithfully represent the configuration space explored by the system. This *inherent trajectory strategy* is unusual in that the sequence of minima and transition states can be associated with the time ordering of the original trajectory. This strategy is used in chapters 3 and 4.

Both connection methods are shown schematically in fig. 2.8.

#### 2.2.3.1 The UNTRAP Method

The energy barrier between a pair of minima is usually correlated with the energy difference between them, but it is often the exceptions that are the most interesting minima on any particular landscape. OPTIM does not always identify the lowest-energy discrete path between a pair of minima, so when two minima with similar energy are separated by a high barrier, it is important to know whether there exists an unknown discrete path that connects them through a lower-energy transition state. If this is the case, we say that the landscape is “artificially frustrated”.

The UNTRAP method<sup>296</sup> may be used to reduce artificial frustration in a connected database. We first define a “product set” of minima, typically the global minimum and those minima connected to it by low barriers. Connections are considered between all pairs of minima  $u$  and  $v$ , where  $v$  lies within the product set and  $u$  does not. These pairs are ranked according to the untrap metric:

$$U(u, v) = \frac{V_{uv}^\dagger - V_u}{|V_u - V_v|} \quad (2.17)$$

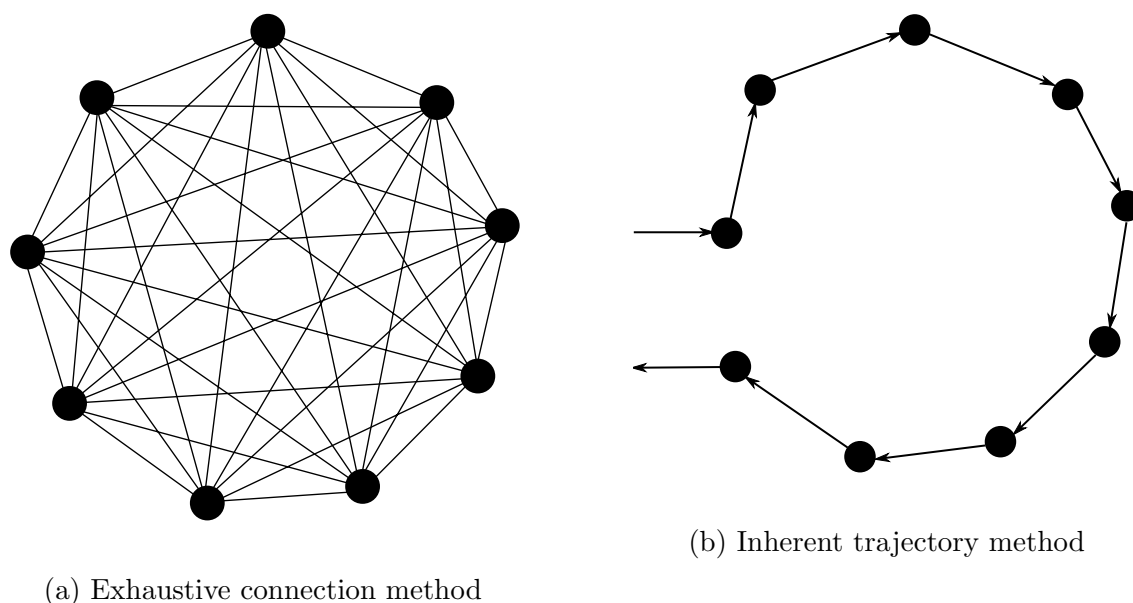


Figure 2.8: Schematic representations of two different connection methods. In each case, nodes represent the local minima that are known at the start of the procedure, and edges represent the pairs for which discrete paths will be computed. In the right panel, the time-ordering of minima is shown by arrows on the graph edges.

where  $V_u$  is the energy of minimum  $u$ .  $V_{uv}^\ddagger$  is the energy of the highest TS on the lowest-energy discrete path between  $u$  and  $v$ .  $U(u, v)$  is large when  $u$  and  $v$  are close in energy but separated by a high barrier.

Connection attempts are made for pairs of minima in decreasing order of  $U(u, v)$ , which will generate new discrete paths and hopefully reduce the energy barrier between  $u$  and the product set. Often, the UNTRAP algorithm will be run repeatedly until the appearance of the landscape on a disconnectivity graph (see §2.2.4) converges.

## 2.2.4 Representing and Characterising the PEL

Visualising the structure of a high-dimensional energy landscape is important. Most methods project  $V(\mathbf{X})$  onto one or two order parameters or “reaction coordinates” to obtain a two- or three-dimensional plot. However, this approach risks losing much information if the chosen coordinates do not discriminate between important regions of the configuration space. Disconnectivity graphs<sup>4,297</sup> avoid the need to select an order parameter by representing the stationary points of a landscape with their true connectivity, and preserve energy barriers through knowledge of the transition states.

To understand the construction of a disconnectivity graph, it is once again convenient to represent the database of a connected landscape as a graph. Nodes of the

---

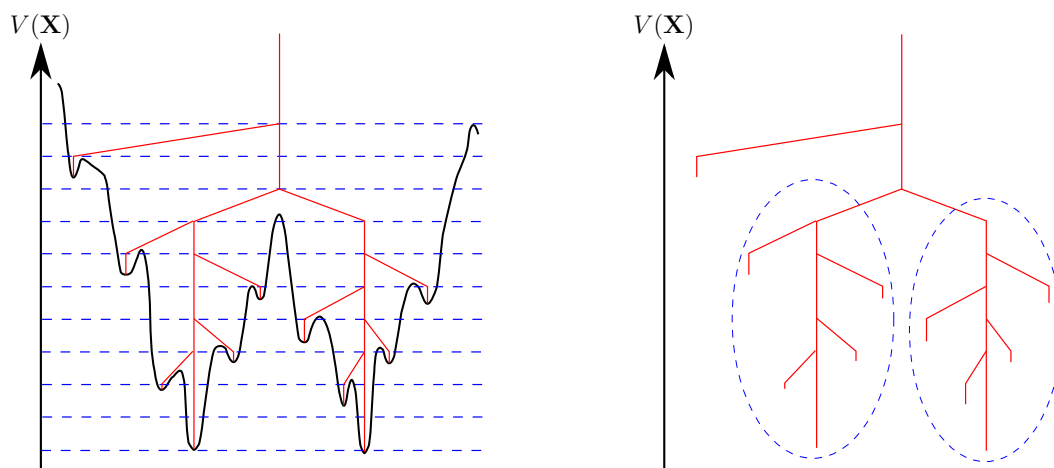
graph are minima and the weight of an edge connecting two minima is the energy of the highest transition state on the minimum-energy pathway between them. Note that this graph representation differs from that used in the previous section. Taking a cut through all edges with weights higher than a threshold energy  $V_p$  divides the minima into disjoint subsets, called *superbasins*.<sup>297</sup> The minima within a subset can be traversed without the potential energy exceeding the threshold. High  $V_p$  will result in a few large superbasins, as few edges are cut. Low  $V_p$  cuts many edges and produces many disjoint sets, some containing a single minimum.

To construct a disconnectivity graph, the superbasin analysis is performed at evenly-spaced threshold energies  $V_1, V_2, \dots, V_n$ . On moving from  $V_p$  to a lower threshold  $V_{p-1}$ , superbasins may divide as minima become cut off. Each superbasin at  $V_p$  has a unique parent superbasin at all thresholds  $V_q > V_p$  and one or more children at each threshold  $V_r < V_p$ . At successively lower threshold energies, superbasins continue to divide until they contain only a single minimum. Each superbasin disappears when the threshold energy is lower than the energy of its last minimum.

The vertical axis of a disconnectivity graph is usually the potential energy. At every threshold energy each superbasin is represented by a single point on the graph. Superbasins are joined to their parents and children at different threshold energies by a straight line. Because parents are unique but children are not, the union of these lines forms a tree structure and it is always possible to order the superbasins along the horizontal axis such that no lines cross. The horizontal axis has no physical meaning, but loosely corresponds to proximity in “connection space”: the closer two points are along the horizontal axis, the fewer transition states lie on the lowest-energy discrete path between them. The line on the graph for each superbasin terminates at the energy of the last minimum.

The relationship between a (one-dimensional) energy landscape and the corresponding disconnectivity graph is shown in fig. 2.9a. Energy barriers between a pair of minima may be rapidly estimated by observing the position on the vertical axis where the relevant superbasins merge. This means that landscape funnels (see §1.6.1) have a characteristic shape on a disconnectivity graph, as indicated in fig. 2.9b. The funnel consists of a main vertical “trunk” corresponding to the lowest minimum of the funnel, with numerous shallow “branches”: minima connected to the funnel bottom by low energy barriers.

The appearance of a disconnectivity graph provides a simple qualitative description of the properties of a landscape.<sup>298</sup> Landscapes for well-folded proteins and simple atomic clusters contain only a single funnel, with the global minimum at the bottom. This type of landscape (fig. 2.10a) resembles a palm tree, and describes



(a) Disconnectivity graph construction for a model PEL. The original landscape is shown in black and the disconnectivity graph in red. Dashed blue lines correspond to the energy thresholds.

(b) The disconnectivity graph that results from the analysis in the first panel. Dashed blue ellipses indicate the two funnel structures on this graph.

Figure 2.9

structure-seeking systems with a single preferred conformation.

A second archetypal landscape (which will not be much discussed in this thesis) is described as a willow-tree. While there is still a clearly-defined global minimum, the energy barriers to reach it are comparable with the energy barriers to leave. The global minimum structure can only be obtained by slow quenching from high temperature, to avoid kinetic trapping behind high energy barriers. This class of landscape is shown in fig. 2.10b, and represents systems such as buckminster fullerene.<sup>298</sup>

Landscapes of glass formers belong to a third class, known as “banyan tree” disconnectivity graphs (fig. 2.10c). These graphs contain a large number of local funnels with a wide distribution of energies and barrier heights. Barriers between funnels are systematically higher than barriers within funnels. There is no dominant low-energy funnel, and no clear global minimum (since the crystal region is excluded). These systems do not structure-seek at all.

Classifying disconnectivity graphs according to these three archetypal forms is usually quick and straightforward, and yields qualitative insight into the structure and dynamics of a model system.

#### 2.2.4.1 The Frustration Index

Useful quantitative information relating to energy barriers may also be extracted from disconnectivity graphs. One way of representing these data is to compute a

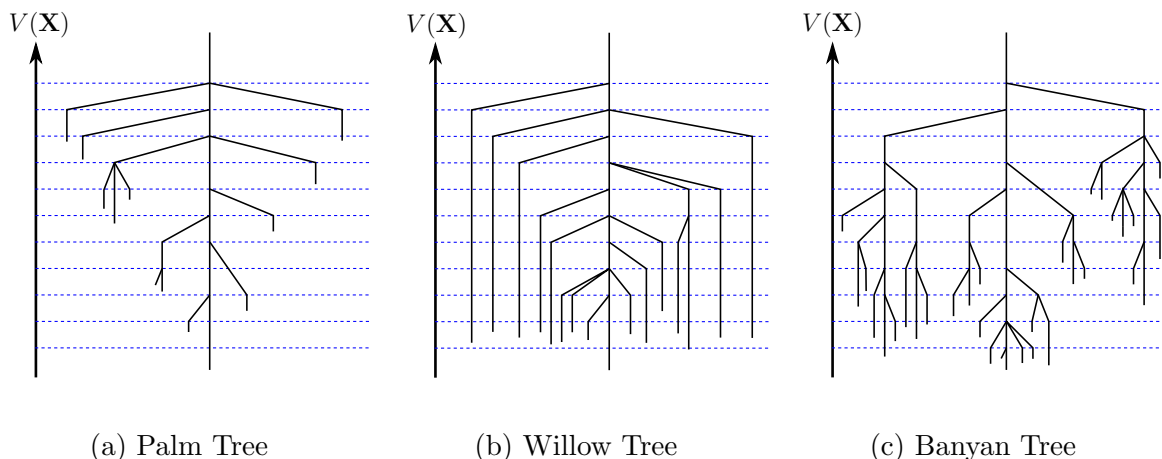


Figure 2.10: Cartoon representations of archetypal disconnectivity graphs.

*frustration index*<sup>246</sup> of the database.

Here, “frustration” describes the existence of competing low-lying potential energy minima separated by high barriers. Highly frustrated landscapes have many such minima, which makes relaxation to the global minimum relatively slow. Good structure-seekers have low frustration, glass formers have high frustration.<sup>246</sup>

This concept is closely linked to the artificial frustration described in §2.2.3.1 and to the UNTRAP metric. The simplest form of the frustration index is given by:

$$f(T) = \sum_{\alpha \neq \text{gmin}} p_{\alpha}^{\text{eq}}(T) \left( \frac{V_{\alpha}^{\dagger} - V_{\text{gmin}}}{V_{\alpha} - V_{\text{gmin}}} \right), \quad (2.18)$$

where  $p_{\alpha}^{\text{eq}}(T)$  is the equilibrium occupation probability of minimum  $\alpha$  at temperature  $T$ , computed using the harmonic superposition approximation (HSA),<sup>4,200</sup> cf. eq. (1.16).  $V_{\alpha}$  is the potential energy of  $\alpha$ , and  $V_{\text{gmin}}$  is the global minimum potential energy.  $V_{\alpha}^{\dagger}$  is the energy of the highest transition state on the lowest-energy pathway from  $\alpha$  to the global minimum, so that the numerator of the fraction in eq. (2.18) is the downhill energy barrier. Since frustration describes the ease of transitions into the global minimum, this minimum is excluded from the sum over  $\alpha$ .

$f(T)$  is simple to calculate from a database of local minima and a disconnectivity graph. It allows quantitative comparison between landscapes of very different systems.<sup>246</sup> To compare systems with different energy functions the temperature is rescaled relative to  $T_m$ , the melting temperature. Here,  $T_m$  is defined as the position of the highest temperature peak in the heat capacity  $C_v(T)$ , which is calculated using the HSA partition function.

At low temperatures, the equilibrium occupation probability is dominated by

the global minimum, so that all terms of the sum in eq. (2.18) become small and  $f(T) \rightarrow 0$  as  $T \rightarrow 0$ . This effect is counterintuitive: lowering  $T$  should increase frustration because crossing high barriers to reach the global minimum becomes more difficult at low  $T$ . To correct this effect, a modified frustration index  $\tilde{f}(T)$  may be used, where  $p_\alpha^{\text{eq}}(T)$  is replaced by  $\tilde{p}_\alpha^{\text{eq}} = p_\alpha^{\text{eq}}/(1 - p_{\text{gmin}}^{\text{eq}})$ .

$\tilde{f}(T)$  successfully discriminates between a wide range of systems with different properties, confirming that simple single-funnelled landscapes have relatively low frustration, but glasses and jammed colloidal systems have high frustration and show no structure-seeking behaviour.<sup>246</sup> Frustration is a convenient numerical description of PEL organisation and structure.

## 2.3 Rigid Body Methods

The OTP model studied in chapter 3 is composed of rigid molecules, which require special treatment in geometry optimisation methods. As noted in §2.1.3, a rigid molecule may either be modelled atomistically, with constraints to fix the bond lengths and angles, or using a generalised coordinate system to describe both position and orientation of the molecule. The cost of geometry optimisation depends strongly on the number of degrees of freedom,<sup>4</sup> so the latter approach is preferred.

A robust and efficient generalised coordinate system is therefore required.

### 2.3.1 Coordinate Systems

Euler’s rotation theorem states that the coordinates of any rigid body may be uniquely described by a translation combined with a rotation. The translation is a Cartesian position vector for the centre of mass (CoM). The rotation maps a reference geometry for the rigid body onto the current orientation of the same body, and hence specifies the orientation of the molecule.

There are several ways to represent this rotation. Rotation matrices are convenient but inefficient for geometry optimisation, as they have many components and constraints to optimise.

Euler angles describe orientation using rotation angles around three globally fixed axes. This method has fewer degrees of freedom to optimise, but suffers from singularities whenever one of the angles becomes equal to 0 or  $\pi$  (the gimbal lock problem), and so is not suitable for geometry optimisation.<sup>299</sup>

Rotation quaternions are the preferred orientational coordinate system in MD simulation.<sup>272,300</sup> They are numerically stable, free of singularities,<sup>301</sup> and support an efficient formulation of the equations of motion.<sup>271</sup> However quaternions use

---

four coordinates rather than the minimal three, and require a normalisation constraint during simulation.<sup>302</sup> For geometry optimisation problems, minimising the number of coordinates that must be optimised is very important for efficiency, and so quaternions are not employed.

In OPTIM, rigid bodies are described using the angle-axis (AA) coordinate system.<sup>302-304</sup> The rotation between the reference geometry and instantaneous molecular orientation is described by a vector along the rotational axis, with magnitude equal to the rotation angle. This system allows for easy transformation between Cartesian atomic coordinates and rigid body coordinates, while retaining the minimal three rotational coordinates.

The disadvantage of the AA system is that  $\mathbf{g}(\mathbf{X})$  and  $\mathbf{H}(\mathbf{X})$  are not invariant under the symmetry operations of the AA vector. For example, adding  $2\pi$  to the magnitude of the AA vector leaves the molecular orientation unchanged, but reduces  $\mathbf{g}(\mathbf{X})$ . For consistency, rotations are always described using the AA vector with the smallest possible rotation angle  $\theta$ . Thus  $-\pi/2 < \theta < \pi/2$ .

### 2.3.2 The Angle-Axis System

OPTIM uses atomistic coordinates to calculate the potential energy, and rigid body AA coordinates when the configuration of the system is changing, e.g. during an energy minimisation. For pairwise isotropic potentials, simple expressions are available to convert  $\mathbf{X}$ ,  $\mathbf{g}(\mathbf{X})$  and  $\mathbf{H}(\mathbf{X})$  between these two coordinate systems.<sup>305</sup> Therefore the rigid body constraint is enforced with little additional computational expense. Since rigidifying a group of atoms eliminates degrees of freedom, the rigid body scheme improves the efficiency of landscape exploration, especially for biomolecules.<sup>306</sup>

Rühle *et al.* have proposed several improvements to the AA framework using a symmetry-independent metric tensor.<sup>304</sup> These improvements include a method to compute the Euclidean distance from angle-axis coordinates, which is required to calculate the spring potential and gradient between images in the DNEB algorithm. For this project I implemented the distance metric in OPTIM, along with various adaptations that enable the AA routines to accommodate periodic boundary conditions.

I also implemented the iSLERP procedure<sup>307</sup> (incremental Spherical Linear Interpolation) to allow construction of an initial DNEB band in AA coordinates. This addition has resulted in improved stability of the DNEB procedure for rigid body systems.

### 2.3.2.1 Euclidean Distance in Angle-Axis Coordinates

The notation used for the AA system in this section is as follows. There are  $N_r$  identical rigid bodies, labelled by index  $I$ . Each body consists of  $n$  sites labelled by index  $i$ . The Cartesian position vector of a site is given by

$$\mathbf{y}_{I,i} = \mathbf{Z}_I + \mathbf{R}_I \mathbf{z}_i \quad (2.19)$$

where  $\mathbf{Z}_I$  is the CoM position for the molecule,  $\mathbf{z}_i$  is the Cartesian position of site  $i$  in the reference geometry of the molecule, and  $\mathbf{R}_I$  is the rotation matrix that maps the reference geometry onto the current orientation of molecule  $I$ .  $\mathbf{R}_I$  is easily obtained from the corresponding AA vector  $\mathbf{p}_I$  using Rodrigues' formula.<sup>305</sup>

The AA expression for the same molecular position is

$$\mathbf{q}_I = \{\mathbf{Z}_I, \mathbf{p}_I\} \quad (2.20)$$

where  $\mathbf{p}_I = \theta \hat{\mathbf{p}}_I$  is the AA rotation vector.  $\hat{\mathbf{p}}_I$  is a normalised vector along the axis of rotation between the reference geometry and the current geometry, and  $\theta$  is the rotation angle. Positive  $\theta$  corresponds to anticlockwise rotation around the positive direction of  $\hat{\mathbf{p}}$ .

The square Euclidean distance between two configurations  $k$  and  $l$  of the system (e.g. two DNEB images) is given by:

$$\begin{aligned} D(k,l)^2 &= \sum_I^{N_r} \sum_i^n |\mathbf{y}_{k,i,I} - \mathbf{y}_{l,i,I}|^2 \\ &= \sum_I^{N_r} \sum_i^n |\mathbf{Z}_{k,I} - \mathbf{Z}_{l,I} + \mathbf{R}_{k,I} \mathbf{z}_i - \mathbf{R}_{l,I} \mathbf{z}_i|^2 \\ &= \sum_I^{N_r} \sum_i^n |\Delta \mathbf{Z}_I + \Delta \mathbf{R}_I \mathbf{z}_i|^2 \\ &= \sum_I^{N_r} \sum_i^n \underbrace{|\Delta \mathbf{Z}_I|^2}_{\text{Translation}} + \underbrace{|\Delta \mathbf{R}_I \mathbf{z}_i|^2}_{\text{Rotation}} + \underbrace{2\Delta \mathbf{Z}_I \cdot (\Delta \mathbf{R}_I \mathbf{z}_i)}_{\text{Mixed}} \end{aligned} \quad (2.21)$$

The expression separates into contributions from the different types of coordinate. Performing the sum over  $i$ , it may be shown that:

$$D(k,l)^2 = \sum_I^{N_r} n |\Delta \mathbf{Z}_I|^2 + \text{Tr}(\Delta \mathbf{R}_I \mathbf{S} \mathbf{R}_I^T) + 2n \Delta \mathbf{Z}_I \cdot (\Delta \mathbf{R}_I \mathbf{Z}_w), \quad (2.22)$$

where  $\mathbf{Z}_w = \sum_i^n \mathbf{z}_i/n$  is the centre of coordinates for the reference geometry and the unweighted gyration tensor  $\mathbf{S}$  is defined by  $S_{\alpha\beta} = \sum_i^n z_{i,\alpha}z_{i,\beta}$ . These two quantities depend only on the reference geometry and so are only calculated once. Moreover, the coordinate origin in the reference geometry may be chosen such that  $\mathbf{Z}_w = \mathbf{0}$ , so that the mixed term vanishes:

$$D(k, l)^2 = \sum_I^{N_r} n |\Delta \mathbf{Z}_I|^2 + \text{Tr} (\Delta \mathbf{R}_I \mathbf{S}_I \mathbf{R}_I^T) \quad (2.23)$$

$D(i, i-1)^2 = |\mathbf{X}_i - \mathbf{X}_{i-1}|^2$  can be used to evaluate eq. (2.8) without needing to transform coordinates from AA to Cartesian. More importantly, evaluating eq. (2.11) for  $\mathbf{g}_i^{\text{spr}}$  requires the gradient of  $D(i, i-1)^2$  with respect to each coordinate  $\mathbf{X}_i$ , including AA coordinates. This gradient can only be obtained by differentiation of eq. (2.23):

$$\frac{\partial D(i, i-1)^2}{\partial \mathbf{Z}_{i,\alpha}} = 2n \Delta \mathbf{Z}_\alpha \quad (2.24)$$

$$\frac{\partial D(i, i-1)^2}{\partial \mathbf{p}_{i,\beta}} = -\text{Tr}(\mathbf{R}_\beta \mathbf{S} \Delta \mathbf{R}^T). \quad (2.25)$$

Here,  $\alpha$  and  $\beta$  indicate particular degrees of freedom (translational and rotational, respectively).

# Chapter 3

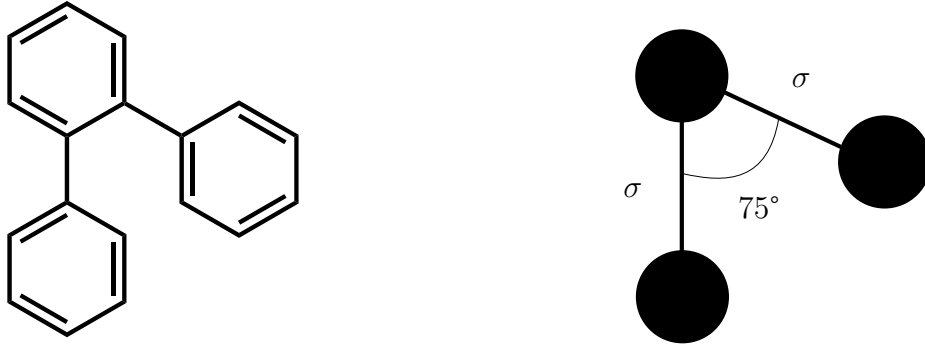
## Energy Landscapes of Atomic and Molecular Fragile Glass Formers

### 3.1 Introduction

As discussed in §1.7, de Souza and Wales have previously developed quantitative descriptions of the supercooled dynamics of the binary Lennard-Jones fluid (BLJ), using the concepts of correlated diffusion and cage-breaking diffusive rearrangements. They also studied the PEL of this system in detail, identifying hierarchical structure that is connected to the diffusion dynamics through the concept of a metabasin.

The BLJ model is popular because it is computationally cheap and convenient to implement, while still capturing most of the experimental phenomenology of fragile glass formers. However, many real fragile liquids are composed of molecules or molecular ions,<sup>25</sup> which might suggest that fragile properties are affected by internal molecular degrees of freedom that are not included in atomic models such as BLJ. Therefore explanations of fragility based on BLJ alone may not apply to all supercooled liquids.

In this chapter, I extend the analysis of §1.7 to a model for ortho-terphenyl (1,2-diphenylbenzene, OTP), a molecular glass former. I show that the presence of intramolecular degrees of freedom makes the PEL and dynamics of this system significantly more complicated than BLJ, but that the broad principles of the cage-breaking and metabasin methods still apply. The results in this chapter, and much of the text, have been adapted from the corresponding paper published in the *Journal of Chemical Physics*.<sup>308</sup>



(a) Structure of ortho-terphenyl (OTP)

(b) Lewis-Wahnström model

Figure 3.1

### 3.2 Model and Simulation Details

OTP (fig. 3.1a) is a well-known fragile glass former, which has been extensively studied by experiments<sup>38,68,309</sup> and simulations.<sup>15,310,311</sup> The melting temperature  $T_m = 328$  K, and the glass transition temperature  $T_g \approx 243$  K.<sup>309</sup>

OTP is a simple molecule containing only carbon and hydrogen, with intermolecular interactions dominated by dispersion forces that are approximately isotropic. Some models treat most of the atoms explicitly,<sup>15</sup> but it is common to rigidify much of the molecule to reduce the complexity of the simulation.<sup>18,310–312</sup>

The most popular coarse-grained model is that of Lewis and Wahnström,<sup>13,17,43,313</sup> which describes OTP as an isosceles triangle of *interaction sites* with fixed bond lengths and fixed unique angle  $75^\circ$  (see fig. 3.1b). Each site interacts pairwise additively with all sites in other molecules according to the Lennard-Jones potential. The bond lengths are set to  $\sigma$ , the Lennard-Jones distance unit.

The model used here retains the Lewis-Wahnström geometry, but adds a Stoddard-Ford quadratic cutoff<sup>314</sup> to the potential, so that both the energy and its distance derivative go smoothly to zero at the cutoff. This property is required for landscape analysis because gradient discontinuities cause unstable behaviour in geometry optimisation.<sup>4</sup> The complete potential for each site-site interaction is given by Eq. (3.1).

$$\begin{aligned}
 V_{ij}(r) &= 4\epsilon \left[ \left( \frac{r}{\sigma} \right)^{-12} - \left( \frac{r}{\sigma} \right)^{-6} \right] + \lambda_1 + \lambda_2 r^2, \quad \text{where} & (3.1) \\
 \lambda_1 &= 4\epsilon \left[ -7 \left( \frac{r_c}{\sigma} \right)^{-12} + 4 \left( \frac{r_c}{\sigma} \right)^{-6} \right] & \text{and} \\
 \lambda_2 &= \frac{4\epsilon}{r_c^2} \left[ 6 \left( \frac{r_c}{\sigma} \right)^{-12} - 3 \left( \frac{r_c}{\sigma} \right)^{-6} \right],
 \end{aligned}$$

$T/\text{K}$	$\rho/\text{g cm}^{-3}$	Production Time/ns
260	1.082	369.04
266	1.079	268.39
275	1.076	100.65
291	1.065	33.549
305	1.055	33.549
346	1.027	33.549

Table 3.1: Input parameters for the MD trajectories as a function of temperature. The equilibration time of  $10^6$  steps (16.7 ns) is excluded.

where  $r_c$  is the cutoff distance and  $\sigma$  is the unit of length.

The well depth,  $\epsilon_0$ , of the modified potential depends weakly on  $r_c$ . Following Mossa *et al.*<sup>43</sup> we chose  $r_c = 2.614\sigma$ , which gives  $\epsilon_0 = -0.9570\epsilon$ . In line with Lewis and Wahnström’s original study, we chose  $\epsilon_0 = 600 k_B \text{ K} = 4.988 \text{ kJ mol}^{-1}$  and  $\sigma = 0.483 \text{ nm}$  to fit the molar volume and diffusion constant to experimental values at 400 K.<sup>313</sup> Therefore the energy unit  $\epsilon = 5.209 \text{ kJ mol}^{-1}$ .

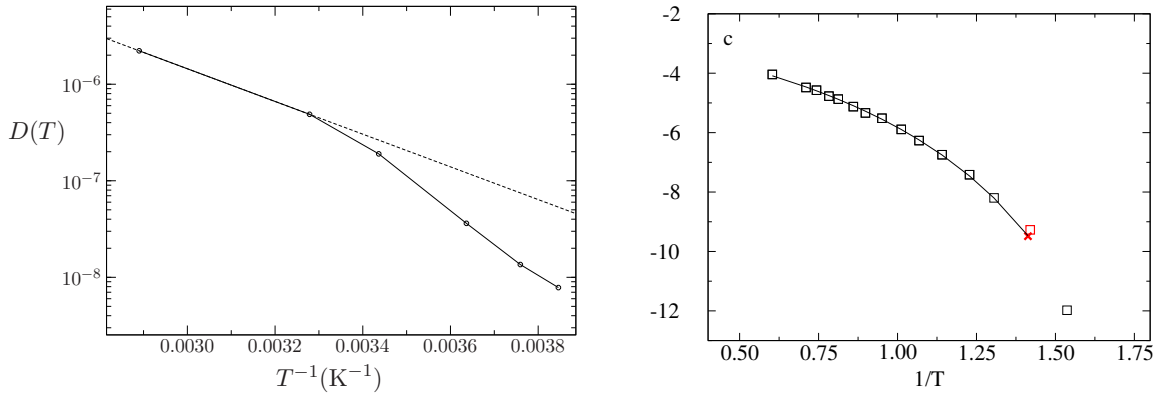
### 3.2.1 Molecular Dynamics Simulation

Canonical MD simulations of bulk OTP were performed by Dr Jacob Stevenson using a program written by Dr Dwaipayan Chakrabarti (see §2.1.3 for details). Several different temperatures in the range 260 K to 346 K were simulated with a timestep of 16.7 fs.

The simulation consisted of 324 OTP molecules in a cubic box with periodic boundary conditions. This system size was large enough to reproduce literature values for the diffusion constants but small enough to mitigate some of the problems associated with landscape analysis of large systems. Following the original study of Lewis and Wahnström,<sup>313</sup> the molar volume was varied with temperature (see table 3.1). This variation prevents comparison with the mode-coupling  $T_c$ , which changes considerably with volume.<sup>43</sup> However, the power law scaling of  $D(T)$  predicted by MCT breaks down rather badly for OTP in the vicinity of  $T_c$ ,<sup>43</sup> so the relevance of this temperature is questionable.

At each temperature,  $10^6$  MD steps (16.7 ns) were allowed for equilibration from a simple cubic starting structure. The simulation length was varied with temperature (table 3.1) to allow the colder trajectories to reach local ergodicity, which was diagnosed using the Mountain-Thirumalai energy fluctuation metric and the non-Gaussian parameter for translational displacement (§2.1.4).

Translational diffusion constants for OTP were calculated using the Einstein expression, eq. (1.3), using the mean squared displacement of molecular centres of



(a) Translational diffusion constants  $D(T)$  for OTP, showing the deviation from hypothetical Arrhenius behaviour (demonstrated by the dashed line, which does not represent any data but is merely intended to guide the eye).  $D(T)$  is given in  $\text{cm}^2 \text{s}^{-1}$ .

(b) Diffusion constants  $D(T)$  for the Kob-Andersen BLJ fluid at density  $1.3 \sigma_{\text{AA}}^{-3}$ . Reprinted from [26] with the permission of AIP Publishing. The solid line represents a VTF fit to the data, showing the super-Arrhenius curvature at lower temperatures.

Figure 3.2

mass instead of the atomic m.s.d. employed previously. The diffusion constants  $D(T)$  are presented in fig. 3.2a. These results exhibit super-Arrhenius temperature dependence, curving downwards below the dashed line that indicates the expected straight-line Arrhenius behaviour. Fig. 3.2b illustrates diffusion constants for the BLJ fluid, calculated in the same way. Comparing these two panels shows that the two systems behave similarly, but the data for OTP cover a smaller temperature range and so display less curvature.

### 3.2.2 Sampling the PEL

As discussed in §2.2.3, there are several approaches for sampling the landscape.<sup>195,283,284</sup> To study dynamics, it is important to explore the landscape in the same way that the liquid does, and so the inherent trajectory approach was used: locally ergodic MD trajectories were quenched onto the PEL using energy minimisation, and discrete pathways were found that connect each pair of adjacent minima in the resulting inherent trajectory.

The OPTIM program was used with the methodology described in §2.2.2 to make the connections. Each OTP molecule was treated as a separate rigid body, using the angle-axis framework introduced in §2.3.

The PEL is temperature-independent, but this sampling method is not, so the landscape appears different when reconstructed from trajectories at different temper-

atures. We considered trajectories obtained at 291 K and 266 K, which correspond to the lower end of the landscape-influenced dynamical regime.<sup>225</sup> Consequently, the regions of the landscape sampled by these trajectories will be relevant to the supercooled dynamics of the system. The analysis of these two trajectories yielded qualitatively similar results and so, for brevity, only the results at 266 K are presented here.

### 3.3 Cage-breaking Analysis

For BLJ, a simple method was proposed<sup>233</sup> to identify the cage-breaking transitions that dominate long-time diffusion (see §1.7.2). By focussing on elementary transitions between PEL minima, non-diffusive particle rattling motion was removed and the smallest relevant non-local motions of the system were identified.

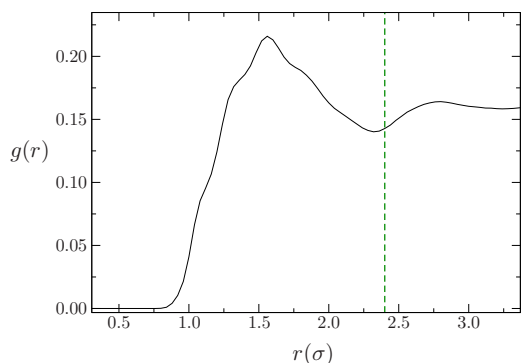
In this section, a new method is presented to identify cage-breaking rearrangements for OTP. Although this method follows the same principles as that for BLJ, the presence of molecular rotations in OTP makes the identification of nearest-neighbour changes significantly more complicated and computationally expensive.

#### 3.3.1 Defining a Cage Break

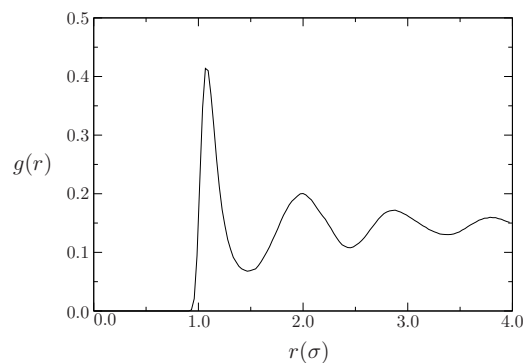
Just as for BLJ, a cage-breaking process in OTP must involve changes to the nearest neighbours of one or more molecules. Correctly identifying the nearest neighbour shell of a molecule is therefore an important step.

For BLJ, nearest neighbours were defined using a fixed cutoff distance  $r_{\text{NN}}(\alpha, \beta)$ , defined as the position of the first minimum in the radial distribution function. The equivalent approach for OTP, using a fixed cutoff in the centre of mass (CoM) displacement between two molecules, was unsuccessful. The CoM-CoM RDF, fig. 3.3a, is not sharply peaked and is significantly non-zero at its first minimum. Hence the nearest-neighbour shell is difficult to define using this metric: any value of  $r_{\text{NN}}$  will misidentify some neighbours and fail to identify others.

However, the nearest-neighbour shell of an individual site in an OTP molecule is much easier to define because the site-site RDF, fig. 3.3b, is more strongly peaked. Consequently, we have adopted a new definition for molecular cage breaks. The neighbours of each site in the OTP molecule are recorded separately, and cage breaks are identified for every site following a rule similar to that used with BLJ. These events are described as *site cage breaks* or SCBs. A *molecular cage break* (MCB) is diagnosed only when all of the constituent sites in a particular molecule



(a) The centre of mass radial distribution function for OTP. The dashed vertical line indicates a possible cutoff distance to define nearest neighbours, but the function is still significantly non-zero at this point.  $\sigma$  is the distance unit of the model.



(b) The site-site radial distribution function of OTP. This function is sharply peaked, so nearest neighbours for individual sites within the OTP molecule are easy to define.

undergo simultaneous SCBs. MCBs, not SCBs, are expected to control translational diffusion.

An SCB is diagnosed when an OTP site gains or loses two of its nearest neighbours. This condition is identical to that used in the cage break definition for BLJ, because the average numbers of nearest neighbours in BLJ and OTP are similar. Unlike for BLJ, nearest neighbours of OTP sites are not defined using a fixed cutoff distance  $r_{\text{NN}}$ . Instead, the solid angle nearest neighbour (SANN) method<sup>315</sup> is used (see below).

For OTP it was found that the number of SCBs and MCBs depended quite strongly on the value of the displacement cutoff  $d_c$  (see sec 1.7.2). To mitigate this problem, and to eliminate a system-dependent parameter, the displacement cutoff was omitted for OTP ( $d_c = 0$ ). This omission is partly compensated by the use of the SANN method, and partly by the requirement for three separate SCBs to occur for each MCB, which should limit the effect of local fluctuations in neighbour positions. However, it seems likely that omitting  $d_c$  will still lead to a modest overidentification of cage breaks.

The definition of MCBs described here is a general method for identifying cage-breaking rearrangements for any rigid molecular model. The only system-dependent parameter is the number of neighbours which must change for an SCB to occur.

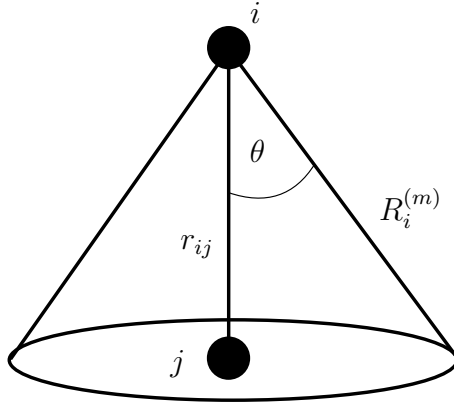


Figure 3.4: Solid angle construction for a central atom  $i$  and possible nearest neighbour  $j$ .

### 3.3.1.1 SANN Method

The SANN method of van Meel *et al.*<sup>315</sup> is a parameter-free, scale-free approach that calculates a local nearest-neighbour cutoff for each “atom”  $i$ , denoted  $R_i^{(m)}$ . In the case of OTP, the atoms are actually interaction sites.

Each possible nearest neighbour of  $i$  is assigned an angle  $\theta_{ij} = \arccos(r_{ij}/R_i^{(m)})$ .  $r_{ij}$  is the distance between  $i$  and  $j$ , and the cutoff  $R_i^{(m)}$  is initially unknown.  $m$  denotes the number of atoms for which  $r_{ij} < R_i^{(m)}$ , i.e. the number of nearest neighbours.  $\theta_{ij}$  is associated with a quantity  $\Omega_{ij} = 2\pi(1 - \cos \theta_{ij})$ , which is the solid angle at the apex of a cone with height  $r_{ij}$  and slant height  $R_i^{(m)}$ . This cone is shown in fig. 3.4.

The SANN algorithm begins with  $m = 0$ , and gradually increases  $R_i^{(m)}$  so that more atoms fall within  $R_i^{(m)}$  and hence  $m$  increases. The algorithm terminates when the total solid angle  $\sum_{j=1}^m \Omega_{ij} = 4\pi$ , the solid angle subtended by a sphere. The final values of  $m$  and  $R_i^{(m)}$  define the nearest neighbour shell of  $i$ .

Compared with the Voronoi tessellation and global cutoff methods, SANN neighbour shells are quite robust against small-amplitude fluctuations in particle position that should not be identified as nearest neighbour changes. However, SANN neighbours are not symmetric:  $j$  can be a neighbour of  $i$  without the converse being true. It is unclear whether this property is desirable in a definition of cage breaks, but asymmetric neighbours do not seem to affect the results significantly.

### 3.3.2 Diffusion Constants

Using the definition of MCBs presented in the previous section, the importance of cage breaks to translational diffusion was assessed by calculating the cage-breaking

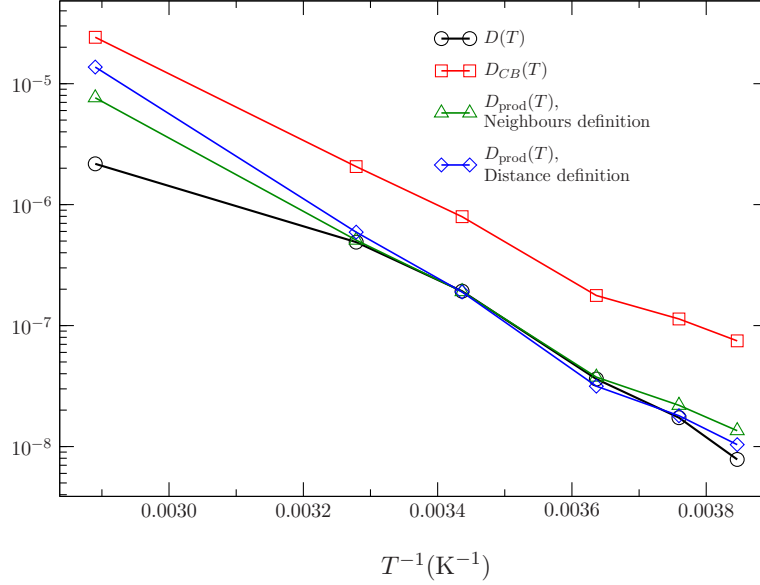


Figure 3.5: Effective diffusion constants for OTP computed by several different methods.  $D(T)$  denotes the correct diffusion constants from the full MD trajectory.  $D_{CB}(T)$  is the effective diffusion constant calculated from all cage breaks.  $D_{\text{prod}}(T)$  is the effective diffusion constant for non-reversed (productive) cage breaks only. Two different methods for identifying productive cage breaks are shown. Apart from  $D(T)$ , all the diffusion constants are calculated from inherent structure trajectories. All diffusion constants are given in  $\text{cm}^2 \text{s}^{-1}$ .

diffusion constants,  $D_{CB}(T)$  and  $D_{\text{prod}}(T)$ , introduced in §1.7.2. MCBs were identified in inherent structure trajectories for a range of temperatures, and used in eq. (1.18) to compute  $D_{CB}(T)$ .

In fig. 3.5, we see that  $D_{CB}(T)$  yields a substantial overestimate of the full-trajectory diffusion constant  $D(T)$ . This error arises from the rather drastic assumption in eq. (1.18) that all cage-breaking displacements are in the same direction. The error can be corrected by accounting for negative correlation of the step direction between consecutive MCBs. The required correction is approximated by identifying all MCBs that are completely reversed in subsequent steps, and discount their contribution to the diffusion constant. When an MCB is directly reversed by another MCB, both events are discounted. The resulting diffusion constant is:

$$D_{\text{prod}}(T) = \frac{1}{6t} \sum_i^N \frac{1}{N_{\text{prod},i}} \sum_{j \in \text{prod}}^{N_{\text{prod},i}} \Delta \mathbf{r}_{i,j}^2, \quad (3.2)$$

which is identical to eq. (1.18) except that now the sum in  $j$  runs over the productive (i.e. unreversed) MCBs rather than over all MCBs.

Recall from §1.7.2 that CB reversals may be direct or indirect, and that in

BLJ these reversals were detected by comparing the mean squared displacements of consecutive cage-breaks against a cutoff distance  $d_{\text{rev}}$ . This *distance method* fails to detect many reversals in the OTP trajectories, because the anisotropy of OTP molecules creates cages that are larger and more sparse than in BLJ. Larger cages mean that a reversed CB could leave a molecule in an equivalent nearest-neighbour environment while still being a considerable distance from its original position. Using an arbitrary small  $d_{\text{rev}}$ , as was done for BLJ, therefore fails to capture most reversal events.

We followed two approaches to identify reversed CBs. Firstly, we continued to use the distance method, but gradually increased  $d_{\text{rev}}$  until a histogram of the correlation angles between consecutive productive CBs indicated that all direct reversals had been identified (cf. fig. 4 in [233]). This analysis gave a value of  $d_{\text{rev}} = 0.3\sigma$  (c.f.  $d_{\text{rev}} = 10^{-5}\sigma_{\text{AA}}$  for BLJ). The resulting effective diffusion constants are shown in fig. 3.5.

We also used a second method to identify reversed CBs, which avoids the need to choose a distance cutoff by considering the changes to nearest-neighbour lists.

Recall from §3.3.1 that we require each site in a molecule to lose or gain two nearest neighbours if a transition is to be counted as a MCB. If a site-neighbour is lost in one SCB and gained in the next, this neighbour change has been reversed directly. If a site-neighbour is lost in two consecutive SCBs, that neighbour change has been reversed indirectly.

If the number of neighbours gained/lost in the first SCB is less than two after discounting all reversed neighbour changes, then the first SCB is considered to have been reversed by the second. Note that the first SCB is still considered to have taken place but is treated differently because it is subsequently reversed. An MCB is treated as reversed if any of its constituent SCBs are reversed. This is the *Neighbours method* of identifying reversals.

The effective diffusion constants  $D_{\text{prod}}(T)$  are shown in fig. 3.5 for the two reversal methods. Both give a dramatic improvement over  $D_{\text{CB}}(T)$ , fitting the correct  $D(T)$  values very well in range 275 K-305 K (roughly corresponding to the landscape-influenced regime). This result indicates that productive CBs (defined using either method) are sufficient to describe translational diffusion in this temperature range. The gradients of both  $D_{\text{prod}}(T)$  lines are more negative than that of the  $D_{\text{CB}}(T)$  line, indicating that incorporating the effect of negative correlation raises the energy barrier to diffusion.

Both sets of productive-CB diffusion constants significantly overestimate the correct values at high temperatures, and the neighbour method gives a small over-

estimate at low temperatures. Moreover, none of the cage breaking lines shows significant super-Arrhenius curvature, which suggests they are not capturing all the details of translational diffusion.

The error at higher temperatures is probably due to the breakdown of the inherent structure description: at higher temperatures the original MD trajectory samples high-energy regions in each basin of attraction,<sup>226</sup> so quenching has a greater effect on the displacement between consecutive frames and inherent structures no longer provide a good description of diffusion.

The small errors at low temperatures may arise because these MD trajectories are less well equilibrated (see fig. 2.2), although this is only a serious concern for the lowest temperature studied. If the errors are genuine, they suggest that the MCB definition misses some negative correlation effects, perhaps indicating the existence of another type of reversal motion that has not been accounted for. For example, some reversals may take place via several CBs rather than by a single pair of consecutive CB events. Failure to detect all reversal events could also explain the lack of super-Arrhenius curvature in  $D_{\text{CB}}(T)$ : in BLJ the super-Arrhenius behaviour arises from increased effective energy barriers to diffusion due to a greater fraction of reversed CBs at low temperature (see §1.7.4).

The distance method appears to be more accurate than the neighbours method at low  $T$ , possibly because the latter is sensitive to rotational motion of a molecule's nearest neighbours but the former is not. It is believed that translational-rotational decoupling may increase the ratio of rotational to translational motion in cold OTP,<sup>13,49</sup> which could cause the neighbours method to miss some reversals that the distance method identifies correctly. Alternatively, the apparent deviation of  $D_{\text{prod}}(T)$  from  $D(T)$  at low temperatures may be a random, rather than systematic, error.

The neighbours method is parameter free, and therefore extends easily to any small rigid molecule. Therefore this reversal method is used in the remainder of this chapter.

Fig. 3.5 demonstrates that molecular rearrangements corresponding to productive CBs dominate translational diffusion in the landscape-influenced temperature regime for OTP. It also demonstrates the importance of negatively correlated motion, described by reversed cage breaks.

Fig. 3.6 reproduces the cage-breaking diffusion coefficients calculated for the BLJ fluid, to compare with fig. 3.5. For BLJ,  $D_{\text{prod}}(T)$  approximates the correct  $D(T)$  very well at intermediate and low temperatures, particularly at number density  $1.3\sigma_{\text{AA}}^{-3}$ . In fact, the agreement between  $D_{\text{prod}}(T)$  and  $D(T)$  in BLJ covers at least

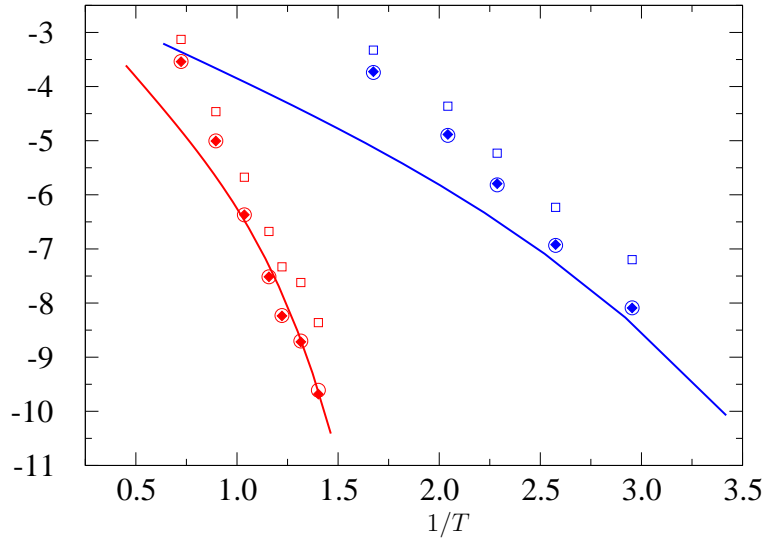


Figure 3.6:  $\log_{10} D(T)$  for a BLJ fluid with  $N = 60$ , reprinted from [233] with the permission of AIP Publishing. Squares and circles represent  $D_{\text{CB}}(T)$  and  $D_{\text{prod}}(T)$ , respectively. Diamonds represent  $D_{\text{CB}}(T)$  with a correction factor added to account for reversed CBs in a coarse-grained manner. Solid lines represent VTF fits to  $D(T)$ . Red symbols correspond to number density  $1.3\sigma_{\text{AA}}^{-3}$ , blue correspond to  $1.1\sigma_{\text{AA}}^{-3}$ . Diffusion constants are given in BLJ natural units.

four orders of magnitude in the diffusion constant whereas these two quantities only agree over two orders of magnitude in OTP. This difference is probably because the cage-breaking definition for OTP does not capture rotational motion well enough.

The other major difference between figs. 3.5 and 3.6 is that the latter does not display a divergence between  $D_{\text{prod}}(T)$  and  $D(T)$  at low temperatures. This difference is consistent with the suggestion made earlier, that the divergence in the OTP results arises from underidentification of reversed MCBs. Reversals in BLJ are much easier to detect because of the lack of orientational freedom and the higher density, which leads to smaller, more rigid cages. Therefore it is unsurprising that the BLJ reversal definition outperforms that for OTP.

### 3.4 Landscape Analysis

The PEL of OTP was sampled using an inherent structure trajectory produced at 266 K, as described in §3.2.2. This temperature lies well below  $T_m$ , and appears to be near the bottom of the landscape-influenced temperature range. Fig. 3.7 shows the disconnectivity graph produced from this sampling.

The graph displays all the typical features of a glassy landscape described in §1.6.2.5. There is no clear global minimum, no overall funnel structure, and no

crystal region on the time scale of these simulations. There is a large range of barrier heights, many of which are much larger than  $k_{\text{B}}T$  in the supercooled regime.

The minima are clustered into many local groups within which they are separated by lower barriers (less than  $\epsilon$ ), corresponding to local funnels (see §1.6.1). Interconversion between funnels requires overcoming significantly larger barriers, so relaxation between them is comparatively slow. This organisation is consistent with the metabasin picture described in §1.6.2.3, which has previously been suggested as the origin of super-Arrhenius behaviour.<sup>221</sup>

As explained in §1.7.3, productive cage breaks in BLJ are thought to represent jumps between metabasins, which correspond loosely to local funnels.<sup>233</sup> To test this description in OTP, we investigate the effect of partitioning the landscape using cage-breaking and non-cage-breaking transition states.

### 3.4.1 Cage-Breaking Analysis of the Landscape

The cage-breaking analysis described in §3.3 may be applied to any two configurations of the system, including two minima connected by a transition state. If any molecules undergo a CB from one structure to the other, the minimum-TS-minimum triple is classified as cage-breaking. Otherwise, it is classified as non-cage-breaking.

Fig. 3.8 shows a disconnectivity graph for OTP from which all non-cage-breaking transition states have been removed. This transformation splits the disconnectivity graph into two fragments wherever a missing transition state provided the only connection between two sets of minima. In fig. 3.8 each fragment is coloured according to the energy at which it becomes disconnected from the rest of the graph, to emphasise the reduced connectivity of this transformed landscape. A few minima which are only connected to the rest of the landscape by non-cage-breaking transitions are omitted entirely from the disconnectivity graph.

In fig. 3.8 most of the landscape belongs to a small number of connected regions, each appearing as a large block of a single colour. Therefore, the removal of non-cage-breaking transition states does not significantly break the connectivity of the landscape: MCBs are largely sufficient to describe the connectivity.

The partial fragmentation when non-CB transition states are removed could suggest that some non-CB rearrangements are required to explore the entire landscape. However, this requirement may be a sampling artefact, because there could be other pathways connecting these fragments by CB transition states which have not been located and included in our database. Since there are only a small number of significant fragments in fig. 3.8, only a few additional cage-breaking transition states would need to be located to connect the entire landscape.

Fig. 3.9 was produced in the same way as fig. 3.8, but with all the cage-breaking transition states removed instead of the non-cage-breaking transition states. In contrast to the CB-only graph, fig. 3.9 is highly fragmented into many small unconnected regions, some of which contain very few minima. A cage break is required to cross between two such regions.

Some of the fragments in fig. 3.9 may be connected by non-cage-breaking transition states that were missed by the sampling protocol, so that locating these additional connections would increase the connectivity of the database. However, there are so many missing connections that the landscape will probably never become globally connected unless cage-breaking transition states are included. This result reinforces the earlier conclusion that cage-breaking rearrangements are an essential component of diffusion. To diffuse requires traversing the landscape, which is impossible without cage breaks.

Fig. 3.10 shows that the non-CB graph contains small locally-connected regions, which can be explored without undergoing a CB transition. Each of these connected regions may be loosely identified with a funnel, but crossing between funnels usually requires a cage-breaking transition. Cage-breaking transition states divide the landscape into funnels, which can themselves be divided into individual minima: a hierarchical arrangement similar to that found for the BLJ fluid.<sup>233</sup>

We hypothesise that the local funnels visible in fig. 3.9 can be identified with the metabasins of Heuer *et al.*<sup>197,229,230</sup> If this hypothesis is correct, transitions between minima within a funnel should be easily reversible. To estimate the reversibility of transitions between the minima of our database, we construct a *connected path* from the inherent trajectory used in §3.4 by replacing each pair of minima in the trajectory with the shortest pathway of minimum-TS-minimum triples between them. This process provides a time-ordered series of elementary rearrangements executed by the system. Because the inherent trajectory frequently revisits regions of configuration space, some of the MCBs which take place in one elementary transition may be reversed in a later transition.

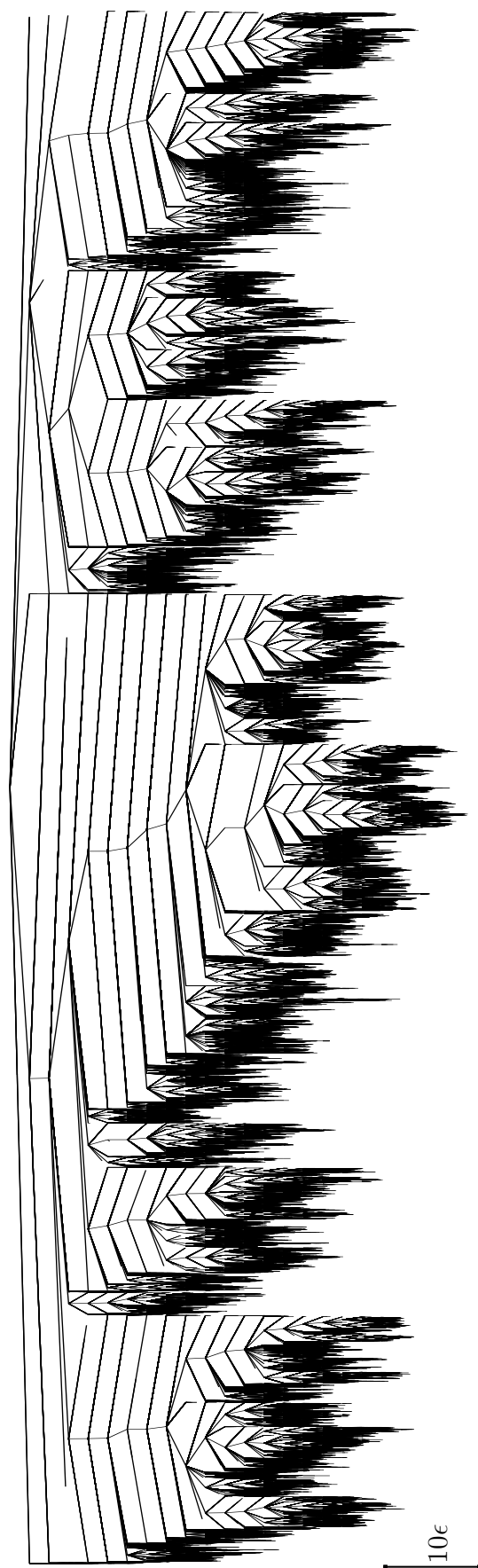


Figure 3.7: Disconnectivity graph for OTP sampled from an MD trajectory at 266 K.

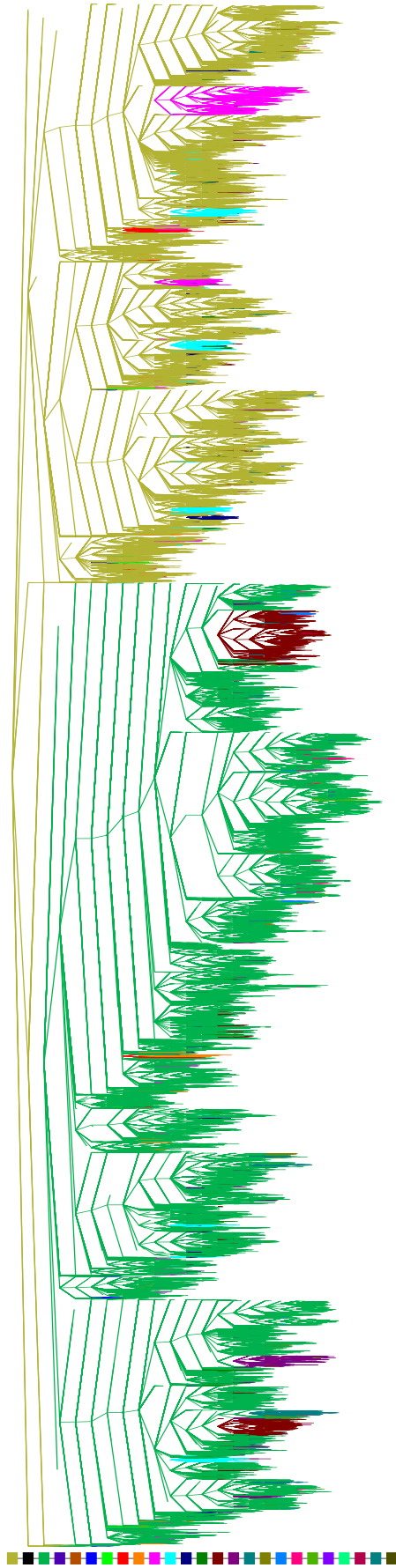


Figure 3.8: Disconnectivity graph for OTP with all non-cage-breaking transition states removed. This process breaks the graph into unconnected fragments, each of which is coloured according to the highest energy level at which it becomes disconnected. Colours correspond to the scale bar at the left. The separation of energy levels is  $2\epsilon$ .

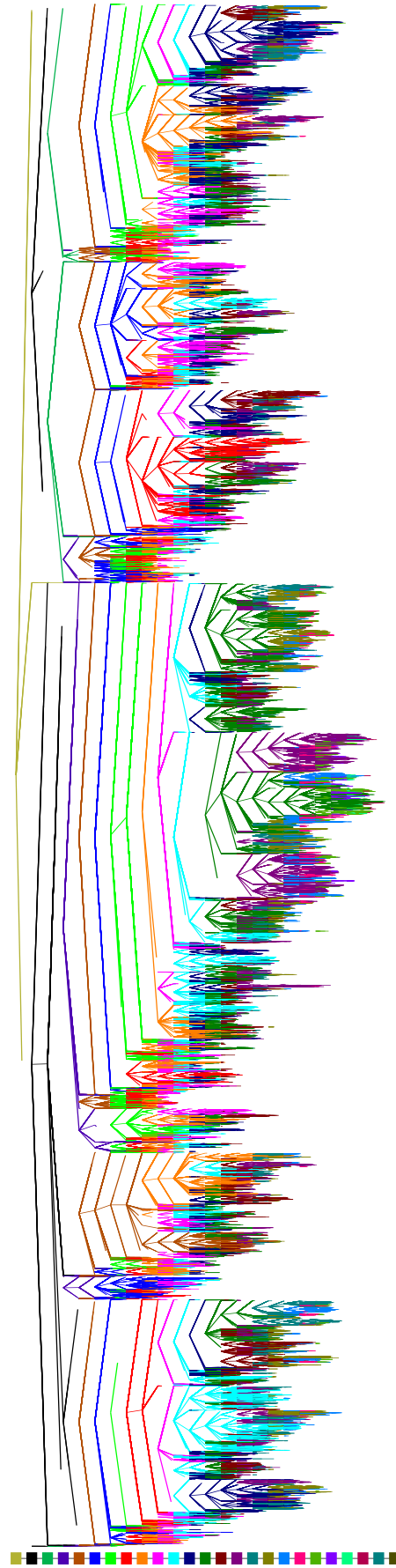


Figure 3.9: As in fig. 3.8 but in this case all non-cage-breaking transition states are retained and all cage-breaking transition states are removed.

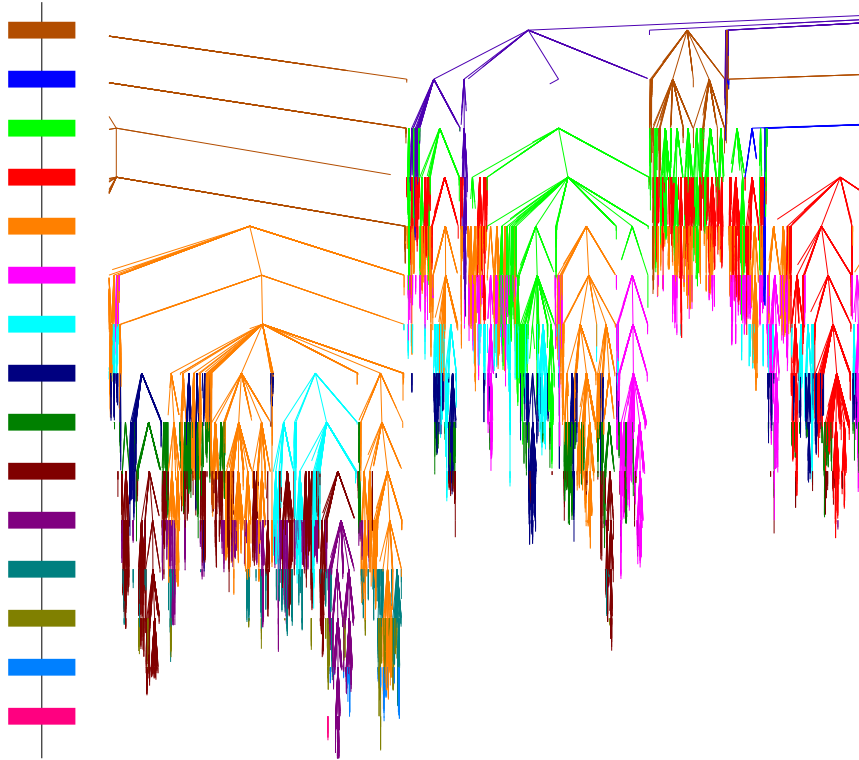


Figure 3.10: Detail from fig. 3.9 showing local connectivity in the non-cage-breaking landscape. The scale bar and colouring scheme are the same as for fig. 3.9.

Every pair of minima on the connected path was analysed for cage breaks and reversals. Productive cage breaks were identified as before (§3.3.2). Energy metabasins (EMBs) are defined by reversibility of transitions within an EMB<sup>229,230</sup>, so any type of motion that is known to be easily reversed - i.e. non-CB rearrangements and reversed CB transitions - must be confined within a metabasin. Therefore we define a *geometrical metabasin transition* as taking place every time a productive cage break occurs. If this definition is meaningful we expect that a disconnection graph with all productive CBs removed from it will fragment into its component metabasins. Otherwise, the disconnection graph will fragment randomly.

Fig. 3.11 shows the landscape with all productive cage breaks removed, and demonstrates that the landscape is indeed partitioned into completely connected regions, which become disconnected from each other at higher energies. Fig. 3.12 shows a detail from this graph corresponding to the same region of the landscape as fig. 3.10, which shows increased connectivity within a funnel once reversed cage breaks are taken into account.

The hierarchical structure observed in the PEL without dynamical information is preserved when that information is included. Restricting the connectivity to include only reversible motion exposes locally connected regions of the landscape, and so

justifies our description of landscape funnels as metabasins.

We have referred to productive cage breaks as defining “geometric metabasins”, but in fact this definition uses dynamical information as well as geometric information, because an MD trajectory is required to identify reversals. Consequently, different MD trajectories could assign the same minima to different metabasins, which is somewhat unsatisfactory. Other definitions of metabasins suffer from the same problem. A goal for future work is to establish geometric indicators for reversed minimum-TS-minimum transitions, and thus remove the dynamical component from this metabasin formulation.

Although the cage-breaking definition of metabasins shares qualitative features with Heuer’s energy metabasin (EMB) transitions,<sup>229,230</sup> it is still not clear how closely the two definitions align. Ongoing studies suggest that they are strongly correlated, but the transition events identified by the two methods do not always coincide.<sup>316</sup>

Cage-breaking and metabasin disconnectivity graphs for the BLJ fluid may be found in [233], but will not be reproduced here for reasons of space. Those graphs exhibit the same general trends as figs. 3.8-3.11, indicating that the metabasin description applies to both systems, as expected if the presence of metabasins is linked to fragile dynamical behaviour.

The main difference between the landscapes of BLJ and OTP is that the metabasins in OTP contain more minima than those in BLJ. Although the PEL database for OTP contains many more minima than that for BLJ, fig. 3.11 contains  $O(10)$  metabasins whereas the equivalent figure for BLJ contains at least  $O(100)$ . This difference could arise because many of the cage breaks in OTP result from rotational motion and are more likely to be reversed than translational CBs in BLJ. A greater proportion of reversals leads to larger metabasins. It is also possible that the difference is due to contrasting temperatures in the two simulations. Developing a scheme for comparing temperatures between different landscapes in an unbiased way is an important outstanding problem.

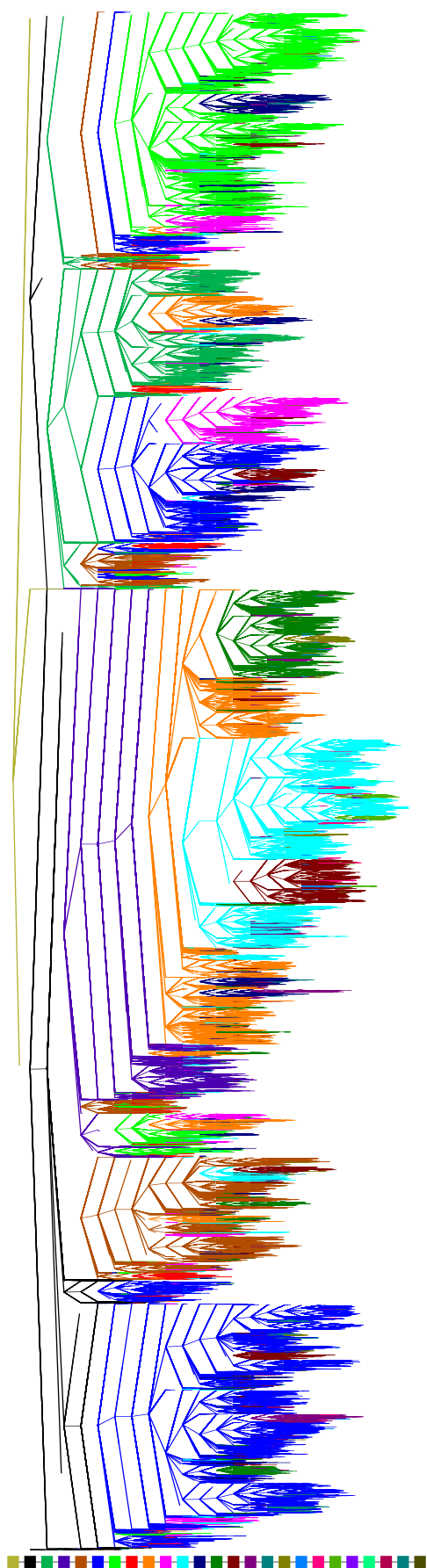


Figure 3.11: Disconnectivity graph for OTP at 266 K after removing all transition states corresponding to productive cage breaks. Disconnected fragments of the graph are coloured according to the energy level at which they become disconnected from the rest of the graph, as shown by the scale bar at the left. The separation of energy levels is  $2\epsilon$ .

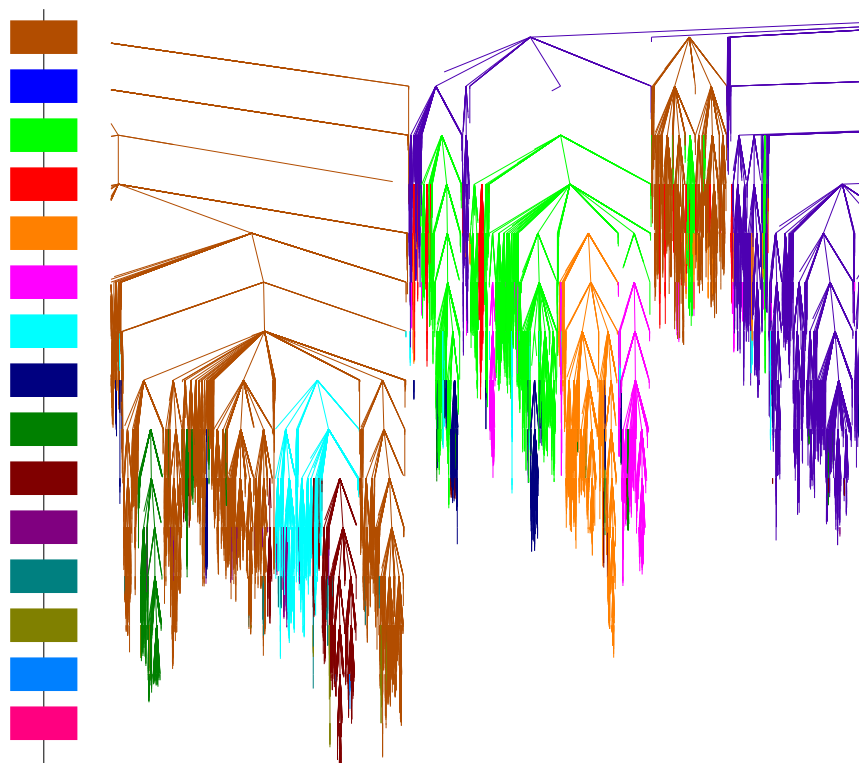


Figure 3.12: Detail from fig. 3.11 showing increased local connectivity compared to fig. 3.10 now that transition states corresponding to reversed cage breaks are included. The scale bar and colouring scheme are the same as for fig. 3.11.

### 3.5 Conclusions and Future Directions

There are two main results in this chapter. Firstly, the development of a generalised definition of cage breaks that is applicable to all small rigid molecules. The definition proposed here is almost entirely parameter free, unlike the original method used for BLJ, which will facilitate comparison of results between different systems in the future.

The cage-breaking rearrangements captured by this definition provide a simplified, but still accurate, description of translational diffusion in OTP at moderately supercooled temperatures. Diffusion constants calculated using only molecular cage breaks provide a good approximation to the correct values in this temperature regime, and cage-breaking rearrangements are both necessary and sufficient to traverse the PEL.

One immediate application of the MCB definition would be to study propylene carbonate (PC). Cicerone and Tyagi<sup>61</sup> have recently performed quasi-elastic and inelastic neutron scattering experiments on this liquid, and concluded that diffusion

of PC occurs on three characteristic time scales corresponding to IS transitions, metabasin transitions and long-term diffusive motion. They attribute the Johari-Goldstein  $\beta$  process<sup>57</sup> (see §1.2.1.3) to the metabasin transition events. An exciting project would be to analyse simulated diffusion of PC using the cage-breaking model described in this chapter, to compare the timescale and relaxation spectrum of productive MCB transitions with the Johari-Goldstein relaxation peak.

Another possible direction would be to extend the MCB definition to sophisticated flexible models of glass-forming molecules. One suitable candidate is the atomistic model of OTP proposed by Eastwood *et al.*<sup>15</sup>

The second major result in this chapter is the hierarchical organisation of the PEL of OTP, the first time that such organisation has been quantified in a molecular liquid. The geometrical definition of productive cage breaks may be used to separate the PEL into superstructures of minima that we identify with metabasins. Diffusion can then be analysed using the CTRW model (see §1.6.2.4), and the results compared with those obtained using energy metabasins. A similar approach has already been used for BLJ.<sup>256</sup>

Although the existence of superstructures in glassy energy landscapes has been hypothesised for some time - indeed, one can argue that this concept is central to the RFOT theory - it is only with the connection to cage breaking that we have been able to observe such organisation directly. Correlating this organisation with the energy-based definition of Heuer *et al.*<sup>197,229,230</sup> is an important task.

The conclusions presented here are consistent with previous results for BLJ, implying that the concepts of cage breaks and metabasins are general to the whole class of fragile liquids, not simply to atomic systems. Unsurprisingly, there are some significant differences between the results for the two systems.

Cage-breaking diffusion constants for the BLJ fluid reproduce the correct  $D(T)$  better at low temperatures than at high,<sup>233</sup> but in OTP the  $D_{CB}(T)$  values also begin to diverge from  $D(T)$  at the lowest temperatures studied. Moreover, the temperature range over which the cage-breaking description is valid appears to be smaller for OTP than for BLJ. Both of these observations suggest that although the broad picture of cage breaks and reversals is a good description of the dynamics in OTP, the MCB definition for OTP is less accurate at identifying important rearrangements than is the CB definition for BLJ. In particular, reversed CBs are difficult to identify in OTP.

The results of this chapter are consistent with a view of spatially heterogeneous cooperative dynamics in OTP. The more mobile molecules at any given time are the ones currently undergoing cage breaks, the less mobile are confined within their

cages. It would be interesting to probe the extent of these regions and the exact nature of cooperative movements by looking for time and spatial correlations in the identified cage breaks.

Another future objective will be to compare our definition of cage-breaks with other methods for identifying important structural changes,<sup>100,111,112</sup> particularly those based on metabasins,<sup>229,230,317</sup> to understand whether they are capturing the same features of supercooled dynamics as cage breaks, and how these different definitions coincide with established theories of the glass transition. In particular, it would be interesting to see how much of the success of the cage-breaking method comes from its non-local character, and whether the rearrangements picked out by other approaches have similar or different effects on the connectivity of the landscape.

The influence of the rotational degrees of freedom for OTP on the nature of cage-breaks, and on the PEL, merits further investigation. It might be possible to define a geometrical motion analogous to the translational cage-break to explain super-Arrhenius behaviour in the rotational diffusion constants, and the decoupling between translational and rotational diffusion constants which is observed in OTP at low temperatures.<sup>13,38</sup> Moreover, it would be interesting to determine whether the presence of rotations changes the hierarchical organisation of the PEL significantly. It is possible that rotational barriers are smaller than translation, which could lead to fine structure within a metabasin. The differences between translational and orientational degrees of freedom on a PEL are still not completely understood.

# Chapter 4

## Comparing Fragile and Strong Glass Formers

### 4.1 Introduction

The previous chapter established that cage breaking provides a simplified and accurate description of the dynamics of fragile supercooled liquids. Cage breaks are related to metabasins in the PEL, which have previously been used to explain super-Arrhenius temperature dependence of diffusion constants.<sup>221</sup> A logical conclusion from these statements is that the landscape of a strong supercooled liquid such as silica should not have metabasins. However, Saksengwitt and Heuer have observed metabasin transitions in the sequences of IS energies sampled by a silica model, suggesting that higher-order structure is present in the PEL for both classes of glass former.<sup>215,234</sup>

In this chapter, the cage-breaking and PEL analysis that was developed for BLJ and OTP is applied to the popular van Beest-Kramer-van Santen (BKS) model of viscous silica, to investigate whether geometrical metabasins are present for this liquid.

Because silica is a strong liquid, its transport coefficients retain Arrhenius temperature dependence deep into the supercooled temperature regime. This behaviour implies a fixed energy barrier to diffusion, which is crossed by thermal activation. In the case of silica, this barrier represents the energy required to break an Si-O chemical bond.

For silica, several phenomena associated with the glass transition are observed at temperatures significantly higher than the melting point,  $T_m \approx 1980$  K. For example, the mode coupling critical temperature of the BKS silica potential occurs at  $T_c = 3300$  K,<sup>220</sup> the landscape-dominated regime extends to  $T \approx 3500$  K, and the

landscape-influenced regime spans 3500 K to 10000 K,<sup>220</sup> even though the liquid is still the thermodynamically stable state in this temperature range.

It is likely that BKS silica has a higher melting temperature than the experimental  $T_m$ ,<sup>318</sup> but not sufficiently high to explain these observations. Nevertheless, the dynamical behaviour of silica near  $T_c$  is similar to the behaviour of other glass formers in the supercooled regime and so, following previous work,<sup>124,125,220,234,319</sup> we consider the diffusive behaviour of undercooled viscous silica in the same way that we have previously studied supercooled liquids.

The dynamics of silica change considerably in the vicinity of  $T_c$ , i.e. near the crossover from the landscape-dominated to landscape-influenced temperature regimes. In particular, a “fragile-strong crossover”<sup>215,220,319–321</sup> occurs in the diffusion constant, above which the apparent activation barrier increases with increasing temperature.

This deviation from straight-line Arrhenius behaviour occurs at 3221 K in experimental measurements of viscosity<sup>320,321</sup> and around 3300–3500 K in simulations.<sup>234,319,322</sup> Some authors<sup>319</sup> associate the crossover with a feature in the heat capacity. Others<sup>124,220</sup> argue that these diffusion constants are best fitted by a power law in  $(T - T_c)$ , and hence the crossover is associated with the transition from flowlike transport to hopping particle motion that is predicted by generalised mode coupling theory. If the high-temperature behaviour can indeed be explained by mode coupling theory then it may arise from a different mechanism to the low-temperature super-Arrhenius behaviour of a fragile glass former. It is also possible that the high-temperature behaviour is not super-Arrhenius at all, but in fact the crossover simply connects two different Arrhenius regimes.<sup>235</sup>

This chapter focusses on the difference between the strong regime of silica and the fragile regime of BLJ, rather than the fragile-strong crossover and the diffusion behaviour of silica above 3300 K. However, these topics are clearly worthy of further study and explanation.

There have been many previous investigations of diffusion in silica, including several seeking to identify diffusive rearrangements, which generally conclude that diffusion is controlled by bond-shifting processes. These rearrangements can involve one Si-O bond breaking and another forming within a short time period,<sup>323,324</sup> or alternatively propagation of a coordination-number defect through the bond network.<sup>220</sup> The former type of rearrangement has a much larger energy barrier, but the rate of the latter type has a smaller pre-exponential factor because defects in the network structure are quite rare.<sup>324</sup> All studies agree that diffusive rearrangements are correlated in time and space.<sup>220,323,324</sup>

The central aim of this chapter is to consider how the PELs of silica and BLJ differ, and how this difference affects diffusive rearrangements in these systems. Heuer *et al.*<sup>215</sup> have previously studied these models, and showed that both PELs contain metabasins, contradicting Stillinger’s view that landscapes of strong glass formers should not be hierarchical.<sup>221</sup> They also showed that the distribution of metabasin energies is broadly Gaussian for both strong and fragile glass formers, but for silica there is a low-energy cutoff below which the density of metabasins is much smaller than predicted by the Gaussian form.<sup>215</sup> They associated this cutoff with the case of zero coordination defects, and argued that it can explain the fragile-strong crossover.

Kushima *et al.*<sup>285</sup> have sampled local minima and saddle points on the PELs of BLJ and silica. They used a basin-climbing algorithm designed to explore the transition states near a starting minimum, crossing them in order of increasing energy.<sup>325</sup> Using the potential energy barriers sampled in this study, they determined a coarse-grained effective activation barrier as a function of temperature, and hence predicted the viscosity. They predict that for both silica and BLJ, the activation barrier has a constant small value at high temperature and a large constant value at low temperature, linked by a “fragility zone” in which the barrier changes. This would imply that both liquids should show not one but two fragile-to-strong crossovers, a result which to our knowledge has not been observed either in simulation or experiment. Interestingly, an analytical model glassy landscape studied by Wales and Doye<sup>199</sup> displayed two fragile-strong crossovers in the thermodynamic, rather than kinetic, fragility. However, the low-temperature crossover in this case corresponded to the kinetic glass transition.

Part of the work presented in this chapter was carried out in collaboration with Myra Biedermann. She parameterised our modifications to the BKS potential, and carried out the initial MD simulations and landscape sampling. Her contributions are indicated clearly in the relevant text. The text of this chapter is based on a paper published in the *Journal of Chemical Physics*.<sup>245</sup>

## 4.2 Model

Liquid silica was modelled using a modified version of the widely-used BKS potential.<sup>326</sup> The original pairwise potential  $V_{\text{BKS}}(r_{ij})$  has the form

$$V_{\text{BKS}}(r_{ij}) = \frac{q_{\mu}q_{\nu}e^2}{r_{ij}} + A_{\mu\nu}e^{-b_{\mu\nu}r_{ij}} - \frac{C_{\mu\nu}}{r_{ij}^6}, \quad (4.1)$$

where  $r_{ij}$  is the distance between atoms  $i$  and  $j$ .  $\mu$  is the atom type of  $i$  (either Si or O) and  $\nu$  is the atom type of  $j$ .  $q_\mu, q_\nu$  are the ionic charges and  $e$  is the elementary charge.  $A_{\mu\nu}, b_{\mu\nu}, C_{\mu\nu}$  are parameters, listed in table 4.1.

The first term in eq. (4.1) accounts for the electrostatic interaction between two ions, the second term describes short-range repulsion and the final term describes the dispersion interaction. The latter two terms were originally proposed by Buckingham.<sup>327</sup>

Accurate calculation of long-ranged interactions, such as electrostatic energies, under periodic boundary conditions remains a computationally demanding task.<sup>328</sup> These energy terms are usually computed using Ewald summation,<sup>329</sup> but this method may be unnecessary in condensed-phase systems if the electrostatic forces between many particles cancel to give an effective shorter range.<sup>330,331</sup> Therefore, for the simulations used in this chapter, we calculated the electrostatic energy using a pairwise sum over ions with a shifted truncation scheme similar to that proposed by Wolf *et al.*,<sup>332</sup> which achieves local charge neutrality.

Stable behaviour of geometry optimisation algorithms requires that the pair potential and associated force go smoothly to zero at the cutoff radius.<sup>4</sup> We use the following expression, proposed by Gezelter *et al.*<sup>328</sup> as a modification to the Wolf method, to calculate the Coulomb energy. The first term in eq. (4.1) is replaced with:

$$V_C(r_{ij}) = q_\mu q_\nu e^2 \left( \frac{1}{r_{ij}} - \frac{1}{r_c} + \frac{1}{r_c^2} (r_{ij} - r_c) \right), \quad (4.2)$$

where  $r_c$  is the cutoff radius.

Carré *et al.*<sup>333</sup> compared this truncation scheme with the Ewald summation for the BKS potential, and found excellent agreement for both static and dynamic properties when  $r_c \geq 10 \text{ \AA}$ . We chose  $r_c = 10 \text{ \AA}$  to minimise computational cost.

Quadratic shifts and cutoffs at the same radius  $r_c$  are introduced for the short-ranged parts of the BKS potential. These schemes are analogous to that used by Stoddard and Ford for the Lennard-Jones potential, which guarantees smooth continuous behaviour at the cutoff.<sup>314</sup> The second and third terms in eq. (4.1) are replaced by the following:

$$\begin{aligned} V_{\text{short}} &= A_{\mu\nu} e^{-b_{\mu\nu} r_{ij}} - \frac{C_{\mu\nu}}{r_{ij}^6} + \lambda_1 + \lambda_2 r_{ij}^2, \quad \text{where} \\ \lambda_1 &= -A_{\mu\nu} e^{-b_{\mu\nu} r_c} \left( 1 + \frac{b_{\mu\nu} r_c}{2} \right) + \frac{4C_{\mu\nu}}{r_c^6} \\ \text{and } \lambda_2 &= \frac{A_{\mu\nu} b_{\mu\nu}}{2r_c} e^{-b_{\mu\nu} r_c} - \frac{3C_{\mu\nu}}{r_c^8}. \end{aligned} \quad (4.3)$$

Table 4.1: Parameters for the modified BKS pair potential used in this study. Si-Si interactions are electrostatic only (hence the parameters for the Buckingham, dispersive and repulsive parts are all zero).

Parameter	Si-O	O-O
$A_{\mu\nu}$ (eV)	18003.7572	1388.7730
$b_{\mu\nu}$ ( $\text{\AA}^{-1}$ )	4.87318	2.76000
$C_{\mu\nu}$ (eV $\text{\AA}^6$ )	133.5381	175.0000
$\epsilon_{\mu\nu}$ (eV)	$3.097948 \times 10^{-3}$	$1.0510505 \times 10^{-3}$
$\sigma_{\mu\nu}$ ( $\text{\AA}$ )	1.313635	1.779239
$r_c/\text{\AA}$	10.0	10.0
$q_\mu$	Si: 2.4	O: 1.2

To avoid unphysical divergence of the Si-O and O-O pair potentials at small  $r_{ij}$ , a short-range repulsive pair potential was added:<sup>319</sup>

$$\begin{aligned}
 V_{\text{rep}}(r_{ij}) &= 4\epsilon_{\mu\nu} \left[ \left( \frac{\sigma_{\mu\nu}}{r_{ij}} \right)^{30} - \left( \frac{\sigma_{\mu\nu}}{r_{ij}} \right)^6 \right] + \lambda_1 + \lambda_2 r_{ij}^2, \\
 \text{where } \lambda_1 &= 4\epsilon_{\mu\nu} \left[ -16 \left( \frac{\sigma_{\mu\nu}}{r_c} \right)^{30} + 4 \left( \frac{\sigma_{\mu\nu}}{r_c} \right)^6 \right] \\
 \text{and } \lambda_2 &= 4\epsilon_{\mu\nu} \left[ 15 \frac{\sigma_{\mu\nu}^{30}}{r_c^{32}} - 3 \frac{\sigma_{\mu\nu}^6}{r_c^8} \right]. \tag{4.4}
 \end{aligned}$$

$\epsilon_{\mu\nu}$  and  $\sigma_{\mu\nu}$  were chosen such that the total pair potential eq. (4.5) increases monotonically for distances  $r_{ij} < r_{ij}^*$  (see table 4.1). As before, the  $\lambda_1$  and  $\lambda_2$  terms guarantee smooth behaviour of the shifting potential at the cutoff, although in fact this term is negligible at  $r_c$ .

The complete potential used in the present work is a combination of the shifted and truncated BKS potential (eq. (4.3)), the Coulombic interactions calculated by the Wolf method (eq. (4.2)) and the repulsive switching potential (eq. (4.4)):

$$V_{ij}(r_{ij}) = \begin{cases} V_{\text{short}}(r_{ij}) + V_C(r_{ij}) + V_{\text{rep}}(r_{ij}) & \text{for } r_{ij} < r_c, \\ 0 & \text{otherwise.} \end{cases} \tag{4.5}$$

All parameters are given in table 4.1.

Table 4.2: Length of the MD trajectories at different temperatures. The equilibration time of  $10^6$  MD steps (1 ns) is excluded.

$T$ (K)	MD steps	length (ns)
2685, 2902, 3085, 3207	$4 \times 10^6$	4
3544, 3854	$2 \times 10^6$	2
4396, 4821, 5257, 5752	$1 \times 10^6$	1

### 4.2.1 Simulation Details

The dynamical data used in this study were obtained from microcanonical molecular dynamics (MD) simulations of bulk silica at a range of different energies, most of which were performed by Myra Biedermann. Periodic boundary conditions were employed, using a cubic simulation box containing 555 ions. The side length of the box was  $20 \text{ \AA}$ , giving a fixed density of  $2.3 \text{ g/cm}^3$ . This density is close to the experimental value and has been studied in previous work.<sup>220,334</sup>

The system size chosen is small enough that finite size effects might be a concern, but we find that the qualitative behaviour of the diffusion constant (including the fragile-strong crossover) is identical to behaviour reported for systems using as many as 8016 atoms.<sup>220</sup> It has previously been shown<sup>216,234,335</sup> that for BKS a system size of 100 particles is sufficient to avoid severe finite-size effects for thermodynamic properties and relaxation times.

Velocity-Verlet MD (see §2.1) was performed with a timestep  $\Delta t = 1 \text{ fs}$ . After an equilibration period of 1 ns, trajectories were propagated until local ergodicity was obtained, diagnosed using the decay of the Mountain-Thirumalai energy fluctuation metric.<sup>26,336</sup> The length of time simulated for each trajectory is shown in table 4.2.

Fig. 4.1 shows the temperature dependence of Si and O diffusion constants calculated using the Einstein formula, eq. (1.3). At lower temperatures,  $D(T)$  follows an Arrhenius relation  $D(T) = D_0 \exp(-E_A/k_B T)$ .  $E_A = 4.88 \text{ eV}$  for oxygen and  $E_A = 5.01 \text{ eV}$  for silicon, values which are in good agreement with other simulations of BKS silica, e.g. Horbach *et al.* (4.45 eV for oxygen and 4.9 eV for silicon)<sup>322</sup> and Saksangwongjit and Heuer (4.84 eV for oxygen).<sup>234</sup> Experimental measurements of diffusion coefficients in vitreous silica were reported by Mikkelsen<sup>337</sup> for oxygen atoms ( $E_A = 4.7 \text{ eV}$ ) and Brebec *et al.*<sup>338</sup> for silicon atoms ( $E_A = 6 \text{ eV}$ ).

At higher temperatures both silicon and oxygen diffusion constants show non-Arrhenius curvature, beginning at around 3600 K. This feature corresponds to the “strong-fragile crossover” described in §4.1. The crossover occurs at a slightly higher temperature in our model than in earlier work.<sup>234,319,322</sup>

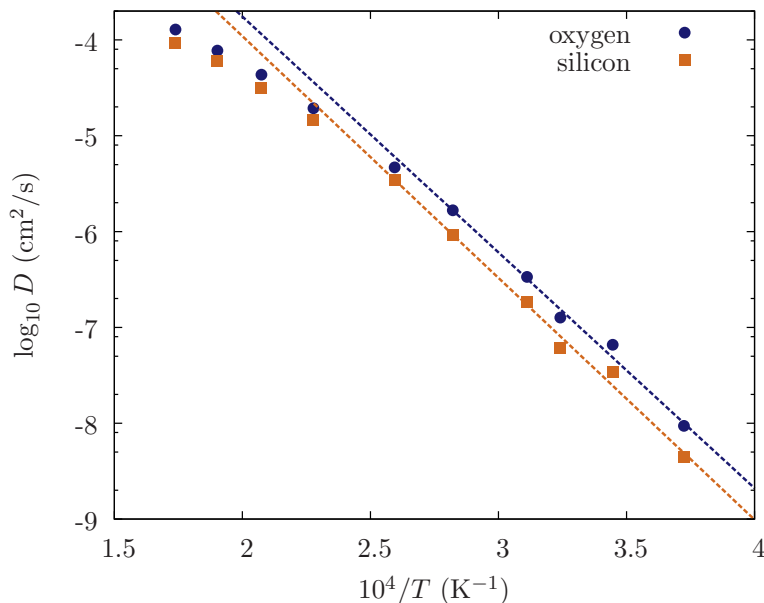


Figure 4.1: Translational diffusion constants  $D(T)$  for silicon and oxygen atoms. The dashed lines represent Arrhenius fits to the low temperature region of the data. This figure was prepared by Myra Biedermann.

### 4.3 Cage Breaking

The first objective in studying supercooled silica was to identify the dominant diffusive rearrangement mechanisms, analogous to cage breaks in OTP and BLJ. Silica is a network material, with strongly directional bonding and a much more open structure than BLJ and OTP: the fragile systems have many more nearest neighbours per atom compared to silica. Therefore there are no repulsive nearest-neighbour cages in silica,<sup>324</sup> but the restoring force exerted on each atom by the chemical bonds to its neighbours produces large energy barriers to particle motion and a cage-like effect in the mean square displacement.<sup>220</sup>

The geometric characteristics of bond-breaking transitions resemble cage breaks in BLJ: the nearest neighbours of the atom breaking its bond must change, and the bond-shifting event leaves behind a vacancy defect in the silica structure which can promote rapid reversal of the transition.<sup>220</sup> Therefore, chemical bonds act as attractive cages for the Si and O atoms. All of these arguments suggest that the BLJ cage break definition may provide a good description of the dynamics in silica as well. This proposal will now be investigated.

#### 4.3.1 Defining a “Cage Break” in Silica

The method of identifying cage breaks employed here is identical to that used for BLJ, but with a different choice of parameters. The parameterisation was performed

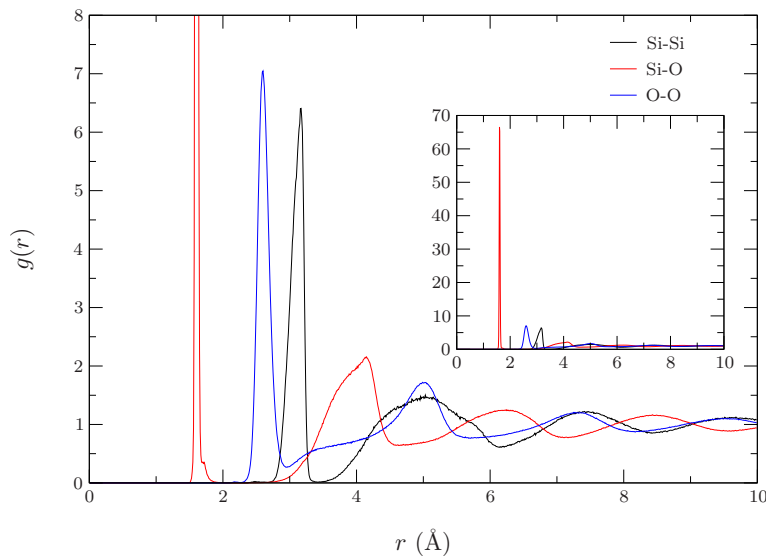


Figure 4.2: Radial distribution functions for Si-Si, Si-O and O-O pairs, calculated from quenched configurations of a trajectory that has been simulated at 3207 K. Consistency with higher temperature simulations has been verified. The inset represents the same plot with different axis scaling.

by Myra Biedermann.

Nearest neighbours of an atom are defined using a fixed cutoff distance  $r_{\text{NN}} = 1.95 \text{ \AA}$ . This is the position of the first minimum in the Si-O RDF (see fig. 4.2). Note that the electrostatic interaction ensures that the nearest neighbours of a Si atom will always be O atoms, and vice versa.

The displacement cutoff,  $d_c$ , was chosen as  $1.19 \text{ \AA}$ , the distance between the points where the first and second peaks in the Si-O RDF fall to 1% of their maximum height. Atoms moving by more than this distance are very likely to have made the jump from one neighbour shell to the next.

For BLJ systems, an atom must either lose or gain at least two neighbours to undergo a cage break. However, particles in BLJ have 11 nearest neighbours on average,<sup>233</sup> while in silica a silicon atom has four nearest neighbours and an oxygen atom has two. Therefore the BLJ parameter values would be overly restrictive. Instead, we require that a particle change at least half of its neighbours (adding losses and gains together) to be classified as cage-breaking. Two neighbour changes are required for a silicon atom to be categorized as cage-breaking, only one change is required for an oxygen atom.

Reversed cage breaks are identified using exactly the same method as for BLJ. For BLJ, the threshold displacement parameter  $d_{\text{rev}} = 10^{-5} \sigma_{\text{AA}}^2$ . However, the “cages” in silica are much less confined than those in BLJ, making it less likely that a reversed cage break will leave the atom close to its original position, so  $d_{\text{rev}}$  must be chosen

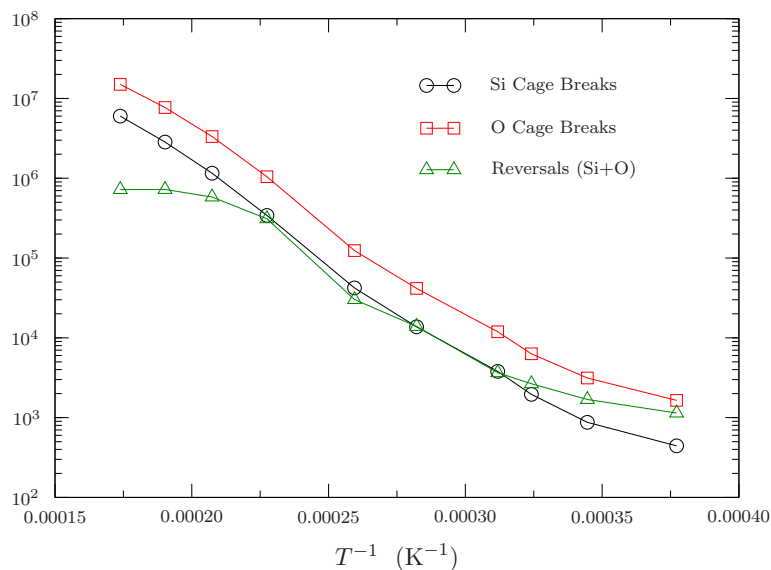


Figure 4.3: Number of cage breaks and reversals per ns of trajectory, as a function of temperature. The number of cage breaks is broken down into contributions from Si and O atoms; the number of reversed cage breaks combines Si and O.

larger relative to the natural distance unit. After some experimentation, we chose  $d_{\text{rev}} = 10^{-2} \text{ \AA}^2$ . Qualitatively similar results are obtained using any  $d_{\text{rev}} > 10^{-4} \text{ \AA}^2$ , but  $d_{\text{rev}} = 10^{-2} \text{ \AA}^2$  gives better quantitative agreement of the diffusion constants with the correct values.

### 4.3.2 Cage-Breaking Results

As before, the applicability of the cage-breaking method to silica was assessed by analysing inherent structure trajectories at a range of temperatures. Fig. 4.3 shows the number of cage breaks and reversals as a function of temperature. The number of cage breaks exhibits approximate Arrhenius temperature dependence, but the number of reversal events reaches a plateau near the temperature of the fragile-strong crossover. Above this temperature, the number of reversals becomes small compared to the number of cage breaks. The absolute number of reversal events decreases at lower temperatures, but the proportion of cage breaks that are reversed increases dramatically. Accounting for reversed cage breaks - and hence for reversals of particle velocity - will be important to describe the dynamics of silica in the same way that it was for BLJ and OTP.

Cage-breaking diffusion constants and productive diffusion constants  $D_{\text{CB}}(T)$  and  $D_{\text{prod}}(T)$  were computed using eqs. (1.18) and (3.2) respectively. We follow convention by treating the diffusion of Si and O atoms separately. The results for silicon are shown in fig. 4.4.

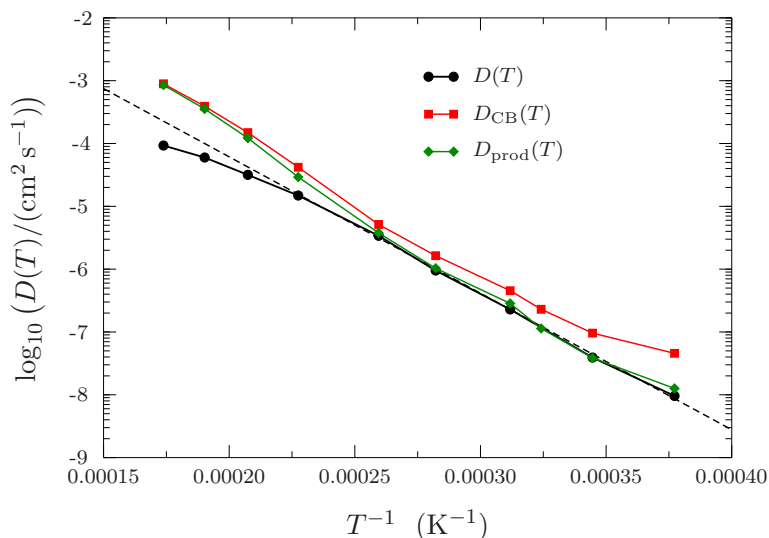


Figure 4.4: Cage-breaking diffusion constants for silicon atoms in silica. Long-time diffusion constants  $D(T)$  are shown for comparison. The dashed line represents an Arrhenius fit to  $D(T)$ . The corresponding graph for O is very similar, so it is omitted.

$D_{\text{CB}}(T)$  has broadly Arrhenius temperature dependence, and overestimates the true diffusion constants across the entire temperature range.  $D_{\text{prod}}(T)$  (with reversed CBs excluded) has better agreement with  $D(T)$  in the strong regime below 3600 K. At high temperatures,  $D_{\text{prod}}(T) \approx D_{\text{CB}}(T)$  because only a small fraction of cage breaks are reversed at temperatures higher than 4000 K (see fig. 4.3). Moreover,  $D_{\text{prod}}(T) \gg D(T)$  above  $T = T_c$ .

Fig. 4.4 demonstrates that productive cage breaks correctly reproduce translational motion in the strong temperature regime for liquid silica. This result shows that our definition of cage breaks successfully captures the bond- and defect-migration processes that dominate diffusive behaviour in silica.

Negatively correlated motion, here represented by reversed cage breaks, is more significant at low temperatures than high, because at higher temperatures the system has more energy and can access more rearrangement paths, so reversals are much less likely. It was previously shown<sup>233,254,255</sup> (see §1.7) that the same correlation effect occurs in BLJ, and that this effect is responsible for super-Arrhenius behaviour in that system. Therefore it is surprising that negative correlation must also be taken into account in silica, to predict diffusive behaviour in a temperature range where there is no super-Arrhenius curvature. The role of negative correlation in diffusion behaviour of strong and fragile systems will be discussed further in chapter 6.

The results in this section demonstrate the qualitative difference between the super-Arrhenius behaviour in BLJ (caused by negative correlations) and the non-Arrhenius curvature in silica at high temperatures, for which no significant negative

correlation effect is present. Therefore the description of the high-temperature behaviour in silica as “fragile” is open to question.

For silica, as for BLJ and OTP,<sup>233,308</sup> diffusion constants calculated from cage breaks significantly overestimate the correct values at higher temperatures. This is because the basins of attraction explored at high temperatures become increasingly anharmonic and atoms wander further away from the local minima.<sup>226,339</sup> Therefore, the use of quenched trajectories to calculate diffusion constants becomes invalid at high temperatures.

#### 4.3.2.1 Reversed Cage Breaks

We have so far incorporated correlation effects into the cage-breaking model by restricting the calculation of diffusion constants to productive cage breaks. Alternatively, correlations may be treated in a “mean-field” approach, by applying a correction factor to the cage-breaking mean squared displacement. This correction factor depends upon the proportion of directly reversed cage breaks.

The *correction sum* (originally developed to study BLJ)<sup>233</sup> is calculated using the reversal chains of a quenched trajectory:

$$c_s = \sum_v \sum_{z=1}^{l_v} \frac{(-1)^z \sum_i n_i^v(z)}{\sum_i M_i}, \quad (4.6)$$

where  $v$  is an index running over all reversal chains in the trajectory and  $M_i$  is the number of cage-breaking events for atom  $i$ .  $l_v$  is the number of reversals in chain  $v$  and  $n_i^v(z) = l_v - z + 1$  is the number of reversals after and including the  $z^{\text{th}}$ .

To use the correction sum, we make the approximation that all cage breaks have squared displacement equal to the average value,  $L$ . The total squared displacement due to cage breaks is then given by:<sup>233</sup>

$$\langle \mathbf{r}^2 \rangle = \sum_i M_i L (1 + 2c_s), \quad \text{so} \quad (4.7)$$

$$D_{\text{CB}}^*(T) = D_{\text{CB}}(T)(1 + 2c_s) \quad (4.8)$$

We assume that  $M_i = \langle M_i \rangle$  for all atoms.

Fig. 4.5 shows that application of the correction term in eq. (4.8) yields effective diffusion constants  $D_{\text{CB}}^*(T)$  that match  $D_{\text{prod}}(T)$  very well. The results for oxygen are similar and so they are omitted for brevity.

The correction sum is expected to work well when the assumptions of constant cage-breaking squared displacement  $L$  and uniform  $M_i = \langle M_i \rangle$  are valid. Fig. 4.6

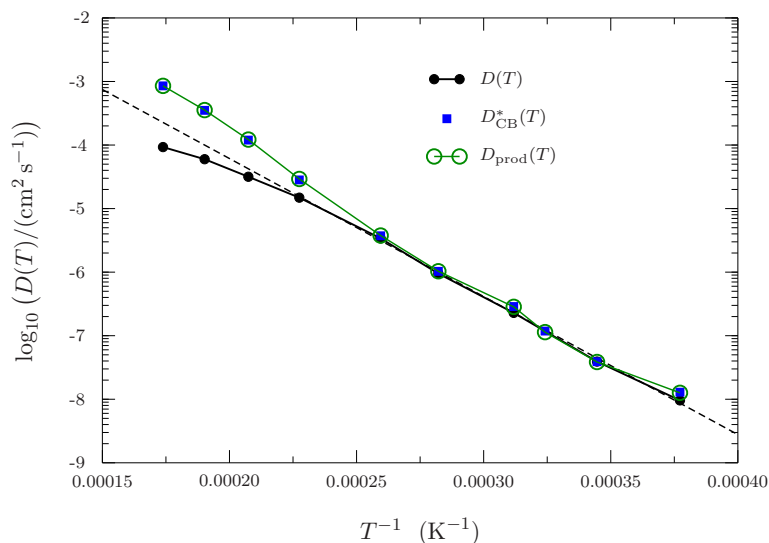


Figure 4.5: Diffusion constants of silicon atoms in silica, calculated from the mean square displacements of all cage breaks corrected with the correlation sum  $c_s$  and from productive cage breaks. The correct diffusion constants obtained from MD are shown for comparison. The dashed line represents an Arrhenius fit to the MD data.

shows the average square displacement of a particle undergoing a cage break as a function of temperature. The standard errors in this average are small relative to the size of the jump, which justifies the assumption of constant  $L$  at fixed temperature.

The temperature dependence of the jump widths is the first quantity in which we have observed a qualitative difference between the oxygen and silicon atoms. In the high- $T$  non-Arrhenius regime, jump width decreases with temperature for both atom types, probably due to the breakdown of the assumption that the system is localised near potential energy minima. In the strong temperature regime, the oxygen jump widths continue to decrease with temperature while the values for silicon remain fairly constant.

Horbach and Kob<sup>220</sup> also found a difference between oxygen and silicon dynamics. They found that the temperature dependence of oxygen diffusion followed the bond lifetime, but silicon diffusion slowed down more quickly. Saksengwitt and Heuer observed a similar effect, by calculating the average mean-square displacement after a large number of energy metabasin transitions.<sup>334</sup> This quantity is temperature independent for O but not Si.

All of these observations may be evidence that dynamics of oxygen ions are more cooperative (or at least, more correlated) than those of silicon.<sup>120,125</sup> Alternatively, there is evidence that rotational processes contribute to the long-range dynamics for oxygen but not for the silicon atoms, and that these processes become more relevant at lower temperatures.<sup>334</sup> A *rotational process* refers to a permutational

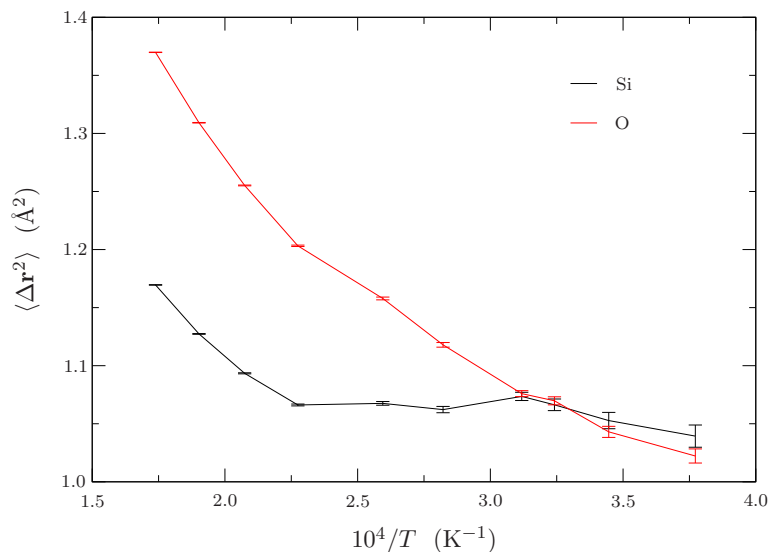


Figure 4.6: Average square displacement in cage-breaking rearrangements for different atom types, as a function of inverse temperature. Error bars indicate the standard error in the mean square displacement.

rearrangement, where two O atoms in an  $\text{SiO}_2$  tetrahedron swap places. These rearrangements do not change the total energy, but do involve crossing an energy barrier comparable to a bond-breaking rearrangement.

An idealised rotational process involves a change of Si-O neighbours, and so is treated as a cage break by the definition used in this chapter. The corresponding jump width will be small compared with a translational cage break. If a greater fraction of the oxygen cage breaks at lower temperature are rotational processes, the observed decrease in average jump width is explained.

## 4.4 Potential Energy Landscape Analysis

The PEL of silica was sampled using the inherent trajectory method (§2.2.3). The initial set of minima were extracted at intervals of 100 fs from a quenched MD trajectory with temperature 3207 K. This temperature was chosen because it lies well within the strong regime, but high enough that a moderate simulation length is sufficient to reach local ergodicity.

The OPTIM calculations to determine discrete paths between pairs of minima were run by Myra Biedermann. I performed the subsequent analysis of the landscape and prepared all the figures.

### 4.4.1 Disconnectivity Graph for Silica

Fig. 4.7 shows the disconnectivity graph for BKS silica. It is very similar to the equivalent graph for OTP, fig. 3.7. As expected, the landscape is highly frustrated, with a wide range of minimum energies and barrier heights, and no crystal region. Higher order structure is evident in the form of local funnels.

Kushima *et al.* have previously reported a disconnectivity graph for silica,<sup>285</sup> which is qualitatively different to fig. 4.7: their graph appears to contain only a single global funnel. This discrepancy is probably because the autonomous basin climbing (ABC) algorithm used by Kushima *et al.*<sup>340</sup> explores the landscape in the vicinity of its starting point in detail. In contrast, fig. 4.7 represents a locally ergodic sample of the entire amorphous configuration space. Moreover, the stationary point database obtained by Kushima *et al.* contains far fewer minima and transition states than the one presented here, which changes the appearance of the graph.

### 4.4.2 Cage-Breaking Analysis of the Landscape

We analyse the role of cage-breaking rearrangements on the silica landscape using the same approach as for BLJ and OTP. Each transition state in the landscape database is classified as cage-breaking or non-cage-breaking, according to whether any atoms undergo a cage break between the two minima connected by this TS.

We visualise the importance of cage breaks in the same way as before, by removing from the disconnectivity graph all transition states corresponding to cage-breaking TSs and observing the resulting fragmented graph fig. 4.8. This graph contains many very small fragments, often containing only two minima. Most local funnels are divided into multiple fragments, which means that cage-breaking transitions are required even to explore minima within a funnel on the silica landscape.

In contrast, the disconnectivity graph produced by excluding all non-cage-breaking TSs is almost indistinguishable from the complete disconnectivity graph in fig. 4.7, so it is not shown here. Removing non-cage-breaking transition states does not significantly affect the connectivity of the landscape, indicating that cage-breaking rearrangements are sufficient to access all regions of the PEL.

These results are qualitatively similar to those for fragile glass formers, but the silica landscape becomes almost completely disconnected on removal of the cage-breaking transition states, whereas the BLJ and OTP landscapes do not. Therefore cage-breaking motion is even more important for diffusion in silica than in BLJ. This importance is not surprising because, as argued in §4.3.2, cage breaks capture diffusive bond-breaking processes in silica very effectively.

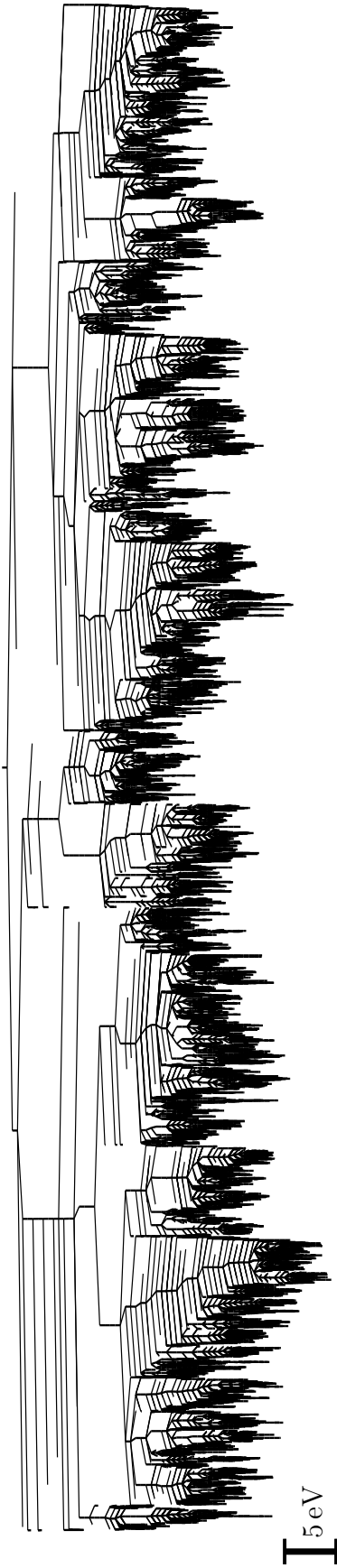


Figure 4.7: Disconnectivity graph for liquid silica. The minima and transition states in this graph have been found by connecting each pair of adjacent minima in a quenched MD trajectory computed at 3207 K.

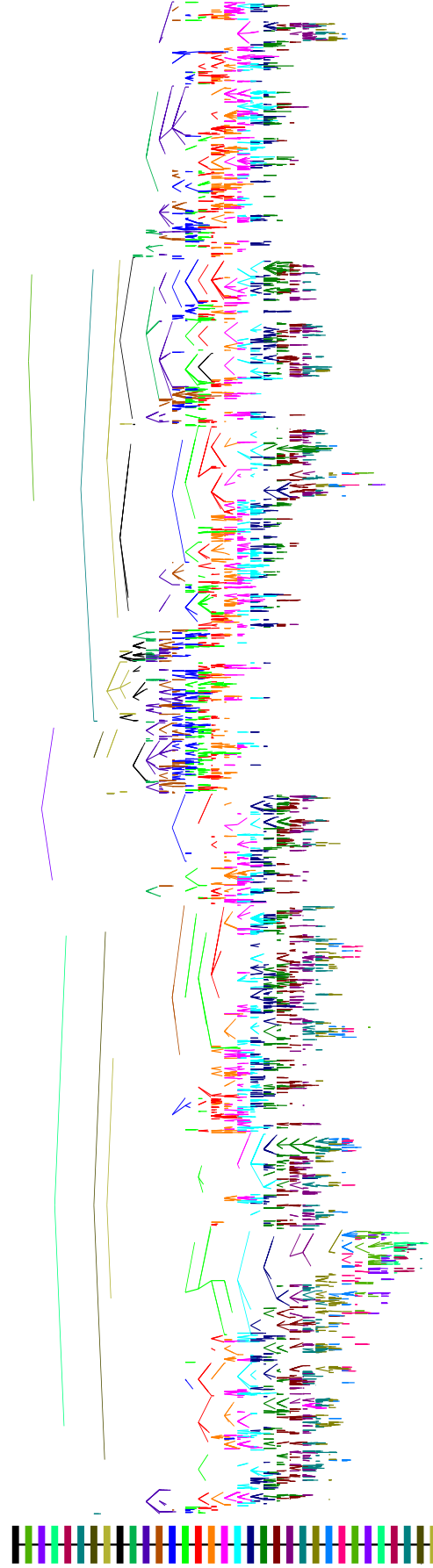


Figure 4.8: Disconnectivity graph for silica with cage-breaking transition states removed. Branches are coloured according to the energy level at which they become disconnected from the rest of the graph. The colour associated with each energy level is indicated by the scale on the left. All fragments at a particular energy level are coloured the same, which is why bands of colour appear to run across the graph despite the presence of many fragments at each energy level. The separation of the energy levels is 1 eV.

### 4.4.3 Geometric Metabasin Analysis

In this section, the cage-breaking definition of metabasins is applied to the silica landscape. Productive cage breaks, which are unreversed and essentially uncorrelated,<sup>233</sup> are equated with metabasin transitions.

A connected path of minima and transition states was constructed, as in §3.4.1. Cage breaks and reversals in this path were identified, and TSs were classified as productive if they contained any productive cage breaks, or unproductive if they did not.

To identify reversed cage breaks using a constant  $d_{\text{rev}}$ , the atomic coordinates for each pair of minima must be consistently aligned with respect to global symmetries (translations and permutations) before checking for cage breaks. This alignment was performed using the recently-developed FASTOVERLAP method.<sup>341</sup> FASTOVERLAP represents each input structure as a sum of Gaussian functions centred on the atomic positions, and identifies the global translation that maximises the overlap between the two representations by analysing their Fourier coefficients. This approach provides an efficient route to translational alignment that is independent of permutational symmetry. Once each pair of minima is correctly aligned, reversed CBs are easily identified.

Productive cage breaks are analogous to metabasin transition events, so removing productive transition states from a disconnectivity graph reveals fragments which correspond to geometric metabasins. Fig. 4.9 shows these metabasins for silica, and fig. 4.10 shows a disconnectivity graph for the BLJ fluid produced in exactly the same way, for comparison. See §4.5 for details of the BLJ system used.

Fig. 4.9 is less fragmented than fig. 4.8, because reversed cage-breaking transition states have been restored to the graph. However, fig. 4.9 is still highly fragmented and contains few clearly-defined metabasins. The metabasins for silica contain very few minima compared to BLJ and incorporate fewer high-energy transition states.

A significant number of reversed CBs were detected, which indicates that geometric metabasins do exist in the landscape of silica (and presumably other strong liquids). This finding contradicts Stillinger’s picture of glassy landscapes,<sup>27,221</sup> but agrees with the results of Heuer *et al.*<sup>215,234,334</sup> The metabasins of silica are significantly smaller than those of fragile liquids, and may be less important for the overall dynamics. The decreased metabasin size also indicates reduced importance of reversed CBs relative to BLJ and OTP, which is explored further in chapter 6.

It should be noted that there are two important variables that control reversal probability and hence metabasin size, which may account for some of the difference between figs. 4.9 and 4.10. These variables are effective temperature and system size.

To compare landscapes between different supercooled liquids, one should probably choose inherent trajectory temperatures at the onset of the landscape-dominated regime. We have used  $T_c$  as a proxy for this temperature. System size (which determines the frequency of metabasin transitions in both the EMB and geometric MB definitions) is harder to control for. We have attempted to do this by scaling the number of minima in the BLJ disconnectivity graph. However, the possible impact of temperature and system size on our results should be investigated more closely in future work.

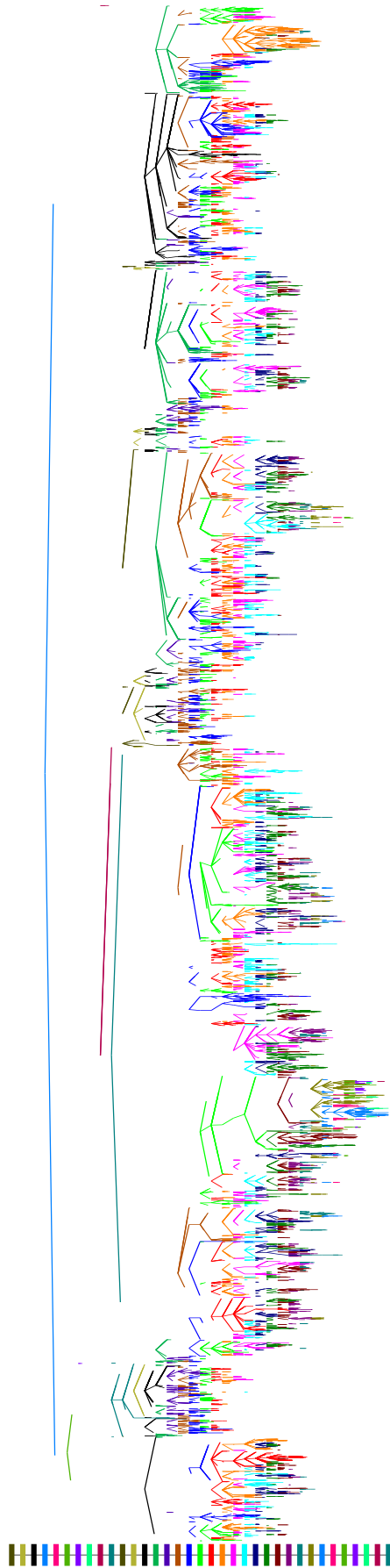


Figure 4.9: Disconnectivity graph showing geometric metabasins for silica. All transition states associated with a productive cage break have been excluded. The colour scheme is the same as fig. 4.8. The separation of the energy levels is 1 eV.

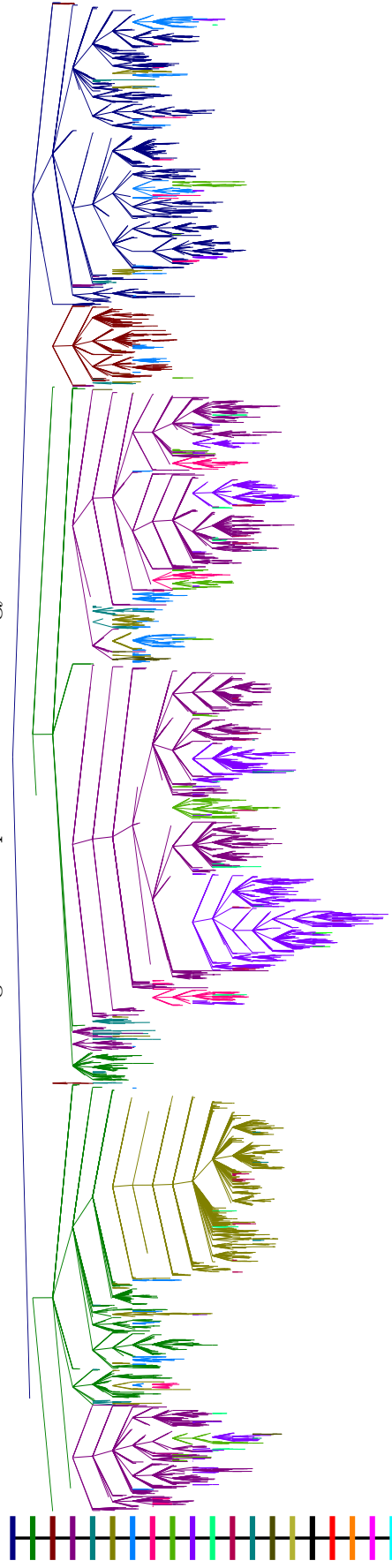


Figure 4.10: Excerpt from a larger disconnectivity graph showing geometric metabasins for the BLJ liquid. Productive cage-breaking transition states have been excluded. The colour scheme is the same as fig. 4.8. The separation of the energy levels is  $2\epsilon_{AA}$ . Fig. 4.9 contains 22995 minima so this figure is restricted to showing  $22995 \times 256/555 = 10606$  minima (rescaling according to the system size). The disconnectivity graph for the entire database is qualitatively identical.

## 4.5 Energy Landscapes for Different Classes of Glass Former

In this section, some simple global properties of the landscapes of strong (silica) and fragile (BLJ) liquids are compared. The BLJ parameter set corresponds to the popular Kob-Andersen model<sup>10</sup> and the system was studied at a density of  $1.3\sigma_{AA}^{-3}$ , with a simulation box containing 256 atoms (204 of type A, 52 of type B).

The inherent structure sampling approach was used for both systems. The silica database in §4.4 was obtained from a trajectory at 3207 K, near the mode coupling critical temperature for this system ( $T_c \approx 3330$  K).<sup>220</sup> To give the most accurate possible comparison we sampled the BLJ landscape using a trajectory at  $T = 0.65\epsilon_{AA}/k_B$ , close to the fitted value of the mode-coupling temperature for this density,  $T_c = 0.66\epsilon_{AA}/k_B$ .<sup>342</sup> The MD time step was  $0.005(m\sigma_{AA}^2/\epsilon_{AA})^{1/2}$  and the simulation was run for  $5 \times 10^5(m\sigma_{AA}^2/\epsilon_{AA})^{1/2}$  to reach local ergodicity.

Different trajectory lengths were required to reach local ergodicity for the two systems, so the two databases contained very different numbers of stationary points. The silica database contained 22995 minima and 24237 transition states, while the BLJ database contained 152913 minima and 184648 transition states. However, since both databases were constructed from a locally ergodic MD trajectory they should each provide a faithful representation of the region of configuration space explored by the liquid.

### 4.5.1 Simple Landscape Metrics

Fig. 4.11 shows normalised distributions of the minima energies in the silica and BLJ databases. Energies are expressed relative to the lowest-energy minimum in the corresponding database, in units of  $k_B T$ . Both distributions are approximately Gaussian, as expected.<sup>215</sup>

The BLJ database has a larger mean and standard deviation of minimum energies than the silica database, which may indicate a higher effective temperature relative to the landscape-dominated regime. Moreover, the BLJ distribution deviates more from Gaussian behaviour than does the silica distribution, exhibiting slight positive skew and a non-Gaussian tail at the low-energy end.

Saksaengwijit *et al.* have argued for the existence of a cutoff in the distribution of minima energies for strong liquids, below which there exist many fewer states than the Gaussian distribution would predict.<sup>215</sup> We do not see such a cutoff in fig. 4.11 because the system is too large and probably contains multiple weakly-interacting subsystems: the effect of the cutoff in each subsystem is smeared out when they are

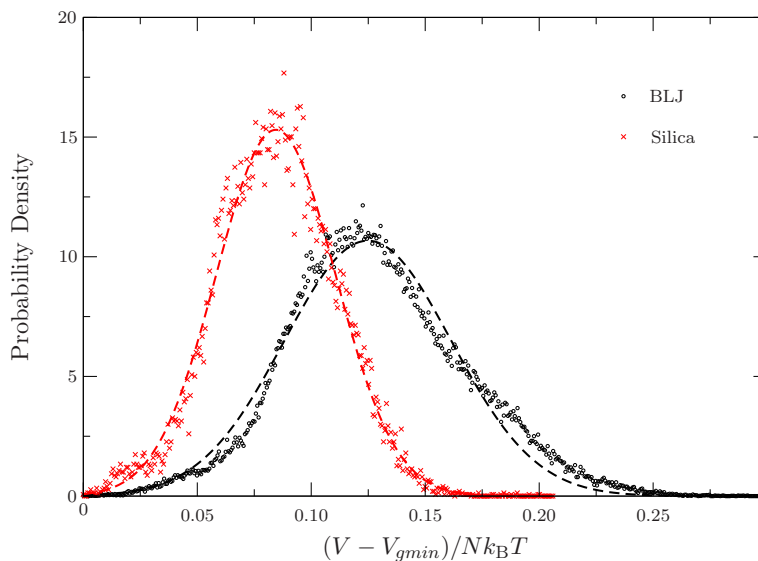
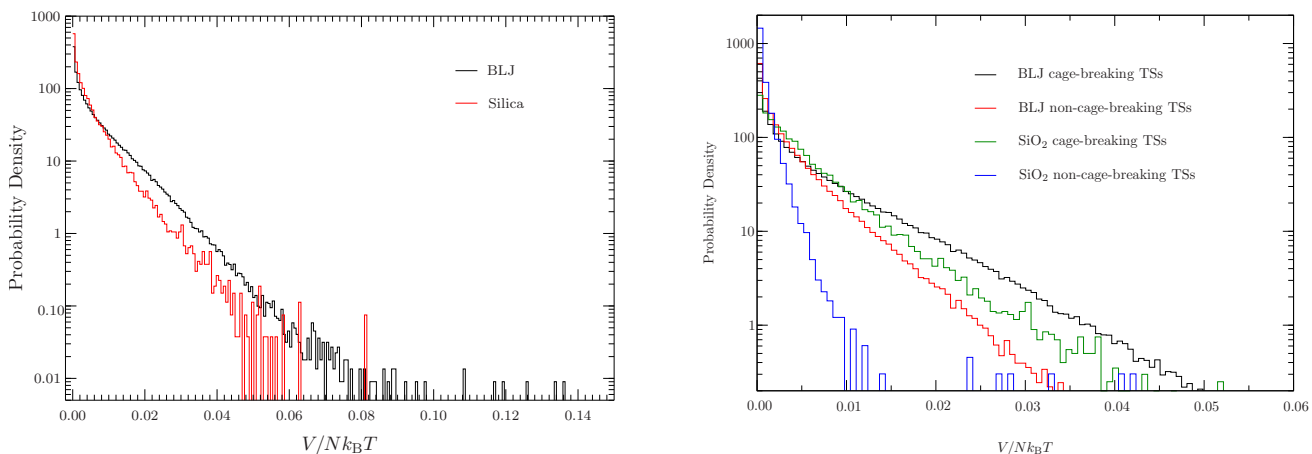


Figure 4.11: Normalised distributions of the energies of minima in the landscape databases for BLJ and silica. Energies are expressed relative to the global minimum energy in each case, and are given in units of  $k_B T$  per particle to allow comparison between the different systems. Dashed lines show Gaussian fits to the distributions of the corresponding colour.

combined.<sup>215</sup> However, the silica distribution in fig. 4.11 has a smaller low-energy tail than the BLJ distribution, which may be a signature of the low-energy cutoff in these larger systems.

Fig. 4.12a shows normalised histograms of the energy barrier heights in the two databases, with the same energy scaling as before. Recall that barrier heights are defined as the energy difference between a minimum and an adjacent transition state. Both histograms show an exponential decrease in probability density with increasing barrier height, with a super-exponential excess of small energy barriers. Although the two systems have comparable temperatures, the distribution of energy barriers sampled by the BLJ fluid is slightly wider than that encountered by silica. High barriers correspond to inter-funnel transitions, so this result indicates deeper funnels and hence larger metabasins on the BLJ landscape.

In fig. 4.12b, the barrier height distributions are decomposed into separate histograms for cage-breaking and non-cage-breaking transition states using the definition described in §4.3.1. As expected, cage-breaking barriers are generally higher than non-cage-breaking. The difference between characteristic barrier heights for cage-breaking and non-cage-breaking processes is much greater for silica than for BLJ. This result quantifies the earlier statement that cage-breaking rearrangements dominate the high-barrier processes more in silica than in BLJ. It is plausible that this represents a general difference between strong and fragile glass formers: fragile liquids exhibit a significant amount of intra-cage motion alongside cage-breaks,



(a) Normalised histograms of the elementary barrier heights in the landscape databases for BLJ and silica. Barriers are expressed in units of  $k_B T$  per particle to allow comparison between the different systems.

(b) Normalised histograms of the elementary energy barrier heights corresponding to CB and non-CB transitions in BLJ and silica. The histograms are truncated at low probabilities to mitigate the difference in resolution arising from the different database sizes.

Figure 4.12

whereas cage breaks account for nearly all particle motion in strong liquids.

### 4.5.2 Frustration Metric

The frustration metric introduced in §2.2.4.1 is used to compare the organisation of the PELs in BLJ and silica. Recall that high frustration indicates the presence of many competing low-lying minima separated by high barriers. The frustration metric facilitates comparison of PELs for very different systems.

The true global minimum of a glass former is the crystal structure, which is excluded from our databases. Hence the frustration index expresses the ability of the system to locate the lowest-energy amorphous minimum in the database.

Fig. 4.13 presents the frustration index  $f(T)$  for the two systems. As temperature decreases, the ability to cross high barriers decreases and frustration increases. A feature of  $f(T)$  is that the occupation probability of the global minimum dominates the frustration calculation at very low temperatures, causing  $f(T)$  to decrease. This behaviour is irrelevant to the present discussion, because the corresponding temperatures are too low to be accessed by equilibrium simulation.

Both liquids have values of  $f(T)$  in the range typical of multi-funnel energy landscapes,<sup>246</sup> as expected for glass formers. The silica database falls near the bottom of the range in  $f(T)$  expected for multi-funnel landscapes, and is less frustrated than the BLJ database at all temperatures. This difference is consistent with the notion

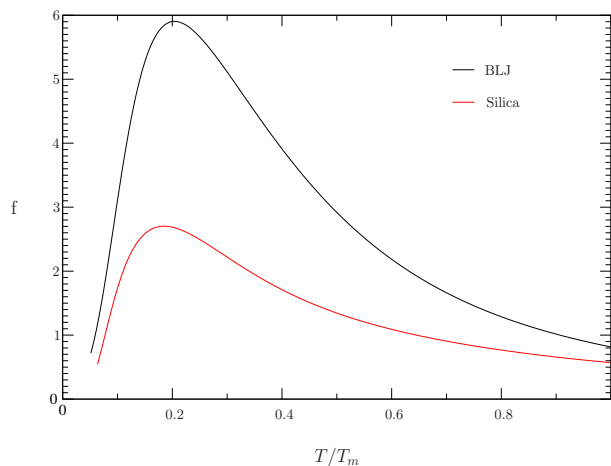


Figure 4.13: Frustration index<sup>246</sup> for BLJ and silica as a function of  $T/T_m$ .  $T_m$  is the melting temperature determined from a peak in the constant volume heat capacity calculated using the harmonic superposition approximation.<sup>4</sup>

that landscapes of fragile glass formers are dominated by large metabasins (which would promote high frustration) while strong glass formers have a more uniform organisation with small metabasins and less frustration.<sup>221</sup>

The disconnectivity graphs of §4.4 and all the landscape metrics studied in this section show that there is no major qualitative difference between the landscapes of silica and BLJ, but that the latter system has larger metabasins and a wider range of barrier heights. The metabasin disconnectivity graph and the frustration index provide the clearest evidence for a difference between two PELs, probably because these are the only two measures we have considered that account for the structure and connectivity of the landscape.

## 4.6 Conclusions

The diffusive behaviour of the BKS model for viscous silica has been studied, using a number of analytical techniques developed previously for fragile glass formers. This model was compared semi-quantitatively with the fragile BLJ fluid.

Silica and BLJ have many dynamical features in common. In both cases, low-temperature diffusion is dominated by hopping events, which we have identified in both systems using a simple definition of cage-breaking rearrangements. Cage breaks become increasingly negatively correlated at low temperatures. Both systems have highly frustrated energy landscapes and, contrary to some expectations, there is no clear structural difference between these landscapes. However, hierarchical organisation of minima appears to be more pronounced in BLJ than in silica.

The differences between strong and fragile glass formers are evidently quite sub-

tle, arising from PEL structure that controls the correlation of cage-breaking jumps. Their contrasting dynamics probably represent two extremes of a single mechanism rather than two fundamentally different processes, so that strong glass formers represent one end of a continuous spectrum of fragilities.<sup>124,125,235,236</sup>

Bond-breaking and forming processes that dominate long-time diffusion in silica below  $T_c$  are accurately described by the same definition of cage-breaking rearrangements that describes diffusion in the BLJ liquid, even though cages in silica are attractive rather than repulsive in origin, and are much more sparse than the cages in BLJ.

The cage-breaking method is very successful in the strong temperature regime of silica. At higher temperatures, the system wanders further from the bottom of the potential energy wells,<sup>226</sup> and cage breaks fail to reproduce the correct diffusion constants. This failure occurs close to the temperature at which non-Arrhenius behaviour emerges in the diffusion constants. Establishing whether these two phenomena are linked might help to explain the origin of the fragile-strong crossover.

The potential energy landscape of silica becomes almost completely disconnected when cage-breaking transition states are removed, but is unaffected when non-cage breaks are removed. Therefore cage-breaking rearrangements are both necessary and sufficient to traverse the energy landscape, and are required for all dynamical processes, including exploration of minima within a local funnel. Moreover, the separation of energy scales between cage-breaking and non-cage-breaking energy barriers is greater for silica than for BLJ. Both these results show that diffusive motion is dominated by cage breaks to a much greater extent in silica than in BLJ.

Geometrical metabasins for silica contain fewer minima than those for BLJ. This observation is in line with previous predictions regarding the difference between the energy landscapes of strong and fragile liquids.<sup>27,221</sup> Transitions between metabasins correspond to an uncorrelated random-walk process, so correlation only exists within a metabasin and hence smaller metabasins mean less correlation in minimum-to-minimum transitions, which helps to explain the lack of super-Arrhenius behaviour in the strong liquid.

Finally, we found that the PEL of silica is less frustrated than that of BLJ. This was shown by a frustration metric that measures the relative height of energy barriers between minima of similar energies. We note that the two measures which distinguish most clearly between strong and fragile landscapes (i.e. metabasins and the frustration metric) are those that take greatest account of the connectivity and topology. Connectivity of the PEL is likely to be crucial in understanding the origins of cage-breaking and negative correlation behaviour in glass formers.<sup>256</sup>

## Chapter 5

# Random Particle Pinning on the Potential Energy Landscape

In §1.5, the method of random pinning was introduced as a theoretical tool to test certain predictions of the RFOT theory. The key idea underlying this approach is that pinning a critical fraction  $c \geq c^*(T)$  of the particles in a supercooled liquid may induce a thermodynamic phase transition at which the complexity vanishes, and that this transition is analogous to the ideal glass transition predicted for unpinned glass formers.

This scenario is analytically provable in mean-field models<sup>175</sup> but efforts are ongoing to determine whether the same picture holds for finite-dimensional glass formers.<sup>182,183,343</sup> If the random pinning glass transition (RPGT) is indeed related to a vanishing complexity, one must still prove that this scenario can be extrapolated reliably to the  $c = 0$  case in order to establish the existence of an equilibrium ideal glass transition.

The RPGT has received a lot of attention in recent years. However, the effect of pinning on the PEL of a system has only been considered briefly,<sup>182</sup> in the context of the “saddle point method” which does not provide an accurate description of landscape structure (see §1.6.2.6). In this chapter, I use geometry optimisation techniques to describe the dramatic changes in landscape structure when some particles are pinned. I propose a new approach for identifying hierarchical structure in the PEL of a glass former, which arises naturally from the RFOT description of pinned liquids. This approach complements the dynamical metabasin methods outlined in the previous two chapters and in §1.6.2.3.

The PEL exhibits several signatures of an entropy-diminishing event that coincides quite closely with previously reported values of  $c^*$ .<sup>182</sup> Although the methods used here are not sufficient to determine whether this event is a thermodynamic

Table 5.1: Parameters for the BLJ potential with Stoddard-Ford cutoff. Different columns indicate different atom types  $\mu$  and  $\nu$ .

Parameter	A-A	A-B	B-B
$\sigma_{\mu\nu}$	1.0	0.8	0.88
$\epsilon_{\mu\nu}$	1.0	1.5	0.5
$r_{c,\mu\nu}$	2.5	2.0	2.2

transition or a smooth crossover, I discuss possible approaches that might answer this question using PEL theory.

The ordering of this chapter is as follows. §5.1 introduces the model system, as well as the tools and concepts used to analyse that model. In §5.2, I show how the distribution of PEL minima changes with pinning fraction, and provide evidence that the number of local funnels accessible to the system decreases strongly as a function of pinning. §5.3 analyses the influence of pinning on the organisation of the landscape more systematically, revealing that high pinning fractions cause the landscape to become less frustrated and less glassy. In §5.4 the mechanism for this change is discussed at the level of local funnels and of individual minima.

## 5.1 Methods

### 5.1.1 Model

This chapter studies the effect of pinning on a binary Lennard-Jones (BLJ) fluid<sup>10</sup> which is identical to the model used by de Souza and Wales to study diffusion dynamics and cage breaking (§1.7). This choice of system allows comparison with many earlier simulation studies, including studies of the RPGT,<sup>170,182,183</sup> and with the earlier work detailed in §1.7 and chapters 3 and 4.

The BLJ fluid is an 80:20 mixture of large A atoms and small B atoms, interacting via the pairwise Lennard-Jones potential with a Stoddard-Ford quadratic cutoff, eq. (3.1). Interaction parameters are given in table 5.1. Throughout this chapter the system contains  $N = 256$  atoms in a cubic unit cell under periodic boundary conditions, with fixed number density  $1.2\sigma_{AA}^{-3}$ .

### 5.1.2 Pinning Particles

Following earlier work,<sup>175,182</sup> atoms are pinned at the positions they occupy in a “reference structure”,  $\mathbf{X}^*$ . This structure is sampled from a locally ergodic micro-canonical MD trajectory of the unpinned system at temperature  $T_0$ . This procedure

ensures that the configurations sampled after pinning represent an equilibrium distribution for the pinned system.<sup>171,175,344</sup> Local equilibration is confirmed using the Mountain-Thirumalai fluctuation metric, as before. The variance of the instantaneous temperature in the microcanonical simulations is small.

Once  $\mathbf{X}^*$  has been obtained, a number  $M = \lfloor cN \rfloor$  atoms are chosen at random, and their positions are fixed (pinned). The notation  $\lfloor x \rfloor$  indicates the largest integer less than or equal to  $x$ . Each set of  $M$  pinned atoms, combined with a reference structure  $\mathbf{X}^*$ , defines a single *realisation of the disorder* in the pinned system (or *disorder realisation*, for brevity).

Pinned atoms continue to affect  $V(\mathbf{X})$  and to exert forces on other atoms, but forces acting on pinned atoms do not contribute to  $\mathbf{g}(\mathbf{X})$  or  $\mathbf{H}(\mathbf{X})$ . Each disorder realisation uniquely corresponds to an external potential applied to the mobile atoms, and so each disorder realisation has a unique PEL associated with it. To obtain robust quantitative results, one should average over these realisations, but to understand the changes to the PEL each realisation must be considered separately.

Consider a landscape with  $M$  pinned atoms, and then unpin a single atom. The dimensionality of the landscape increases by three, and the original PEL is now a subspace embedded within the new landscape. Configurations that were minima of the old landscape are unlikely also to be minima of the new landscape, but nevertheless the two PELs are much more similar than if we had selected two disorder realisations at random. To study a range of  $c$  values, we have usually generated a single disorder realisation at high  $c$  and then progressively unpinned atoms.

It is important to distinguish between  $\mathbf{X}^*$ , selected directly from the locally equilibrated MD trajectory, and the reference minimum  $\mathbf{X}_0$ , which is obtained by local geometry optimisation of  $\mathbf{X}^*$  with the pinning constraints in place.

### 5.1.3 Comparing Structures

In the following sections it will prove necessary to define a measure of similarity between two configurations  $\mathbf{X}_i$  and  $\mathbf{X}_j$  (which are usually local minima). We borrow the concept of *overlap*, which is used as an order parameter in mean field theories of glassy behaviour. Following previous work,<sup>173,178,182,345</sup> we define:

$$Q(\mathbf{X}_i, \mathbf{X}_j) = \frac{1}{N_m} \sum_{k=1}^{N_m} \theta(a - |\mathbf{r}_{k,i} - \mathbf{r}_{k,j}|). \quad (5.1)$$

Here,  $k$  runs over the set of  $N_m$  unpinned A-type atoms.  $\theta$  is the Heaviside step function, and  $\mathbf{r}_{k,i}$  is the position vector of atom  $k$  in configuration  $\mathbf{X}_i$ .  $a$  is a length scale parameter, which we set to  $0.3\sigma_{AA}$  following earlier work.<sup>72,178,182,183,345</sup>

Before calculating the overlap,  $\mathbf{X}_i$  and  $\mathbf{X}_j$  are aligned with respect to their permutational symmetries using the shortest augmenting path algorithm.<sup>346,347</sup> This alignment ensures that the shortest distance  $|\mathbf{r}_{k,i} - \mathbf{r}_{k,j}|$  is used, accounting for indistinguishability of mobile A atoms.

$Q(\mathbf{X}_i, \mathbf{X}_j)$  counts the fraction of atoms that have approximately the same position in configurations  $i$  and  $j$ . If  $Q(\mathbf{X}_i, \mathbf{X}_j) > 0.7$ , we describe  $\mathbf{X}_i$  and  $\mathbf{X}_j$  as being structurally similar, and if  $Q(\mathbf{X}_i, \mathbf{X}_j) < 0.7$  they are structurally distinct. The threshold parameter  $Q^*(\mathbf{X}_i, \mathbf{X}_j) = 0.7$  corresponds to the typical value of  $Q$  at the caging plateau,<sup>348</sup> and also falls in the gap between the high- and low- $Q$  states of the BLJ system reported in earlier work.<sup>182,349</sup>

Eq. (5.1) will most often be used to compute the overlap of a local minimum with the reference minimum  $\mathbf{X}_0$ . This quantity is denoted

$$Q_0(\mathbf{X}) = Q(\mathbf{X}, \mathbf{X}_0), \quad (5.2)$$

or simply  $Q_0$ , for brevity.

### 5.1.4 Metastable States

Some thermodynamic theories of the glass transition predict an entropy-vanishing ideal glass transition at the Kauzmann temperature,  $T_K$ . In §1.4.1, it was explained that the entropy contribution that vanishes in this hypothetical event is actually the complexity,  $\Sigma(T)$ , related to the number of metastable states (in mean-field models) or quasistates (in finite-dimensional models). By analogy with the ideal glass transition,  $\Sigma(T, c)$  should also vanish at the RPGT. Recall that  $\Sigma$  is often referred to in the glasses literature as the “configurational entropy”,  $S_c$ , but I am not using this convention.

In this chapter, a landscape signature of the RPGT will be revealed, and therefore a landscape definition of quasistates is required. Three ways of identifying groups of minima that might be interpreted as quasistates will now be considered. One is based on the structure of the PEL, one on simulated dynamics and one on real-space structure. A major result of this chapter is that at least two and possibly all three of the definitions identify similar regions of configuration space as quasistates.

Local minima and their associated basins of attraction are not appropriate quasistates,<sup>350</sup> because the number of accessible minima is still large even at  $T_K$ ,<sup>92</sup>

and because residence time in a minimum is very short near to  $T_c$ .<sup>32</sup> However, the residence time within a local funnel (§1.6.1.4) is expected to be longer. Moreover, analytical results for a model glassy landscape suggest that the number of funnels explored in the limit of long observation time goes to one at low temperatures.<sup>199</sup> Therefore funnels may be equivalent to quasistates in the RFOT description. This proposition is considered in the following sections.

The longest-lived dynamical structures currently known are metabasins, which can be identified by the energy method or by productive cage breaks. Transitions between metabasins control relaxation, in the same way that transitions between metastable states control relaxation in the RFOT theory.<sup>31</sup> Therefore metabasins could possibly be used to define quasistates.

The third definition of quasistates, that will be used most often in the subsequent discussion, is that of *packings*. Packings are groups of PEL minima with a high mutual overlap, and low average overlap with minima belonging to other packings. Therefore all minima in a packing have roughly the same arrangement of unpinned atoms. Different minima within a packing are separated by small displacements of atoms without significant structural change.

This qualitative definition of packings is similar to the definition of metastable states in mean-field-like theories,<sup>152,175,345</sup> so packings are expected to correspond closely with quasistates. In §5.3.2, a practical definition of packings in the PEL is presented, and used to evaluate how well our three definitions of quasistates agree.

The mean-field prediction of the RPGT is that  $\lim_{N \rightarrow \infty} \Sigma(T, c)/N$  vanishes continuously at  $c = c^*$ . Therefore, the number of thermally-accessible quasistates must be super-exponential in  $N$  for  $c > c^*$ , but sub-exponential for  $c \leq c^*$ . For sizes  $N = O(100)$ , exhaustive enumeration of quasistates is impractical on both sides of the putative transition, and we must rely on more approximate methods to characterise the numbers of funnels, packings and metabasins as the pinning fraction increases.

Potential energy minima are fundamental to all three quasistate definitions. Therefore, we begin by examining changes to the distribution of minima as a function of  $c$ .

## 5.2 Potential Energy Minima

Several previous studies<sup>175,182,343</sup> have observed a dramatic decrease in the complexity of a supercooled liquid when the pinning fraction  $c$  exceeds a critical value, in agreement with the argument of the previous section. In this section this decrease

is shown to arise directly from the structure of the PEL.

### 5.2.1 Return Times

The pinning procedure increases the energy of many configurations, due to strain caused by the immovable atoms. However, the reference minimum  $\mathbf{X}_0$  is less affected by this strain, since it is derived from the reference structure  $\mathbf{X}^*$  in which the interactions between the pinned and mobile atoms are not frustrated. Therefore,  $\mathbf{X}_0$  usually lies near the bottom of a pinned PEL, and is expected always to belong to a thermally accessible funnel.

In the case of high pinning, so many configurations are disfavoured that there will be few accessible funnels, and so the system should show a high propensity to return to structures similar to  $\mathbf{X}_0$  (high  $Q_0$ ). In contrast, at low pinning there may be many low-energy funnels that the system can explore, and the probability of returning to  $\mathbf{X}_0$  should be small.

This hypothesis was tested using basin-hopping global optimisation (§2.2.1.1), exploiting the efficiency of this method and its ability to locate low-energy minima. Let  $\mathbf{X}(s)$  be the local minimum obtained after step  $s$  of the basin-hopping algorithm, and define  $Q_0(s) = Q(\mathbf{X}_0, \mathbf{X}(s))$ .

All calculations were carried out using a single reference structure  $\mathbf{X}^*$  generated at  $T_0 = 0.5 \epsilon_{AA}/k_B$ . 10 different values of  $c$  in the range  $[0.10, 0.20]$  were used. The set of pinned atoms at each  $c$  was a subset of the atoms pinned at higher  $c$ .

30 basin-hopping calculations were performed for each  $c$  value, each with a different starting minimum  $\mathbf{X}(0)$ . These minima were selected from microcanonical MD simulations performed with the pinning constraints in place. The simulation energy was set high enough to ensure that  $Q(\mathbf{X}_0, \mathbf{X}(0))$  was small, and that mutual overlap between the different starting minima was small ( $\leq 0.4$ ). The average temperatures in these MD simulations varied from  $0.7 \epsilon_{AA}/k_B$  at  $c = 0.10$  to  $2.5 \epsilon_{AA}/k_B$  at  $c = 0.20$ , so most of the starting minima had high energy. The basin-hopping calculation corresponds to a downhill walk between local minima towards the nearest low-energy region of the landscape.

Each basin-hopping calculation was run for  $10^5$  steps.  $T_{bh}$  was initially set to a moderately high value ( $5 \epsilon_{AA}$ ) to avoid trapping in small funnels, and varied during the calculation to maintain a step acceptance rate of 70%.

$Q_0(s)$  was averaged over all 30 simulations to give  $\overline{Q}_0(s)$ , which is plotted for several  $c$  values in fig. 5.1. For  $c \geq 0.15$ ,  $\overline{Q}_0(s)$  rapidly converges to a large value (greater than 0.7), but  $\overline{Q}_0(s) \leq 0.4$  for all  $s$  when  $c \leq 0.13$ . When  $c = 0.14$ , the variance in  $Q_0(s)$  between different calculations is very high, so  $\overline{Q}_0(s)$  converges

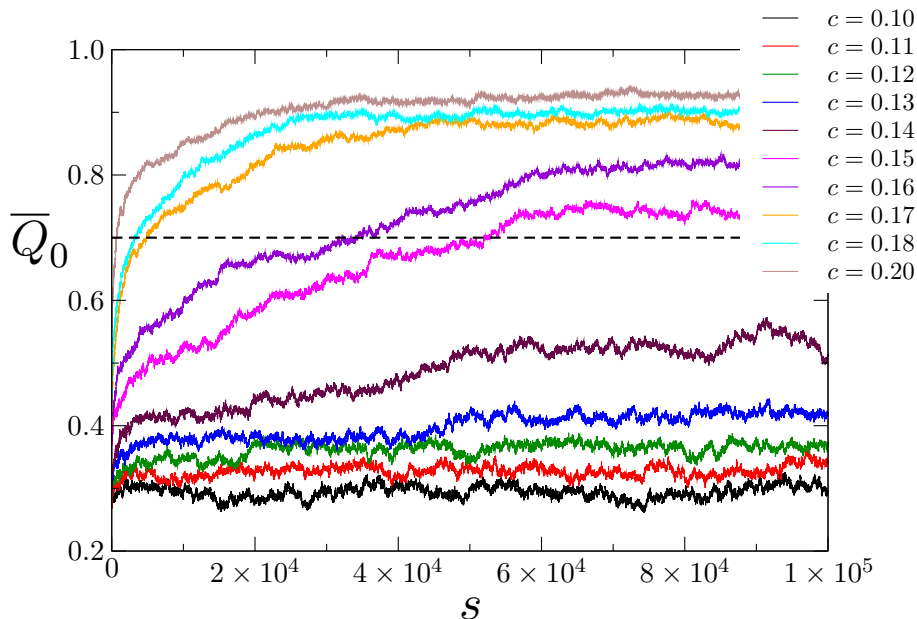


Figure 5.1: Plot showing how basin-hopping calculations explore overlap space at several different pinning fractions.  $s$  denotes the number of basin-hopping steps taken, and  $\overline{Q}_0(s)$  is the average over 30 basin-hopping runs of the overlap with the reference minimum. The dashed horizontal line shows  $Q_0 = 0.7$ , which is the threshold used to define when structures are similar to the reference.

slowly to an intermediate value (around 0.5).

These results are consistent with our expectation of complexity reduction. There is a rather sharp crossover around  $c = 0.14$  where the average overlap goes from small to large. The low- $c$  results match what would be observed for an unpinned landscape with high complexity, where there are many low- $Q_0$  funnels accessible but only a small number with high  $Q_0$ . The high- $c$  results indicate very different behaviour.

## 5.2.2 Distribution of Local Minima

To explore the crossover in more detail, further landscape exploration was carried out using parallel-tempering basin-hopping (PTBH, §2.2.1.2). This method is more efficient than basin-hopping for crossing between different funnels on the landscape, and so should be more effective for estimating the number of funnels.

The aim was to estimate the density of minima,  $g_{\text{IS}}$ , introduced in §1.6.1, as a function both of  $Q_0$  and of energy  $V$ . As explained in §2.2.1.1 and §2.2.1.2, basin-hopping methods generate an approximate density of states,  $\rho_{\text{IS}}$ , that is expected to be close to  $g_{\text{IS}}$  at low energies.

PTBH calculations were carried out for a range of  $c$  values, using the same  $\mathbf{X}^*$  as before. 12 replicas were used, with  $T_{\text{bh},i}$  spaced geometrically between  $0.5\epsilon_{\text{AA}}$

and  $25.0 \epsilon_{AA}$ . 10 runs of  $10^5$  basin-hopping steps each were performed for each replica, with step size varied dynamically to ensure that 70% of steps located a new minimum. One configuration swap between replicas was attempted every 10 basin-hopping steps.

Fig. 5.2 shows contour plots of  $\log_{10} \rho(V, Q_0)$  for several values of  $c$ . Note that although minima in the  $Q_0 < 0.7$  region are dissimilar to the reference, they are not all structurally similar to one another.

These graphs indicate a significant change in the  $Q_0$  distribution of low-energy minima. For  $c \geq 0.17$ , all minima at low energies have  $Q_0 \geq 0.7$ , but for  $c \leq 0.16$  there is a significant density of low-energy minima with  $Q_0 < 0.7$ . These results indicate that the set of accessible minima at low  $c$  is structurally diverse, but the set at high  $c$  is not.

Using the terminology introduced in §5.1.4, landscapes with  $c > 0.17$  have only one low-energy packing, whereas landscapes with  $c \leq 0.16$  have at least two. The crossover between these regimes occurs over a narrow range of  $c$ : the difference between  $c = 0.16$  and  $c = 0.17$  corresponds to pinning 3 atoms out of 256.

In all panels of fig. 5.2 there is a large density of minima at low  $Q_0$  and high  $V$ . This result is expected for a Gaussian distribution of local minima, but the relative weight of this region in  $\rho_{IS}$  may be exaggerated because the PTBH algorithm used many high-temperature replicas to encourage exploration of multiple funnels, which may have resulted in over-sampling the high-energy minima. Regardless, we expect that the density  $\rho(V, Q_0)$  is quite accurate at low  $V$ , since this quantity shows little change when the number of PTBH steps is increased. Therefore we are confident that the regions where  $\rho(V, Q_0) = 0$  have  $g_{IS}(V, Q_0) \approx 0$  also.

## Random Particle Pinning on the Potential Energy Landscape

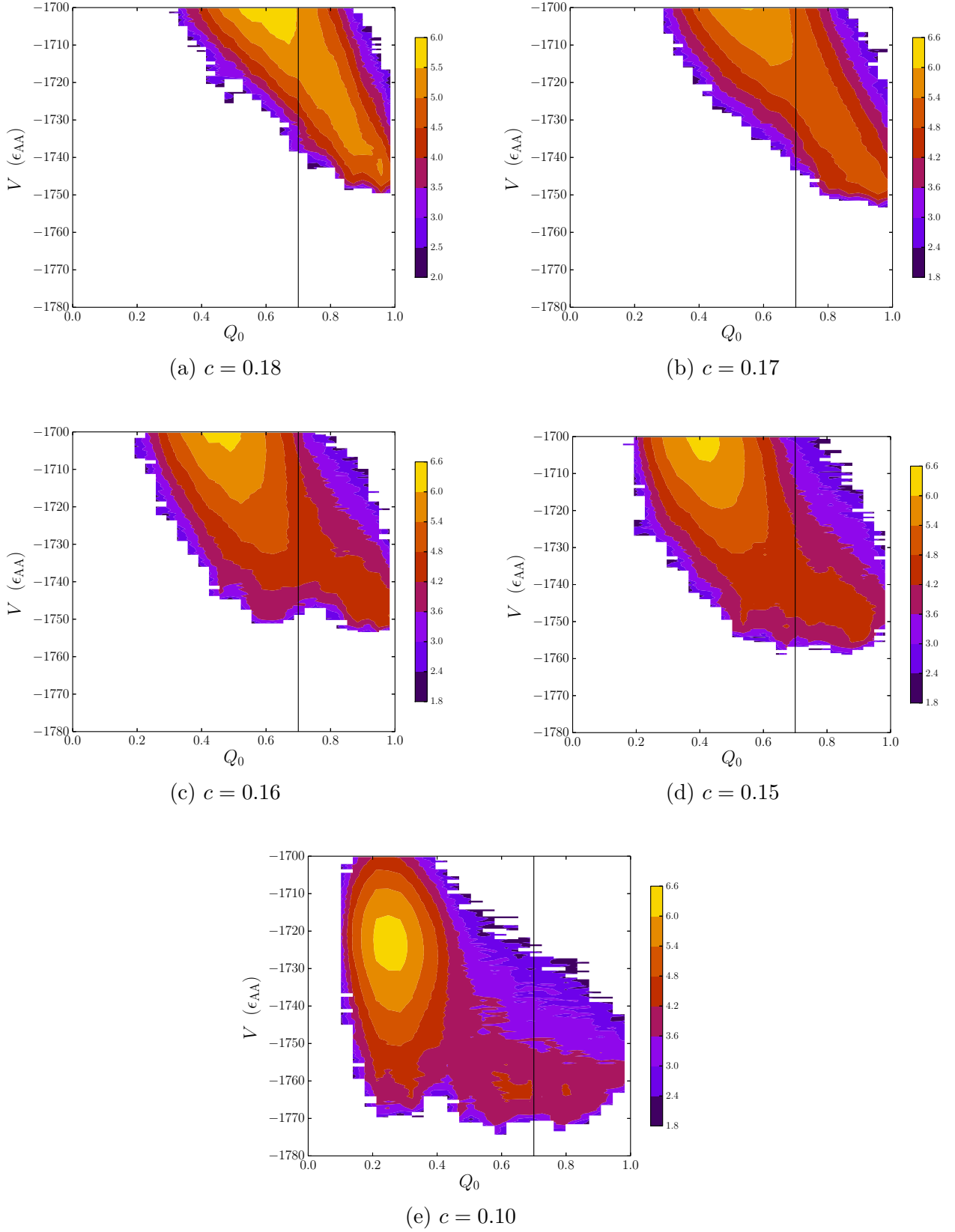


Figure 5.2: Contour plots of  $\log_{10} \rho(V, Q_0)$  for databases produced using PTBH with a reference temperature  $T_0 = 0.5 \epsilon_{AA}/k_B$ .  $\rho(V, Q_0)$  is proportional to the number of minima in the database that have potential energy  $V$  and overlap  $Q_0$  with the reference minimum.

## Random Particle Pinning on the Potential Energy Landscape

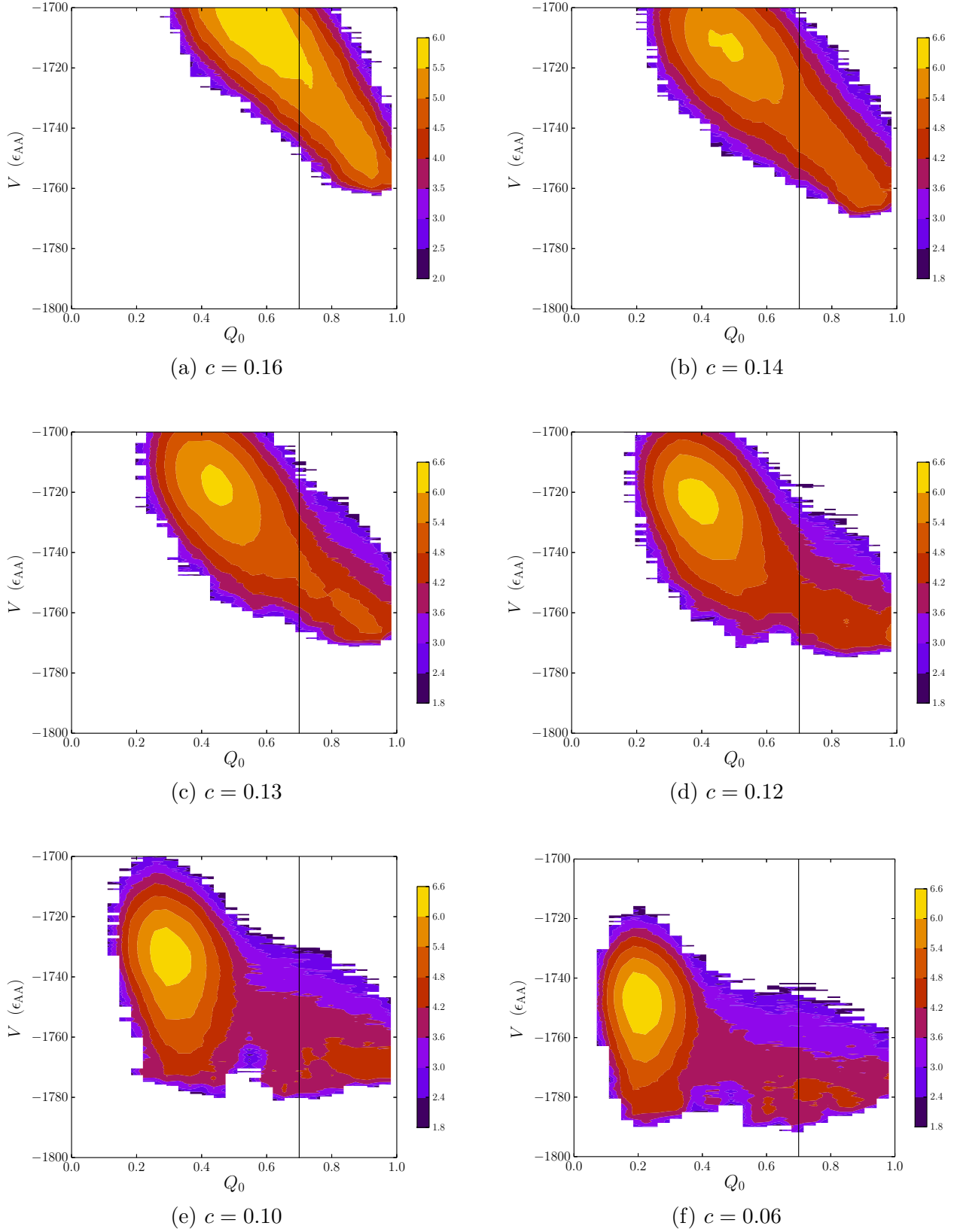


Figure 5.3: Contour plots of  $\log_{10} \rho(V, Q_0)$  for databases produced using PTBH with a reference temperature  $T_0 = 0.43 \epsilon_{AA}/k_B$ .

### 5.2.2.1 Effect of Reference Temperature

The RFOT description of the RPGT predicts that the critical pinning fraction  $c^*$  decreases with reference temperature  $T_0$ .<sup>175,182</sup> This effect is related to the system exploring different regions of the PEL at different temperatures, so a low- $T_0$  reference structure will be lower in energy than a high- $T_0$  reference.

To test this prediction, PTBH sampling has been performed using a reference structure generated at  $T_0 = 0.43 \epsilon_{AA}/k_B$ . This temperature is close to  $T_c$  for this density of BLJ,<sup>10</sup> and so obtaining the locally equilibrated MD trajectory from which to select  $\mathbf{X}^*$  was significantly more expensive than at  $T_0 = 0.5 \epsilon_{AA}/k_B$ . Because of this expense, use of the energy fluctuation metric to diagnose local ergodicity proved impractical. Instead, the trajectory was propagated for  $2.25 \times 10^6 (m\sigma_{AA}^2/\epsilon_{AA})^{1/2}$ . This time is more than  $100 \tau_s$ , the structural relaxation time estimated from the decay of  $\langle Q_0(t) \rangle$  over the trajectory.

Most PTBH parameters were the same as for the calculations at  $T_0 = 0.5 \epsilon_{AA}/k_B$ . The range of temperatures covered by the 12 basin-hopping replicas was reduced to  $[0.4 \epsilon_{AA}/k_B, 8 \epsilon_{AA}/k_B]$  to improve the acceptance rate for replica exchanges.

The resulting  $\rho(V, Q_0)$  distributions are shown in fig. 5.3. The behaviour of these distributions is qualitatively the same as fig. 5.2: low- $V$  minima are structurally diverse when  $c$  is small, but all have  $Q_0 > 0.7$  when  $c$  is large. The crossover happens at a lower  $c$  than previously observed, with  $c^* \approx 0.12$  for this particular disorder realisation. The reduction in  $c^*$  agrees qualitatively with earlier work, but Ozawa *et al.* found a slightly lower  $c^* \approx 0.1$  for this reference temperature.<sup>182</sup> This discrepancy is probably due to the different methods for identifying the transition: one should not expect the PEL method to agree exactly with calculations based on finite-temperature MD simulations and thermodynamic integration.

### 5.2.3 Disorder Averages

So far, only a single disorder realisation has been considered for each  $T_0$ . To obtain meaningful results, a disorder average is required. Therefore, PTBH calculations were performed for multiple disorder realisations and multiple reference structures. Different realisations were compared by calculating the probability that a low-energy minimum is structurally similar to the reference:

$$P(Q_0 > 0.7) = \int_{-\infty}^{V_c} \int_{0.7}^1 \rho_{\text{IS}}(V, Q_0) \, dQ_0 \, dV \quad (5.3)$$

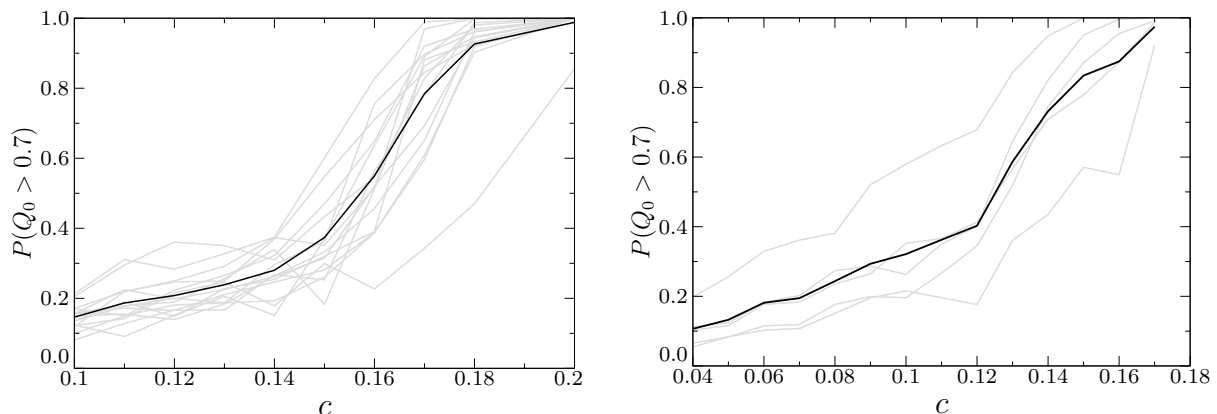


Figure 5.4: Probability that a low-energy minimum selected at random will be similar to the reference minimum,  $\mathbf{X}_0$ . The left panel shows landscapes with  $T_0 = 0.5 \epsilon_{AA}/k_B$ , the right panel shows  $T_0 = 0.43 \epsilon_{AA}/k_B$ . In both cases, the grey lines represent individual disorder realisations and the black line represents  $\overline{P}(Q_0 > 0.7)$ .

where  $V_c$  is an energy cutoff that restricts the integral to exclude the surplus of high-energy minima identified by PTBH. These high-energy minima have an approximately Gaussian distribution in  $V$ , so  $V_c$  is chosen by fitting a Gaussian function to the high-energy region of  $\rho_{\text{IS}}(V)$ . Then  $V_c = \overline{V} - 2\sigma_V$ , where  $\overline{V}$  is the mean of the fitted Gaussian and  $\sigma_V$  is its standard deviation.

Fig. 5.4 shows  $P(Q_0 > 0.7)$  as a function of  $c$  for several different realisations of the disorder. The average of this quantity, over the different realisations,  $\overline{P}(Q_0 > 0.7)$ , is also shown. The left panel represents  $T_0 = 0.5 \epsilon_{AA}/k_B$  and shows 15 disorder realisations produced from 3 different reference structures. The right panel represents  $T_0 = 0.43 \epsilon_{AA}/k_B$  and shows 5 disorder realisations, each from a different reference structure.

In both cases, the different reference structures were selected to have low mutual overlap. Variation of  $P(Q_0 > 0.7)$  between different disorder realisations with the same reference structure is similar to the variation between different references.

For both panels, every realisation of the disorder exhibits a crossover in  $c$  where the probability of a given low-energy minimum being in the reference packing increases from around 0.3 to almost unity. Although its position and sharpness varies between different disorder realisations, this crossover is present for all landscapes, as well as in the disorder average, providing confidence that it is a general property of pinned systems.

The crossover occurs at  $c \approx 0.15-0.17$  for  $T_0 = 0.5 \epsilon_{AA}/k_B$ , and at  $c \approx 0.12-0.14$  for  $T_0 = 0.43 \epsilon_{AA}/k_B$ , which agrees with the expectation that  $c^*$  decreases with  $T_0$ . Therefore, the landscape transformation during pinning is qualitatively similar to

the behaviour expected for an equilibrium RPGT.

The exact crossover value of  $c$  is not comparable with  $c^*$  obtained by other methods,<sup>182</sup> because  $\rho_{\text{IS}}(V, Q_0)$  is not a Boltzmann sample of minima and because eq. ((5.3)) does not weight the contributions of the minima by their occupation probabilities. However, the position of the crossover for the high- $T_0$  case is comparable with the critical  $c$  predicted by Ozawa *et al.* using thermodynamic integration and using overlap averages from a thermal simulation.<sup>182</sup> This similarity is further evidence that the transformation in the landscape is related to the RPGT.

In an equilibrium transition,  $\bar{P}(Q_0 > 0.7)$  should jump discontinuously between its two limiting values.<sup>182</sup> Neither panel of fig. 5.4 shows such a jump, despite the fact that  $T_0 = 0.43 \epsilon_{\text{AA}}/k_{\text{B}}$  is well below the predicted RPGT critical temperature  $T^*(c)$  in this system.<sup>182</sup> This result may challenge the accepted view that the RPGT is an equilibrium phase transition, but it could also be due to insufficient disorder averaging or to finite size effects, which would “round” the transition by smoothing out the discontinuity.<sup>351,352</sup> An initial test of this scenario will now be described.

### 5.2.4 Effect of System Size

If the RPGT is a thermodynamic phase transition, the complexity should vanish completely at a critical  $c^*$ , corresponding to a sudden decrease in the number of quasistates and hence a discontinuity in  $\bar{P}(Q_0 > 0.7)$ . However, a true discontinuity is expected only in the thermodynamic limit, being replaced by a smooth crossover for finite system sizes.

In principle, the existence of the discontinuity could be tested by finite-size scaling, calculating  $\bar{P}(Q_0 > 0.7)$  for increasing system sizes and extrapolating the change in slope at the crossover to test for divergence as  $N \rightarrow \infty$ . Computational limitations prevent this approach at the present time. Moreover, increasing the number of particles will increase the number of weakly-interacting subsystems, which might also smooth out the discontinuity in  $\bar{P}(Q_0 > 0.7)$ .<sup>197</sup>

As an initial attempt to examine the finite size effects in this system, fig. 5.5 shows  $\rho_{\text{IS}}(V, Q_0)$  for a smaller BLJ simulation cell containing 180 atoms (144 A-type and 36 B-type). These figures are compared with equivalent plots for the 256-atom landscapes. No qualitative differences are observed between the two systems, which may indicate that the landscape properties being probed by  $\rho_{\text{IS}}(V, Q_0)$  are broadly independent of system size. On the other hand, one would normally expect probability distributions, such as  $\rho_{\text{IS}}(V, Q_0)$ , to become narrower in a smaller system. The fact that this distribution does not narrow might indicate the presence of interatomic correlations that span the simulation cell and produce finite size effects.

Greater availability of computer power, particularly GPU acceleration,<sup>293</sup> may allow an accurate finite size scaling calculation to be carried out in the near future.

### 5.3 Organisation of the Landscape

The results in §5.2 show that the distribution of local minima in the PEL of a glass former changes dramatically under the influence of random particle pinning. However, this analysis relied upon use of the overlap function as an order parameter. In projecting the  $3N$ -dimensional landscape onto two coordinates,  $V$  and  $Q_0$ , a large amount of information is lost because structurally distinct regions of the landscape that have similar values of  $Q_0$  are grouped together.<sup>4</sup>

Projection onto  $Q_0$  reveals that multiple low-energy packings are present at low  $c$ , but it cannot resolve the number of distinct low- $Q_0$  packings, which is required to evaluate  $\Sigma$ .

Observing changes to the structure of the PEL without low-dimensional projection requires knowledge of the connectivity of the landscape, i.e. transition states. Independent transition state sampling was performed for landscapes with  $T_0 = 0.5$  at several values of  $c$  in the range  $[0.10, 0.18]$ . To initialise the transition state searches, 101 local minima were selected from databases generated by PTBH.  $\mathbf{X}_0$  was always selected, along with 100 low-energy minima chosen from a uniform distribution in  $Q_0$ . The exhaustive connection strategy (fig. 2.8) was used to connect these minima, obtaining a dense sample of stationary points in configuration space.

The resulting databases appeared to suffer from artificial frustration, so further connection attempts were made using the UNTRAP method (see §2.2.3.1) for some databases.

#### 5.3.1 Disconnectivity Graphs

Disconnectivity graphs for the pinned landscapes are shown in fig. 5.6. Each minimum (and corresponding branch) is coloured according to its overlap,  $Q_0$ , with the reference minimum.

The graph for  $c = 0.10$  resembles an unpinned glassy PEL, similar to those in earlier chapters. It has many local funnels with comparable energy, which were previously identified as metabasins. There is no dominant lowest-energy region of the PEL. The funnel containing the reference structure is much larger than other funnels, but this is partly due to oversampling in that funnel.

At high  $c$ , the PEL has a very different structure: fig. 5.6e contains a single main funnel, which is a morphology associated with structure seeking systems.<sup>353</sup>

Therefore at high pinning fractions, the landscape no longer resembles that of a structural glass former. Note, however, that the main funnel in this figure contains many competing low-energy minima, so although the system will seek out this region of the PEL very rapidly, it will not always locate the global minimum.

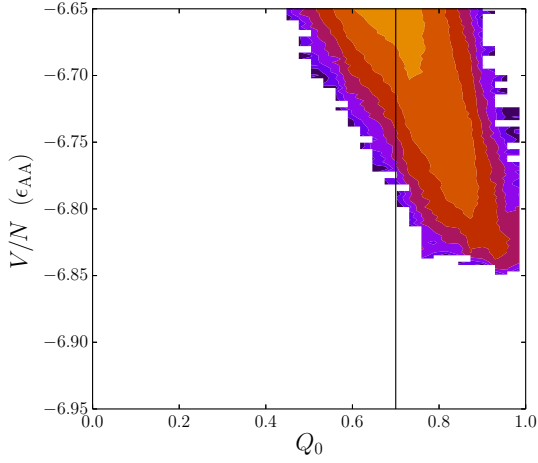
As might be expected, the low-energy minima in the main funnel of fig. 5.6e all have high  $Q_0$ , indicating that pinning 18% of particles is sufficient to suppress configurations that are structurally different from  $\mathbf{X}_0$ . Low- $Q_0$  minima do not disappear entirely, and indeed are still organised into small funnels, but these minima are very high in energy and will not be populated in equilibrium.

Recall that fig. 5.2 shows a relatively sharp crossover between  $c = 0.16$  and  $c = 0.17$ , where the minima with low energy and  $Q_0 < 0.7$  disappear quite suddenly. The improved dimensional resolution in fig. 5.6 reveals a smoother crossover. At  $c = 0.16$ , there are several funnels with  $Q_0 < 0.7$  which compete with the reference. These funnels do not disappear at  $c = 0.17$ , but instead seem to be shifted to higher energies that are no longer comparable with the reference. This shifting process is investigated in §5.4.

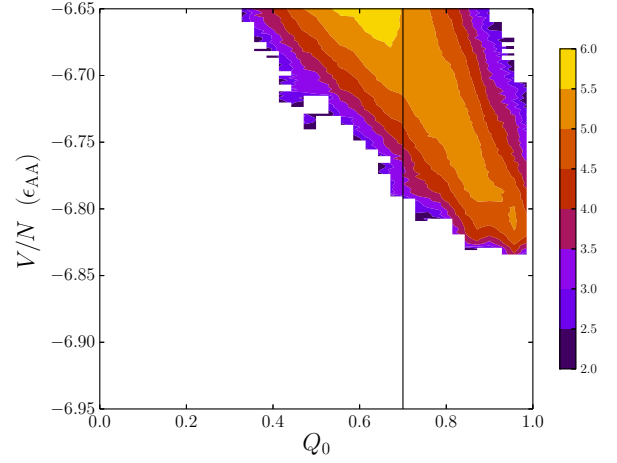
As an aside, consider the likely effect of pinning on the dynamics and relaxation behaviour of BLJ. Results in the previous chapters have linked super-Arrhenius behaviour of diffusion constants to the presence of large metabasins, related to local funnels in the landscape. If these results still apply to pinned systems, one would expect highly-pinned BLJ to be a strong liquid, since its PEL contains only a single low-energy funnel and therefore presumably only one metabasin. This expectation agrees with the results of Chakrabarty *et al.*, who found that the kinetic fragility of BLJ decreases significantly with increasing pinning.<sup>183</sup> The consequences of this observation are discussed further in chapter 6.

In the high- $c$  panels of fig. 5.6, there are some minima with high  $Q_0$  and low  $V$  that appear to be separated from the reference funnel by large energy barriers. These barriers may be due to artificial frustration that was not removed by the UNTRAP procedure. In this interpretation, low-barrier pathways between these minima and the reference minimum probably do exist, but have not yet been found in our transition state sampling. However, some of the large energy barriers may be genuine, and caused by the immovable pinned atoms.

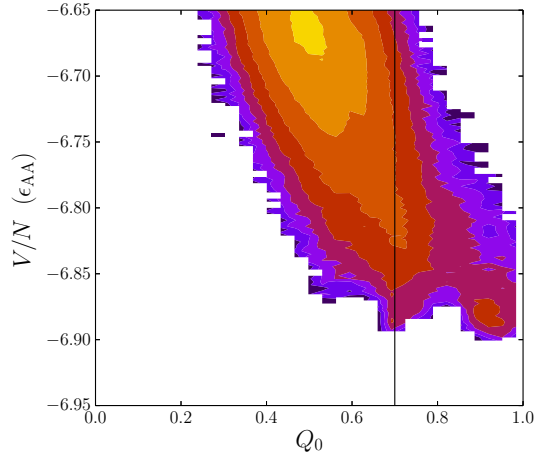
## Random Particle Pinning on the Potential Energy Landscape



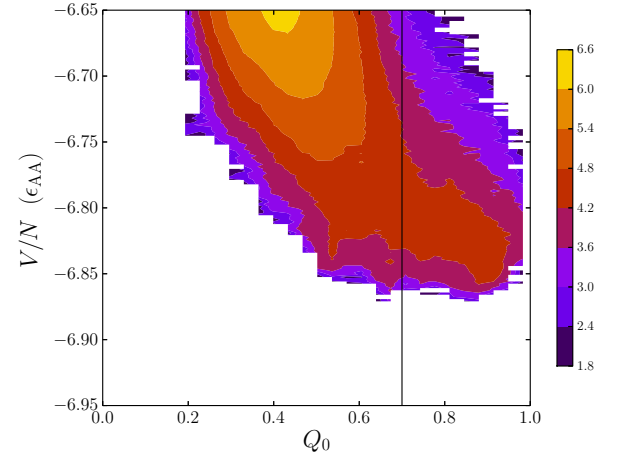
(a)  $N = 180, c = 0.20$



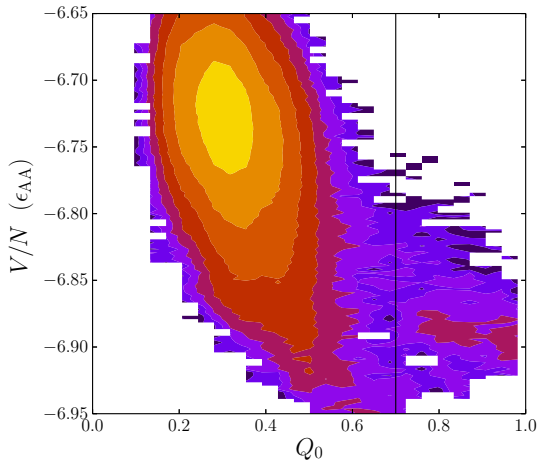
(b)  $N = 256, c = 0.18$



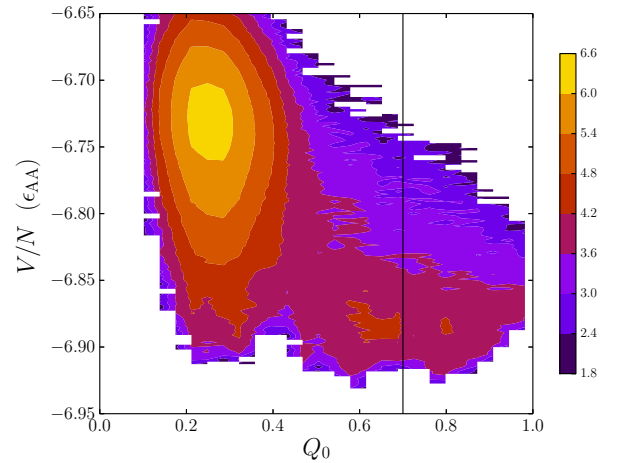
(c)  $N = 180, c = 0.15$



(d)  $N = 256, c = 0.15$



(e)  $N = 180, c = 0.10$



(f)  $N = 256, c = 0.10$

Figure 5.5: Contour plots of  $\log_{10} \rho_{IS}(V, Q_0)$  for different system sizes. Panels on the left correspond to a system of 180 atoms, and panels on the right are size 256. Energy is given per particle.  $T_0 = 0.5 \epsilon_{AA}$  in both cases.

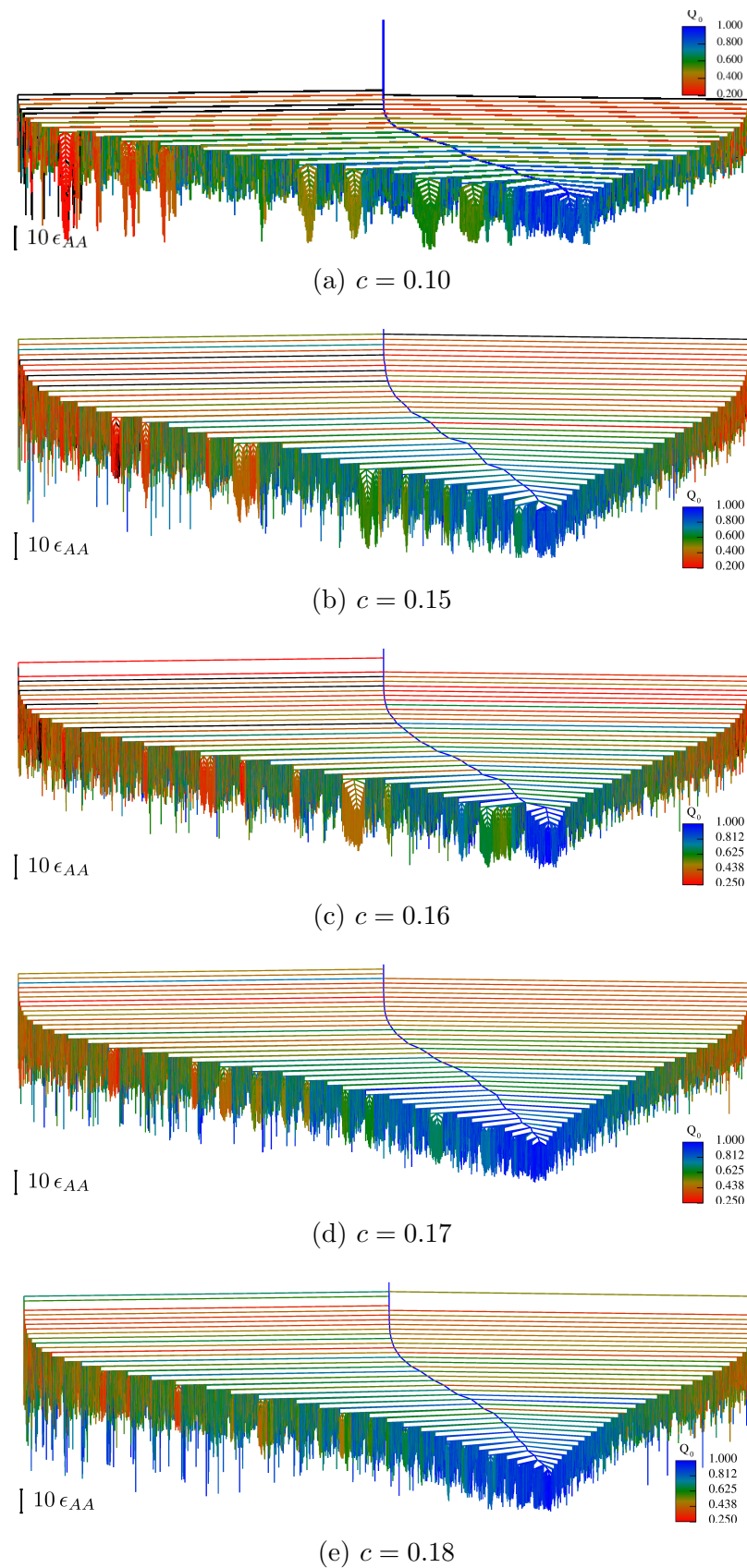


Figure 5.6: Disconnection graphs for BLJ landscapes at several different pinning fractions. Minima are coloured by their value of  $Q_0$ .

### 5.3.2 Packings on the PEL

The analysis in §5.2 probes the number of packings on the PEL as a function of  $c$ . §5.3.1 follows a similar approach for landscape funnels. Here, we consider the relationship between packings and funnels, two possible definitions of RFOT quasistates.

In fig. 5.6 most minima in each local funnel have the same colour, suggesting that they may be structurally similar. To confirm that this is the case, an algorithmic definition of packings will now be presented. The approach is to cluster the known minima into groups with high mutual overlap. The boundaries between groups are defined by the usual similarity cutoff  $Q^* = 0.7$ , so that these groups correspond to quasistates in the mean-field-like description.

Many efficient methods exist<sup>354–356</sup> for detecting highly connected sets in a graph with edge weights given by a similarity measure, such as  $Q(\mathbf{X}_a, \mathbf{X}_b)$ . However, these methods typically require evaluating all edge weights. The databases used here contain  $O(10^5)$  minima, making such a calculation impractical. A cheaper greedy algorithm is used instead:

1. The “parent minimum”,  $\mathbf{X}_p$ , for the first packing is always  $\mathbf{X}_0$ .
2. Calculate  $Q(\mathbf{X}_p, \mathbf{X}_m)$ , where  $\mathbf{X}_m$  is the lowest-energy minimum not currently assigned to a packing.
3. If  $Q(\mathbf{X}_p, \mathbf{X}_m) > Q^*$ ,  $m$  is added to the same packing as  $p$ .
4. Steps 2-3 are repeated for all minima not currently assigned to a packing.
5. The lowest-energy unassigned minimum becomes  $\mathbf{X}_p$  for a new packing.
6. Steps 2-5 are iterated until all minima are assigned, or until all unassigned minima lie above a predefined energy threshold.

The greedy algorithm does not guarantee that every minimum in a packing is more similar to the parent of that packing than to any other parent. However, it does guarantee that all minima within a packing are structurally similar, and that all parents are dissimilar to each other.

Fig. 5.7 shows the results of the greedy algorithm applied to a database at  $c = 0.10$ . Each packing is assigned a unique colour, and branches are coloured according to the packing to which the corresponding minimum belongs. Most local funnels visible on the landscape correspond to a single packing. This is an important result with several implications.

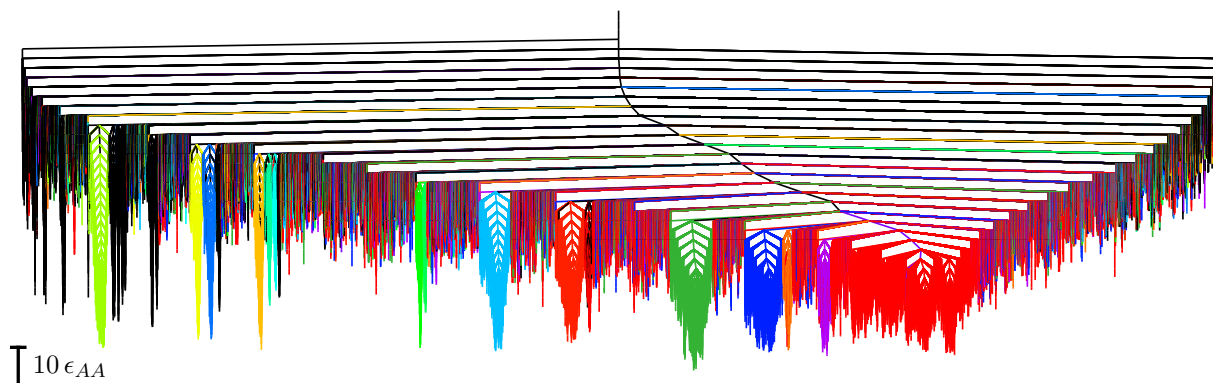


Figure 5.7: Disconnectivity graph for the database with  $c = 0.10$ . Minima are assigned to packings using a greedy algorithm, and each packing is coloured differently in the graph. Only packings containing more than 1000 minima are shown, all other minima are coloured black.

Firstly, it confirms the value of the disconnectivity graph approach by showing that some pairs of funnels with the same  $Q_0$  in fig.5.6 belong to different packings in fig. 5.7, i.e. they are structurally dissimilar. This visualisation method preserves the distinction between distant regions of configuration space, which is lost by projection onto a small number of order parameters.

Secondly, fig. 5.7 validates the common assumption that landscape funnels can usually be associated with a single amorphous structure, where higher-energy minima are minor perturbations of the lowest minimum in the funnel. The greedy algorithm may be useful in future work as a quick and objective method for identifying funnels in the landscapes of atomic systems. The relationship between funnels, packings and metabasins is explored further in sec 5.3.2.1.

Finally, this result shows that local funnels correspond approximately to quasistates defined using the mean-field order parameter  $Q$ , therefore validating the analysis in §5.3.1. The greedy algorithm provides a systematic method for identifying and enumerating quasistates. Although the present results have not sampled the landscape sufficiently to obtain an accurate calculation of  $\Sigma(T, c)$ , the principles are now established for a future systematic study of this quantity.

Note that in fig. 5.7 there are numerous minima that are assigned to a packing but which do not belong to a funnel. As in fig. 5.6, this may result from artificial frustration, because the transition state connecting the minima to their funnel has not yet been found. It is also possible that these minima have been misassigned: the precise set of packings identified by the greedy algorithm depends on its parameters, so there is inevitably some uncertainty over the assignment of high-energy minima.

### 5.3.2.1 Packings in Unpinned Landscapes

To test its general utility, the packing detection algorithm was applied to an unpinned BLJ landscape database. Fig. 5.8 shows that the agreement between packings and funnels persists in the absence of pinning. This figure demonstrates the strong link between real-space structure and connectivity on the PEL.

It has previously been shown<sup>233</sup> that metabasins defined by productive cage breaks also correspond quite closely with landscape funnels. Therefore the three possible definitions of quasistates proposed in §5.1.4 are broadly equivalent, indicating a link between metabasin dynamics and quasistate thermodynamics.

However, this equivalence appears to break down for lower temperatures. Figs. 5.8 and 4.10 were produced from the same landscape database, which was obtained by inherent trajectory sampling at  $T \approx T_c$  for this system. Recall that the different colours in fig. 4.10 correspond to geometric metabasins, and that this figure only represents part of the database, to facilitate comparison with the silica landscape.

At the low temperature used to produce these databases, dynamical metabasins often span several local funnels, due to an increased frequency of reversed cage breaks. Consequently, the connection between dynamical metabasins and landscape funnels breaks down at lower temperatures, whereas the connection between packings and funnels does not.

Although metabasins and packings may agree rather well at higher temperatures and for smaller systems, the packings detection algorithm will be used to define quasistates for the remainder of this chapter.

### 5.3.3 Comparing Pinned Landscapes

The discussion in §5.3.1 demonstrates that the PEL becomes less glassy and more funnelled as the fraction of pinned particles increases. In this section, the change is expressed numerically through simple quantitative characteristics of the landscape.

Fig. 5.9 shows histograms of the energy barriers between local minima and the reference minimum for each landscape database. The barriers are divided into “uphill”, (smallest barrier to go from  $\mathbf{X}_0$  to a local minimum) and “downhill” (from a local minimum to  $\mathbf{X}_0$ ).

The variance of the uphill barriers (fig. 5.9a) increases with  $c$ , due to an increase in the number of high barriers. These barriers appear due to increased funnelling of the landscape: minima with high uphill barriers are found on the sides of the steep global funnel. At  $c = 0.10$  the landscape is much “flatter” and hence there are fewer high energy barriers.

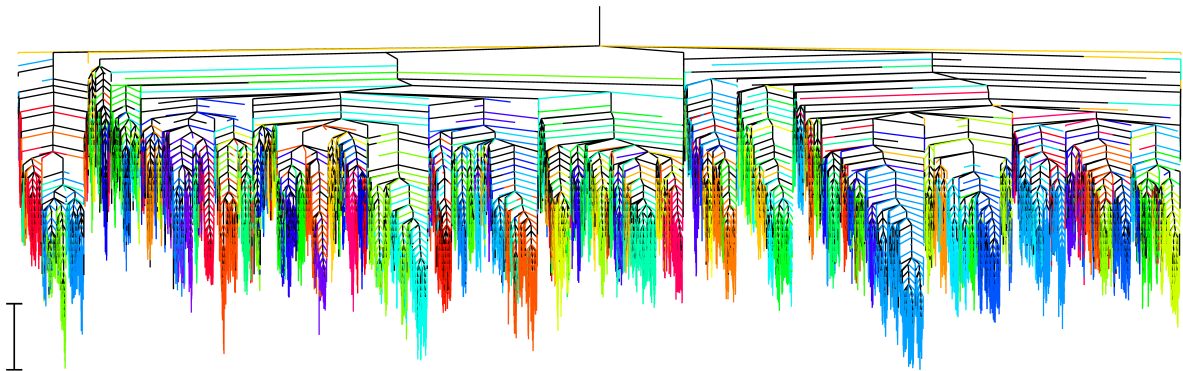


Figure 5.8: Disconnectivity graph for an unpinned BLJ database ( $c = 0$ ) with density  $1.3 \sigma_{AA}^{-3}$ . The landscape was explored using an inherent trajectory produced at  $T = 0.65 \epsilon_{AA}/k_B$ . Minima are divided into packings using the greedy packings detection algorithm, each of which is coloured differently in the graph. Only packings containing more than 100 minima are shown, all other minima are coloured black. The scale bar represents  $10 \epsilon_{AA}$ .

The downhill barrier height distribution is largely independent of  $c$ , and has a much smaller variance than the uphill barriers. Landscapes at low  $c$  have more high downhill barriers than those at high  $c$ . The long tail in the histogram for  $c = 0.10$  is due to minima in packings distinct from the reference, which must cross high inter-funnel barriers to reach  $\mathbf{X}_0$ .

Figs. 5.6 and 5.9 indicate that the PEL of BLJ becomes less frustrated as  $c$  increases, because the number of competing low-energy funnels decreases. Unfortunately, the usual frustration metric  $\tilde{f}$  is unable to capture this qualitative trend for two reasons. Firstly,  $\tilde{f}$  is calculated from energy barriers relative to the global minimum, but here it is barriers to  $\mathbf{X}_0$  that are most relevant. Secondly,  $\tilde{f}$  is dominated by minima that are nearly degenerate with the reference. These minima are mostly in the same packing as  $\mathbf{X}_0$ , and their density appears to be constant in  $c$ , so that  $\tilde{f}$  is very large for all landscapes, and unable to discriminate between the different pinning fractions.

To avoid these problems, we consider frustration on the level of entire packings, rather than individual minima. This approach is equivalent to calculating the frustration of different quasistates. A modified frustration metric is introduced:

$$\tilde{f}_p = \sum_{\alpha \neq p_0} \tilde{p}_\alpha^{\text{eq}}(T) \left( \frac{V_\alpha^\ddagger}{V_\alpha - V_0} \right). \quad (5.4)$$

Here,  $p_0$  is the packing that contains reference minimum, and the sum over  $\alpha$  includes all minima that do not belong to  $p_0$ .  $\tilde{p}_\alpha^{\text{eq}} = p_\alpha^{\text{eq}} / (1 - \sum_{\beta \in p_0} p_\beta^{\text{eq}})$  is the renormalised

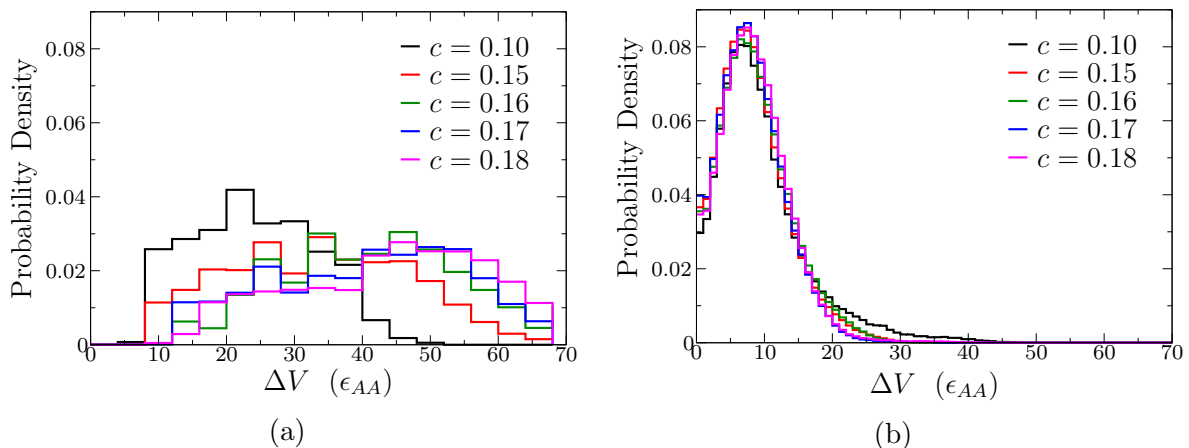


Figure 5.9: Histograms of the heights of energy barriers between local minima and the reference minimum. The first panel shows the “uphill” barriers, the second panel shows “downhill” barriers. The scale is the same for both panels.

equilibrium occupation probability of minimum  $\alpha$  once all minima belonging to  $p_0$  are excluded.  $V_0$  and  $V_\alpha$  are the energies of the reference minimum and minimum  $\alpha$ , respectively.

$V_\alpha^\ddagger$  is the uphill barrier from the reference minimum to minimum  $\alpha$ , given by  $V_\alpha^\ddagger = \max\{(V_\alpha^\dagger - V_0), \Delta V\}$  where  $V_\alpha^\dagger$  is the energy of the highest transition state on the minimum-energy pathway connecting  $\alpha$  to the reference.  $\Delta V$  is a parameter chosen to avoid divergence of  $\tilde{f}_p$  in cases where the reference minimum is not the global minimum. It turns out that the choice of  $\Delta V$  does not affect the ordering of the different pinning fractions by their  $\tilde{f}_p$  values, nor does it significantly affect  $\tilde{f}_p$  for highly-pinned landscapes. We have selected  $\Delta V = 0.1 \epsilon_{AA}$  to reduce the influence of minima with  $V_\alpha < V_0$ .

Fig. 5.10 shows that  $\tilde{f}_p(T)$  decreases as function of  $c$  at all temperatures, providing clear evidence of the transition from a multi-funnelled supercooled liquid landscape to a single-funnel pinned glass. Although the numerical values of  $\tilde{f}_p$  are not directly comparable with those of  $\tilde{f}$ , we note that the range of  $\tilde{f}_p$  values in fig. 5.10 is large compared with the total range in  $\tilde{f}$  previously reported.<sup>246</sup> This large range emphasises the difference in organisation between these landscapes.

At low  $T$ , the frustration metric becomes more temperature-dependent, as the number of populated minima decreases and the sum in eq. (5.4) becomes increasingly dominated by a few large terms. In particular, the frustration of the  $c = 0.16$  landscape increases dramatically and eventually exceeds the frustration of the  $c = 0.15$  landscape. This result is probably a peculiarity of the specific disorder realisation that was used here, due to the presence of several packings on the  $c = 0.16$  that are almost degenerate with the reference structure.

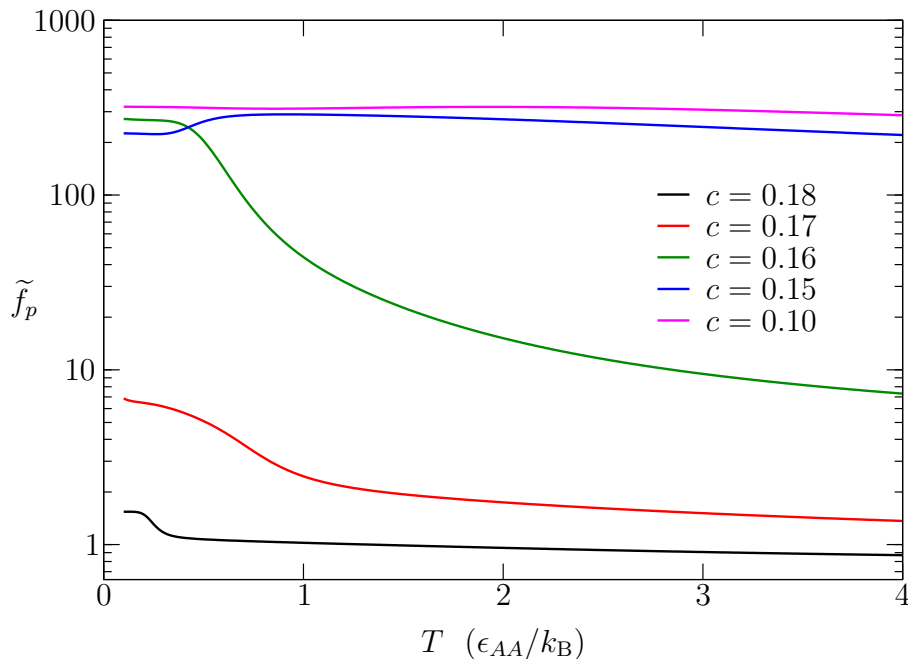


Figure 5.10: Modified frustration index  $\tilde{f}_p(T)$  for landscapes with different pinning fractions.

## 5.4 Evolution of the PEL with Pinning Fraction

In this section, the effect of random pinning on the PEL is examined by following the behaviour of individual minima and packings as  $c$  changes. The natural choice would be to study the behaviour of minima as  $c$  increases from 0, where sampling many different packings is trivial. However, mapping a minimum  $\mathbf{X}_i$  from a landscape with  $M$  pinned atoms onto a new landscape with  $M + 1$  pinned atoms and reference  $\mathbf{X}^\dagger$  is not a well defined procedure, because the  $(M + 1)^{\text{th}}$  pinned atom must be somehow moved from its position in  $\mathbf{X}_i$  to the correct position in  $\mathbf{X}^\dagger$ . The correct way to perform this movement is unclear, so progressively pinning a database from  $c = 0$  is not possible.

In contrast, mapping a minimum from the high- $c$  landscape to a low- $c$  landscape is straightforward: the unwanted pinning constraints are released, obtaining a non-minimised configuration. Following the steepest-descent pathway to the new minimum is a mathematically well-defined operation, so a landscape database may be relaxed from high  $c$  to low  $c$  in an unambiguous fashion.

The drawback of this approach is that sampling multiple packings at high  $c$  is difficult because most of them are very high in energy, and the set of minima sampled at high  $c$  may not be important at low  $c$ . One must be careful to account for this possibility in drawing any firm conclusions from the results.

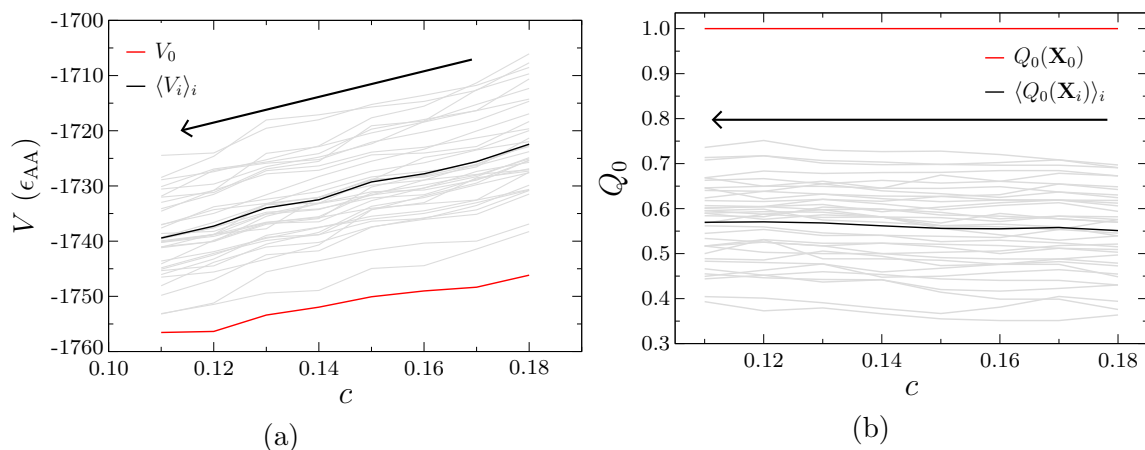


Figure 5.11: Figures showing how  $V$  and  $Q_0$  evolve for a set of minima as a  $c = 0.18$  landscape is progressively unpinned. Each grey line represents the parent minimum of a large packing on the  $c = 0.18$  landscape. The thick black line represents the average value over the grey lines. The red line represents the reference minimum, and the arrow indicates the direction of relaxation.

### 5.4.1 Evolution of Minima

Unpinning analysis was performed on a subset of minima obtained at  $c = 0.18$ . The subset consisted of the reference minimum, and the lowest energy minimum from each packing that contains more than 1000 minima.

Fig. 5.11a shows that the energy of each minimum decreases during unpinning, as expected because we re-minimise after unpinning each atom. For most minima the decrease is substantial: around  $20 \epsilon_{AA}$  on average. The reference minimum decreases by only  $10 \epsilon_{AA}$  over the same interval, so the energy gap between the reference minimum and the other funnels decreases during unpinning. Fig. 5.11b shows little change in  $Q_0$  during unpinning, indicating that most packings do not undergo significant structural change as pinned atoms are released.

These results suggest that most or all packings on a high- $c$  landscape are still present on landscapes at lower  $c$ , and that low- $Q_0$  packings become gradually more competitive the reference during unpinning. However, they do not prove that every packing on a low- $c$  landscape has a corresponding funnel on a given high- $c$  landscape. In fact, this scenario is quite unlikely.

Fig. 5.6 shows that for  $c \leq 0.15$  there are typically several low- $Q$  funnels with energies equal to or lower than the reference minimum, but none of the minima shown in fig. 5.11a have energies equal to that of the reference. This may indicate that the lowest-energy packings at  $c = 0.15$  do not evolve from high- $c$  packings, but rather appear due to other funnels bifurcating during unpinning.

An alternative explanation is that the lowest local minimum in a given packing

can change as  $c$  is decreased, so that the minima being followed in fig. 5.11 are no longer relevant. This possibility may be avoided by sampling entire packings as a function of unpinning.

### 5.4.2 Evolution of the Packings

To follow the evolution of packings with decreasing  $c$ , a sample of 100 minima was selected from the landscape at  $c = c_0$ . This sample contained the reference and at least one low-energy minimum from each packing with more than 1000 minima.

Each minimum in the sample was unpinned to  $c = c_1 < c_0$  and relaxed. The new low- $c$  minima were connected using the exhaustive connection strategy. The resulting databases differ significantly from those represented in fig. 5.6, because the methods of generating initial minima to connect are very different. The two sets of databases correspond to different ways of sampling configuration space.

The greedy packings algorithm was used to detect all packings containing at least 1000 minima in the new database. Packings were then compared between databases at different pinning fractions using the mutual overlap, defined as:

$$Q_p(A, B) = \frac{1}{\mathcal{N}_A \mathcal{N}_B} \sum_{X \in A} \sum_{Y \in B} Q(X, Y), \quad (5.5)$$

where  $X$  and  $Y$  are minima belonging to packings  $A$  and  $B$ , respectively, and  $\mathcal{N}_A$  is the number of minima in packing  $A$ . In practice,  $Q_p$  was estimated by restricting the sums to run over 10 minima selected at random from each packing.

In the elementary overlap calculation,  $Q(X, Y)$ , the sum over atoms runs over all atoms that are mobile in the low- $c$  system.

If  $Q_p(A, B) > 0.7$ , packings  $A$  and  $B$  are considered to *correspond*. Fig. 5.12 shows a pair of landscapes ( $c_0 = 0.17$ ,  $c_1 = 0.16$ ) with some pairs of corresponding packings indicated by black lines. This figure shows that most packings persist largely unchanged when a small number of atoms are unpinned. The energy of each packing decreases relative to the reference, and the barrier to the reference may also decrease slightly, but the average  $Q_0$  hardly changes. The energies of low-overlap packings tend to decrease faster than high-overlap packings, with the result that more low-overlap packings become thermally accessible as  $c$  is reduced.

Fig. 5.13 shows  $Q_p(A, B)$  for all pairs of packings. In each case, the vertical axis corresponds to packings in the high- $c$  landscape and the horizontal axis corresponds to the low- $c$  landscape. The labelling of the packings is arbitrary, so they have been ordered using the Hungarian algorithm<sup>357,358</sup> to maximise the overlap along the main diagonal of each panel.

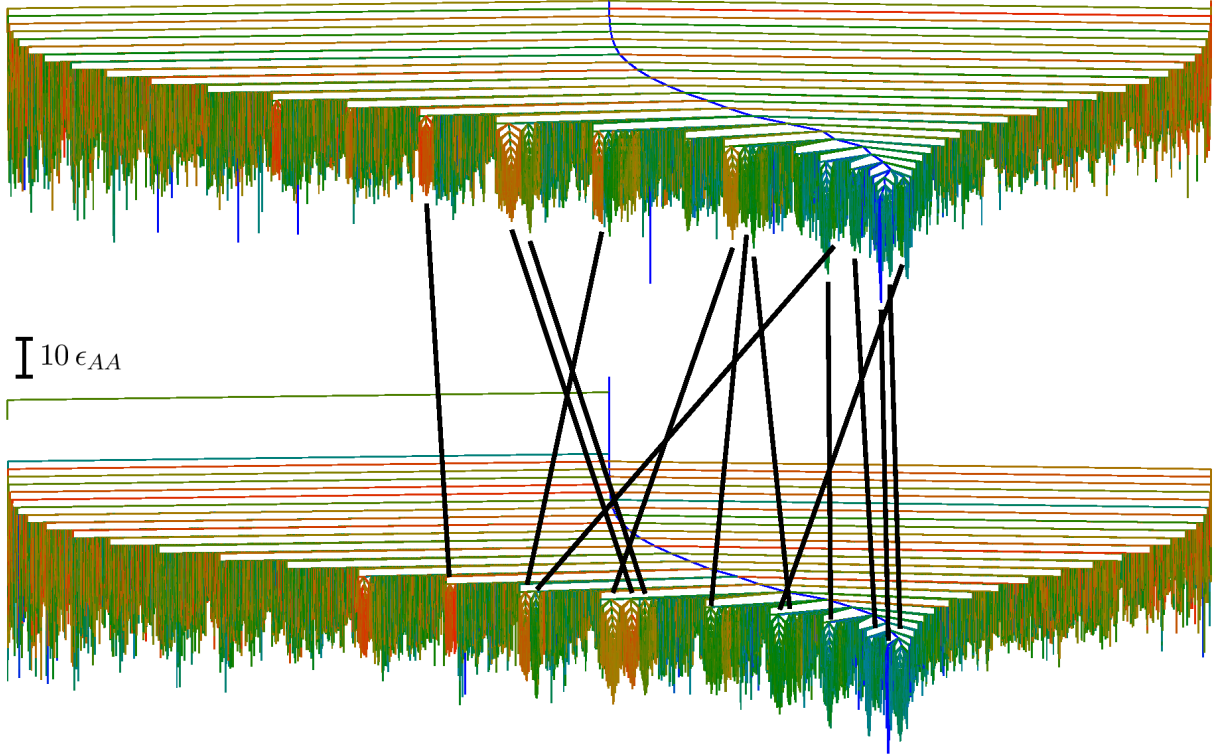


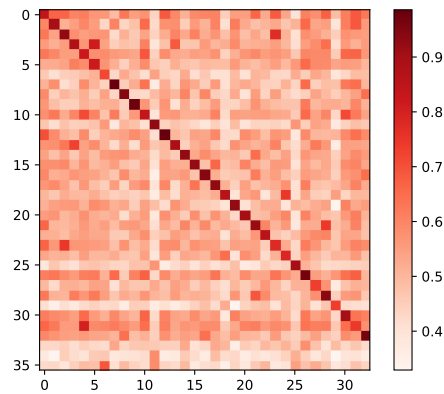
Figure 5.12: Graph to show correspondences between packings in different disconnectivity graphs. The upper graph represents a landscape with  $c = 0.17$ , the lower graph is at  $c = 0.16$ . Minima are coloured according to their  $Q_0$  values, using the same colour scale as before. Black lines connect some pairs of packings for which  $Q_p > 0.7$ . The scale bar represents  $10 \epsilon_{AA}$ .

Most packings at the lower value of  $c$  have exactly one correspondence on the high- $c$  landscape, called a *parent packing*. This observation means that most funnels retain their identities during the unpinning operation, as previously seen.

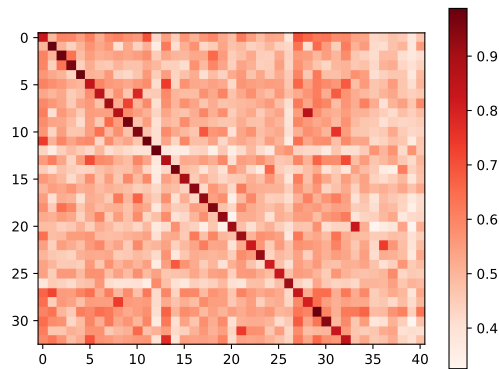
Beyond the simple parent-daughter relationship, there are several other scenarios that can and do occur in fig. 5.13. First, some low- $c$  packings have no known parent on the high- $c$  landscape. These cases are identified by columns of the matrix that contain no large values (see particularly fig. 5.13b). This scenario indicates that new packings become stable when pinning constraints are released, consistent with an increase in complexity at lower  $c$ .

Secondly, some packings at high  $c$  have no clear daughter packings - see the rows in fig. 5.13a that have no large values. Unpinning some atoms in these minima causes a significant structural rearrangement, presumably because the structure in question was stabilised by one of the pinned atoms. The packing is therefore destroyed by unpinning.

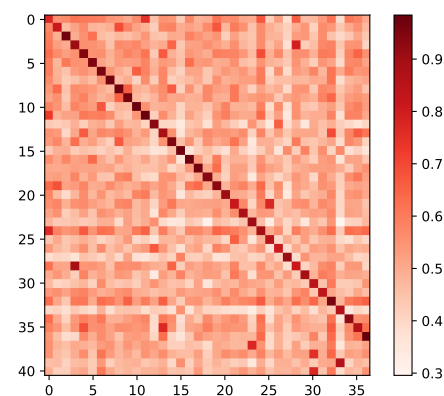
The third scenario is that some daughter packings have multiple parents and some parents have multiple daughters, indicated by a triangle of large  $Q_p$  values in



(a)  $c = 0.18$  (vertical) and  $c = 0.17$  (horizontal)



(b)  $c = 0.17$  (vertical) and  $c = 0.16$  (horizontal)



(c)  $c = 0.16$  (vertical) and  $c = 0.15$  (horizontal)

Figure 5.13: Heat maps representing  $Q_p(A, B)$  for pairs of packings on two landscapes with different  $c$ . The vertical axis represents packings of the high- $c$  landscape, the horizontal axis represents the low- $c$  landscape. Packings have been ordered to maximise overlap along the main diagonal.

the matrix. These situations correspond to splitting and merging of packings during unpinning.

Note that the first two scenarios could be explained by incomplete landscape sampling: possibly the missing parents and daughters do exist but were not captured by the exhaustive connection protocol. However, the region of configuration space defined by the initial set of minima has been sampled very thoroughly, so missing an entire packing is quite unlikely.

The third scenario could be an artefact of the packings detection algorithm: if two high- $c$  packings are structurally similar, but not quite similar enough to be grouped together by the algorithm, then both of them will have high overlap with the corresponding daughter packing.

The behaviour of the PEL during unpinning is clearly very complicated, and merits further study. Nevertheless, we can state that packings identified for a high- $c$  landscape are usually still present on corresponding low- $c$  landscapes, although they may bifurcate or merge. The average  $Q_0$  of minima within a packing changes very little during unpinning, and the energy relative to the reference decreases.

## 5.5 Conclusions

The transformation of the PEL that accompanies the random pinning glass transition (RPGT) has been described in detail for the BLJ fluid. Changes to the distribution of local minima, and to the connectivity of the landscape, were considered. Landscape exploration was performed independently at a range of pinning fractions, and quasi-continuously as a function of unpinning from a highly-pinned initial landscape.

Mean-field theories predict that the number of metastable states accessible to the system decreases to one as the pinning fraction  $c$  is increased. In non-mean-field systems, the *packings* analogous to these states are identified using the overlap order parameter. We have shown that these packings correspond very closely with local funnels on the PEL, and in some conditions they are also similar to dynamical metabasins.

The PELs of pinned glass formers change dramatically in the vicinity of a crossover point,  $c = c^*$ , identified with the RPGT. At low  $c$  there are many structurally distinct funnels on the landscape, but when  $c > c^*$  most of these packings retreat to high energy and only one accessible funnel remains, corresponding to the pinning reference structure. This picture is consistent with the theoretical prediction that the complexity  $\Sigma(T)$  vanishes at the RPGT.<sup>175</sup>

The crossover pinning fraction  $c^*$  decreases at reduced reference temperature  $T_0$ , as expected for the second order phase transition within the RFOT theory. However, the data presented here cannot resolve whether this event corresponds to a thermodynamic phase transition, and the value of  $c^*(T_0)$  predicted from the landscape differs slightly from that obtained by thermodynamic integration.<sup>182</sup>

The simplest mean-field picture of the RPGT predicts that some metastable states simply disappear as atoms are pinned, because they are inconsistent with the new pinning pattern. We have shown that real systems differ somewhat from this prediction, because very few local funnels disappear completely under pinning - instead they are shifted to higher energy. The crossover at  $c^*$  appears smoother when the full dimensionality of the PEL is considered than it appears when the configuration space is projected onto a small number of order parameters.

From the perspective of PEL theory, this chapter contributes several useful tools and observations. Firstly, the connection between real-space structure and the PEL is made explicit through the use of the structural overlap as an order parameter. This quantity provides a quick and intuitive way to identify local funnels numerically.

Secondly, it is now clear that the pinning operation induces a qualitative change in the landscape frustration. Pinning represents an intriguing means of controlling landscape structure and system behaviour, both for supercooled liquids and for other models.

Finally, some interesting questions have been raised regarding the behaviour of landscape funnels as a function of (un)pinning. The behaviour of local structures under perturbations of the landscape is clearly rather complicated, and merits closer study.

The results in this chapter establish a methodology for systematic investigation of the RPGT using landscape methods. To establish whether a thermodynamic transition really occurs for pinned BLJ, one should perform extensive basin-sampling<sup>359</sup> calculations to generate equilibrium distributions of minima in the noncrystalline region of the PEL, for a range of pinning fractions and system sizes. Enumerating the distinct packings present on the landscape would allow  $\Sigma(c, T)$  to be evaluated, and hence determine whether this quantity vanishes at  $(c^*, T^*)$ . Current computational limitations prohibit this scheme of work, but improvements in hardware and methodology may make it feasible in the future.

# Chapter 6

## Correlated Motion in Model Glass Formers

### 6.1 Introduction

In this final results chapter, we return to the subject of supercooled dynamics and consider a method of analysis that does not probe the PEL directly, although PEL concepts will prove useful to interpret the results. All three of the glass forming systems described in this thesis (OTP, silica and pinned BLJ) will be considered, and common themes in their behaviour will emerge.

The analysis follows an approach used by de Souza and Wales to study BLJ,<sup>254,255</sup> which was discussed briefly in §1.7.1. Their method in turn closely resembles the three-point correlation function introduced by Doliwa and Heuer to detect signatures of caged motion,<sup>47,106</sup> which has also been used to study the cage effect in experimental hard-sphere colloids.<sup>45,46</sup> Both methods found that the motion of a particle in a supercooled liquid is negatively correlated over short time periods, due to the confining effect of a nearest-neighbour cage. Here, the same approach is used to probe correlations on a wider range of time scales.

First, the details of the method are presented, and then the results are discussed for OTP (§6.3), silica (§6.4) and pinned BLJ (§6.5).

### 6.2 Short-time Diffusion Constants

The key idea of this chapter is to divide a long, locally ergodic MD trajectory into a sequence of short non-ergodic time intervals. Diffusion is then studied as a function of the interval length, equivalent to a short observation time. The simplest way to

perform this analysis is to calculate a short-time effective diffusion constant:

$$D(\tau, T) = \lim_{t \rightarrow \infty} \frac{1}{6t} \langle \mathbf{r}_i(t, \tau)^2 \rangle, \quad \text{where} \quad (6.1)$$

$$\mathbf{r}_i(t, \tau)^2 = \sum_{j=1}^m \Delta \mathbf{r}_i(j)^2. \quad (6.2)$$

The sum is over  $m$  time intervals of length  $\tau = t/m$ .  $\Delta \mathbf{r}_i(j) = \mathbf{r}_i(j\tau) - \mathbf{r}_i((j-1)\tau)$  is the displacement of particle  $i$  in time interval  $j$ .

Eq. (6.1) closely resembles eq. (1.3), the usual expression for the diffusivity  $D(T)$ . To calculate  $D(\tau, T)$ , the mean square displacement is evaluated over the intervals rather than over the entire trajectory, and long-time behaviour is approximated by adding together many short-time displacements.

### 6.2.1 Correlation-corrected Diffusion Constants

$D(\tau, T)$  will turn out to give a rather poor approximation to  $D(T)$ , when  $\tau$  is small. To understand why, consider the effects that are neglected by  $D(\tau, T)$ , namely correlations in  $\Delta \mathbf{r}_i$  between different time intervals.

These correlations may be quantified by expressing the true displacement  $\mathbf{r}_i(t)$  of particle  $i$  at time  $t = m\tau$  in terms of the short-time displacements  $\Delta \mathbf{r}_i(j)$ :

$$\begin{aligned} \mathbf{r}_i(t) &= \sum_{j=1}^m \Delta \mathbf{r}_i(j), \text{ so} \\ \mathbf{r}_i(t)^2 &= \left( \sum_{j=1}^m \Delta \mathbf{r}_i(j) \right) \cdot \left( \sum_{k=1}^m \Delta \mathbf{r}_i(k) \right) \\ &= \sum_{j=1}^m \Delta \mathbf{r}_i(j)^2 + 2 \sum_{j=1}^m \sum_{k=j+1}^m \Delta \mathbf{r}_i(j) \cdot \Delta \mathbf{r}_i(k) \\ &= \sum_{j=1}^m \Delta r_i(j)^2 + 2 \sum_{j=1}^m \sum_{k=j+1}^m \Delta r_i(j) \Delta r_i(k) \cos \theta_{jk}. \end{aligned} \quad (6.3)$$

$\theta_{jk}$  is the angle between the displacement vectors in intervals  $j$  and  $k$ , and  $\Delta r_i(j)$  represents the magnitude of  $\Delta \mathbf{r}_i(j)$ .

Recognising that the first term of eq. (6.3) is equal to  $\mathbf{r}_i(t, \tau)^2$  in eq. (6.2), it is clear that the short-time diffusion constants  $D(\tau, T)$  neglect the correlation terms in  $\cos \theta_{jk}$ . To confirm this result, an approximate correlation term may be reintroduced in  $\langle \mathbf{r}_i(t, \tau)^2 \rangle$  to recover the full super-Arrhenius behaviour.<sup>254</sup> This correlation term

is analogous to the correction sum ( $c_s$ ) defined for cage breaks in §4.3.2.1.

The average of  $\cos \theta_{jk}$  over all particles and time intervals is denoted by  $\langle \cos \theta_{jk} \rangle$ . As will be shown below, this quantity is usually negative when  $k = j + 1$  and approximately 0 otherwise. At very small  $\tau$ ,  $\langle \cos \theta_{jk} \rangle$  displays damped oscillatory behaviour in  $k - j$  due to cage-rattling motion.<sup>256</sup> However, the correlation of consecutive time intervals still dominates.  $\langle \cos \theta_{j,j+1} \rangle$  becomes more negative as the temperature decreases.

These properties of  $\langle \cos \theta_{jk} \rangle$  mean that the second term of eq. (6.3) may be simplified by setting all  $\cos \theta_{jk}$  terms to 0 unless  $k = j + 1$ . We then obtain a corrected form of eq. (6.1):

$$\begin{aligned}
 D^*(\tau, T) &= \lim_{t \rightarrow \infty} \frac{1}{6t} \langle \mathbf{r}_i^*(t, \tau)^2 \rangle \\
 &= \lim_{t \rightarrow \infty} \frac{1}{6t} \left\langle \sum_{j=1}^m (\Delta \mathbf{r}_i(j)^2 + 2\Delta r_i(j)\Delta r_i(j+1) \cos \theta_{j,j+1}) \right\rangle \\
 &\approx \lim_{t \rightarrow \infty} \frac{1}{6t} \left\langle \sum_{j=1}^m \Delta r_i(j)^2 (1 + 2 \cos \theta_{j,j+1}) \right\rangle \\
 &\approx \lim_{t \rightarrow \infty} \frac{1}{6t} \left\langle \sum_{j=1}^m \Delta r_i(j)^2 \right\rangle \times (1 + 2\langle \cos \theta_{j,j+1} \rangle) \tag{6.4}
 \end{aligned}$$

$$= D(\tau, T)(1 + 2\langle \cos \theta_{j,j+1} \rangle). \tag{6.5}$$

The third line assumes that the magnitudes of the displacement vectors for adjacent time intervals are similar when averaged over large  $m$ , so that  $\Delta r_i(j+1) \approx \Delta r_i(j)$ . The fourth line uses a “mean-field” approximation, assuming that  $\cos \theta_{j,j+1}$  takes its average value for all  $j$ , and is therefore a constant term which can be factored out of the average.

There are two major objectives in this chapter. Firstly, to establish whether  $D^*(\tau, T)$  can provide a reasonable estimate of  $D(T)$  without needing to compute a long ergodic trajectory. Secondly, to examine the situations in which  $D(\tau, T)$  and  $D^*(\tau, T)$  fail to describe  $D(T)$ , and hence determine the importance of the observation time scale in calculations of diffusion for model glass formers.

### 6.3 Fragile Glass Formers

In this section, the short-time diffusion analysis is applied to the MD trajectories of OTP that were used in chapter 3. The results agree qualitatively with those

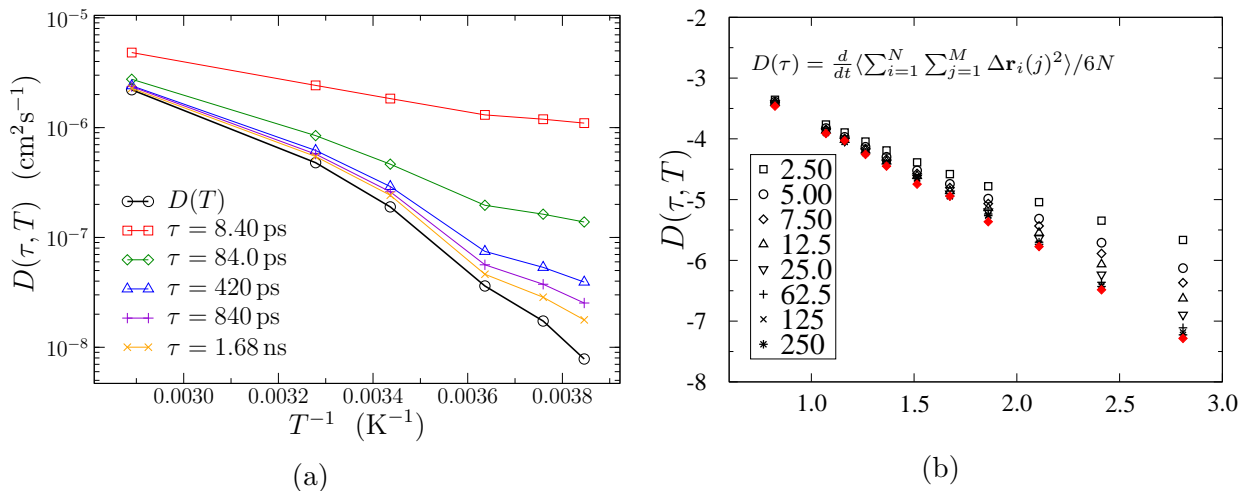


Figure 6.1: Short-time translational diffusion constants  $D(\tau, T)$ , for OTP (a) and BLJ with number density  $1.1 \sigma_{\text{AA}}^{-3}$  (b). Results for several values of the interval length  $\tau$  are shown, along with the long-time diffusion constants  $D(T)$  (filled diamonds in the BLJ plot). BLJ figure reproduced from [254] with the permission of APS Publishing. In the BLJ figure, all quantities are given in reduced units and the horizontal axis is  $T^{-1}$ .

obtained for BLJ in the earlier study,<sup>254,255</sup> and so they may be representative of fragile glasses in general. Results for the two systems will be compared side-by-side in this section, and most of the discussion applies equally to both.

Short-time diffusion constants  $D(\tau, T)$  are presented in fig. 6.1. Their temperature dependence is roughly Arrhenius for small  $\tau$ , but super-Arrhenius curvature reappears as  $\tau$  increases. As the interval length approaches local ergodicity, the curvature increases and  $D(\tau, T)$  tends towards  $D(T)$ .

The failure of  $D(\tau, T)$  to reproduce super-Arrhenius behaviour at small  $\tau$  shows that the neglected displacement correlations are fundamentally important in diffusion for these fragile systems.  $D(\tau, T)$  overestimates  $D(T)$  for all temperatures, indicating that the average effect of the neglected correlation is negative, i.e. anticorrelation dominates.  $D(\tau, T)$  and  $D(T)$  agree reasonably well at high temperature for all but the smallest  $\tau$ , so the strength of the correlations decreases with increasing temperature.

A more detailed picture of the correlation behaviour is obtained by examining  $\langle \cos \theta_{jk} \rangle$ , the average angle between single-particle displacement vectors in time intervals  $j$  and  $k$  (see eq. (6.3)). Fig. 6.2 plots this quantity as a function of  $k - j$  for an OTP trajectory.

$\langle \cos \theta_{jk} \rangle \approx 0$  for  $(k - j) > 1$ , indicating that the direction of motion in non-adjacent intervals is uncorrelated on all but the shortest time scales.  $\langle \cos \theta_{j,j+1} \rangle < 0$ , showing that motion at short times is negatively correlated. The magnitude of  $\langle \cos \theta_{j,j+1} \rangle$  increases with decreasing  $\tau$  and decreasing  $T$ , in agreement with the

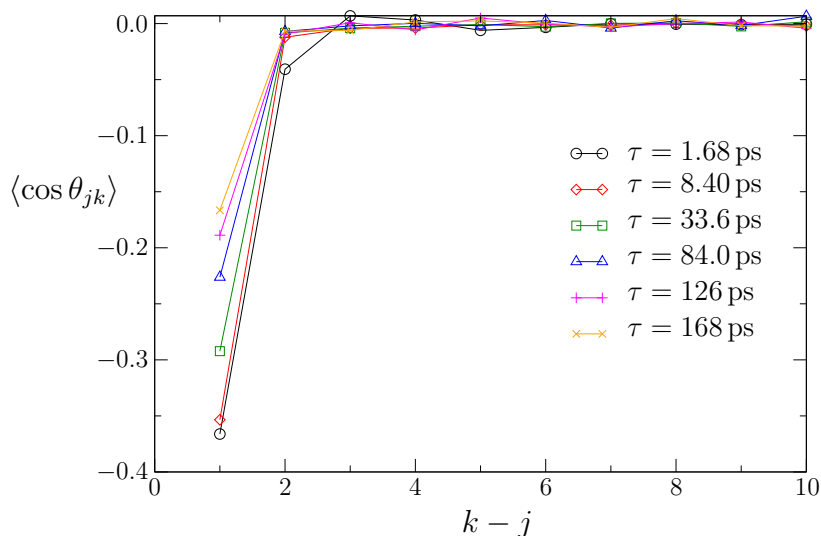


Figure 6.2: Average correlation factor between translational displacements in time intervals of length  $\tau$ .  $\theta_{jk}$  is the angle between the displacement vectors in interval  $j$  and interval  $k$ . These data represent an OTP trajectory at  $T = 291\text{ K}$ .

previous figure.

Fig. 6.2 indicates that only correlations between adjacent  $\tau$  windows are significant, and so the corrected diffusion constant  $D^*(\tau, T)$  should recapture the long-time behaviour. This expectation is confirmed in fig. 6.3: for all  $\tau$ ,  $D^*(\tau, T)$  is significantly closer than  $D(\tau, T)$  to the correct  $D(T)$ , and the super-Arrhenius curvature is recovered at much lower  $\tau$  values once the correlation correction is included. For BLJ, agreement of  $D^*(\tau, T)$  with  $D(T)$  is excellent for almost the entire range of  $T$  and  $\tau$  considered.

The correlation correction is less effective for OTP than for BLJ, presumably because the mechanisms of translational and rotational diffusion are coupled, which reduces the effectiveness of this simple description of the dynamics. Nevertheless, these results show that incorporating anticorrelation of particle displacements is necessary to reproduce super-Arrhenius behaviour in both atomic and molecular fragile liquids.

The magnitude of anticorrelation increases as temperature decreases, leading to smaller diffusion constants and an apparent increase in the effective barrier to diffusion. This increase is entropic in nature: the proportion of available rearrangements that involve reversal motion increases at lower  $T$ , and hence the number of available diffusive pathways decreases.<sup>256</sup> The temperature-dependent entropic barrier is superposed over a constant short- $\tau$  activation energy, which is dominated by temperature-independent potential energy barriers.

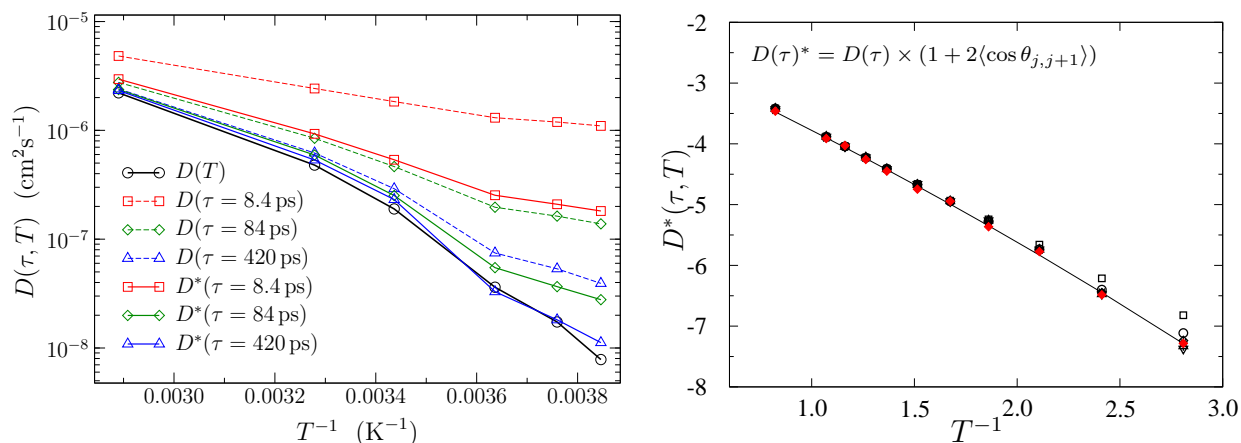


Figure 6.3: Correlation-corrected diffusion constants  $D^*(\tau, T)$ , for OTP (left) and BLJ with number density  $1.1 \sigma_{\text{AA}}^{-3}$  (right). Several values of the interval length  $\tau$  are shown, along with the long-time values  $D(T)$  (filled diamonds in the BLJ plot). The OTP plot also includes some uncorrected  $D(\tau, T)$  curves for comparison. The BLJ figure uses the same symbols as fig. 6.2 for different values of  $\tau$ . The BLJ figure is reproduced from [254] with the permission of APS Publishing.

$D(\tau, T)$  and  $D^*(\tau, T)$  represent a coarse-graining approach, using progressively less information from the trajectory as  $\tau$  decreases. The cage-breaking diffusion constants seen in previous chapters ( $D_{\text{CB}}(T)$ ) are also a result of coarse-graining the full trajectory into a relatively small number of CB events. However, even for the coldest OTP trajectory the frequency of CBs is  $\approx 0.5 \text{ ps}^{-1}$ , while  $\tau > 1500 \text{ ps}$  is required to give  $D(\tau, T)$  that fit the correct values as closely as  $D_{\text{prod}}(T)$ . Short-time diffusion constants provide a coarse-grained representation of the cage effect, averaging over many CB events to obtain the correct diffusive behaviour at long  $\tau$ .

The CB method coarse-grains the trajectory by picking out the key events and discarding all other information. The  $D(\tau, T)$  approach applies arbitrary coarse-graining independent of the microscopic details of the system, and therefore longer trajectories are required to reproduce the diffusion constant correctly using  $D(\tau, T)$  than using  $D_{\text{prod}}(T)$ .

### 6.3.1 A More Sophisticated Intermolecular Potential for OTP

The short-time diffusion method is a very general approach that does not depend on details of the model. Therefore, it can be applied easily to potentials that go beyond rigid body models and isotropic pair potentials.

Eastwood *et al.* have used a partially-flexible atomistic model for OTP,<sup>15</sup> which allows the phenyl rings to rotate. The Shaw group provided a trajectory for this model at 290 K, from which  $\langle \cos \theta_{jk} \rangle$  was calculated as a function of  $\tau$ . These

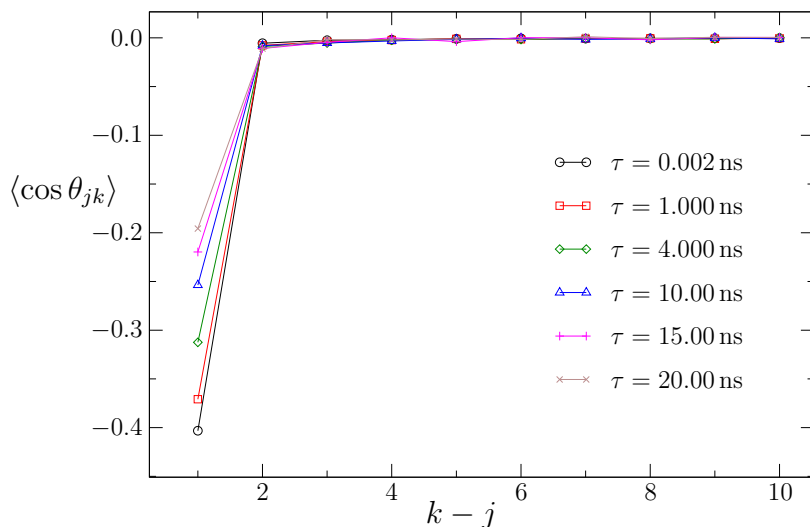


Figure 6.4: Average correlation factor between displacements in time intervals of length  $\tau$  using the Shaw group atomistic trajectory computed at 290 K.

results are shown in fig. 6.4, and appear qualitatively identical to fig. 6.2.  $D(\tau, T)$  for this model is therefore expected to show similar behaviour to that of the Lewis-Wahnström model.

These preliminary results show that the anticorrelation effect still holds for the Shaw model of OTP, which implies that the Lewis-Wahnström potential captures the essential physics on this level of coarse-graining and therefore that cage-breaking motion is a useful description of supercooled dynamics. However, the exact atomic mechanisms by which these cage breaks take place will be different in a more flexible model and so identifying these events would probably require a more sophisticated definition than that used in chapter 3.

## 6.4 Strong Glass Formers

Having established that super-Arrhenius behaviour arises from negative correlations in particle displacements, the role of these correlations in strong liquids will now be discussed.

Since silica does not display super-Arrhenius behaviour in the low-temperature regime, one might expect that negative correlation effects would be absent, but fig. 6.5 shows this is not the case. Once again,  $D(\tau, T)$  does not reproduce the correct long-time behaviour, indicating that correlation between displacement vectors is significant here as well as in OTP and BLJ. The effect of this correlation is surprisingly different.

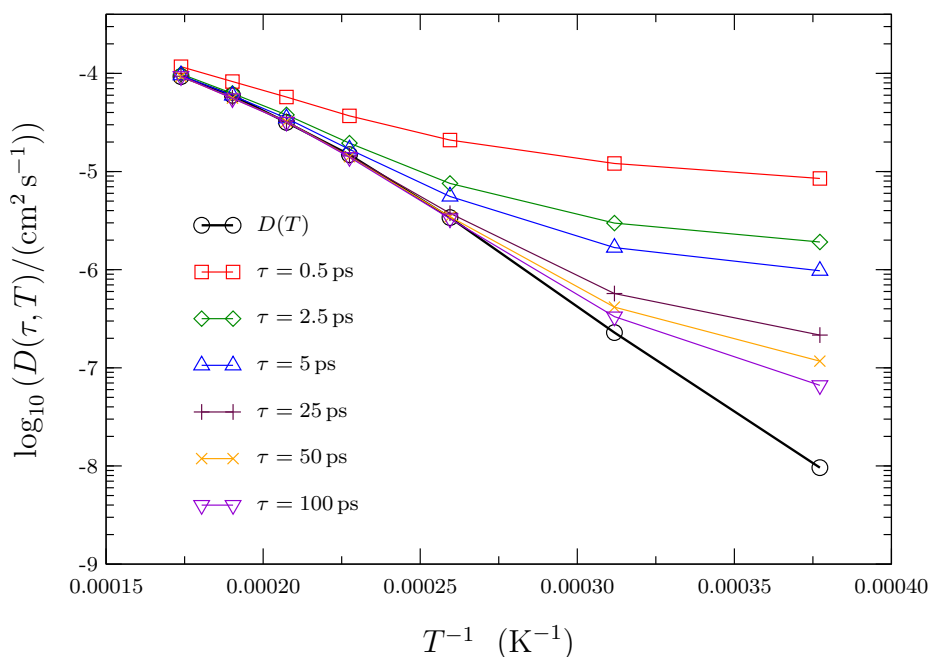


Figure 6.5: Short-time diffusion constants  $D(\tau, T)$  for silicon in liquid silica as a function of inverse temperature. Several values of the interval length  $\tau$  are shown. The correct diffusion constants  $D(T)$  are shown for comparison. The equivalent plot for oxygen diffusion is qualitatively the same.

For fragile liquids, diffusion constants have Arrhenius behaviour at small  $\tau$  and recover super-Arrhenius curvature on longer time scales. For silica, positive deviation from the Arrhenius law is observed at small values of  $\tau$  and straight-line behaviour is recovered as  $\tau$  increases.

Therefore the upwards deviation of  $D(\tau, T)$  at small  $\tau$  may result from the transition between caged and diffusive motion. Both of these regimes contain negative correlations: intra-cage motion consists of fast oscillations or “rattling”, and we have already seen that cage-breaking rearrangements can be easily reversed. The time scale of anticorrelation in cage-breaking motion is much longer than that of rattling. Cage breaks are correlated on times comparable with  $t_p$ , which the upper limit of the caging plateau in the mean squared displacement or intermediate scattering function.

$D(\tau, T)$  implicitly includes the effect of correlations between events with periods faster than  $\tau$ . At high temperatures, when  $t_p$  is small, an interval of length  $\tau$  includes some reversed cage breaks, but when  $t_p > \tau$  at lower temperatures these correlations are not captured by  $D(\tau, T)$ . Therefore,  $D(\tau, T)$  reports a smaller effective activation barrier as the temperature decreases.

An alternative description of the same effect is that on short time scales the

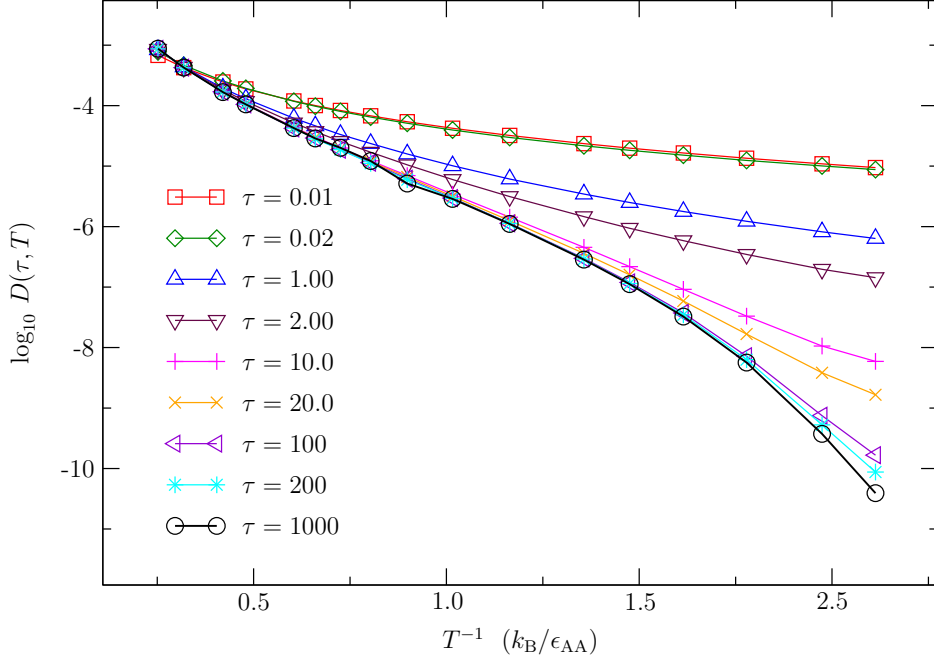


Figure 6.6:  $D(\tau, T)$  for A-type atoms in a 256-atom BLJ system with density  $1.2 \sigma_{AA}^{-3}$ . The  $\tau$  values used here are significantly shorter than in fig. 6.1b. Times are given in  $(m\sigma_{AA}^2/\epsilon_{AA})^{1/2}$ .

low-temperature trajectories mostly sample small potential energy barriers for intra-cage motion, while the high-temperature trajectories are able to access a significant number of high energy barriers corresponding to cage-breaking motion.<sup>228,232</sup> Hence there is a reduction in the effective activation barrier at the temperature for which  $\tau \approx t_p$ , and  $D(\tau, T)$  crosses over to a new Arrhenius line with shallower gradient.

If this interpretation of fig. 6.5 is correct then the same behaviour ought to be observed for any glass former (strong or fragile) at low enough temperatures and short enough time scales. Fig. 6.6 shows  $D(\tau, T)$  for a BLJ system at much smaller  $\tau$  than previously considered. As predicted, the slope of  $D(\tau, T)$  at small  $\tau$  shows positive deviation from  $D(1000, T) \approx D(T)$ . For the smallest observation time scales,  $D(\tau, T)$  converges, indicating an intra-cage activation barrier that is independent of  $\tau$  and  $T$ . The small- $\tau$  behaviour of  $D(\tau, T)$  seems to be general to both classes of supercooled liquid.

Fig. 6.7 shows both the corrected and uncorrected silicon diffusion constants ( $D^*(\tau, T)$  and  $D(\tau, T)$  respectively) for selected values of  $\tau$ . As before,  $D^*(\tau, T)$  agrees much more closely than  $D(\tau, T)$  with the correct long-time values, and Arrhenius temperature dependence is recovered at much smaller  $\tau$ . Both intra-cage and inter-cage correlation is accurately described by the average correction factor, so  $D^*(\tau, T)$  gives a good estimate of the long-time behaviour for quite small  $\tau$ .

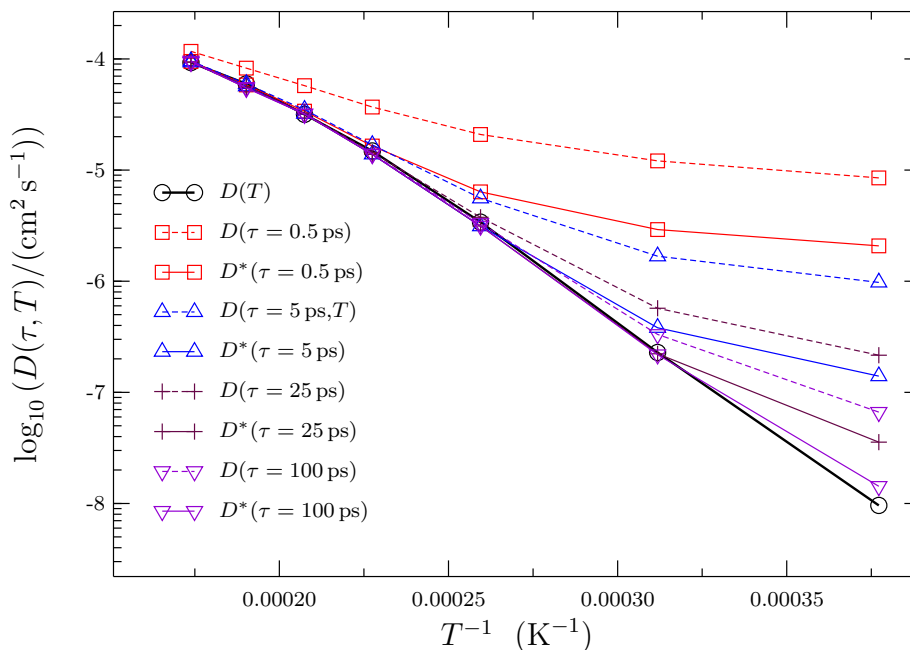


Figure 6.7: Correlation corrected short-time Si diffusion constants for silica. The long-time values and uncorrected short-time diffusion constants are shown for comparison.

The difference between strong and fragile behaviour should be explicable in terms of correlation effects. Strong temperature dependence requires a constant effective energy barrier, which implies that the magnitude of negative correlations is independent of temperature. The previous discussion shows that this condition is not met for silica for small  $\tau$ , but presumably it is true for  $\tau \rightarrow \infty$ . In contrast, negative correlations in BLJ grow with decreasing temperature for the entire range of  $\tau$  studied here.

The difference between strong and fragile liquids could be explained by the time scale on which the negative correlations decay. It is possible that correlations in fragile liquids are longer-lived than in strong liquids, and so their effect on the diffusion constant is greater.

For this hypothesis to be true, the negative correlations in silica would need either to vanish or to become temperature-independent on times comparable to  $t_p$ . This scenario implies that cage breaks in silica are weakly correlated compared with BLJ, so that the difference between strong and fragile liquids may be described as a competition between the time scales of caging and negative correlation. Both of these time scales increase at low temperatures. Only if the correlation time scale grows faster than  $t_p$  will the proportion of negative cage breaks increase, producing super-Arrhenius behaviour.

This interpretation argues that there is no fundamental difference between strong

and fragile diffusive behaviour: negative correlations are important for both, but in fragile liquids they exist on longer time scales than strong liquids. A simple test of this hypothesis is given in the next section.

For a more comprehensive investigation of correlation time scales, the temperature-dependence of  $\langle \cos \theta_{j,j+1} \rangle$  should be investigated. When  $\tau \approx t_p$ , we expect that this quantity will either be small or temperature-independent for silica, but will still grow with decreasing  $T$  for BLJ. This test cannot be undertaken at the present time, because we have not previously produced MD trajectories long enough to obtain a good average of  $\cos \theta_{j,j+1}$  for such long  $\tau$  values. These calculations will be performed in the near future as a test of the competing-timescales hypothesis.

#### 6.4.0.1 Correlation Times Scales in Cage Breaks

Comparing time scales between different model liquids requires the adoption of consistent reduced units. One approach to this problem uses the cage-breaking method described in earlier chapters.

The caging time may be estimated from the distribution of waiting times between consecutive cage breaks for an atom. This distribution shows approximately exponential decay, so the corresponding time constant,  $t_{cage}$ , is a reasonable estimate of the caging time  $t_p$ .

To estimate the correlation time scale, we use the distribution of reversal chain times, defined as the length of simulation time elapsed between the start and end of a chain of reversed cage breaks. Fig. 6.8 shows histograms of this distribution for silica and for the BLJ fluid described in §4.5. The inherent trajectories used to identify cage breaks were both obtained at  $T \approx T_c$  for the corresponding system.

Both probability distributions decay with increased chain time, with a small number of chains persisting for hundreds or thousands of caging times. The BLJ histogram decays more slowly than the silica system, and has more long chains. The longest chains for BLJ are at least an order of magnitude longer than the longest chains for silica.

These results show that the timescale of negative correlation in BLJ is appreciably longer than that for silica, which is consistent with our description of the differences between strong and fragile liquids. However, negative correlations in silica persist to times significantly greater than the typical cage waiting time, in conflict with the prediction of the previous section. This contradiction may indicate that better characteristic times are called for, or that the exact ratio between these two time scales is less important than was suggested by the short-time diffusion analysis.

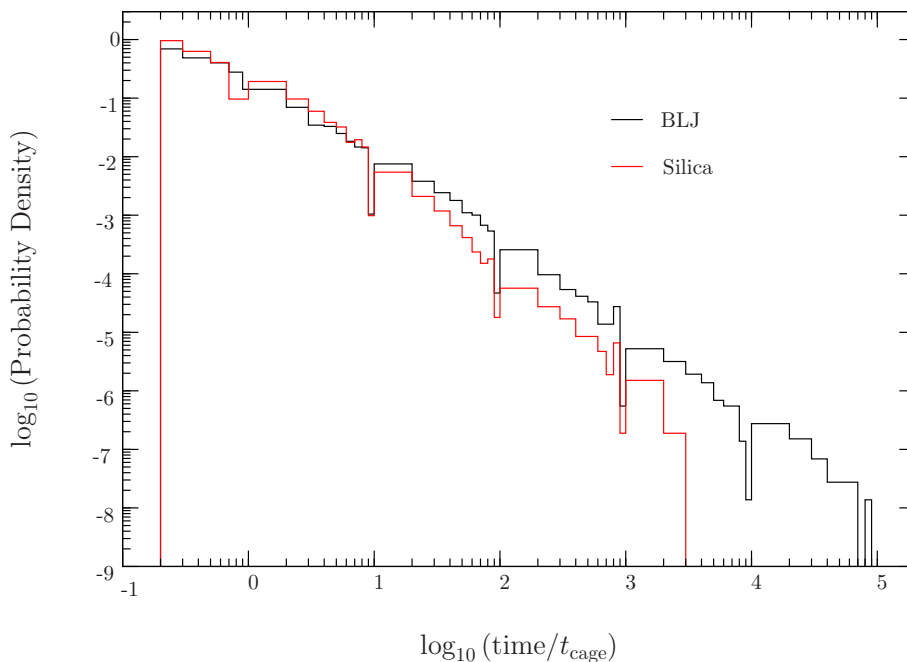


Figure 6.8: Normalised histograms for the time spent in cage-breaking reversal chains. A silica trajectory at 3207 K is compared with a 256-atom BLJ liquid with density  $1.3 \sigma_{AA}^{-3}$  and temperature  $0.65 \epsilon_{AA}/k_B$ . The data bins have unequal widths, for greater clarity on the double logarithmic scale. Times are quoted in units of the characteristic caging time (see text) for each system.

## 6.5 Pinned Glass Formers

In §5.3.3, it was argued that increasing the pinning fraction  $c$  in a model glass former decreases the frustration of the landscape, which is expected to correspond with a decrease in kinetic fragility. Chakrabarty *et al.* have previously observed this decrease using MD simulations of pinned BLJ systems.<sup>183</sup>

Fig. 6.9 shows the transport behaviour in a series of microcanonical MD simulations of pinned BLJ with various pinning fractions. Each simulation used the same reference structure, which was obtained at  $T_0 = 0.5 \epsilon_{AA}/k_B$ .

All characteristic temperatures are functions of  $c$  in a pinned system, so the inverse temperature in fig. 6.9 must be rescaled to compare between different simulations. The diffusion constants are plotted against  $T_g/T$ , where  $T_g$  is defined by  $D(T_g) = 10^{-14} \sigma_{AA} (\epsilon_{AA}/m)^{1/2}$  and determined from a VTF fit to the data. Other small values of  $D(T_g)$  provide similar results.

Fig. 6.9 shows that increasing  $c$  reduces the curvature of the Angell plot, confirming the hypothesis of chapter 5 that highly-pinned landscapes are less fragile. Based on the discussion of §6.4, we expect the behaviour of the short-time diffusion constants to change as  $c$  increases.

Fig. 6.10 shows the uncorrected and corrected diffusion constants  $D(\tau, T)$  and

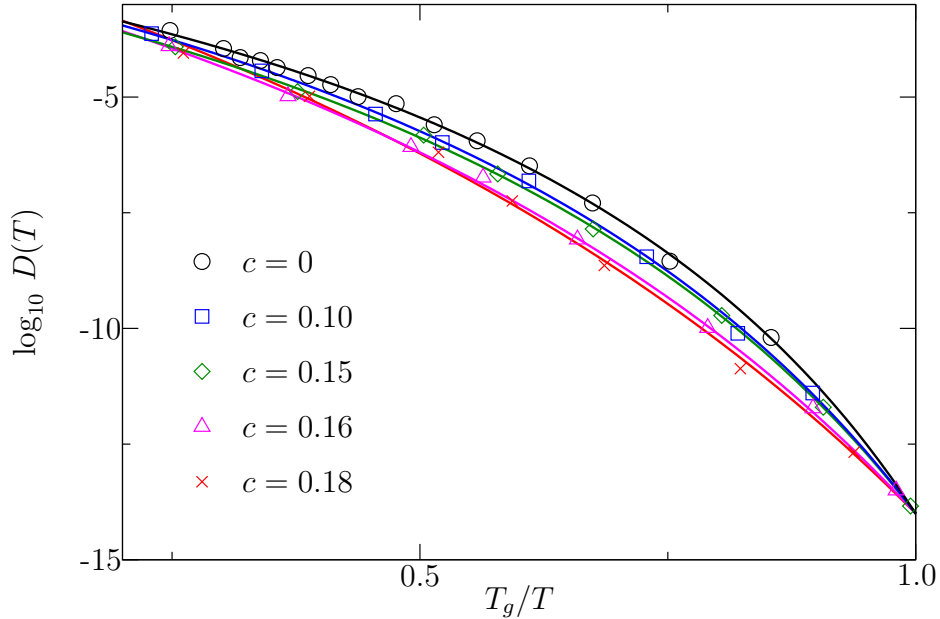


Figure 6.9: Diffusion constants for BLJ systems at a range of pinning fractions  $c$ , with a constant reference structure  $\mathbf{X}_0$  obtained at  $T_0 = 0.5 \epsilon_{AA}/k_B$ . Solid lines show VTF fits to the data points.

$D^*(\tau, T)$  for two pinned systems:  $c = 0.10$ , which is more fragile, and  $c = 0.18$ , which is relatively strong. As with all the other systems,  $D(\tau, T)$  increasingly overestimates  $D(T)$  at low  $T$  due to the emergence of anticorrelation between time intervals. Positive deviation from Arrhenius behaviour is observed at short  $\tau$  for both systems, but particularly for  $c = 0.18$ . Moreover, the temperature at which  $D(\tau, T)$  first deviates from  $D(T)$  is higher for the  $c = 0.18$  system. Both of these observations imply that the condition  $\tau < t_p$  for positive deviation of  $D(\tau, T)$  is satisfied at a higher temperature in  $c = 0.18$ , indicating that the caging time is greater at high  $c$  than low. Longer  $t_p$  means that a larger  $\tau$  is required to describe diffusion correctly for the  $c = 0.18$  system.

The correlation correction is rather successful here: remarkably good agreement is obtained between  $D^*(\tau, T)$  and  $D(T)$  at high and intermediate temperatures, even for very short  $\tau$ . The correction is better for  $c = 0.10$  than  $c = 0.18$ , probably due to the increased caging time.

These observations agree with intuitive expectations for pinned systems. Structural relaxation slows dramatically on the introduction of pinned atoms, indicating a reduced frequency of cage breaks, so it is unsurprising that the caging time scale increases with increasing  $c$ .

The decrease in kinetic fragility with increasing pinning may also be understood in terms of the correlation effect. It has been argued throughout this thesis

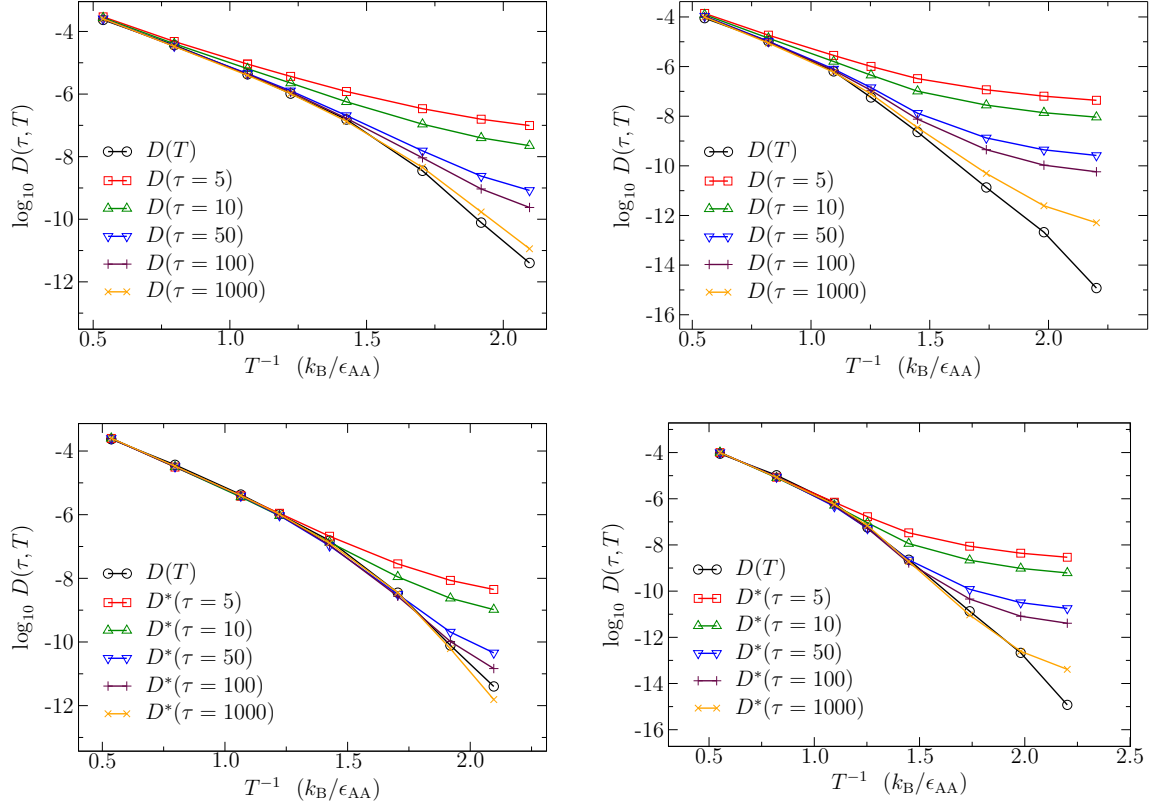


Figure 6.10: Short-time diffusion constants  $D(\tau, T)$  for two pinned BLJ systems. The two left panels show  $c = 0.10$ , the two right panels show  $c = 0.18$ . The upper two panels show  $D(\tau, T)$ , the lower two panels show the correlation-corrected behaviour  $D^*(\tau, T)$ . In each panel, a range of  $\tau$  values are presented and also the long- $\tau$  limit  $D(T)$ . Times are given in  $(m\sigma_{AA}^2/\epsilon_{AA})^{1/2}$ .

that negative correlations of cage-breaking motion arise from the presence of large metabasins, which can be loosely identified with landscape funnels. Cage-breaking transitions within a metabasin are easily reversed, because the energy barriers to return to the lowest minimum are smaller than the barriers to escape the metabasin.<sup>197</sup> Metabasins in silica contain fewer minima than those in BLJ, hence there is less driving force for anticorrelation of cage-breaking jump directions, and long-time correlation is reduced.

We saw in chapter 5 that the landscape of a highly-pinned glass former has only a single global funnel structure and consequently very few metabasins. Therefore negative correlations on the cage-breaking time scale are shorter-lived at  $c = 0.18$  than at  $c = 0.10$ , and so the super-Arrhenius curvature decreases.

## 6.6 Conclusions

In this chapter, a coarse-grained description of diffusion in supercooled liquids has been presented. The scale of the coarse-graining is set by a time parameter  $\tau$ , that serves to probe the time scales of correlated single-particle motion.

It is well established that there are two distinct mechanisms of atomic motion in a supercooled liquid: rattling within a cage of nearest neighbours, and rare jumps between cages. Both types of motion are anticorrelated on their respective time scales.

When  $\tau$  is very small, short-time diffusion analysis excludes both types of anti-correlations, yielding a significant overestimate of the true diffusion constant. Anti-correlations of rattling motion are included when  $\tau$  exceeds the typical vibrational time, but correlations between cage breaks may require much longer  $\tau$  for an accurate description. If  $\tau$  is long enough to capture individual cage breaks, but not the correlations between them, then  $D(\tau, T)$  will display Arrhenius temperature dependence regardless of the correct long-time behaviour.

We hypothesise that in strong liquids, correlations between cage breaks are comparatively weak and/or temperature-independent, as indicated by their small metabasins. Therefore  $D(T)$  and the relaxation time  $\tau_s$ , which are controlled by cage-breaking rearrangements, do not experience a temperature-dependent activation energy and the Arrhenius law is obeyed. The activation energy calculated from  $D(T)$  represents the typical free energy barrier for a cage break.

Super-Arrhenius behaviour arises when negatively correlated motions are long-lived, so that their effect extends into the diffusive regime. Then a much longer  $\tau$  is required to describe diffusion accurately.

Although much of this discussion remains to be proved definitively, its validity could be checked by comparing three important time scales,  $t_p$ ,  $t_v$  and  $t_c$  between the various systems.  $t_p$  is the time scale on which particles are confined within a cage,  $t_v$  is the average vibration time, and  $t_c$  is the correlation time for cage breaks. All three quantities depend on temperature. Comparing them requires appropriate reduced units to be devised, which is a task for future work.

$t_p$ , the caging time scale, is the simplest of the three time scales to estimate manually (e.g. from a plot of mean square displacement against time) but a precise definition is more challenging. In §6.4.0.1 the decay constant of the cage waiting time distribution was used as an estimate.

$t_v$ , the time scale of anticorrelation for rattling motion, could be estimated using the average vibrational frequency of an amorphous inherent structure. This quantity is temperature-dependent, but for a crude order-of-magnitude estimate this

dependence may be neglected.

$t_c$  is the least well-defined of the three characteristic times. One possible definition is the decay constant of the reversal chain length distribution for cage-breaking events (see §6.4.0.1). Another is the decay constant for a correlation function that uses the displacement vectors of successive cage breaks, for example:

$$C(t) = \langle \Delta \mathbf{r}_i^{\text{CB}}(t') \cdot \Delta \mathbf{r}_i^{\text{CB}}(t' + t) \rangle. \quad (6.6)$$

Here  $\Delta \mathbf{r}_i^{\text{CB}}(t')$  is the displacement vector of particle  $i$  during a cage break at time  $t'$ .  $\langle \dots \rangle$  indicates an average over particles  $i$  and over initial times  $t'$ . The problem with this method is that one can only accumulate the average by comparing pairs of cage breaks, which are comparatively rare, so an extremely long MD trajectory is required to calculate  $C(t)$  accurately at low temperatures.

Pinned glass formers may be particularly useful to test the hypothesis that super-Arrhenius behaviour arises from significant correlations between cage breaks. Highly-pinned systems are stronger than weakly-pinned, so pinning allows the fragility of a model liquid to be varied without needing to change the pairwise potential. This tunability may arise from the reduction in the number of metabasins with increasing pinning, which reduces the negative correlation of cage-breaking rearrangements.

# Chapter 7

## Conclusions

In this thesis, I have demonstrated that the potential energy landscapes of glass-forming liquids contain a significant degree of higher-order structure, characterised by the organisation of minima into *local funnels*. The variation in structure between different glass forming systems is considerable, particularly when quenched disorder is introduced by the method of random particle pinning. The presence or absence of higher order structure has a significant effect on the dynamic and structural behaviour of liquids in the supercooled temperature regime.

I have shown that cage-breaking rearrangements, defined by changes to the nearest-neighbour environments of rearranging particles, provide a good description of dynamics in viscous silica (a strong liquid) as well as in the fragile BLJ and OTP fluids. The origin of caging is different in the different systems, but analogous definitions of a cage break are able to describe the important structural rearrangements in all three models. A generalisation of the cage break definition for simple rigid molecules was proposed, which is almost entirely free of system-dependent parameters.

The success of the cage-breaking method derives from its connection to the potential energy landscape (PEL). Transitions in which particles undergo cage breaks are both necessary and sufficient for a system to traverse a complicated PEL. Moreover, selecting only unreversed cage-breaking transitions captures the higher-order structure of local funnels very effectively in fragile systems. The regions of the landscape that are bounded by these *productive cage breaks* are identified with *geometric metabasins*, which provide an effective coarse-grained description of glassy dynamics.

The geometric metabasin description is valid for the landscape of the Lewis-Wahnström OTP model, as well as for BLJ. Metabasins are present in the landscape of the strong glass former silica, but they contain many fewer minima than the equivalent structures in the PELs of fragile liquids. This result adds to a

growing body of evidence that the diffusion mechanisms of strong and fragile liquids are fundamentally the same, but differ quantitatively in some key dynamical properties.<sup>124,125,235,236</sup>

One such quantity is the time scale of correlation. Previously,<sup>254,255</sup> negative correlations of particle displacement vectors were shown to produce super-Arrhenius behaviour in fragile BLJ, and so it was assumed that these correlations would be absent in silica. In fact, correlation effects are still important in the strong liquid at short times corresponding to cage-rattling motion. I have presented some evidence to suggest that cage breaks are less strongly correlated in silica than in OTP or BLJ. This suggestion is compatible with earlier work, which found that “strings” of highly-mobile particles which characterise low- $T$  dynamics are much longer in fragile liquids than in silica.<sup>124,125</sup>

Negative correlation of jump direction between consecutive cage breaks is believed to result from the presence of local funnels on the PEL (i.e. metabasins). Transitions away from the bottom of the funnel are likely to be reversed, since the downhill energy barriers are smaller than the uphill barriers.<sup>197</sup> The reversal probability increases at lower temperature, because the system is more likely to be found in the lower-energy regions of the funnel. Explaining why reversals are less likely for silica than for BLJ in terms of local funnel properties is an important challenge.

The differences in structure of the PEL between strong and fragile liquids are subtle and quantitative. A much greater change in the PEL is observed when some particles are pinned in place. The PEL of a pinned system depends on the disorder realisation - i.e. the number, positions and atom types of the pinned particles. As the concentration  $c$  of pinned particles increases, the number of low-energy landscape funnels accessible to the mobile particles decreases dramatically, undergoing a crossover in  $c$  to a *pinned glass* state where only structures similar to the original reference configuration are accessible. This crossover almost certainly corresponds to the random pinning glass transition (RPGT) predicted by the random first order transition theory (RFOT).<sup>175</sup>

To analyse the crossover, a new method for identifying local structure on a PEL has been introduced. This method uses the overlap function, which is the natural order parameter for phase transitions in mean-field model glasses.<sup>152,175</sup> The *packings* identified by the new method agree remarkably well with local funnels visible in disconnectivity graphs of glass formers, and with dynamical metabasins under some conditions. At low temperatures, residence of the system within a packing will be quite long, so that these structures may also be identified with the *quasistates* needed to formulate a mean-field-like theory of structural glass formers.<sup>32,153</sup>

High- $c$  landscapes are qualitatively different to those of unpinned glasses, and resemble a single global funnel with the reference structure near its base. This global funnel has significant internal structure, with a wide range of intra-funnel barrier heights and minima energies. However, the global funnel is well defined because the energy barriers that must be crossed to reach a different funnel are much larger than the barriers within the funnel. Large-scale structural reorganisation requires crossing between funnels, and therefore becomes very slow in a highly-pinned system. Increasing  $c$  at fixed  $T$  causes further slowing of dynamics, and eventually induces structural arrest over finite observation times. RFOT theory predicts that this arrest persists in the thermodynamic limit as an equilibrium phase transition. Testing this prediction is an important task for future work, and I have suggested a landscape method of performing this test.

Pinning particles also causes the kinetic fragility (the degree of super-Arrhenius curvature in the diffusion constant) to decrease. I have explained this effect using the changes in landscape structure: fewer low-energy funnels at high  $c$  means that there are fewer accessible metabasins and fewer reversed cage breaks, hence super-Arrhenius behaviour is reduced. However, note that the presence of global structure makes the PEL of a pinned fragile glass former very different from the PEL of an unpinned strong glass former. Therefore, one should not expect the dynamics of these two types of system to be identical.

The results in this thesis provide a coherent, simplified description of dynamics in the moderately supercooled temperature range, roughly corresponding to the landscape-influenced regime described by Sastry *et al.*<sup>225</sup> Key challenges for future work include relating this description to other theories of the glass transition, and adapting it to make quantitative predictions of experimental properties.

Cage breaks and metabasins relate to dynamical descriptions of glassy behaviour, while the division of configuration space into long-lived quasistates (i.e. packings) arises from thermodynamic theories, particularly the RFOT approach. I have shown that these methods are linked by dependence on higher-order structure in the PEL.

Cage breaks are an effective tool for identifying important structural rearrangements, especially near and below the MCT critical temperature. These events involve larger structural rearrangements than single-particle jumps detected using short-time square displacements,<sup>107</sup> and are probably more collective in nature. Identifying productive cage breaks with the metabasin description of Heuer *et al.*<sup>197,229,230</sup> provides a link between dynamical descriptions of the glass transition and the PEL approach.

To elaborate these links further, a closer investigation of the spatiotemporal

correlations of cage breaks is required. Such an investigation would test the negative correlation description of fragility, and would help to connect glassy theories such as dynamical facilitation and the string method to the PEL picture. Correlations between consecutive cage breaks of a single particle are already known to increase at lower temperatures,<sup>233,245,308</sup> so an important question is whether simultaneous cage-breaks are also correlated in space. We expect that some regions of space-time in a simulation should contain much higher densities of cage breaks than others, resulting in spatially heterogeneous dynamics as observed by experiment. It would be interesting to see whether clusters of cage breaks resemble the strings observed by Glotzer *et al.*,<sup>120</sup> and whether the occurrence of a cage break facilitates subsequent rearrangements nearby as expected in the space-time thermodynamic description of Chandler and coworkers.<sup>74</sup>

The close relationship between the RPGT and the changes in structure of the PEL emphasise that the RFOT theory is connected with the landscape description of supercooled liquids. The RFOT approach claims that a liquid system separates into weakly-interacting domains on cooling below the MCT temperature  $T_c$ , and that each of these domains selects an amorphous structure at random from a “library” of possible states.<sup>31</sup> In the landscape description, each domain has its own PEL that can be explored independently of the other domains (since they are non-interacting). Selection of an amorphous structure from the library is equivalent to the system becoming trapped in a particular landscape funnel on the observation time scale. Quantitative examination of the relationship between the RFOT and PEL descriptions will require a careful size-scaling analysis of PEL properties and structure.

The literature of the glass transition is extensive and convoluted, containing so many competing theories that resolving the contradictions between them is a daunting task. My results represent a step towards connecting some of these approaches, by proposing links between several popular analysis methods and by describing supercooled dynamics using concepts from several different theories. The potential energy landscape remains one of the most powerful and fundamental concepts in the study of model glass formers, therefore methods based on the properties and structure of this landscape have significant potential to bridge the divides between different schools of thought in this complex field.

# References

- [1] Ericson, J.E., Makishima, A., Mackenzie, J.D. and Berger, R., *J. Non-Cryst. Solids*, **17**, 129 (1975)
- [2] Greer, A.L., *Materials Today*, **12**, 14 (2009)
- [3] Yu, L., *Adv. Drug Deliv. Rev.*, **48**, 27 (2001)
- [4] Wales, D.J., *Energy Landscapes*, (Cambridge University Press, Cambridge, 2003)
- [5] Angell, C., *J. Phys. Chem. Solids*, **49**, 863 (1988)
- [6] Karmakar, S., Dasgupta, C. and Sastry, S., *Rep. Prog. Phys.*, **79**, 016601 (2016)
- [7] Angell, C., Ngai, K., McKenna, G.B., McMillan, P.F. and Martin, S.W., *J. Appl. Phys.*, **88**, 3113 (2000)
- [8] Angell, C.A., *Chem. Rev.*, **102**, 26272650 (2002)
- [9] Pedersen, U. and Harrowell, P., *J. Phys. Chem. B*, **115**, 14205 (2011)
- [10] Kob, W. and Andersen, H., *Phys. Rev. E*, **51**, 4626 (1995)
- [11] Osamu, H., Hiroshi, S. and Syz, S., *Chem. Lett.*, **2**, 79 (1973)
- [12] Ediger, M.D., *J. Chem. Phys.*, **147**, 210901 (2017)
- [13] Lombardo, T.G., Debenedetti, P.G. and Stillinger, F.H., *J. Chem. Phys.*, **125**, 174507 (2006)
- [14] Shi, Z., Debenedetti, P.G. and Stillinger, F.H., *J. Chem. Phys.*, **138**, 12A526 (2013)
- [15] Eastwood, M.P., Chitra, T., Jumper, J.M., Palmo, K., Pan, A.C. and Shaw, D.E., *J. Phys. Chem. B*, **117**, 12898 (2013)
- [16] Li, Y.w., Zhu, Y.l. and Sun, Z.y., *J. Chem. Phys.*, **142**, 124507 (2015)
- [17] Rinaldi, A., Sciortino, F. and Tartaglia, P., *Phys. Rev. E*, **63**, 061210 (2001)
- [18] Mossa, S., Ruocco, G. and Sampoli, M., *Phys. Rev. E*, **64**, 021511 (2001)

- 
- [19] Ninarello, A., Berthier, L. and Coslovich, D., *Mol. Phys.*, **113**, 2707 (2015)
- [20] Taborek, P., Kleiman, R.N. and Bishop, D.J., *Phys. Rev. B*, **34**, 1835 (1986)
- [21] Rössler, E. and Eiermann, P., *J. Chem. Phys.*, **100**, 5237 (1994)
- [22] Dixon, P.K., *Phys. Rev. B*, **42**, 8179 (1990)
- [23] Hansen, C., Richert, R. and Fischer, E., *J. Non-Cryst. Solids*, **215**, 293 (1997)
- [24] Pardo, L.C., Lunkenheimer, P. and Loidl, A., *Phys. Rev. E*, **76**, 030502 (2007)
- [25] Angell, C.A., *Science*, **267**, 1924 (1995)
- [26] de Souza, V.K. and Wales, D.J., *J. Chem. Phys.*, **123**, 134504 (2005)
- [27] Debenedetti, P.G. and Stillinger, F.H., *Nature*, **410**, 259 (2001)
- [28] Raza, Z., Alling, B. and Abrikosov, I.A., *J. Phys. Cond. Mat.*, **27**, 293201 (2015)
- [29] Stillinger, F.H., *J. Chem. Phys.*, **89**, 6461 (1988)
- [30] Adam, G. and Gibbs, J.H., *J. Chem. Phys.*, **43**, 139 (1965)
- [31] Lubchenko, V. and Wolynes, P.G., *Ann. Rev. Phys. Chem.*, **58**, 235 (2007)
- [32] Cavagna, A., *Phys. Rep.*, **476**, 51 (2009)
- [33] Chen, S.H., Mallamace, F., Mou, C.Y., Broccio, M., Corsaro, C., Faraone, A. and Liu, L., *Proc. Natl. Acad. Sci. USA*, **103**, 12974 (2006)
- [34] Vollmayr-Lee, K., Kob, W., Binder, K. and Zippelius, A., *J. Chem. Phys.*, **116**, 5158 (2002)
- [35] Fujara, F., Geil, B., Sillescu, H. and Fleischer, G., *Z. Phys. B.*, **88**, 195 (1992)
- [36] Chang, I., Fujara, F., Geil, B., Heuberger, G., Mangel, T. and Sillescu, H., *J. Non-Cryst. Solids*, **172-174**, 248 (1994)
- [37] Swallen, S.F., Bonvallet, P.A., McMahon, R.J. and Ediger, M.D., *Phys. Rev. Lett.*, **90**, 015901 (2003)
- [38] Mapes, M.K., Swallen, S.F. and Ediger, M.D., *J. Phys. Chem. B*, **110**, 507 (2006)
- [39] Frenkel, D. and Smit, B., *Understanding Molecular Simulation*, Second Edition (Academic Press, San Diego, 2002)
- [40] Zwanzig, R., *J. Chem. Phys.*, **79**, 4507 (1983)
- [41] Erpenbeck, J.J. and Wood, W.W., *Phys. Rev. A*, **43**, 4254 (1991)
-

- 
- [42] Fernández, G.A., Vrabec, J. and Hasse, H., *Int. J. Thermophys.*, **25**, 175 (2004)
- [43] Mossa, S., Nave, E.L., Stanley, H.E., Donati, C., Sciortino, F. and Tartaglia, P., *Phys. Rev. E*, **65**, 041205 (2002)
- [44] Edmond, K.V., Elsesser, M.T., Hunter, G.L., Pine, D.J. and Weeks, E.R., *Proc. Natl. Acad. Sci. USA*, **109**, 17891 (2012)
- [45] Weeks, E.R. and Weitz, D.A., *Phys. Rev. Lett.*, **89**, 095704 (2002)
- [46] Weeks, E.R. and Weitz, D., *Chem. Phys.*, **284**, 361 (2002)
- [47] Doliwa, B. and Heuer, A., *Phys. Rev. Lett.*, **80**, 4915 (1998)
- [48] Mazza, M.G., Giovambattista, N., Stanley, H.E. and Starr, F.W., *Phys. Rev. E*, **76**, 031203 (2007)
- [49] Chong, S.H. and Kob, W., *Phys. Rev. Lett.*, **102**, 025702 (2009)
- [50] Richert, R., *J. Phys. Cond. Mat.*, **14**, 703 (2002)
- [51] Chen, S.H. and Tartaglia, P., *Scattering Methods in Complex Fluids*, (Cambridge University Press, Cambridge, 2015)
- [52] van Megen, W. and Underwood, S.M., *Phys. Rev. Lett.*, **70**, 2766 (1993)
- [53] Berthier, L. and Biroli, G., *Rev. Mod. Phys.*, **83**, 587 (2011)
- [54] Kohlrausch, R., *Annalen der Physik*, **167**, 179 (1854)
- [55] Williams, G. and Watts, D.C., *Trans. Faraday Soc.*, **66**, 80 (1970)
- [56] Dixon, P.K., Wu, L., Nagel, S.R., Williams, B.D. and Carini, J.P., *Phys. Rev. Lett.*, **65**, 1108 (1990)
- [57] Johari, G.P. and Goldstein, M., *J. Chem. Phys.*, **53**, 2372 (1970)
- [58] Williams, G. and Watts, D.C., *Trans. Faraday Soc.*, **67**, 1971 (1971)
- [59] Wu, L., *Phys. Rev. B*, **43**, 9906 (1991)
- [60] Ngai, K.L., Lunkenheimer, P., Len, C., Schneider, U., Brand, R. and Loidl, A., *J. Chem. Phys.*, **115**, 1405 (2001)
- [61] Cicerone, M.T. and Tyagi, M., *J. Chem. Phys.*, **146**, 054502 (2017)
- [62] Galley, W. and Purkey, R., *Proc. Natl. Acad. Sci. USA*, **67**, 1116 (1970)
- [63] Chamberlin, R.V., Schiener, B. and Bhmer, R., *MRS Proceedings*, **455**, 117 (1996)
- [64] Heuer, A., *Phys. Rev. E*, **56**, 730 (1997)
-

- 
- [65] Vidal Russell, E. and Israeloff, N.E., *Nature*, **408**, 695 (2000)
- [66] Tracht, U., Wilhelm, M., Heuer, A., Feng, H., Schmidt-Rohr, K. and Spiess, H.W., *Phys. Rev. Lett.*, **81**, 2727 (1998)
- [67] Reinsberg, S.A., Heuer, A., Doliwa, B., Zimmermann, H. and Spiess, H.W., *J. Non-Cryst. Solids*, **307-310**, 208 (2002)
- [68] Cicerone, M.T., Blackburn, F.R. and Ediger, M.D., *J. Chem. Phys.*, **102**, 471 (1995)
- [69] Ediger, M.D., *Annu. Rev. Phys. Chem.*, **51**, 99 (2000)
- [70] Kob, W., Donati, C., Plimpton, S.J., Poole, P.H. and Glotzer, S.C., *Phys. Rev. Lett.*, **79**, 2827 (1997)
- [71] Qian, J., Hentschke, R. and Heuer, A., *J. Chem. Phys.*, **111**, 10177 (1999)
- [72] Glotzer, S.C., Novikov, V.N. and Schröder, T.B., *J. Chem. Phys.*, **112**, 509 (2000)
- [73] Berthier, L., *Phys. Rev. E*, **69**, 020201 (2004)
- [74] Chandler, D. and Garrahan, J.P., *Ann. Rev. Phys. Chem.* **61**, 191 (2009)
- [75] Ediger, M.D. and Harrowell, P., *J. Chem. Phys.*, **137**, 080901 (2012)
- [76] Lačević, N. and Glotzer, S.C., *J. Phys. Cond. Mat.*, **15**, S2437 (2003)
- [77] Kauzmann, W., *Chem. Rev.*, **43**, 219 (1948)
- [78] Mézard, M. and Parisi, G., *Phys. Rev. Lett.*, **82**, 747 (1999)
- [79] Biroli, G. and Garrahan, J.P., *J. Chem. Phys.*, **138**, 12A301 (2013)
- [80] Moynihan, C.T., Macedo, P.B., Montrose, C.J., Gupta, P.K., DeBolt, M.A., Dill, J.F., Dom, B.E., Drake, P.W., Eastal, A.J., Elterman, P.B., Moeller, R.P., Sasabe, H. and Wilder, J.A., *Ann. N. Y. Acad. Sci.*, **279**, 15 (1976)
- [81] Hodge, I., *J. Non-Cryst. Solids*, **169**, 211 (1994)
- [82] Velikov, V., Borick, S. and Angell, C.A., *Science*, **294**, 2335 (2001)
- [83] Keys, A.S., Garrahan, J.P. and Chandler, D., *Proc. Natl. Acad. Sci. USA*, **110**, 4482 (2013)
- [84] Badrinarayanan, P., Zheng, W., Li, Q. and Simon, S.L., *J. Non-Cryst. Solids*, **353**, 2603 (2007)
- [85] Angell, C.A., *J. Res. Natl Inst. Stand. Technol.*, **102**, 171 (1997)
- [86] Alder, B.J. and Wainwright, T.E., *J. Chem. Phys.*, **27**, 1208 (1957)
- [87] Wood, W.W. and Jacobson, J.D., *J. Chem. Phys.*, **27**, 1207 (1957)
-

- 
- [88] Hoover, W.G. and Ree, F.H., *J. Chem. Phys.*, **49**, 3609 (1968)
- [89] Frenkel, D. and Ladd, A.J.C., *J. Chem. Phys.*, **81**, 3188 (1984)
- [90] Kearns, K.L., Swallen, S.F., Ediger, M.D., Wu, T., Sun, Y. and Yu, L., *J. Phys. Chem. B*, **112**, 4934 (2008)
- [91] Berthier, L., Charbonneau, P., Coslovich, D., Ninarello, A., Ozawa, M. and Yaida, S., *Proc. Natl. Acad. Sci. USA*, **114**, 11356 (2017)
- [92] Stillinger, F.H., *J. Chem. Phys.*, **88**, 7818 (1988)
- [93] Bengtzelius, U., Götze, W. and Sjölander, A., *J. Phys. C*, **17**, 5915 (1984)
- [94] Geszti, T., *J. Chem. Phys.*, **16**, 5805 (1983)
- [95] Götze, W. and Sjögren, L., *J. Phys. C*, **21**, 3407 (1988)
- [96] Ediger, M.D., Angell, C.A. and Nagel, S.R., *J. Phys. Chem.*, **100**, 13200 (1996)
- [97] Adichtchev, S., Bagdassarov, N., Benkhof, S., Blochowicz, T., Novikov, V., Rssler, E., Surovtsev, N., Tschirwitz, C. and Wiedersich, J., *J. Non-Cryst. Solids*, **307**, 24 (2002)
- [98] Berthier, L. and Garrahan, J.P., *Phys. Rev. E*, **68**, 041201 (2003)
- [99] Götze, W. and Sjögren, L., *Z. Phys. B*, **65**, 415 (1987)
- [100] Pastore, R., Coniglio, A. and Pica Ciamarra, M., *Soft Matter*, **10**, 5724 (2014)
- [101] Rabani, E., Gezelter, J.D. and Berne, B.J., *J. Chem. Phys.*, **107**, 6867 (1997)
- [102] Rabani, E., Gezelter, J.D. and Berne, B.J., *Phys. Rev. Lett.*, **82**, 3649 (1999)
- [103] Rabani, E., Gezelter, J.D. and Berne, B.J., *J. Chem. Phys.*, **110**, 3444 (1999)
- [104] Rabani, E., Gezelter, J.D. and Berne, B.J., *Phys. Rev. Lett.*, **85**, 467 (2000)
- [105] Widmer-Cooper, A., Perry, H., Harrowell, P. and Reichman, D., *Nat. Phys.*, **4**, 711 (2008)
- [106] Doliwa, B. and Heuer, A., *J. Phys. Cond. Mat.*, **11**, A277 (1999)
- [107] Pica Ciamarra, M., Pastore, R. and Coniglio, A., *Soft Matter*, **12**, 10 (2015)
- [108] Pastore, R., Pesce, G., Sasso, A. and Pica Ciamarra, M., *J. Phys. Chem. Lett.*, **8**, 1562 (2017)
- [109] Helfferich, J., Ziebert, F., Frey, S., Meyer, H., Farago, J., Blumen, A. and Baschnagel, J., *Phys. Rev. E*, **89**, 042603 (2014)
- [110] Helfferich, J., Vollmayr-Lee, K., Ziebert, F., Meyer, H. and Baschnagel, J., *Europhys. Lett.*, **109**, 36004 (2015)
-

- 
- [111] Kluge, M. and Schober, H.R., *Phys. Rev. B*, **70**, 224209 (2004)
- [112] Vollmayr-Lee, K., *J. Chem. Phys.*, **121**, 4781 (2004)
- [113] Candelier, R., Widmer-Cooper, A., Kummerfeld, J.K., Dauchot, O., Biroli, G., Harrowell, P. and Reichman, D.R., *Phys. Rev. Lett.*, **105**, 135702 (2010)
- [114] Candelier, R., Dauchot, O. and Biroli, G., *Phys. Rev. Lett.*, **102**, 088001 (2009)
- [115] Vollmayr-Lee, K., Bjorkquist, R. and Chambers, L.M., *Phys. Rev. Lett.*, **110**, 017801 (2013)
- [116] Pastore, R., Coniglio, A. and Ciamarra, M.P., *Sci. Rep.*, **5**, 11770 (2015)
- [117] Pastore, R., Pica Ciamarra, M., Pesce, G. and Sasso, A., *Soft Matter*, **11**, 622 (2015)
- [118] Hurley, M.M. and Harrowell, P., *Phys. Rev. E*, **52**, 1694 (1995)
- [119] Hansen, J.P. and McDonald, I.R., *Theory of Simple Liquids*, Third Edition, (Academic Press, Burlington, 2006)
- [120] Donati, C., Douglas, J.F., Kob, W., Plimpton, S.J., Poole, P.H. and C.Glotzer, S., *Phys. Rev. Lett.*, **80**, 2338 (1998)
- [121] Dasgupta, C., Indrani, A.V., Ramaswamy, S. and Phani, M.K., *Europhys. Lett.*, **15**, 307 (1991)
- [122] Donati, C., Franz, S., Glotzer, S.C. and Parisi, G., *J. Non-Cryst. Solids*, **307-310**, 215 (2002)
- [123] Schroder, T.B., Sastry, S., Dyre, J.C. and Glotzer, S.C., *J. Chem. Phys.*, **112**, 9834 (2000)
- [124] Vogel, M. and Glotzer, S.C., *Phys. Rev. E*, **70**, 061504 (2004)
- [125] Vogel, M. and Glotzer, S.C., *Phys. Rev. Lett.*, **92**, 255901 (2004)
- [126] Oligschleger, C. and Schober, H.R., *Phys. Rev. B*, **59**, 811 (1999)
- [127] Mosayebi, M., Ilg, P., Widmer-Cooper, A. and Del Gado, E., *Phys. Rev. Lett.*, **112**, 105503 (2014)
- [128] Manning, M.L. and Liu, A.J., *Phys. Rev. Lett.*, **107**, 108302 (2011)
- [129] Cubuk, E.D., Schoenholz, S.S., Rieser, J.M., Malone, B.D., Rottler, J., Durian, D.J., Kaxiras, E. and Liu, A.J., *Phys. Rev. Lett.*, **114**, 108001 (2015)
- [130] Schoenholz, S.S., Cubuk, E.D., Sussman, D.M., Kaxiras, E. and Liu, A.J., *Nat. Phys.*, **12**, 469 (2016)
- [131] Cubuk, E.D., Schoenholz, S.S., Kaxiras, E. and Liu, A.J., *J. Phys. Chem. B*, **120**, 6139 (2016)
-

- 
- [132] Malins, A., Williams, S.R., Eggers, J. and Royall, C.P., *J. Chem. Phys.*, **139**, 234506 (2013)
- [133] Malins, A., Eggers, J., Royall, C.P., Williams, S.R. and Tanaka, H., *J. Chem. Phys.*, **138**, 12A535 (2013)
- [134] Speck, T., Malins, A. and Royall, C.P., *Phys. Rev. Lett.*, **109**, 195703 (2012)
- [135] Pinney, R., Liverpool, T.B. and Royall, C.P., *J. Chem. Phys.*, **143**, 244507 (2015)
- [136] Ritort, F. and Sollich, P., *Adv. Phys.*, **52**, 219 (2003)
- [137] Garrahan, J.P. and Chandler, D., *Proc. Natl. Acad. Sci. USA*, **100**, 9710 (2003)
- [138] Widmer-Cooper, A. and Harrowell, P., *J. Chem. Phys.*, **126**, 154503 (2007)
- [139] Merolle, M., Garrahan, J.P. and Chandler, D., *Proc. Natl. Acad. Sci. USA*, **102**, 10837 (2005)
- [140] Ruelle, D., *Thermodynamic Formalism* (Addison-Wesley, Reading, MA, 1978)
- [141] Garrahan, J.P., Jack, R.L., Lecomte, V., Pitard, E., van Duijvendijk, K. and van Wijland, F., *Phys. Rev. Lett.*, **98**, 195702 (2007)
- [142] Dellago, C., Bolhuis, P.G., Csajka, F.S. and Chandler, D., *J. Chem. Phys.*, **108**, 1964 (1998)
- [143] Bolhuis, P.G., Chandler, D., Dellago, C. and Geissler, P.L., *Ann. Rev. Phys. Chem.*, **53**, 291 (2002)
- [144] Szamel, G. and Flenner, E., *Phys. Rev. E*, **74**, 021507 (2006)
- [145] Stariolo, D.A. and Fabricius, G., *J. Chem. Phys.*, **125**, 064505 (2006)
- [146] Swallen, S.F., Traynor, K., McMahon, R.J., Ediger, M.D. and Mates, T.E., *J. Phys. Chem. B*, **113**, 4600 (2009)
- [147] Biroli, G., Bouchaud, J.P. and Tarjus, G., *J. Chem. Phys.*, **123**, 044510 (2005)
- [148] Chandler, D. and Garrahan, J.P., *J. Chem. Phys.*, **123**, 044511 (2005)
- [149] Candelier, R., Dauchot, O. and Biroli, G., *Europhys. Lett.*, **92**, 24003 (2010)
- [150] Biroli, G. and Bouchaud, J., in *Structural Glasses and Supercooled Liquids*, eds P. G. Wolynes and V. Lubchenko (John Wiley & Sons, Hoboken, NJ, 2012) pp31–113,
- [151] Angell, C. and Borick, S., *J. Non-Cryst. Solids*, **307-310**, 393 (2002)
- [152] Kirkpatrick, T.R. and Wolynes, P.G., *Phys. Rev. B*, **36**, 8552 (1987)
-

- 
- [153] Biroli, G. and Kurchan, J., *Phys. Rev. E*, **64**, 016101 (2001)
- [154] Bouchaud, J.P. and Biroli, G., *J. Chem. Phys.*, **121**, 7347 (2004)
- [155] Stillinger, F.H. and Debenedetti, P.G., *Ann. Rev. Cond. Mat. Phys.*, **4**, 263 (2013)
- [156] Johari, G.P., *J. Chem. Phys.*, **112**, 8958 (2000)
- [157] Kirkpatrick, T.R. and Thirumalai, D., *Phys. Rev. Lett.*, **58**, 2091 (1987)
- [158] Kirkpatrick, T.R. and Thirumalai, D., *Phys. Rev. B*, **36**, 5388 (1987)
- [159] Castellani, T. and Cavagna, A., *J. Stat. Mech. Theory Exp.*, **2005**, P05012 (2005)
- [160] Tracht, U., Wilhelm, M., Heuer, A., Feng, H., Schmidt-Rohr, K. and Spiess, H.W., *Phys. Rev. Lett.*, **81**, 2727 (1998)
- [161] Cammarota, C. and Biroli, G., *Proc. Natl. Acad. Sci. USA*, **109**, 8850 (2012)
- [162] Singh, Y., Stoessel, J.P. and Wolynes, P.G., *Phys. Rev. Lett.*, **54**, 1059 (1985)
- [163] Kirkpatrick, T.R., Thirumalai, D. and Wolynes, P.G., *Phys. Rev. A*, **40**, 1045 (1989)
- [164] Stevenson, J.D. and Wolynes, P.G., *J. Phys. Chem. B*, **109**, 15093 (2005)
- [165] Xia, X. and Wolynes, P.G., *Phys. Rev. Lett.*, **86**, 5526 (2001)
- [166] Whitford, P.C. and Phillips, G.D.J., *Phys. Rev. E*, **72**, 021203 (2005)
- [167] Sausset, F. and Tarjus, G., *Phys. Rev. Lett.*, **104**, 065701 (2010)
- [168] Berthier, L., Biroli, G., Bouchaud, J.P., Cipelletti, L., El Masri, D., L'Hôte, D., Ladieu, F. and Pierno, M., *Science*, **310**, 1797 (2005)
- [169] Biroli, G., Bouchaud, J.P., Cavagna, A., Grigera, T.S. and Verrocchio, P., *Nat. Phys.*, **4**, 771 (2008)
- [170] Berthier, L. and Kob, W., *Phys. Rev. E*, **85**, 011102 (2012)
- [171] Scheidler, P., Kob, W., Binder, K. and Parisi, G., *Philos. Mag. B*, **82**, 283 (2002)
- [172] Kim, K., Miyazaki, K. and Saito, S., *J. Phys. Cond. Mat.*, **23**, 234123 (2011)
- [173] Fullerton, C.J. and Jack, R.L., *Phys. Rev. Lett.*, **112**, 255701 (2014)
- [174] Kim, K., *Europhys. Lett.*, **61**, 790 (2003)
- [175] Cammarota, C. and Biroli, G., *Proc. Natl. Acad. Sci. USA*, **109**, 8850 (2011)
- [176] Krakoviack, V., *Phys. Rev. E*, **84**, 050501 (2011)
-

- 
- [177] Szamel, G. and Flenner, E., *Europhys. Lett.*, **101**, 66005 (2013)
- [178] Kob, W. and Coslovich, D., *Phys. Rev. E*, **90**, 052305 (2014)
- [179] Chakrabarty, S., Das, R., Karmakar, S. and Dasgupta, C., *J. Chem. Phys.*, **145**, 034507 (2016)
- [180] Cammarota, C. and Seoane, B., *Phys. Rev. B*, **94**, 180201 (2016)
- [181] Das, R., Chakrabarty, S. and Karmakar, S., *Soft Matter*, **13**, 6929 (2017)
- [182] Ozawa, M., Kob, W., Ikeda, A. and Miyazaki, K., *Proc. Natl. Acad. Sci. USA*, **112**, 6914 (2015)
- [183] Chakrabarty, S., Karmakar, S. and Dasgupta, C., *Sci. Rep.*, **5**, 12577 (2015)
- [184] Chakrabarty, S., Karmakar, S. and Dasgupta, C., *Proc. Natl. Acad. Sci. USA*, **112**, E4819 (2015)
- [185] Ozawa, M., Kob, W., Ikeda, A. and Miyazaki, K., *Proc. Natl. Acad. Sci. USA*, **112**, E4821 (2015)
- [186] Zheng, W., Tsai, M.Y., Chen, M. and Wolynes, P.G., *Proc. Natl. Acad. Sci. USA*, **113**, 11835 (2016)
- [187] Zhang, B. and Wolynes, P.G., *Biophys. J.*, **112**, 427 (2017)
- [188] Joseph, J.A., Roder, K., Chakraborty, D., Mantell, R.G. and Wales, D.J., *Chem. Commun.*, **53**, 6974 (2017)
- [189] Chebaro, Y., Ballard, A.J., Chakraborty, D. and Wales, D.J., *Sci. Rep.*, **5**, 10386 (2015)
- [190] Husic, B.E., Schebarchov, D. and Wales, D.J., *Nanoscale*, **8**, 18326 (2016)
- [191] Seymour, I.D., Wales, D.J. and Grey, C.P., *J. Phys. Chem. C*, **120**, 19521 (2016)
- [192] Das, R. and Wales, D.J., *Phys. Rev. E*, **93**, 063310 (2016)
- [193] Goldstein, M., *J. Chem. Phys.*, **51**, 3728 (1969)
- [194] Stillinger, F.H. and Weber, T.A., *Phys. Rev. A*, **25**, 978 (1982)
- [195] Stillinger, F.H. and Weber, T.A., *Science*, **225**, 983 (1984)
- [196] Stillinger, F.H., *Phys. Rev. E*, **59**, 48 (1999)
- [197] Heuer, A., *J. Phys. Cond. Mat.*, **20**, 373101 (2008)
- [198] Sciortino, F., Kob, W. and Tartaglia, P., *Phys. Rev. Lett.*, **83**, 3214 (1999)
- [199] Wales, D.J. and Doye, J.P.K., *Phys. Rev. B*, **63**, 214204 (2001)
-

- 
- [200] Wales, D.J., *Mol. Phys.*, **78**, 151 (1993)
- [201] Büchner, S. and Heuer, A., *Phys. Rev. E*, **60**, 6507 (1999)
- [202] Doye, J.P.K. and Wales, D.J., *J. Chem. Phys.*, **102**, 9659 (1995)
- [203] Calvo, F., Doye, J.P.K. and Wales, D.J., *J. Chem. Phys.*, **115**, 9627 (2001)
- [204] Murrell, J.N. and Laidler, K.J., *Trans. Faraday Soc.*, **64**, 371 (1968)
- [205] Wales, D.J., *Mol. Phys.*, **100**, 3285 (2002)
- [206] Trygubenko, S.A. and Wales, D.J., *J. Chem. Phys.*, **124**, 234110 (2006)
- [207] Wales, D.J., *J. Chem. Phys.*, **130**, 204111 (2009)
- [208] Chakraborty, D., Collepardo-Guevara, R. and Wales, D.J., *J. Am. Chem. Soc.*, **136**, 18052 (2014)
- [209] Röder, K. and Wales, D.J., *J. Chem. Theor. Comput.*, **13**, 1468 (2017)
- [210] Wales, D.J. and Bogdan, T.V., *J. Phys. Chem. B*, **110**, 20765 (2006)
- [211] Levinthal, C., in *Mössbauer Spectroscopy in Biological Systems: Proceedings of a meeting held at Allerton House, Monticello, Illinois* (University of Illinois Press, Urbana, IL, 1969)
- [212] Wolynes, P.G., *Biochimie*, **119**, 218 (2015)
- [213] de Souza, V.K. and Wales, D.J., *J. Stat. Mech.*, **2016**, 074001 (2016)
- [214] Doliwa, B. and Heuer, A., *J. Phys. Cond. Mat.*, **15**, S849 (2003)
- [215] Saksengwijit, A., Reinisch, J. and Heuer, A., *Phys. Rev. Lett.*, **93**, 235701 (2004)
- [216] Saksengwijit, A. and Heuer, A., *J. Phys. Cond. Mat.*, **19**, 205143 (2007)
- [217] Rehwald, C. and Heuer, A., *Phys. Rev. E*, **86**, 051504 (2012)
- [218] Rehwald, C., Rubner, O. and Heuer, A., *Phys. Rev. Lett.*, **105**, 117801 (2010)
- [219] Horbach, J., Kob, W., Binder, K. and Angell, C.A., *Phys. Rev. E*, **54**, R5897 (1996)
- [220] Horbach, J. and Kob, W., *Phys. Rev. B*, **60**, 3169 (1999)
- [221] Stillinger, F.H., *Science*, **267**, 1935 (1995)
- [222] Skilling, J., *AIP Conference Proceedings*, **735**, 395 (2004)
- [223] Skilling, J., *Bayesian Anal.*, **1**, 833 (2006)
- [224] Saika-Voivod, I., Poole, P.H. and Sciortino, F., *Nature*, **412**, 514 (2001)
-

- 
- [225] Sastry, S., Debenedetti, P.G. and Stillinger, F.H., *Nature*, **393**, 554 (1998)
- [226] Jund, P. and Jullien, R., *Phys. Rev. Lett.*, **83**, 2210 (1999)
- [227] Büchner, S. and Heuer, A., *Phys. Rev. Lett.*, **84**, 2168 (2000)
- [228] Middleton, T.F. and Wales, D.J., *Phys. Rev. B*, **64**, 024205 (2001)
- [229] Doliwa, B. and Heuer, A., *Phys. Rev. E*, **67**, 031506 (2003)
- [230] Doliwa, B. and Heuer, A., *Phys. Rev. E*, **67**, 030501(R) (2003)
- [231] Doliwa, B. and Heuer, A., *Phys. Rev. Lett.*, **91**, 235501 (2003)
- [232] Middleton, T.F. and Wales, D.J., *J. Chem. Phys.*, **118**, 4583 (2003)
- [233] de Souza, V.K. and Wales, D.J., *J. Chem. Phys.*, **129**, 164507 (2008)
- [234] Saksengwitt, A. and Heuer, A., *Phys. Rev. E*, **73**, 061503 (2006)
- [235] Berthier, L., *Phys. Rev. E*, **76**, 011507 (2007)
- [236] Coslovich, D. and Pastore, G., *J. Phys. Cond. Mat.*, **21**, 285107 (2009)
- [237] Ohmine, I., *J. Phys. Chem.*, **99**, 6767 (1995)
- [238] Appignanesi, G.A., Fris, J.A., Montani, R.A. and Kob, W., *Phys. Rev. Lett.*, **96**, 8 (2006)
- [239] Heuer, A., Doliwa, B. and Saksengwitt, A., *Phys. Rev. E*, **72**, 021503 (2005)
- [240] Rubner, O. and Heuer, A., *Phys. Rev. E*, **78**, 011504 (2008)
- [241] Stariolo, D.A., Arenzon, J.J. and Fabricius, G., *Physica A*, **340**, 316 (2004)
- [242] Jung, Y., Garrahan, J.P. and Chandler, D., *J. Chem. Phys.*, **123**, 084509 (2005)
- [243] Chaudhuri, P., Berthier, L. and Kob, W., *Phys. Rev. Lett.*, **99**, 060604 (2007)
- [244] Doye, J.P.K. and Wales, D.J., *J. Chem. Phys.*, **116**, 3777 (2002)
- [245] Niblett, S.P., Biedermann, M., Wales, D.J. and de Souza, V.K., *J. Chem. Phys.*, **147**, 152726 (2017)
- [246] Souza, V.K.D., Stevenson, J.D., Niblett, S.P., Farrell, J.D. and Wales, D.J., *J. Chem. Phys.*, **146**, 124103 (2017)
- [247] Angelani, L., Ruocco, G., Sampoli, M. and Sciortino, F., *J. Chem. Phys.*, **119**, 2120 (2003)
- [248] Angelani, L., Di Leonardo, R., Ruocco, G., Scala, A. and Sciortino, F., *Phys. Rev. Lett.*, **85**, 5356 (2000)
-

- 
- [249] Angelani, L., De Michele, C., Ruocco, G. and Sciortino, F., *J. Chem. Phys.*, **121**, 7533 (2004)
- [250] Keyes, T., *J. Phys. Chem. A*, **101**, 2921 (1997)
- [251] Donati, C., Sciortino, F. and Tartaglia, P., *Phys. Rev. Lett.*, **85**, 1464 (2000)
- [252] Bembenek, S.D. and Laird, B.B., *Phys. Rev. Lett.*, **74**, 936 (1995)
- [253] Lennard-Jones, J.E., *Proc. R. Soc. A*, **106**, 463 (1924)
- [254] de Souza, V.K. and Wales, D.J., *Phys. Rev. B*, **74**, 134202 (2006)
- [255] de Souza, V.K. and Wales, D.J., *Phys. Rev. Lett.*, **96**, 057802 (2006)
- [256] de Souza, V.K. and Wales, D.J., *J. Chem. Phys.*, **130**, 194508 (2009)
- [257] Voter, A.F., Montalenti, F. and Germann, T.C., *Ann. Rev. Mater. Res.*, **32**, 321 (2002)
- [258] Tuckerman, M.E., *Statistical Mechanics: Theory and Molecular Simulation* (Oxford University Press, Oxford, 2010)
- [259] Allen, M.P. and Tildesley, D.J., *Computer Simulation of Liquids*, Second Edition (Oxford University Press, Oxford, 2017)
- [260] Adcock, S.A. and McCammon, J.A., *Chem. Rev.*, **106**, 1589 (2006)
- [261] Verlet, L., *Phys. Rev.*, **159**, 98 (1967)
- [262] Swope, W.C., Andersen, H.C., Berens, P.H. and Wilson, K.R., *J. Chem. Phys.*, **76**, 637 (1982)
- [263] Gear, C.W., *Math. Comp.*, **21**, 146 (1967)
- [264] Tuckerman, M., Berne, B.J. and Martyna, G.J., *J. Chem. Phys.*, **97**, 1990 (1992)
- [265] Eastwood, M.P., Stafford, K.A., Lippert, R.A., Jensen, M., Maragakis, P., Predescu, C., Dror, R.O. and Shaw, D.E., *J. Chem. Theor. Comput.*, **6**, 2045 (2010)
- [266] Andersen, H.C., *J. Chem. Phys.*, **72**, 2384 (1980)
- [267] Nos, S., *Mol. Phys.*, **52**, 255 (1984)
- [268] Hoover, W.G., Ladd, A.J.C. and Moran, B., *Phys. Rev. Lett.*, **48**, 1818 (1982)
- [269] Ryckaert, J., Ciccotti, G. and Berendsen, H., *J. Comp. Phys.*, **23**, 327 (1977)
- [270] Andersen, H.C., *J. Comp. Phys.*, **52**, 24 (1983)
- [271] Okumura, H., Itoh, S.G. and Okamoto, Y., *J. Chem. Phys.*, **126**, 084103 (2007)
-

- 
- [272] Evans, D.J., *Mol. Phys.*, **34**, 317 (1977)
- [273] Thirumalai, D., Mountain, R.D. and Kirkpatrick, T.R., *Phys. Rev. A*, **39**, 3563 (1989)
- [274] Rahman, A., *Phys. Rev.*, **136**, A405 (1964)
- [275] Mountain, R.D. and Thirumalai, D., *J. Phys. Chem.*, **93**, 6975 (1989)
- [276] Wales, D.J., GMIN: A program for finding global minima and calculating thermodynamic properties
- [277] Wales, D.J., OPTIM: A program for characterising stationary points and reaction pathways
- [278] Wales, D.J., PATHSAMPLE: A driver for OPTIM to create stationary point databases using discrete path sampling and perform kinetic analysis
- [279] Wales, D.J., PELE: the Python Energy Landscape Explorer
- [280] Nocedal, J., *Math. Comput.*, **35**, 773 (1980)
- [281] Liu, D. and Nocedal, J., *Math. Prog.*, **45**, 503 (1989)
- [282] Chill, S.T., Stevenson, J., Ruehle, V., Shang, C., Xiao, P., Farrell, J.D., Wales, D.J. and Henkelman, G., *J. Chem. Theor. Comput.*, **10**, 5476 (2014)
- [283] Kirkpatrick, S., Gelatt, C.D. and Vecchi, M.P., *Science*, **220**, 671 (1983)
- [284] Wales, D.J. and Doye, J.P.K., *J. Phys. Chem. A*, **101**, 5111 (1997)
- [285] Kushima, A., Lin, X. and Yip, S., *J. Phys. Cond. Mat.*, **21**, 504104 (2009)
- [286] Strodel, B., Lee, J.W.L., Whittleston, C.S. and Wales, D.J., *J. Am. Chem. Soc.*, **132**, 13300 (2010)
- [287] Henkelman, G. and Jónsson, H., *J. Chem. Phys.*, **113**, 9978 (2000)
- [288] Henkelman, G., Uberuaga, B.P. and Jónsson, H., *J. Chem. Phys.*, **113**, 9901 (2000)
- [289] Trygubenko, S.A. and Wales, D.J., *J. Chem. Phys.*, **120**, 2082 (2004)
- [290] Sheppard, D., Terrell, R. and Henkelman, G., *J. Chem. Phys.*, **128**, 134106 (2008)
- [291] Munro, L.J. and Wales, D.J., *Phys. Rev. B*, **59**, 3969 (1999)
- [292] Zeng, Y., Xiao, P. and Henkelman, G., *J. Chem. Phys.*, **140**, 044115 (2014)
- [293] Mantell, R.G., Pitt, C.E. and Wales, D.J., *J. Chem. Phys.*, **12**, 6182 (2016)
- [294] Dijkstra, E., *Numerische Mathematik*, **1**, 269 (1959)

- 
- [295] Carr, J.M., Trygubenko, S.A. and Wales, D.J., *J. Chem. Phys.*, **122**, 234903 (2005)
- [296] Strodel, B., Whittleston, C.S. and Wales, D.J., *J. Am. Chem. Soc.*, **129**, 16005 (2007)
- [297] Becker, O.M. and Karplus, M., *J. Chem. Phys.*, **106**, 1495 (1997)
- [298] Wales, D.J., Miller, M.A. and Walsh, T.R., *Nature*, **394**, 758 (1998)
- [299] Wales, D.J. and Ohmine, I., *J. Chem. Phys.*, **98**, 7257 (1993)
- [300] Rapaport, D., *J. Chem. Phys.*, **60**, 306 (1985)
- [301] Altmann, S.L., *Rotations, Quaternions, and Double Groups*, Clarendon Press, Oxford, 1986
- [302] Chakrabarti, D., Kusumaatmaja, H., Rühle, V. and Wales, D.J., *Phys. Chem. Chem. Phys.*, **16**, 5014 (2014)
- [303] Kusumaatmaja, H., Whittleston, C.S. and Wales, D.J., *J. Chem. Theor. Comput.*, **8**, 5159 (2012)
- [304] Rühle, V., Kusumaatmaja, H., Chakrabarti, D. and Wales, D.J., *J. Chem. Theor. Comput.*, **9**, 4026 (2013)
- [305] Chakrabarti, D. and Wales, D., *Phys. Chem. Chem. Phys.*, **11**, 1970 (2009)
- [306] Joseph, J.A., Whittleston, C.S. and Wales, D.J., *J. Chem. Theor. Comput.*, **12**, 6109 (2016)
- [307] Li, X., *J. Graphics Tools*, **12**, 1 (2007)
- [308] Niblett, S.P., de Souza, V.K., Stevenson, J.D. and Wales, D.J., *J. Chem. Phys.*, **145**, 024505 (2016)
- [309] Mallamace, F., Corsaro, C., Leone, N., Villari, V., Micali, N. and Chen, S.H., *Sci. Rep.*, **4**, 3747 (2014)
- [310] Kudchadkar, S.R. and Wiest, J.M., *J. Chem. Phys.*, **103**, 8566 (1995)
- [311] Mossa, S., Di Leonardo, R., Ruocco, G. and Sampoli, M., *Phys. Rev. E*, **62**, 612 (2000)
- [312] Ghosh, J. and Faller, R., *Mater. Res. Soc. Symp. Proc.*, **924**, 0924 (2006)
- [313] Lewis, L.J. and Wahnström, G., *Phys. Rev. E*, **50**, 3865 (1994)
- [314] Stoddard, S.D. and Ford, J., *Phys. Rev. A*, **8**, 1504 (1973)
- [315] van Meel, J.A., Filion, L., Valeriani, C. and Frenkel, D., *J. Chem. Phys.*, **136**, 234107 (2012)

- 
- [316] de Souza, V. K., personal communication
- [317] Cao, P., Li, M., Heugle, R.J., Park, H.S. and Lin, X., *Phys. Rev. E*, **86**, 016710 (2012)
- [318] Soules, T.F., Gilmer, G.H., Matthews, M.J., Stolken, J.S. and Feit, M.D., *J. Non-Cryst. Solids*, **357**, 1564 (2011)
- [319] Saika-Voivod, I., Sciortino, F. and Poole, P.H., *Phys. Rev. E*, **69**, 041503 (2004)
- [320] Hess, K.U., Dingwell, D. and Rössler, E., *Chem. Geol.*, **128**, 155 (1996), 5<sup>th</sup> Silicate Melt Workshop
- [321] Rössler, E., Hess, K.U. and Novikov, V., *J. Non-Cryst. Solids*, **223**, 207 (1998)
- [322] Horbach, J., Kob, W. and Binder, K., *Philos. Mag. B*, **77**, 297 (1998)
- [323] Sarnthein, J., Pasquarello, A. and Car, R., *Phys. Rev. B*, **52**, 12690 (1995)
- [324] Vollmayr-Lee, K. and Zippelius, A., *Phys. Rev. E*, **88**, 052145 (2013)
- [325] Kushima, A., Lin, X., Li, J., Qian, X., Eapen, J., Mauro, J.C., Diep, P. and Yip, S., *J. Chem. Phys.*, **131**, 164505 (2009)
- [326] van Beest, B.W.H., Kramer, G.J. and van Santen, R.A., *Phys. Rev. Lett.*, **64**, 1955 (1990)
- [327] Buckingham, R.A., *Proc. R. Soc. A*, **168**, 264 (1938)
- [328] Fennell, C.J. and Gezelter, J.D., *J. Chem. Phys.*, **124**, 234104 (2006)
- [329] Ewald, P.P., *Annalen der Physik*, **369**, 253 (1921)
- [330] Wolf, D., in *Computer Simulation Studies in Condensed-Matter Physics VIII*, eds. D. Landau and H. Schüttler (Springer-Verlag Berlin, Heidelberg, 1995)
- [331] Woodcock, L., in *Advances in molten salt chemistry* Vol. 3, eds. J. Braunstein *et al.*, (Plenum Press, New York, 1975)
- [332] Wolf, D., Koblinski, P., Phillpot, S.R. and Eggebrecht, J., *J. Chem. Phys.*, **110**, 8254 (1999)
- [333] Carr, A., Berthier, L., Horbach, J., Ispas, S. and Kob, W., *J. Chem. Phys.*, **127**, 114512 (2007)
- [334] Saksengwijit, A. and Heuer, A., *Phys. Rev. E*, **74**, 051502 (2006)
- [335] Reinisch, H. and Heuer, A., *Phys. Rev. Lett.*, **95**, 155502 (2005)
- [336] Thirumalai, D., Mountain, R.D. and Kirkpatrick, T.R., *Phys. Rev. A*, **39**, 3563 (1989)
-

- 
- [337] Mikkelsen Jr, J., *Appl. Phys. Lett.*, **45**, 1187 (1984)
- [338] Brebec, G., Seguin, R., Sella, C., Bevenot, J. and Martin, J., *Acta Metallurgica*, **28**, 327 (1980)
- [339] La Nave, E., Stanley, H.E. and Sciortino, F., *Phys. Rev. Lett.*, **88**, 035501 (2002)
- [340] Kushima, A., Lin, X., Li, J., Eapen, J., Mauro, J.C., Qian, X., Diep, P. and Yip, S., *J. Chem. Phys.*, **130**, 224504 (2009)
- [341] Griffiths, M., Niblett, S. and Wales, D.J., *J. Chem. Theor. Comput.*, **13**, 4914 (2017)
- [342] de Souza, V.K., *Glassy Dynamics and the Potential Energy Landscape*, Ph.D. thesis, University of Cambridge (2008)
- [343] Kob, W. and Berthier, L., *Phys. Rev. Lett.*, **110**, 245702 (2013)
- [344] Krakoviack, V., *Phys. Rev. E*, **75**, 031503 (2007)
- [345] Berthier, L., *Phys. Rev. E*, **88**, 022313 (2013)
- [346] Jonker, R. and Volgenant, A., *Computing*, **38**, 325 (1987)
- [347] Wales, D.J. and Carr, J.M., *J. Chem. Theor. Comput.*, **8**, 5020 (2012)
- [348] Berthier, L., Biroli, G., Bouchaud, J.P., Kob, W., Miyazaki, K. and Reichman, D.R., *J. Chem. Phys.*, **126**, 184503 (2007)
- [349] Berthier, L. and Jack, R.L., *Phys. Rev. Lett.*, **114**, 205701 (2015)
- [350] Jack, R.L. and Berthier, L., **021120**, 021120 (2012)
- [351] Yeomans, J.M., *Statistical Mechanics of Phase Transitions* (Clarendon Press, Oxford, 1992)
- [352] Goldenfeld, N., *Lectures on phase transitions and the renormalization group* (Addison-Wesley, Reading, MA, 1992)
- [353] Wales, D.J., *Phil. Trans. Roy. Soc. A*, **370**, 2877 (2012)
- [354] Jr., J.H.W., *J. Am. Stat. Assoc.*, **58**, 236 (1963)
- [355] Girvan, M. and Newman, M.E.J., *Proc. Natl. Acad. Sci. USA*, **99**, 7821 (2002)
- [356] Szekely, G.J. and Rizzo, M.L., *Journal of Classification*, **22**, 151 (2005)
- [357] Kuhn, H.W., *Naval Research Logistics Quarterly*, **2**, 83 (1955)
- [358] Munkres, J., *Journal of the Society for Industrial and Applied Mathematics*, **5**, 32 (1957)
- [359] Bogdan, T.V., Wales, D.J. and Calvo, F., *J. Chem. Phys.*, **124**, 044102 (2006)